

Advances in Dielectrics
Series Editor: Friedrich Kremer

Marian Paluch *Editor*

Dielectric Properties of Ionic Liquids

 Springer

Advances in Dielectrics

Series editor

Friedrich Kremer, Leipzig, Germany

Aims and Scope

Broadband Dielectric Spectroscopy (BDS) has developed tremendously in the last decade. For dielectric measurements it is now state of the art to cover typically 8–10 decades in frequency and to carry out the experiments in a wide temperature and pressure range. In this way a wealth of fundamental studies in molecular physics became possible, e.g. the scaling of relaxation processes, the interplay between rotational and translational diffusion, charge transport in disordered systems, and molecular dynamics in the geometrical confinement of different dimensionality—to name but a few. BDS has also proven to be an indispensable tool in modern material science; it plays e.g. an essential role in the characterization of Liquid Crystals or Ionic Liquids and the design of low-loss dielectric materials.

It is the aim of “Advances in Dielectrics” to reflect this rapid progress with a series of monographs devoted to specialized topics.

Target Group

Solid state physicists, molecular physicists, material scientists, ferroelectric scientists, soft matter scientists, polymer scientists, electronic and electrical engineers.

More information about this series at <http://www.springer.com/series/8283>

Marian Paluch
Editor

Dielectric Properties of Ionic Liquids

 Springer

Editor
Marian Paluch
Institute of Physics
University of Silesia in Katowice
Katowice
Poland

ISSN 2190-930X

Advances in Dielectrics

ISBN 978-3-319-32487-6

DOI 10.1007/978-3-319-32489-0

ISSN 2190-9318 (electronic)

ISBN 978-3-319-32489-0 (eBook)

Library of Congress Control Number: 2016939383

© Springer International Publishing Switzerland 2016

This work is subject to copyright. All rights are reserved by the Publisher, whether the whole or part of the material is concerned, specifically the rights of translation, reprinting, reuse of illustrations, recitation, broadcasting, reproduction on microfilms or in any other physical way, and transmission or information storage and retrieval, electronic adaptation, computer software, or by similar or dissimilar methodology now known or hereafter developed.

The use of general descriptive names, registered names, trademarks, service marks, etc. in this publication does not imply, even in the absence of a specific statement, that such names are exempt from the relevant protective laws and regulations and therefore free for general use.

The publisher, the authors and the editors are safe to assume that the advice and information in this book are believed to be true and accurate at the date of publication. Neither the publisher nor the authors or the editors give a warranty, express or implied, with respect to the material contained herein or for any errors or omissions that may have been made.

Printed on acid-free paper

This Springer imprint is published by Springer Nature

The registered company is Springer International Publishing AG Switzerland

Preface

Over the past decade, ionic liquids (ILs) have received a considerable scientific attention due to their unique physical properties (such as low melting points, low vapor pressure, non-flammability, thermal and chemical stability, or broad electrochemical window) and wide range of potential applications. An appropriate combination of cations and anions makes them attractive as potential pharmaceutical ingredients, green solvents as well as, promising electrolytes for fuel cells and batteries. However, progress in electrochemical field is still hindered by the limited understanding of the charge transport mechanism as well as the interplay between molecular structure and dynamics in ionic conductors. Therefore, in the last years many efforts of scientific community have been dedicated to comprehend the behavior of electric conductivity in various ion-containing systems (protic, aprotic as well as polymerized ionic liquids) and under various thermodynamic conditions.

This book provides a comprehensive survey of electrical properties of ionic liquids and solids obtained from studies involving broadband dielectric spectroscopy (BDS) both at ambient and elevated pressure. The book begins by reviewing the synthesis, purification and characterization of ionic liquids, presented in Chap. 1. In the “*Introduction to Ionic Liquids*” selected physical properties of ionic liquids such as thermal stability, melting point, glass transition, semi-crystallinity and viscosity are also discussed.

In Chap. 2, with the ambitious title “*Rotational and translational diffusion in ionic liquids*”, new insights into the dominant mechanisms of ionic conductivity and structural dynamics obtained from studies involving broadband dielectric spectroscopy (BDS), pulsed field gradient nuclear magnetic resonance, dynamic mechanical spectroscopy, and dynamic light scattering techniques are presented. Additionally, in the same section a novel approach to extract diffusion coefficients from dielectric spectra in an extra-ordinarily broad range spanning over 10 orders of magnitude is provided.

On the other hand, Chap. 3 discusses the molecular motions of room temperature ionic liquids (RTILs) in the timescale ranging from femto- to nanoseconds at ambient temperatures. Therein, we show that the interactions in RTILs are not only

governed by long-ranged Coulombic forces. Also hydrogen-bonding, pi–pi stacking and dispersion forces contribute significantly to the local potential energy landscape, making RTIL dynamics extremely complex.

Chapter 4 summarizes recent advances in high pressure dielectric studies of ionic liquids and solids. The pressure sensitivity of DC-conductivity is discussed in terms of activation volume parameter and dT_g/dP coefficient. Within this section the transport properties of ionic conductors are analyzed not only in T-P thermodynamic space but also as a function of volume. This procedure enable us to discuss the contributions of density and thermal effects to ion dynamics near T_g as well as to verify the validity of the thermodynamic scaling concept for ionic systems. We also address the role played by charge transport mechanism (vehicle vs. Grotthuss type) on the isobaric and isothermal dependences of DC-conductivity and conductivity relaxation times when approaching the glass transition.

Chapters 5 and 6 review recent efforts to investigate polymerized ionic liquids and polymer electrolytes, being respectively macromolecular counterparts of ILs and salts inserted into polymer matrix. Chapter 5 discusses the fundamental properties of polymerized ionic liquids such as molecular dynamics, charge transport and mesoscopic structure and compares them with the properties of monomers.

At the beginning of Chap. 6 we give a brief overview of the protocols usually employed to analysis the dielectric spectrum of polymer electrolytes. The quantitative change of dielectric relaxation in polymers with the addition of salts will then be discussed primarily based on results from polypropylene glycols. The focus of the last part of the chapter is placed on the relationship between ionic transport and polymer relaxation.

Chapter 7 describes the current level of understanding of the electrode | IL interface. We show that broadband impedance spectroscopy in a three-electrode setup yields electrode-potential-dependent double layer capacitance values of the electrode | IL interface. The results of dielectric studies are compared with information obtained from other techniques, such as scanning tunnelling microscopy, atomic force microscopy, surface force apparatus measurements, X-ray reflectivity measurements, surface-enhanced Raman spectroscopy and sum-frequency generation vibrational spectroscopy.

In Chap. 8 an overview on the recent results for electrochemical double layers in ionic liquids at flat, rough, and porous electrodes is given. We show that electrode polarization effects can be used to directly determine the complex dielectric function of ionic liquids at the interface with a metal electrode. Our approach allows thus a systematic investigation of the electric and dielectric properties of ionic liquids at metal interfaces and opens the perspectives of a better understanding of the physics of charge transport at solid interfaces.

The decoupling between structural and conductivity relaxation in various aprotic ionic liquids is reported in Chap. 9. Therein, we took advantage from several calorimetric techniques (e.g. AC-calorimetry, temperature modulated differential scanning calorimetry (TMDSC)) to probe the dynamic glass transition of ionic systems. We demonstrate that for ion conducting materials, a significant difference

between conductivity relaxation and shear relaxation (viscosity) can be found. Consequently, in some cases it is not an easy task to determine definitely the dynamic glass transition from dielectric relaxation data.

Editor would like to thank all the contributors to this volume for their efficient collaborations. Contributions of M. Paluch and Z. Wojnarowska to this book were made as a part of research Opus 8 project (No. DEC-2014/15/B/ST3/04246). J. Hunger and R. Buchner also thank the Deutsche Forschungsgemeinschaft for funding within the priority program SPP 1191. The writing of fifth chapter was supported by the Oak Ridge National Laboratory's Center for Nanophase Materials Sciences, which is a DOE Office of Science User Facility. Joshua Sangoro acknowledges the National Science Foundation for financial support through the award number DMR-1508394. The authors of Chap. 5 are grateful for the financial support from the Deutsche Forschungsgesellschaft under the DFG-projects: Neue Polymermaterialien auf der Basis von funktionalisierten ionischen Flüssigkeiten für Anwendungen in Membranen 'Erkenntnistransfer-Projekt' (KR 1138/24-1); and DFG SPP 1191 Priority Program on Ionic Liquids.

March 2016

Marian Paluch

Contents

1	Introduction to Ionic Liquids	1
	Veronika Strehmel	
2	Rotational and Translational Diffusion in Ionic Liquids	29
	Joshua Sangoro, Tyler Cosby and Friedrich Kremer	
3	Femto- to Nanosecond Dynamics in Ionic Liquids: From Single Molecules to Collective Motions	53
	Johannes Hunger and Richard Buchner	
4	High-Pressure Dielectric Spectroscopy for Studying the Charge Transfer in Ionic Liquids and Solids	73
	Z. Wojnarowska and M. Paluch	
5	Glassy Dynamics and Charge Transport in Polymeric Ionic Liquids	115
	Falk Frenzel, Wolfgang H. Binder, Joshua Rume Sangoro and Friedrich Kremer	
6	Ionic Transport and Dielectric Relaxation in Polymer Electrolytes	131
	Yangyang Wang	
7	Electrochemical Double Layers in Ionic Liquids Investigated by Broadband Impedance Spectroscopy and Other Complementary Experimental Techniques	157
	Bernhard Roling, Marco Balabajew and Jens Wallauer	
8	Dielectric Properties of Ionic Liquids at Metal Interfaces: Electrode Polarization, Characteristic Frequencies, Scaling Laws	193
	A. Serghei, M. Samet, G. Boiteux and A. Kallel	

9 Decoupling Between Structural and Conductivity Relaxation in Aprotic Ionic Liquids	213
Evgeni Shoifet, Sergey P. Verevkin and Christoph Schick	
Index	235

Chapter 1

Introduction to Ionic Liquids

Veronika Strehmel

Abstract Ionic liquids and polymerized ionic liquids possess a high application potential in synthesis, separation processes, and in processes relating to transport and storage of energy. Therefore, this introduction discusses synthetic ways to obtain ionic liquids as well as selected properties of ionic liquids. Knowledge of chemical reactions occurring during ionic liquid synthesis including purification procedures gives an insight into possible impurities, which may remain after the manufacturing process. The liquid range of ionic liquids with the glass transition temperature or the melting point as lower limit on the one hand and temperatures where weight loss is higher than 0.5 wt% during thermal treatment as possible upper limit is important for both investigation of ionic liquids as well as their application. A brief discussion of selected physical properties, such as viscosity, density, and polarity of ionic liquids should give a first impression about the broad variety of ionic liquid properties that are discussed in more detail in the following chapters. Furthermore, discussion of both polymerization of ionic liquid monomers using different polymerization mechanisms and selected properties of the polymer materials obtained will complete this introduction. The significant increase of the glass transition temperature of polymerized aprotic ionic liquids caused by polymerization of aprotic ionic liquid monomers exhibits differences in the properties between ionic liquids and polymerized ionic liquids.

Efficient use of naturally occurring energy resources, energy transport, and storage of energy belong to the important tasks in the twenty-first century. In this context, the understanding of the mobility of charge carriers is crucial to increase the efficiency of both the transport and the storage of energy. Charge carriers can be electrons and/or ions. The latter strongly relates to salts as neat material as well as

V. Strehmel (✉)

Institute for Coatings and Surface Chemistry, Niederrhein University of Applied Sciences,
Adlerstrasse 32, 47798 Krefeld, Germany
e-mail: veronika.strehmel@hs-niederrhein.de

the appearance in solution. Although the behavior of salt solutions is strongly affected by the properties of the solvent, ion mobility in salts strongly depends on their melting point. Ion mobility significantly increases in a salt melt compared to the solid state. Therefore, salts bearing low melting points are interesting for transport and storage of energy.

Development of ionic liquids started with the search for lower melting salts. They may be used as electrolytes because application of traditional molten salts efforts construction materials, which are stable during long time operation at elevated temperatures and do not undergo corrosion under the operation conditions [1]. The decrease of the melting point was first obtained by using eutectic mixtures of different inorganic salts, and second by variation of the structure of either the cation or the anion or both ions [2–5]. Structural variation of ions included not only inorganic ions but also organic ions resulting in a huge variety of salts with drastically reduced melting temperatures. Also ethyl ammonium nitrate, which was firstly described by Paul Walden in 1914, belongs to salts exhibiting a low melting temperature [2, 6]. This salt is generally considered as the first ionic liquid. The reduction of the melting temperature of molten salts from usually several hundred Celsius degree [1] to a significant lower temperature, e.g., lower than 100 °C or even below room temperature, opens the possibility to use additional methods for investigation of these low melting salts that are called ionic liquids [2]. Furthermore, the lower melting temperature of the ionic liquids has extended the application areas from batteries to electrochemical synthesis [7–10], solvents for inorganic [11–14], organic [2, 15–18] and polymer synthesis [19–23], co-solvents in biocatalytic processes [15, 24–26], solvents or additives in separation processes [27–31], lubricants [29] and so on [32, 33].

The name ionic liquids was created to separate the newly developed salts showing drastically reduced melting temperatures from the traditional molten salts. Furthermore, various definitions have been given for ionic liquids. One early definition indicates ionic liquids as molten salts, which are liquid below the boiling point of water [2, 34]. This definition of ionic liquids shows the enormous difference in the melting temperature compared to the traditional molten salts. However, systematic variation of the cation structure for example by variation of the alkyl substituent from methyl to a significantly larger alkyl substituent, e.g., an octadecyl group, does clearly show the limitation of this definition [35, 36]. An increase in the size of the alkyl substituent bound at either the cation or the anion results also in an increase of the melting point or glass transition temperature of the ionic liquid. Therefore, some of these substances are liquid only above 100 °C. A further definition was given by Ken Seddon, who called ionic liquids as “liquids that consist in their pure form entirely of ions” [37]. This definition does clearly separate ionic liquids from electrolyte solutions even if electrolyte solutions are highly concentrated.

Ionic liquids bearing a mobile proton are protic ionic liquids [38]. The mobile proton results in more intensive hydrogen bonding compared to the aprotic ionic liquids. Interesting developments in the field of ionic liquids cover their functionalization by the introduction of a functional group that may undergo various

interactions with solutes or even chemical reactions, e.g., polymerizations. Examples for functional groups attached to the cation of ionic liquids are hydroxyl [39–43], nitrile [44], vinyl [45–68], or (meth)acrylate groups, respectively [69–86]. Mostly, ionic liquids substituted with a polymerizable functional group are aprotic ionic liquids, although a few examples exist for polymerizable protic ionic liquids either [87]. Nevertheless, the resulting polymer materials no longer belong to ionic liquids because polymerization results in significant increase in glass transition temperature, and therefore, in significant decrease of the mobility of the single segments bound in the polymer chain. Nevertheless, they derive from an ionic liquid ion substituted with a polymerizable functional group. However, mobility of the counter ion significantly distinguishes from the mobility of single ionic segments of the polymer chain in case of non-crosslinked polymers derived from ionic liquids. Furthermore, ionic liquid monomer structures grafted to a silica surface [88] distinguish from polymerized ionic liquids caused by the lower concentration of the ionic structures as well as by the interactions with the silica surface.

This chapter covers examples of traditional and functionalized ionic liquids as well as polymers made of them including possible impurities originating from the ionic liquid manufacturing process. Furthermore, selected properties of ionic liquids are discussed. These are liquid range, viscosity, density, and polarity. These properties may be important for further discussions and understanding of dielectric properties of ionic liquids.

1.1 Synthetic Ways to Ionic Liquids as Source for Possible Impurities

Several methods have been applied for synthesis of ionic liquids. Protic ionic liquids are made by neutralization reaction of a strong acid with a strong base followed by distillation of the resulting water [38]. This method was already applied by Paul Walden, who obtained ethyl ammonium nitrate by neutralization of nitric acid with ethyl amine (Fig. 1.1a). Other primary amine compounds, such as methyl amine, *n*-butyl amine or 2-hydroxyethyl amine, and an organic acid, e.g., formic acid result in formation of methyl ammonium formate, ethyl ammonium formate, *n*-butylammonium formate, and 2-hydroxyethyl ammonium formate [89, 90]. The organic acid is less acidic compared to the inorganic acid. Therefore, the equilibrium between the non-dissociated acid and the ions formed are necessary to take into consideration.

Furthermore, neutralization of an oligoether bearing a carboxylic acid group at one end, e.g., 2,5,8,11-tetraoxatridecan-13-oic acid with an alkali hydroxide, e.g., lithium hydroxide, sodium hydroxide, or potassium hydroxide, results in alkali methyl oligoether carboxylates while water formed must be removed by distillation (Fig. 1.1b) [91, 92].

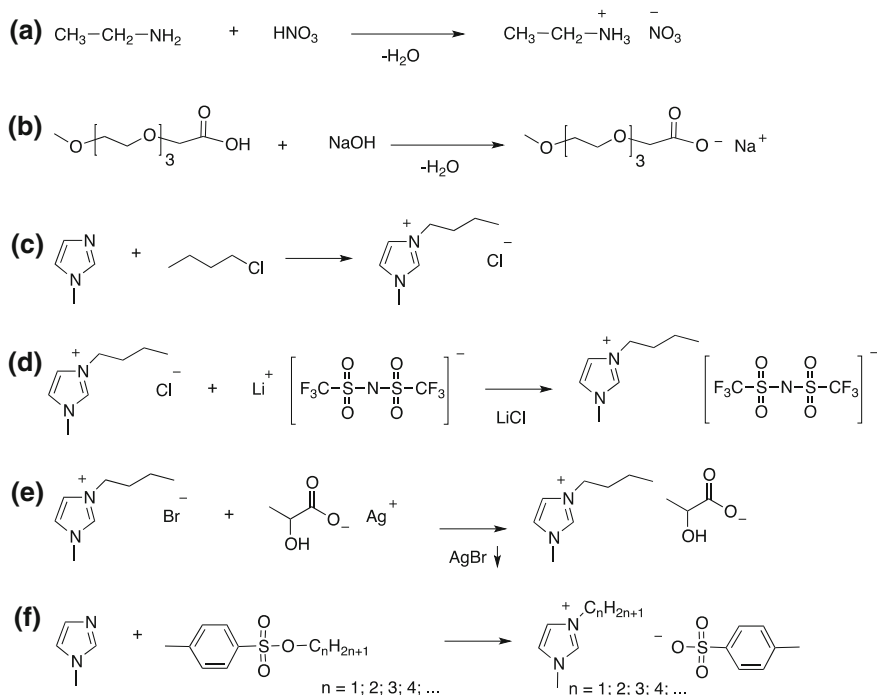


Fig. 1.1 Synthetic ways to ionic liquids: **a** neutralization of a strong acid with a strong base to obtain a protic ionic liquid; **b** neutralization of an oligoethylene oxide substituted with a carboxylic acid group by a strong base; **c** alkylation of an organic base using an alkyl halide (chloride, bromide or iodide) to make starting materials for a huge variety of ionic liquids; **d** anion exchange resulting in a hydrophobic ionic liquid; **e** anion exchange using a silver salt resulting in an aprotic ionic liquid; **f** alkylation of an organic base using alkyl-*p*-toluene sulfonate to give halide free ionic liquids

A widely applied way to synthesize ionic liquids is alkylation of an organic base, e.g., *N*-methyl imidazole, with alkyl halide, e.g., 1-chloro butane. This reaction results for example in 1-butyl-3-methylimidazolium chloride (Fig. 1.1c) [93]. Various other organic bases, such as tertiary aliphatic or cycloaliphatic amines, and further aromatic heterocyclic compounds containing at least one nitrogen atom are available for alkylation, and further alkyl halides are useful in this reaction as well. The quaternary ammonium halide can be applied as starting material for a huge number of ionic liquids bearing various anions. One example is anion exchange with lithium bis(trifluoromethylsulfonyl)imide in water solution resulting in e.g., 1-butyl-3-methylimidazolium bis(trifluoromethylsulfonyl)imide (Fig. 1.1d) [94]. The starting materials and the lithium chloride, which is formed as by-product, dissolve well in water. In contrast to this, 1-butyl-3-methylimidazolium bis(trifluoromethylsulfonyl)imide is a hydrophobic ionic liquid separating well from the water phase. Nevertheless, washing of the ionic liquid with water with the focus to remove traces of halide requires intensive drying of the resulting ionic liquid. These

steps are necessary for purification. A further method for anion exchange includes reaction of the ammonium halide with a silver salt resulting in precipitation of silver halide from the solution although the ionic liquid, e.g., 1-butyl-3-methylimidazolium lactate, keeps in solution (Fig. 1.1e) [95]. Quantitative precipitation of the silver halide formed as by product and quantitative removal of the solvent are required to obtain a pure ionic liquid in this synthetic route. Furthermore, direct alkylation of a tertiary amine, e.g., 1-methylimidazole, using alkyl tosylates results in halide free ionic liquids (Fig. 1.1f).¹ Moreover, other ester compounds, such as alkyl sulfonates, alkyl sulfates, and alkyl phosphates may be applied for synthesis of halide free ionic liquids either [95, 96].

In case that the organic base comprises a polymerizable functional group, e.g., a vinyl group or a methacrylate group, quaternization of the organic base with alkyl halide followed by counter ion exchange results in functionalized ionic liquids (Fig. 1.2 [97]). These functionalized ionic liquids are starting materials for manufacture of new ionic polymers.

Quantitative conversion or quantitative removal of nonconverted starting materials and remaining traces of solvents used for synthesis of ionic liquids is necessary in all reactions discussed in Fig. 1.1. Furthermore, all ionic liquids discussed in Fig. 1.1 may contain traces of water. Therefore, determination of the water content, e.g., by Karl Fischer Analysis [98, 99] is necessary because water affects the physical properties of the ionic liquids and dielectric spectra of ionic liquids either. Moreover, traces of halide remaining in the ionic liquids made by the methods discussed in Figs. 1.1d, e and 1.2b, d require removal as well. These ions have an impact on both physical properties of the ionic liquids and dielectric spectra measured.

Physical properties of ionic liquids are important for their application. They strongly relate to the structure of ionic liquids. The broad structural variability of the cation and the anion as well as their combination in ionic liquids results in a broad variation of their properties on the one hand. This makes selection of an ionic liquid also difficult for a special application on the other hand. Among the physical properties, the liquid range determines the temperature range for application of ionic liquids.

¹In a general procedure for synthesis of the 1-alkyl-3-methylimidazolium tosylates a mixture of 1-methylimidazole dissolved in dry acetonitrile was slowly dropped into a stirred solution of alkyltosylate dissolved in acetonitrile at 5 °C. The mole ratio was 1.2 for 1-methylimidazole to the alkyltosylate. The resulting mixture was further stirred during heating up to room temperature for 1 h and then refluxing at 70 °C for 5 h. After the reaction was complete, acetonitrile was removed under vacuo. The residue was washed several times with ethyl acetate to remove the remaining excess of 1-methylimidazole. The crystalline product was heated in fresh dry ethyl acetate up to the boiling point of the solvent. Crystallization of the 1-alkyl-3-methylimidazolium tosylates occurred again after cooling to room temperature. Isolation of the crystalline material and drying under vacuo resulted in halide free 1-alkyl-3-methylimidazolium tosylates.

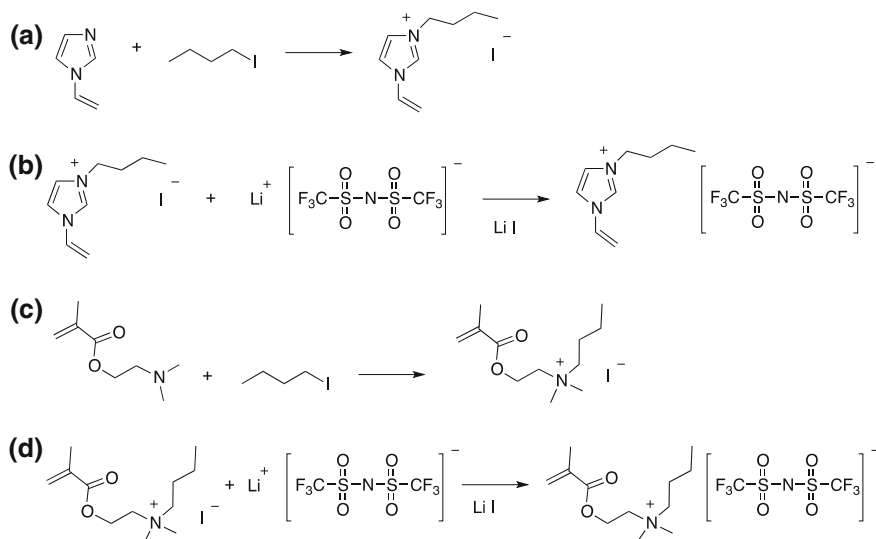


Fig. 1.2 Synthetic ways to functionalized ionic liquids bearing a polymerizable functional group at the cation: **a** alkylation of *N*-vinylimidazole with alkyl iodide; **b** anion exchange using lithium bis(trifluoromethylsulfonyl)imide resulting in a hydrophobic vinyl imidazolium salt; **c** alkylation of *N,N*-dimethylaminoethyl methacrylate with alkyl iodide; **d** anion exchange using lithium bis(trifluoromethylsulfonyl)imide resulting in a hydrophobic *N*-alkyl-*N*-methacryloyloxyethyl-*N,N*-dimethyl ammonium salt

1.2 Liquid Range of Ionic Liquids

In analogy to molecular liquids, the lower limit of the liquid range of ionic liquids belongs to the solid liquid transition. This can be a glass transition or a melting point. Some ionic liquids are semi-crystalline materials. Those exhibit a glass transition temperature, a recrystallization above the glass transition and melting of the crystal structures formed at higher temperature. Heating and cooling rates strongly affect the occurrence of the transitions during DSC measurements. In general, the chemical structure of the ionic liquid, thermal history, and impurities influence the solid liquid transition of ionic liquids [53, 63, 97, 100–114]. Figure 1.3 depicts chemical structures of selected ionic liquids used in dielectric measurements. Among them are imidazolium-based ionic liquids bearing various anions, such as tetrafluoroborate, hexafluorophosphate, triflate, bis(trifluoromethylsulfonyl)imide, dicyanamide, tris(pentafluoroethyl)trifluorophosphate, and dimethylsulfate. Further ionic liquids comprise the pyrrolidinium cation bearing as anion either bis(trifluoromethylsulfonyl)imide, dicyanamide, or tris(pentafluoroethyl)trifluorophosphate. Furthermore, ammonium and phosphonium ionic liquids belong to the aprotic ionic liquids either. Moreover, oligoethylene oxide bearing a carboxylate group with sodium as cation belongs to ionic liquids as well. This aprotic ionic liquid significantly distinguishes from the aforementioned aprotic ionic liquids because of the small cation and a

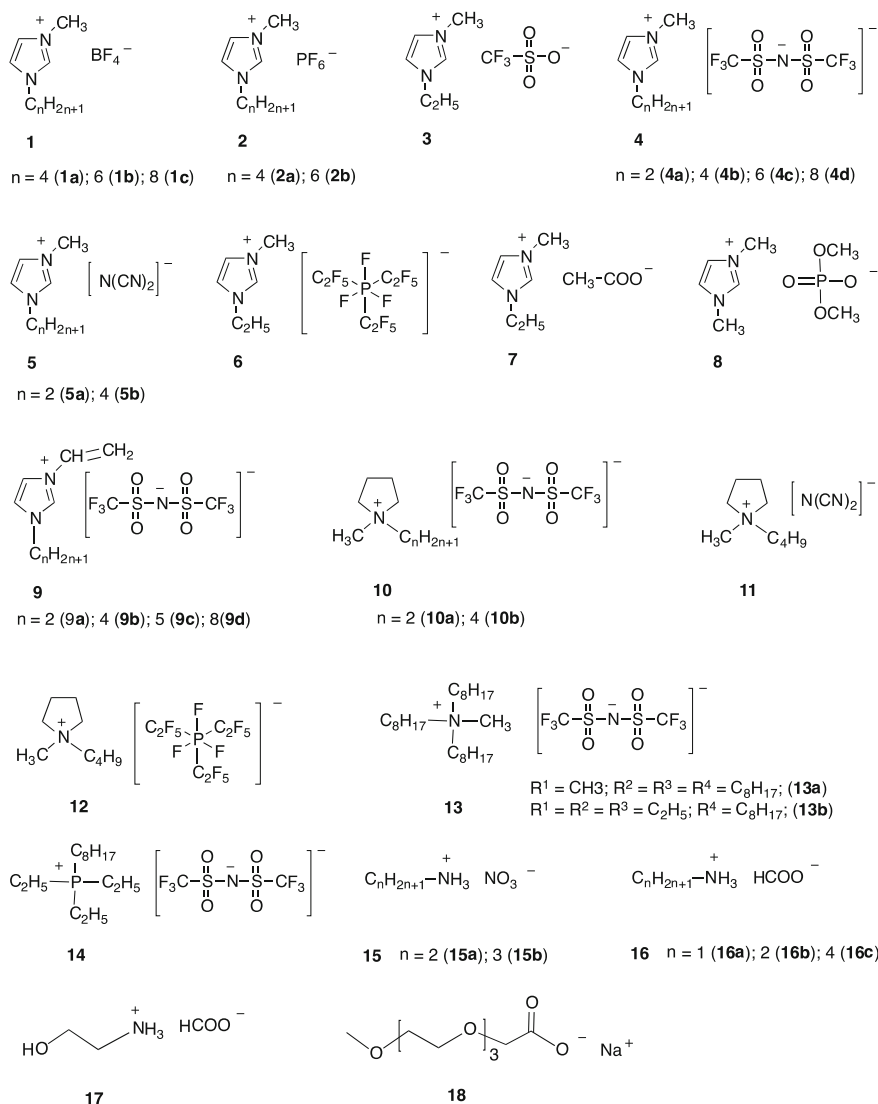


Fig. 1.3 Chemical structure of examples for ionic liquids

longer oligoethylene oxide chain at the anion. Moreover, protic ammonium-based ionic liquids bearing nitrate or format as anion have been interesting for investigation with dielectric spectroscopy as well [115–121].

Mobility of ionic liquids strongly relates to the liquid region. However, mobility is significantly reduced in the solid state. Table 1.1 summarizes glass transition

Table 1.1 Glass transition temperature (T_g), temperature of recrystallization (T_{recryst}) and melting temperature (T_m) of selected ionic liquids (IL) depicted in Fig. 1.3 that were measured visually [5] or by DSC using the given cooling and heating rates; water content containing in the ionic liquids was included if available in the reference

IL	T_g (°C)	T_{recryst} (°C)	T_m (°C)	Water content (%)	Cooling rate (K/min)	Heating rate (K/min)	Reference
1a	-87			1.6	5	5	[100]
1b	-86			0.4	5	5	[100]
1c	-86			0.5	5	5	[100]
2a	-78			0.1	5	5	[100]
2b	-74			0.2	5	5	[100]
3			-9			Visually	[5]
4a			-3			Visually	[5]
4b	-87		-4	1.4	5	Visually	[5]
			-1	0.04		5	[53]
4c	-84	-23	-5	0.1	5	5	[53]
4d	-80			<0.001	10	10	[101]
	-84			0.07	5	5	[53]
5b	-90	-29	-6		10	10	[102]
6			-103 (T_{m1})	2×10^{-5}	5	5	[63]
			5 (T_{m2})				[103]
7			-45				[104]
8	-64			0.08	5	5	[100]
9a	-84		18	0.02	5	5	[97, 105]
9b	-76		23	0.03	5	5	[63, 97]
9c	-76			0.08	5	5	[63]
9d	-78			0.07	5	5	[53]
10a			86				[106]
10b	-81		-13		10	5	[107]
11	-106		-55				[108]
12	-116		4			10	[109]
13a	-81				5	5	[110]
13b			-77				[111]
14			-82				[111]
15a			14	<0.01	5	5	[112]
			9	0.22			[113]
15b			3.5				[112]
16a	-114		13	0.42	5/2.5 ^a	5/2.5 ^a	[113]
16b	-106		-15	0.38	5/2.5 ^a	5/2.5 ^a	[113]
16c	-95		2	0.32		5	[113]
17	-85			0.55		5	[113]
18	-57			0.02	10	10	[114]

^a5 K/min heating and cooling rates for detection of T_g , 2.5 K/min heating and cooling rates for detection of T_m

temperature (T_g) and/or melting point (T_m) of selected ionic liquids. Mostly differential scanning calorimetry (DSC) was used for measurement of these data. Water content of ionic liquids and heating as well cooling rates used in DSC measurements are added as they are available. These parameters are important to compare measured data from different references. Most ionic liquids summarized in Table 1.1 exhibit low glass transition temperatures and/or low melting temperatures indicating a broader liquid range, which often starts below room temperature. Therefore, the temperature window for investigation of the ionic liquid mobility begins below room temperature in many examples.

The upper limit of the liquid range, and therefore, the upper limit of the temperature window for investigation of the ionic liquid mobility strongly relate to the temperature stability of these materials because ionic liquids possess a negligible vapor pressure [122, 123]. Therefore, a liquid vapor phase transition as in case of molecular liquids does not exist in case of ionic liquids. Thermogravimetric analysis (TGA) can be applied to get information about decomposition of ionic liquids. A weight loss determined by TGA of not more than 0.5 wt% may be considered as experimental error to measure the weight. Therefore, it may also indicate the upper limit of the liquid range of ionic liquids [110]. Figure 1.4 depicts examples of TGA curves for some selected aprotic ionic liquids. These imidazolium-based ionic liquids mainly distinguish in the anion while the alkyl substituent at the cation is either a methyl, ethyl, or butyl group. Selection of tetrafluoroborate (**1a**) or bis(trifluoromethylsulfonyl)imide (**4b**) as anion results in weight loss only at higher temperature whereas ionic liquids with dicyanamide (**5a**) or dimethylphosphate (**8**) as anion start to decompose already at significantly lower temperature [63, 110, 124, 125]. Furthermore, large differences exist in the non-evaporable char-like residue remaining after thermal treatment under nitrogen. It is negligible if the anion does not contain any carbon, although a significant higher amount on non-evaporable

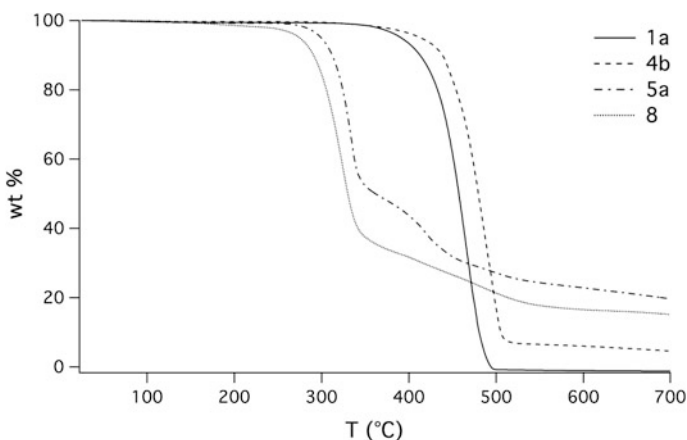


Fig. 1.4 Thermogravimetric analysis of selected aprotic imidazolium based ionic liquids **1a**, **4b**, **5a**, and **8** (chemical structures are given in Fig. 1.3) using heating rates of 20 K/min [63, 110]



Fig. 1.5 Condensation reaction of protic alkylammonium-based ionic liquids [113]

residue remains at 700 °C in case of ionic liquids with carbon in the anion. However, this does not directly correspond to the carbon content in the ionic liquid.

TGA investigation of protic ionic liquids is more complex because some examples show weight loss starting from ambient temperature [113]. Reaction of protic alkyl ammonium salts resulting in formation of an amide structure and water was detected in some protic ionic liquids bearing an organic anion (Fig. 1.5). This condensation reaction shows a further possibility to generate impurities during storage of some protic ionic liquids. Nevertheless, this reaction was not observed in case of protic ionic liquids bearing an inorganic anion, e.g., nitrate.

Generally, thermogravimetric data give information only about weight loss of both aprotic and protic ionic liquids. However, chemical reactions, which do not relate to formation of evaporable products, are not detectable with this method. Furthermore, TGA cannot give information about changes of ionic liquids during thermal loading over a long time period because there is only a limited time frame for measurements. Therefore, TGA determines the maximum of the processing temperature for a short time period only. Maximum processing temperature for a longer time period is significantly lower compared to the decomposition temperature determined by TGA measurements.

Furthermore, viscosity is a crucial property within the liquid range of ionic liquids. It is very important for practical applications of ionic liquids as well.

1.3 Viscosity of Ionic Liquids

Ionic liquids are usually significantly higher viscous [126–131] compared to molecular solvents, such as dimethyl sulfoxide [132] and even triacetin [133]. Therefore, viscosity influences diffusion processes in ionic liquids with a significant higher impact compared to molecular solvents. Furthermore, the structure of both the cation and the anion of ionic liquids also affects the viscosity of ionic liquids as shown by selected viscosity data summarized in Table 1.2. Increasing size of the alkyl substituent at the cation results in an increase in the viscosity of ionic liquids. Pyrrolidinium-based ionic liquids are higher viscous compared to imidazolium-based ionic liquids. A vinyl substituent at the imidazolium cation results in higher viscous ionic liquids compared to analogous methyl substituted imidazolium-based ionic liquids. Furthermore, 1-alkyl-3-methylimidazolium ionic liquids bearing

Table 1.2 Viscosity of selected ionic liquids, dimethylsulfoxide (DMSO), and triacetin

IL	Viscosity (mPa s)	T ($^{\circ}\text{C}$)	Reference
1a	33	23	[100, 141]
1b	177	23	[100]
1c	294	23	[100, 142]
2a	231	23	[100, 140]
2b	499	23	[100, 140]
3	41	25	[129]
4a	36.5	25	[128, 141]
4b	40	25	[126, 141]
	50	23	[128, 94]
4c	66	23	[94, 142]
4d	104	23	[94, 142]
5a	16.09	25	[130]
5b	28.8	25	[128]
	30.496	25	[130]
6	70	23	[63]
7	73.1	25	[129]
8	276	23	[100]
9a	57	24	[105]
9b	90	24	[105]
9c	105	24	[105]
10a	13	80	[131]
10b	86	24	[127, 140, 142]
11	36.5	25	[128]
13a	558	25	[129, 143]
13b	227	24	[111]
14	123.3	24	[111]
15a	32	25	[113]
16a	17	25	[113]
16b	32	25	[113]
16c	70	25	[113]
17	220	25	[113]
DMSO	1.993	25	[132]
Triacetin	16.8	25	[133]

hexafluorophosphate or trifluoromethylsulfonate (triflate) exhibit higher viscosity compared to similar ionic liquids comprising tetrafluoroborate or dicyanamide as anion. The 1-alkyl-3-methylimidazolium bis(trifluoromethylsulfonyl)imides (NTf₂) are relatively low viscous while this anion exhibits a large volume. Interestingly, 1-ethyl-3-methylimidazolium bis(trifluoromethylsulfonyl)imide possesses a lower viscosity compared to similar ionic liquids bearing tris(pentafluoroethyl)trifluorophosphate (FAP) or acetate as anion. In contrast to this, 1,3-dimethylimidazolium

dimethylphosphate exhibits a high viscosity. Furthermore, a hydroxy group at a protic ionic liquid causes a significant increase of the viscosity. This is caused by additional hydrogen bonding interactions.

Furthermore, the temperature used for measurements strongly affects viscosity of ionic liquids. An increase of temperature results in significant decrease of the viscosity of ionic liquids (Fig. 1.6) [127, 134, 135]. However, differences exist in the temperature dependence of single ionic liquids. Both, anion (Fig. 1.6a) as well

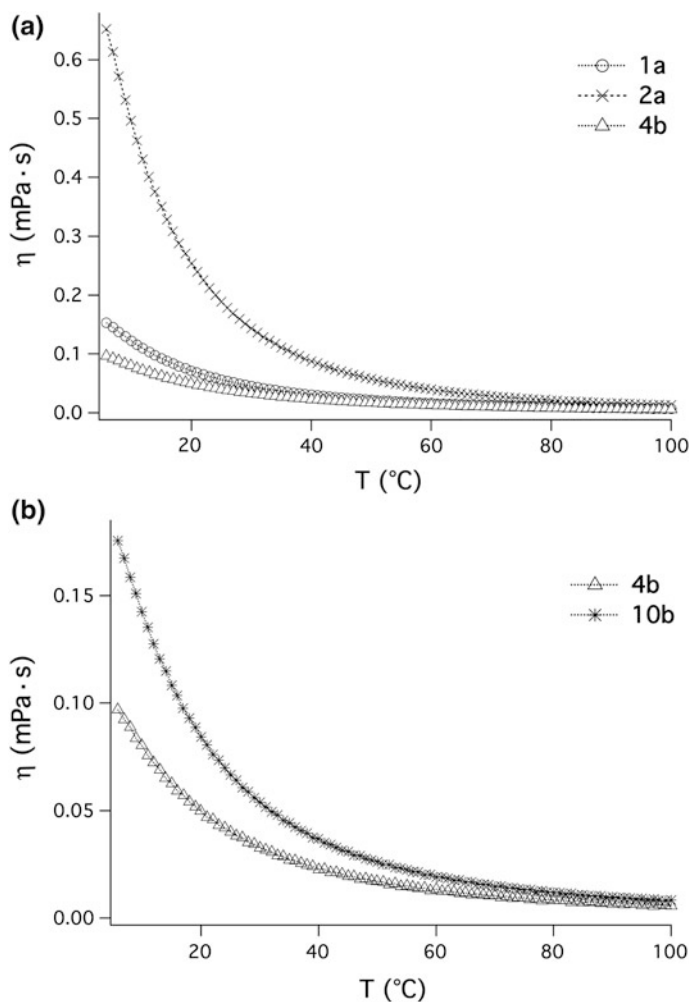


Fig. 1.6 Temperature dependence of viscosity using 4 K/min heating rate and 10 s^{-1} shear rate for measurements of **a** imidazolium-based ionic liquids bearing tetrafluoroborate (**1a**), hexafluorophosphate (**2a**), and bis(trifluoromethylsulfonyl)imide (**4b**) as anion and **b** imidazolium (**4b**) and pyrrolidinium (**10b**) bis(trifluoromethylsulfonyl)imides bearing similar alkyl substituents at the cation [134, 135]

cation (Fig. 1.6b) variations cause the differences in the temperature dependence of the ionic liquid viscosity.

The Vogel–Fulcher–Tammann–Hesse equation (Eq. (1.1)) [136–138] quantifies the temperature (T) dependence of the viscosity (η) of ionic liquids [124, 134, 135]. The parameters A , C , and T_0 in Eq. (1.1) are constants [136–138]. Knowledge of these constants makes calculation of viscosity possible at temperatures where no experimental data are available. Figure 1.7 exemplifies linear plots for the ionic liquids **1a** and **4b**, which distinguish only in the anion, and therefore, in their viscosity [134, 135].

$$\ln \eta = \ln A + \frac{C}{T - T_0} \quad (1.1)$$

Furthermore, temperature dependent investigation of solutes, e.g., stable radicals, in ionic liquids gives information about free volume effects in ionic liquids. Mobility of these solutes strongly relates to both macroscopic viscosity of ionic liquids and microviscosity [134, 135]. The latter corresponds to diffusion into the free volume.

Moreover, presence of water influences viscosity of hydrophobic ionic liquids as well. An increase in water content results in a decrease in the viscosity of ionic liquids [139]. In contrast to this, influence of water differs on the density of ionic liquids.

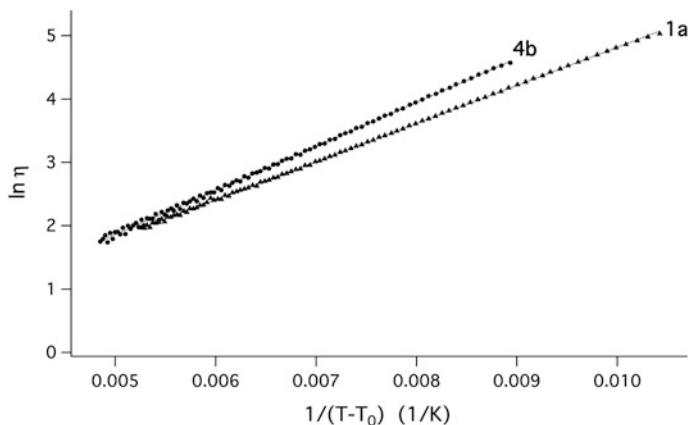


Fig. 1.7 Viscosity (η) of **1a** and **4b** as function of temperature (T) using 4 K/min heating rate and 10 s^{-1} shear rate for the measurements and the Vogel–Fulcher–Tammann–Hesse equation (Eq. (1.1)) for analysis (**1a**: $\eta_0 = -1.2034$; $C = 602.4$; $T_0 = 183$; **4b**: $\eta_0 = -1.6079$; $C = 694.8$; $T_0 = 167$) [134, 135]

1.4 Density of Ionic Liquids

Cation and anion structures as well as temperature influence the density of ionic liquids (Table 1.3) [94, 111, 113, 130, 140–143]. An increase of the alkyl substituent size at the cation results in a reduction of density at a given temperature in case of both aprotic [94, 130, 140–143] as well as protic [111, 113] ionic liquids. The presence of both polar and nonpolar regions in ionic liquids may be responsible for this effect [142]. Furthermore, molecular weight and molecular volume of the anion influence density of ionic liquids. This may cause deviations from a linear relationship between density measured and only one single factor of influence [142]. Comparing density of aprotic ionic liquids with density of dimethylsulfoxide shows individual differences of the ionic liquids compared to this molecular solvent at a given temperature (Table 1.3). Interestingly, influence of water is very small on the density of ionic liquids [142].

Furthermore, increase in temperature results in decrease in density as expected [142, 143]. The thermal expansion coefficients of ionic liquids calculated from temperature dependent density measurements are $6.47 \times 10^{-4} \text{ K}^{-1}$ for **4a**, $6.84 \times 10^{-4} \text{ K}^{-1}$ for **4b**, and $6.73 \times 10^{-4} \text{ K}^{-1}$ for **13a** in the temperature range between 278 and 348 K [143], and $6.18 \times 10^{-4} \text{ K}^{-1}$ for **1c**, $6.66 \times 10^{-4} \text{ K}^{-1}$ for **4b**, $6.89 \times 10^{-4} \text{ K}^{-1}$ for **4c**, $6.75 \times 10^{-4} \text{ K}^{-1}$ for **4d**, $6.32 \times 10^{-4} \text{ K}^{-1}$ for **10b** at 298 K using density data obtained between 278 and 308 K [142]. Thermal expansion coefficients of ionic liquids may be useful for construction of devices working in a broad temperature range. Furthermore, application of ionic liquids as solvents in chemical reactions and in separation processes requires knowledge not only about their density and their viscosity. This also requires information about polarity to make an efficient selection for the best suitable ionic liquid.

1.5 Polarity of Ionic Liquids

Polarity of ionic liquids is mostly expressed by interactions with solvatochromic dyes [144–158], changes of fluorescence by embedding of solvatochromic fluorescent probes [159], FTIR active substances [160], or stable radicals [94, 134, 135, 161, 162] (Fig. 1.8). The latter have been called spin probes. Furthermore, relative permittivity is included in polarity discussion in some examples [163–166].

Application of various methods to describe polarity causes various polarity scales, which exist independently from each other. Among the polarity scales based on solvatochromic dyes are the E_T^N scale using Reichardt's dye (**19**) [144–150]. The Kamlet–Taft equation (Eq. (1.2)) uses the hydrogen bond donating ability (α), the hydrogen bond accepting ability (β), and the dipolarity/polarizability (π^*) together with a correction parameter (δ) to describe polarity [151–158]. The latter is 1.0 for

Table 1.3 Density of selected ionic liquids and dimethylsulfoxide (DMSO) dimethylsulfoxide (DMSO)

IL	Density (g/cm ³)	<i>T</i> (°C) density	Reference
1a	1.20205	25	[100, 141]
1c	1.09918	25	[100, 142]
2a	1.367	25	[100, 140]
2b	1.292	25	[100, 140]
4a	1.51891	25	[128, 141]
4b	1.43679	25	[94, 126, 128, 141]
4c	1.36442	25	[94, 142]
4d	1.31073	25	[94, 142]
5a	1.104	25	[130]
5b	1.06	25	[128, 130]
10b	1.190	25	[127, 140]
	1.39435	25	[142]
13a	1.1046	25	[129, 143]
13b	1.249	24	[111]
14	1.244	4	[111]
15a	1.216	27	[113]
16a	1.087	27	[113]
16b	1.039	27	[113]
16c	0.968	27	[113]
17	1.184	27	[113]
DMSO	1.0953	25	[132]

aromatic surrounding, 0.5 for polyhalogenated surrounding, and zero for aliphatic surrounding. Furthermore, the parameter XYZ (Eq. (1.2)) represents the physico-chemical property of the solvatochromic dye in the surrounding under consideration, XYZ₀ corresponds to this property in the gas phase or in a reference surrounding, and *a*, *b*, and *s* are solvent-independent regression coefficients in Eq. (1.2). Figure 1.8 depicts examples for solvatochromic dyes (**20**, **21**, **22**), which give information about hydrogen bond donating ability (**20**), hydrogen bond accepting ability (**21**), and dipolarity/polarizability (**22**).

$$XYZ = (XYZ)_0 + a \cdot \alpha + b \cdot \beta + s(\pi^* + d \cdot \delta) \quad (1.2)$$

Absorption of solvatochromic dyes need to be outside of the absorption spectrum of the neat ionic liquid. This demand is fulfilled for colorless and many

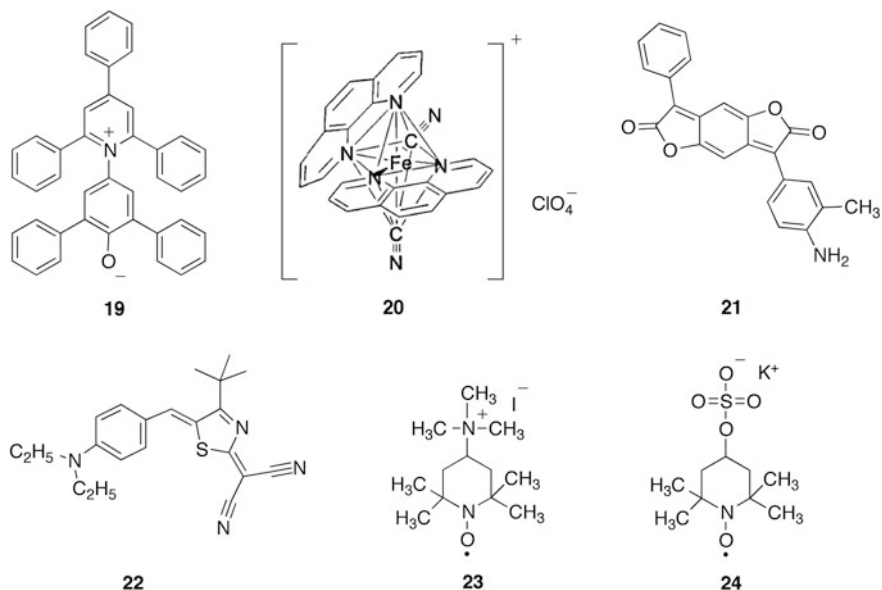


Fig. 1.8 Probes for polarity investigation of ionic liquids: Reichardt's dye (**19**) for E_T^N scale; solvatochromic dyes (**20**, **21**, **22**) for determination of the Kamlet–Taft parameters, which are the hydrogen bond donating ability α (**20**), the hydrogen bond accepting ability β (**21**), and the dipolarity/polarizability π^* (**22**); as well as stable radicals comprising a cationic (**23**) or an anionic (**24**) substituent in the 4-position to the nitroxyl group for ESR spectroscopic analysis resulting in the hyperfine coupling constant ($A_{\text{iso}}(^{14}\text{N})$); structural elements of **20** were taken from Ref. [155]

slightly yellow colored ionic liquids. Nevertheless, solvatochromic dyes cannot describe polarity of dark colored ionic liquids.

Furthermore, spin probes are useful for micropolarity investigation of ionic liquids by ESR spectroscopy. Intrinsic color of the matrix does not interfere such studies. However, only spin probes substituted with charged groups [trimethylammonium group (**23**), sulfate group (**24**)] exhibit significant changes in the ESR spectrum by variation of the length of the alkyl substituent at the cation of the ionic liquid. The hyperfine coupling constant ($A_{\text{iso}}(^{14}\text{N})$) is the parameter describing well micropolarity of ionic liquids. Comparison of the three Kamlet–Taft parameters with the hyperfine coupling constant of the spin probes during investigation of imidazolium-based ionic liquids with different alkyl chain length bearing anions such as tetrafluoroborate, hexafluorophosphate, dicyanamide, and bis(trifluoromethylsulfonyl)imide shows an increasing trend for the hydrogen bond accepting ability (β) and the hyperfine coupling constant ($A_{\text{iso}}(^{14}\text{N})$) of the spin probe containing the anionic substituent [156, 157].

Moreover, the concept of ionicity focuses on the contribution of conductive motion and diffusive motion of ionic liquids [167, 168]. This parameter gives information about the ionic character of ionic liquids, that means how ionic are ionic liquids. Depending on the structure of ionic liquids differences exist between conductive motion and diffusive motion in some examples. The molar conductivity ratio was obtained from ionic conductivity (Λ_{imp}) and ionic self diffusion coefficients. The latter were determined by pulse-field-gradient spin-echo NMR spectroscopy (Λ_{NMR}). Ionic conductivity (Λ_{imp}) was measured with impedance spectroscopy. The ratio $\Lambda_{\text{imp}}/\Lambda_{\text{NMR}}$ can be seen as a quantitative expression for the ionicity. The relation between ionicity and polarity, which is described by solvatochromic probes, shows a strong nonlinear correlation between these parameters [168].

Furthermore, motion of ionic liquids substituted with a polymerizable functional group may significantly differ from motion of similar structures, which are covalently bound in the polymer chain. Polymerization of ionic liquid monomers results in solid materials with different properties compared to the starting material.

1.6 New Polymer Materials Derived from Ionic Liquids

Imidazolium as well as ammonium-based ionic liquids comprising polymerizable functional groups have been used as starting materials for synthesis of new polyelectrolytes (Fig. 1.9). The latter are aprotic (**27** and **29**) [86, 97] or protic (**28**) [54] polyelectrolytes. They comprise protic structures in each segment of the polymer chain. Thermal initiation using 2,2'-Azobis(2-methylpropionitrile) (AIBN) as initiator (Fig. 1.9a) [97], photoinitiation in the presence of 2-hydroxy-2-methyl propiophenone as photoinitiator and UV light (Fig. 1.9b) [54] or group transfer polymerization in an ionic liquid (1.9c) [86] have been successfully applied in polymer synthesis starting with ionic liquid monomers.

The glass transition temperatures of the aprotic polymerized ionic liquids (Table 1.4) are significantly higher compared to the glass transition temperatures of the ionic liquid monomers used for their manufacture (Table 1.1) [86, 97]. The polymerized protic ionic liquid (**28**) shows a lower glass transition temperature than monomer **25** [54]. This is attributed to the high water content in this polymer that functions as plasticizer. Nevertheless, the polymer materials are solid [54, 86, 97] whereas the ionic liquid monomers discussed in Fig. 1.9 are viscous materials at room temperature [54, 105]. Furthermore, the polymerized ionic liquids exhibit typical polymer properties. Therefore, they are interesting for many applications.

A good understanding of ionic liquids and polymerized ionic liquids is a necessary prerequisite for an efficient application of these interesting materials. The following chapters focus on physical properties and various physical processes in ionic liquids investigated by dielectric spectroscopy. Further modern methods will

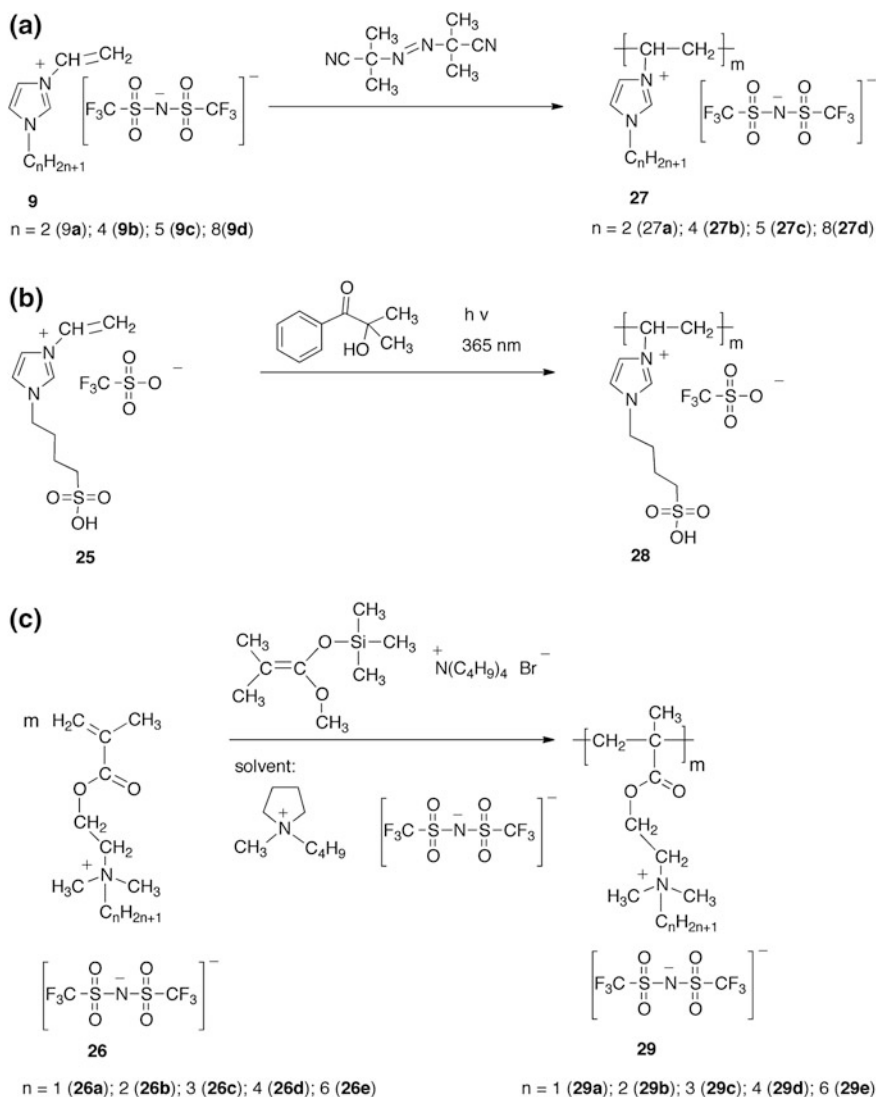


Fig. 1.9 Chemical structures for ionic liquids comprising a polymerizable functional group and their polymerization resulting in polymerized ionic liquids: **a** free radical polymerization of **9** in bulk at $70\text{ }^{\circ}\text{C}$ using 2,2'-Azobis(2-methylpropionitrile) (AIBN) as initiator [97]; **b** photoinitiated polymerization of **25** using UV light (365 nm , light intensity: 30 mW/cm^2) [54]; and **c** group transfer polymerization (GTP) of **26** using 1-methoxy-2-methyl-1-(trimethylsiloxy)propene, tetrabutylammonium bromide, and 1-butyl-1-methylpyrrolidinium bis(trifluoromethylsulfoniyl) imide as solvent [86]

Table 1.4 Glass transition temperature (T_g) of polymerized ionic liquids (Poly-IL) made by polymerization of ionic liquids monomers (Fig. 1.9) that were measured by traditional DSC measurements (cooling and heating rates correspond to 10 K/min) in case of **27** and **29** [86, 97] as well as by stochastic temperature-modulated DSC in the frequency range from 4 to 40 MHz in a single measurement using a heating rate of 0.5 K/min in case of **28** [54]

Poly-IL	Polymerization	T_g (°C)	Reference
27a	Thermal (AIBN)	53	[97]
27b	Thermal (AIBN)	46	[97]
27c	Thermal (AIBN)	55	[97]
28	Photoinitiated	-47	[54]
29a	Thermal (AIBN)	83	[97]
	GTP	58	[86]
29b	Thermal (AIBN)	64	[97]
	GTP	55	[86]
29c	Thermal (AIBN)	29	[97]
	GTP	46	[86]
29d	Thermal (AIBN)	42	[97]
	GTP	43	[86]
29e	Thermal (AIBN)	39	[97]
	GTP	32	[86]

also contribute to improve the understanding of ionic liquids and polymers derived of them. Therefore, the following chapters will help to increase application areas of ionic liquids as well as of corresponding polymers made of them.

References

- Swinkels DAJ (1971) Molten salt batteries and fuel cells. In: Braunstein J, Mamantov G, Smith GP (eds) *Advances in molten salts chemistry*. Plenum Press, New York, pp 165–223
- Wasserscheid P, Welton T (eds) (2003) *Ionic liquid in synthesis*. Wiley-VCH Verlag GmbH & Co. KGaA, Weinheim
- Wilkes JS, Levisky JA, Wilson RA, Hussy CL (1982) Dialkylimidazolium Chloroaluminate melts: a new class of room-temperature ionic liquids for electrochemistry, spectroscopy, and synthesis. *Inorg Chem* 21:1263–1264
- Cooper EI, O’Sullivan EJM (1992) New, stable, ambient-temperature molten salts. *Electrochem Proc* 386–396
- Bonhôte P, Dias A-P, Papageorgiou N, Kalyanasundaram K, Grätzel M (1996) Hydrophobic, highly conductive ambient-temperature molten salts. *Inorg Chem* 35:1168–1178
- Walden P (1914) Molecular weights and electrical conductivity of several fused salts. *Bull Acad Sci* 405–422
- Ohno H (ed) (2005) *Electrochemical aspects of ionic liquids*. Wiley-Interscience, Hoboken
- Endres F, Abbott AP, MacFarlane DR (eds) (2008) *Electrodeposition from ionic liquids*. Wiley-VCH Verlag GmbH & Co. KGaA, Weinheim
- Torriero AAJ (ed) (2015) *Electrochemistry in ionic liquids*. Springer International Publishing, Switzerland

10. Hapiot P, Lagrost C (2008) Electrochemical reactivity in room-temperature ionic liquids. *Chem Rev* 108:22238–22264
11. Freudenmann D, Wolf S, Wolff M, Feldmann C (2011) Ionic liquids: new perspectives for inorganic synthesis. *Angew Chem Int Ed* 50(47):11050–11060
12. Zhen W, Li D, Guo W (2015) Applications of Ionic Liquids (ILs) in synthesis of inorganic nanomaterials. In: Handy S (ed) *Materials science fluids “Ionic Liquids—current state of the art*. INTECH open science 2015, [cdn.intechopen.com, http://dx.doi.org/10.5772/59048](http://dx.doi.org/10.5772/59048)
13. Antonietti M, Kuang D, Smarsly B, Zhou Y (2004) Ionische Flüssigkeiten für die Synthese funktioneller Nanopartikel und anderer anorganischer Nanostrukturen. *Angew Chem* 116:5096–5100
14. Zhou Y, Antonietti M (2003) Synthesis of very small TiO₂ nanocrystals in a room-temperature ionic liquid and their self-assembly toward mesoporous spherical aggregates. *J Am Chem Soc* 125:14960–14961
15. Dupont J, Itoh T, Lozano P, Malhotra SV (eds) (2015) Environmentally friendly syntheses using ionic liquids. In: Cann MC (series ed) *Sustainability: contributions through science and technology*. CRC Press, Taylor & Francis Group, Boca Raton, London
16. Muthyala MK, Veliseti K, Parang K, Kumar A (2014) Advances in functionalized ionic liquids as reagents and scavengers in organic synthesis. *Current Org Chem* 18:2530–2554
17. Kuchenbuch A, Giernoth R (2015) Ionic liquids beyond simple solvents: glimpses at the state of the art in organic chemistry. *Chem Open* 4:677–681
18. Păvulescu VI, Hardacre C (2007) Catalysis in ionic liquids. *Chem Rev* 107:2615–2665
19. Kubisa P (2004) Application of ionic liquids as solvents for polymerization processes. *Prog Polym Sci* 29:3–12
20. Brazel CS, Rogers RD (eds) (2005) Ionic liquids in polymer systems: solvents, additives, and novel applications. *ACS Symp Ser* 913
21. Kubisa P (2009) Ionic liquids as solvents for polymerization processes—Progress and challenges. *Prog Polym Sci* 34:1333–1347
22. Strehmel V (2011) Ionische Flüssigkeiten in der Polymersynthese. *Chem Ing Tech* 83(9):1443–1453
23. Duchet-Rumeau M, Gérard JF, Galli G (eds) (2014) *Macromol Symp Spec Issue Polym Ionic Liquids* 342
24. Lozano P, De Diego T, Iborra JL (2010) Biocatalytic processes using ionic liquids and supercritical carbon dioxide, Part 3. In: *Biocatalysis*. Wiley VCH
25. Habulin M, Primozić M, Knez Z (2011) Application of ionic liquids in biocatalysis. In: Kokorin A (ed) *Ionic liquids: applications and perspectives*. InTech Europe, Chap 19, www.interchopen.com
26. Tavares APM, Rodriguez O, Macedo EA (2013) New generations of ionic liquids applied to enzymatic biocatalysis. In: Kadowaka J (ed) *Ionic liquids—new aspects for the future* InTech, Chap 20, www.interchopen.com
27. Stepinski DC, Jensen MP, Dzielawa JA, Dietz ML (2005) Synergistic effects in the facilitated transfer of metal ions into room-temperature ionic liquids. *Green Chem* 7:151–158
28. Berthod A, Ruiz-Angel MJ, Huguet S (2005) Nonmolecular solvents in separation methods: dual nature of room temperature ionic liquids. *Anal Chem* 77:4071–4080
29. Anastas PT, Wasserscheid P, Stark A (eds) (2010) *Handbook of green chemistry. Ionic Liquids 6*. Wiley-VCH Verlag GmbH & Co. KGaA
30. Rodríguez H (ed) (2016) *Green chemistry and sustainable technology, ionic liquids for better separation processes*. Springer, Berlin
31. Sun X, Juo H, Dai S (2012) Ionic liquids-based extraction: a promising strategy for the advanced nuclear fuel cycle. *Chem Rev* 112:2100–2128
32. Rogers RD, Seddon KR (eds) (2003) *Ionic liquids as green solvents, progress and prospects*. ACS Symposium Series 856. American Chemical Society, Washington, DC
33. Rogers RD, Seddon KR (eds) (2002) *Ionic liquids, industrial applications for green chemistry*. ACS Symposium Series 818. American Chemical Society, Washington, DC

34. Wilkes JS (2002) A short history of ionic liquids—From molten salts to neoteric solvents. *Green Chem* 4:73–80
35. Holbrey JD, Seddon KR (1999) The phase behavior of 1-alkyl-3-methylimidazolium tetrafluoroborates; ionic liquids and ionic liquid crystals. *J Chem Soc Dalton Trans* 2133–2139
36. Zhang S, Sun N, He X, Lu X, Zhang X (2006) Physical properties of ionic liquids: database and evaluation. *J Phys Chem Ref Data* 35(4):1475–1517
37. Seddon K (2008) Definition of ionic liquids given at the Bunsen Discussion meeting in Clausthal-Zellerfeld, 23–25 Nov 2008
38. Greaves TL, Drummond CJ (2008) Protic ionic liquids: properties and applications. *Chem Rev* 108:206–237
39. Fukaya Y, Iizuka Y, Sekikawa K, Ohno H (2007) Bio ionic liquids: room temperature ionic liquids composed wholly of biomaterials. *Green Chem* 9:1155–1157
40. Winther-Jensen O, Vijayaraghavan R, Sun J, Winther-Jensen B, MacFarlane DR (2009) Self polymerizing ionic liquid gel. *Chem Commun* 3041–3043
41. Sundar DS, Vijayaraghavan R, Subramaniam J, Surianarayanan M, Mandal AB (2011) Role of choline formate ionic liquid in the polymerization of vinyl and methacrylic monomers. *J Appl Polym Sci* 120:3733–3739
42. Aparicio S, Atilhan M (2012) A Computational study on choline benzoate and choline salicylate ionic liquids in the pure state and after CO₂ adsorption. *J Phys Chem B* 116:9171–9185
43. Aparicio S, Atilhan M (2012) Choline-based ionic liquids on graphite surfaces and carbon nanotubes solvation: a molecular dynamics study. *J Phys Chem C* 116:12055–12065
44. Carlisle TK, Bara JE, Gabriel CJ, Noble RD, Gin DL (2008) Interpretation of CO₂ solubility and selectivity in nitrile-functionalized room-temperature ionic liquids using a group contribution approach. *Ind Eng Chem Res* 47:7005–7012
45. Hirao M, Ito-Akita K, Ohno H (2000) Polymerization of molten salt monomers having a phenylimidazolium group. *Polym Adv Technol* 11:534–538
46. Nakajima H, Ohno H (2005) Preparation of thermally stable polymer electrolytes from imidazolium-type ionic liquid derivatives. *Polymer* 46:11499–11504
47. Ohno H (2007) Design of ion conductive polymers based on ionic liquids. *Macromol Symp* 249–250:551–556
48. Cardiano P, Mineo PG, Neri F, Schiavo SL, Piraino P (2008) A new application of ionic liquids: hydrophobic properties of tetraalkylammonium-based poly(ionic liquids). *J Mater Chem* 18:1253–1260
49. Mori H, Yahagi M, Endo T (2009) RAFT Polymerization of N-vinylimidazolium salts and synthesis of thermoresponsive ionic liquid block copolymers. *Macromolecules* 42:8082–8092
50. Shaplov AS, Goujon L, Vidal F, Lozinskaya EI, Meyer F, Malyskhina IA, Chevrot C, Teyssie D, Odinets IL, Vygodskii YS (2009) Ionic IPNs as novel candidates for highly conductive solid polymer electrolytes. *J Polym Sci A Chem Ed* 47:4245–4266
51. Nakamura K, Saiwaki T, Fukao K (2010) Dielectric relaxation behavior of polymerized ionic liquid. *Macromolecules* 43:6092–6098
52. Becht GA, Lee S, Seifert S, Firestone MA (2010) Solvent tunable optical properties of a polymerized vinyl- and thienyl-substituted ionic liquid. *J Phys Chem B* 114:14703–14711
53. Sangoro JR, Iacob C, Naumov S, Valiullin R, Rexhausen H, Hunger J, Buchner R, Strehmel V, Kärger J, Kremer F (2011) Diffusion in ionic liquids: the interplay between molecular structure and dynamics. *Soft Matter* 7:1678–1681
54. Wojnarowska Z, Knapik J, Diaz M, Ortiz A, Ortiz I, Paluch M (2014) Conductivity mechanism in polymerized imidazolium-based protic ionic liquid [HSO₃–BVIIm][OTf]: dielectric relaxation studies. *Macromolecules* 47:4056–4065
55. Pinaud J, Fèvre M, Coupillaud P, Vignolle J, Taton D (2011) Synthesis of 1-Vinyl-3-ethylimidazolium-based ionic liquid (Co)polymers by cobalt-mediated radical polymerization. *Macromolecules* 44:6397–6404

56. Nakamura K, Saiwaki T, Fukao K, Inoue T (2011) Viscoelastic behavior of the Polymerized Ionic Liquid Poly(1-ethyl-3-vinylimidazolium bis(trifluoromethanesulfonylimide)). *Macromolecules* 44:7719–7726
57. González-Álvarez J, Blanco-Gomis D, Arias-Abrodo P, Díaz-Llorente D, Ríos-Lombardía N, Busto E, Gotor-Fernández V, Gutiérrez-Álvarez MD (2012) Polymeric imidazolium ionic liquids as valuable stationary phases in gas chromatography: chemical synthesis and full characterization. *Anal Chim Acta* 721:173–181
58. Nakamura K, Fukao K, Inoue T (2012) Dielectric relaxation and viscoelastic behavior of polymerized ionic liquids with various counteranions. *Macromolecules* 45:3850–3858
59. He H, Zhong M, Adzima B, Luebke D, Nulwala H, Matyjaszewski K (2013) A simple and universal gel permeation chromatography technique for precise molecular weight characterization of well-defined poly(ionic liquid)s. *J Am Chem Soc* 135:4227–4230
60. Smith TW, Zhao M, Yang F, Smith D, Cebe P (2013) Imidazole polymers derived from ionic liquid 4-vinylimidazolium monomers: their synthesis and thermal and dielectric properties. *Macromolecules* 46:1133–1143
61. Carrasco PM, Tzounis L, Mompean FJ, Strati K, Georgopoulos P, Garcia-Hernandez M, Stamm M, Gabanero G, Odriozola I, Avgeropoulos A, Garcia I (2013) Thermoset magnetic materials based on poly(ionic liquid)s block copolymers. *Macromolecules* 46:1860–1867
62. Allen MH Jr, Wang S, Hemp ST, Chen Y, Madsen LA, Winey KI, Long TE (2013) Hydroxyalkyl-containing imidazolium homopolymers: correlation of structure with conductivity. *Macromolecules* 46:3037–3045
63. Strehmel V, Berdzinski S, Rexhausen H (2014) Interactions between ionic liquids and radicals. *J Mol Liq* 192:153–170
64. Berdzinski S, Strehmel B, Strehmel V (2015) Photogenerated lophyl radicals in 1-alkyl-3-vinylimidazolium bis(trifluoromethylsulfonyl)-imides. *Photochem Photobiol Sci* 14:714–725
65. Kumar R, Bocharova V, Strelcov E, Tselev A, Kravchenko II, Berdzinski S, Strehmel V, Ovchinnikova OS, Minutolo JA, Sangoro JR, Agapov AL, Sokolov AP, Kalinin SV, Sumpter BG (2015) Ion transport and softening in a polymerized ionic liquid. *Nanoscale* 7:947–955
66. Bocharova V, Agapov AL, Tselev A, Collins L, Kumar R, Berdzinski S, Strehmel V, Kisluk A, Kravchenko II, Sumpter BG, Sokolov AP, Kalinin SV, Strelcov E (2015) Controlled nanopatterning of a polymerized ionic liquid in a strong electric field. *Adv Funct Mater* 25:805–811
67. Wojnarowska Z, Knapik J, Jacquemin J, Berdzinski S, Strehmel V, Sangoro JR, Paluch M (2015) Effect of pressure on decoupling of ionic conductivity from segmental dynamics in polymerized ionic liquids. *Macromolecules* 48(23):8660–8666
68. Cordella D, Kermagoret A, Debuigne A, Jérôme C, Mecerreyes D, Isik M, Taton D, Detrembleur C (2015) All poly(ionic liquid)-based block copolymers by sequential controlled radical copolymerization of vinylimidazolium monomers. *Macromolecules* 48:5230–5243
69. Washiro S, Yoshizawa M, Nakajima H, Ohno H (2004) Highly ion conductive flexible films composed of network polymers based on polymerizable ionic liquids. *Polymer* 45:1577–1582
70. Chen H, Choi J-H, Salas-de la Cruz D, Winey KI, Elabd YA (2009) Polymerized ionic liquids: the effect of random copolymer composition on ion conduction. *Macromolecules* 42:4809–4816
71. Green O, Grubjesic S, Lee S, Firestone MA (2009) The design of polymeric ionic liquids for the preparation of functional materials. *J Macromol Sci C Polym Rev* 49:339–360
72. Lee M, Choi UH, Colby RH, Gibson HW (2010) Ion conduction in imidazolium acrylate ionic liquids and their polymers. *Chem Mater* 22:5814–5822
73. Matsumoto K, Talukdar B, Endo T (2011) Methacrylate-based ionic liquid: radical polymerization/copolymerization with methyl methacrylate and evaluation of molecular weight of the obtained homopolymers. *Polym Bull* 66:199–210
74. Shaplov AS, Lozinskaya EI, Ponkratov DO, Malyskhina IA, Vidal F, Aubert P-H, Okatova OV, Pavlov GM, Komarova LI, Wandrey C, Vygodskii YS (2011) Bis

- (trifluoromethylsulfonyl)amide based “polymeric ionic liquids”: synthesis, purification and peculiarities of structure–properties relationships. *Electrochim Acta* 57:74–90
75. Becht GA, Sofos M, Seifert S, Firestone MA (2011) Formation of a liquid-crystalline interpenetrating poly(ionic liquid) network hydrogel. *Macromolecules* 44:1421–1428
 76. Shaplov AS, Vlasov PS, Lozinskaya EI, Ponkratov DO, Malyshkina IA, Vidal F, Okatova OV, Pavlov GM, Wandrey C, Bhide A, Schönhoff M, Vygodskii YS (2011) Polymeric ionic liquids: comparison of polycations and polyanions. *Macromolecules* 44:9792–9803
 77. Choi UH, Lee M, Wang S, Liu W, Winey KI, Gibson HW, Colby RH (2012) Ionic conduction and dielectric response of poly(imidazolium acrylate) ionomers. *Macromolecules* 45:3974–3985
 78. Tokuda M, Minami H (2013) Specific solubility behavior of quaternary ammonium-based poly(ionic liquid) particles by changing counter anion. *J Coll Interf Sci* 398:120–125
 79. Choi UH, Mittal A, Price TL Jr, Gibson HW, Runt J, Colby RH (2013) Polymerized ionic liquids with enhanced static dielectric constants. *Macromolecules* 46:1175–1186
 80. Tokuda M, Shindo T, Minami H (2013) Preparation of polymer/poly(ionic liquid) composite particles by seeded dispersion polymerization. *Langmuir* 29:11284–11289
 81. Tokuda M, Sanada T, Shindo T, Suzuki T, Minami H (2014) Preparation of submicrometer-sized quaternary ammonium-based poly(ionic liquid) particles via emulsion polymerization and switchable responsiveness of emulsion film. *Langmuir* 30:3406–3412
 82. Chen J, Wang S, Peng J, Li J, Zhai M (2014) New lipophilic polyelectrolyte gels containing quaternary ammonium salt with superabsorbent capacity for organic solvents. *ACS Appl Mater Interfaces* 6:14894–14902
 83. Meek KM, Elabd YA (2015) Alkaline chemical stability of polymerized ionic liquids with various cations. *Macromolecules* 48:7071–7084
 84. Tejero R, Arbe A, Fernández-García M, López D (2015) Nanostructuring by self-assembly in N-Alkyl Thiazolium and Triazolium side-chain polymethacrylates. *Macromolecules* 48:7180–7193
 85. Fan F, Wang Y, Hong T, Heres MF, Saito T, Sokolov AP (2015) Ion conduction in polymerized ionic liquids with different pendant groups. *Macromolecules* 48:44461–44470
 86. Strehmel V, Senkowski V (2015) Synthesis of traditional and ionic polymethacrylates by anion catalyzed group transfer polymerization. *J Polym Sci A Polym Chem Ed* 53(24): 2849–2859
 87. Cavicchi KA (2012) Synthesis and polymerization of substituted ammonium sulfonate monomers for advanced materials applications. *ACS Appl Mater Interfaces* 4:518–526
 88. Qiu H, Takafuji M, Sawada T, Liu X, Jiang S, Ihara H (2010) New strategy for drastic enhancement of selectivity via chemical modification of counter anions in ionic liquid polymer phase. *Chem Commun* 46:8740–8742
 89. Anouti M, Jacquemin J (2014) Structuring reductive media containing protic ionic liquids and their application to the formation of metallic nanoparticles. *Colloids Surf A Physicochem Eng Aspects* 445:1–11
 90. Krüger M, Huang M-M, Brüdermann E, Weingärtner H, Havenith M (2011) Combined THz and microwave dielectric spectroscopy of intermolecular interactions in homologous protic ionic liquids. *IEEE Trans Terahertz Sci Technol* 1(1):313–320
 91. Zech O, Kellermeier M, Thomaier S, Maurer E, Klein R, Schreiner C, Kunz W (2009) Alkali metal oligoether carboxylates—A new class of ionic liquids. *Chem Eur J* 15:1341–1345
 92. Sangoro JR (2014) Charge transport and dipolar relaxation in an alkali metal oligoether carboxylate ionic liquid. *Colloid Polym Sci* 292:1933–1938
 93. Huddleston JG, Visser AE, Reichert WM, Willauer HD, Broker GA, Rogers RD (2001) Characterization and comparison of hydrophilic and hydrophobic room temperature ionic liquids incorporating the imidazolium cation. *Green Chem* 3:156–164
 94. Strehmel V, Rexhausen H, Strauch P (2010) Influence of imidazolium bis (trifluoromethylsulfonylimide)s on the rotation of spin probes comprising ionic and hydrogen bonding groups. *Phys Chem Chem Phys* 12:1933–1940

95. BMImLactat-Synthese über Silberlactat, Harjani JR, Farrell J, Garcia MT, Singer RD, Scammells PJ (2009) Further investigation of the biodegradability of imidazolium ionic liquids. *Green Chem* 11:821–829
96. Holbrey JD, Reichert WM, Swatloski RP, Broker GA, Pitner WR, Seddon KR, Rogers RD (2002) Efficient, halide free synthesis of new, low cost ionic liquids: 1,3-dialkylimidazolium salts containing methyl- and ethylsulfate anions. *Green Chem* 4:407–413
97. Strehmel V, Berdzinski S, Ehrentraut L, Faßbender C, Horst J, Leeb E, Liepert J, Ruby M-P, Senkowski V, Straßburg P, Wenda A, Strehmel C (2015) Application of ionic liquids in synthesis of polymeric binders for coatings. *Prog Org Coat* 89:297–313
98. Scholz E (1984) Karl Fischer-Titration Methoden zur Wasserbestimmung. In: *Anleitungen für die chemische Laboratoriumspraxis*, vol XX. Springer, Berlin
99. Bruttel P, Schlink R (2003) Wasserbestimmung durch Karl Fischer- Titration. *Metrohm Monographie* 8.026.5001–2003-06; Metrohm AG, Herisau, Switzerland
100. Strehmel V, Laschewsky A, Wetzel H, Görnitz E (2006) Free radical polymerization of *n*-butyl methacrylate in ionic liquids. *Macromolecules* 39:923–930
101. Tokuda H, Hayamizu K, Ishii K, Susan MABH, Watanabe M (2005) Physicochemical properties and structures of room temperature ionic liquids. 2. Variation of alkyl chain length in imidazolium cation. *J Phys Chem B* 109(13):6103–6110
102. Fredlake CP, Crostwaite JM, Hert DG, Aki SNVK, Brennecke JF (2004) Thermophysical properties of imidazolium-based ionic liquids. *J Chem Eng Data* 49(4):954–964
103. Nazet A, Sokolov S, Sonnleitner T, Makino T, Kanakubo M, Buchner R (2015) Densities, viscosities, and conductivities of the imidazolium ionic liquids [Emim][Ac], [Emim][FAP], [Bmim][BETI], [Bmim][FSI], [Hmim][TFSI], and [Omim][TFSI]. *J Chem Eng Data* 60:2400–2411
104. Wilkes JS, Zaworotko MJ (1992) Air and water stable 1-ethyl-3-methylimidazolium based ionic liquids. *Chem Commun* 965–967
105. Berdzinski S, Strehmel B, Strehmel V (2015) Photogenerated lophyl radicals in 1-alkyl-3-vinylimidazolium bis(trifluoromethylsulfonyl)-imides. *Photochem Photobiol Sci* 14: 714–725
106. Bernard UL, Izgorodina EI, MacFarlane DR (2010) New insights into the relationship between ion-pair binding energy and thermodynamic and transport properties of ionic liquids. *J Phys Chem C* 114(48):20472–20478
107. Martinelli A, Matic A, Jacobsson P, Börjesson L, Fericola A, Scrosati B (2009) *J Phys Chem B* 113(32):11247–11251
108. MacFarlane DR, Forsyth SA, Golding J, Deacon GB (2002) Ionic liquids based on imidazolium, ammonium and pyrrolidinium salts of the dicyanamide anion. *Green Chem* 4:444–448
109. Fletcher SI, Sillars FB, Hudson NE, Hall PJ (2010) Physical properties of selected ionic liquids for use as electrolytes and other industrial applications. *J Chem Eng Data* 55:778–782
110. Strehmel V (2007) Selection of ionic liquids for free radical polymerization processes. *Macromol Symp* 254:25–33
111. Shirota H, Fukazawa H, Fujisawa T, Wishart JF (2010) Heavy atom substitution effects in non-aromatic ionic liquids: ultrafast dynamics and physical properties. *J Phys Chem B* 114:9400–9412
112. Atkin R, Warr GG (2008) The smallest amphiphiles: nanostructure in protic room-temperature ionic liquids with short alkyl groups. *J Phys Chem B* 112(14):4164–4166
113. Greaves TL, Weerawardena A, Fong C, Krodkiewska I, Drummond CJ (2006) Protic ionic liquids: solvents with tunable phase behavior and physicochemical properties. *J Phys Chem B* 110:22479–22487
114. Zech O, Kellermeier M, Thomaier S, Maurer E, Klein R, Schreiner C, Kunz W (2009) Alkali metal oligoether carboxylates—A new class of ionic liquids. *Chem Eur J* 15:1341–1345
115. Weingaertner H, Knocks A, Schrader W, Kaatze U (2001) Dielectric spectroscopy of the ethylammonium nitrate. *J Phys Chem A* 105(38):8646–8650

116. Huang M, Weingaertner H (2008) Protic ionic liquids with unusually high dielectric permittivities. *ChemPhysChem* 9(15):2172–2173
117. Huang M-M, Jiang Y, Sasisanker P, Driver G, Gordon W, Weingärtner H (2011) Static relative dielectric permittivities of ionic liquids at 25°. *J Chem Eng Data* 56(4):1494–1499
118. Krueger M, Huang MM, Bruendermann E, Weingaertner H, Havenith M (2011) Combined THz and microwave dielectric spectroscopy of intermolecular interactions in homologous protic ionic liquids. *IEEE Trans Terahertz Sci Technol* 1(1):313–320
119. Zheng Z-P, Fan W-H, Roy S, Mazur K, Nazet A, Buchner R, Bonn M, Hunger J (2015) Ionic liquids: not only structurally but also dynamically heterogeneous. *Angew Chem Int Ed.* 54(2):687–690
120. Sonnleitner T, Turton DA, Hefter G, Ortner A, Waselikowski S, Walther M, Wynne K, Buchner R (2015) Ultra-broadband dielectric and optical kerr-effect study of the ionic liquids ethyl and propylammonium nitrate. *J Phys Chem B* 119(29):8826–8841
121. Wojnarowska Z, Paluch M (2015) Recent progress on dielectric properties of protic ionic liquids. *J Phys Condens Matter* 27(7):073202/1–073202/20
122. Zaitsau DH, Yermalayeu AV, Emel'yanenko VN, Heintz A, Verevkin SP, Schick C, Berdzinski S, Strehmel V (2014) Structure–property relationships in ILs: vaporization enthalpies of pyrrolidinium based ionic liquids. *J Mol Liquids* 192:171–176
123. Villanueva M, Coronas A, Garcia J, Salgado J (2013) Thermal stability of ionic liquids for their application as new absorbents. *Ind Eng Chem Res* 52:15718–15727
124. Stoppa A, Zech O, Kunz W, Buchner R (2010) The conductivity of imidazolium-based ionic liquids from (–35 to 195)° CA variation of cation's alkyl chain. *J Chem Eng Data* 55:1768–1773
125. Tao R, Tamas G, Xue L, Simon SL, Quitevis EL (2014) Thermophysical properties of imidazolium-based ionic liquids: the effect of aliphatic versus aromatic functionality. *J Chem Eng Data* 59:2717–2724
126. Strehmel V, Wishart JF, Polyanski DE, Strehmel B (2009) Recombination of photogenerated lophyl radicals in imidazolium-based ionic liquids. *ChemPhysChem* 10:3112–3118
127. Berdzinski S, Horst J, Straßburg P, Strehmel V (2013) Recombination of lophyl radicals in pyrrolidinium-based ionic liquids. *ChemPhysChem* 14:1899–1908
128. McHale G, Hardacre C, Ge R, Doy N, Allen RWK, MacInnes JM, Bown MR, Newton MI (2008) Density-viscosity product of small-volume ionic liquid samples using quartz crystal impedance analysis. *Anal Chem* 80:5806–5811
129. Alcade R, Garcia G, Atilhan M, Aparicio S (2015) Systematic study on the viscosity of ionic liquids: measurement and prediction. *Ind Eng Chem Res* 54:10918–10924
130. Neves CMSS, Kurnia KA, Coutinho JAP, Marrucho IM, Lopes JNC, Freire MG, Rebelo LPN (2013) Systematic study of the thermophysical properties of imidazolium-based ionic liquids with cyano-functionalized anions. *J Phys Chem B* 117:10271–10283 (including Supporting Information)
131. Rox ET, Weaver JEF, Henderson WA (2012) Tuning binary ionic liquid mixtures: linking alkyl chain length to phase behavior and ionic conductivity. *J Phys Chem C* 116:5270–5274
132. Ciocirlan O, Iulian O (2009) *J Serb Chem Soc* 74:317–329
133. Asano T (1999) *Pure Appl Chem* 71:1691–1704
134. Strehmel V, Rexhausen H, Strauch P, Görmitz E, Strehmel B (2008) Temperature dependence of interactions between stable piperidine-1-yloxyl derivatives and a semicrystalline ionic liquid. *ChemPhysChem* 9:1294–1302
135. Strehmel V, Rexhausen H, Strauch P, Strehmel B (2010) Temperature dependence of interactions between stable piperidine-1-yloxyl derivatives and a semicrystalline ionic liquid. *ChemPhysChem* 11:2182–2190
136. Vogel H (1921) *Phys Z* 22:645–646
137. Fulcher GS (1925) *J Am Chem Soc* 8:339–355, 789–794
138. Tamman G, Hesse WH, Anorg Z (1926) *Allg Chem* 156:245–257
139. Widgren JA, Laesecke A, Magee JW (2005) The effect of dissolved water on the viscosities of hydrophobic room-temperature ionic liquids. *Chem Commun* 1610–1612

140. AlTuwaim MS, Alkhalidi KHAE, Al-Jimaz AS, Mohammad AA (2014) Temperature dependence of physicochemical properties of imidazolium-, pyrrolidinium-, and phosphonium-based ionic liquids. *J Chem Eng Data* 59:1955–1963
141. Atilhan M, Jacquemin J, Rooney D, Khraisheh M, Aparicio S (2013) Viscous behavior of imidazolium-based ionic liquids. *Ind Eng Chem Res* 52:16774–16785
142. Kolbeck C, Lehmann J, Lovelock KRJ, Cremer T, Paape N, Wasserscheid P, Fröba AP, Maier F, Steinrück H-P (2010) Density and surface tension of ionic liquids. *J Phys Chem B* 114:17025–17036
143. Wandschneider A, Lehmann JK, Heintz A (2008) Surface tension and density of pure ionic liquids and some binary mixtures with 1-propanol and 1-butanol. *J Chem Eng Data* 53: 596–599
144. Chiappe C, Pieraccini D (2005) Ionic liquids: solvent properties and organic reactivity. *J Phys Org Chem* 18:275–297
145. Carmichael AJ, Seddon KR (2000) Polarity study of some 1-alkyl-3-methylimidazolium ambient-temperature ionic liquids with solvatochromic dye, Nile Red. *J Phys Org Chem* 13:591–595
146. Muldoon MJ, Gordon CM, Dunkin IR (2001) Investigations of solvent-solute interactions in room temperature ionic liquids using solvatochromic dyes. *Chem Soc Perkin Trans* 2:433–435
147. Dzyuba SV, Bartsch RA (2002) Expanding the polarity range of ionic liquids. *Tetrahedron Lett* 43:4657–4659
148. Kimura Y, Hamamoto T, Terazima M (2007) Raman spectroscopic study on the solvation of N, N-dimethyl-p-nitroaniline in room-temperature ionic liquids. *J Phys Chem A* 111: 7081–7089
149. Ferrer B, Garcia H, Schultz KP, Nelson SF (2007) Mixed valence compounds as probes to determine the polarity of 1-Butyl-3-methylimidazolium ionic liquids. *J Phys Chem B* 111:13967–13970
150. Ciappe C, Pomelli CS, Rajamani S (2011) Influence of structural variations in cationic and anionic moieties on the polarity of ionic liquids. *J Phys Chem B* 115:9653–9661
151. Crowhurst L, Mawdsley PR, Perez-Arlandis JM, Salter PA, Welton T (2003) Solvent-solute interactions in ionic liquids. *Phys Chem Chem Phys* 5:2790–2794
152. Lee MM, Ruckes S, Prausnitz JM (2008) Solvent polarities and kamlet-taft parameters for ionic liquids containing a pyridinium cation. *J Phys Chem B* 112:1473–1476
153. Kobrak MN (2008) The relationship between solvent polarity and molar volume in room-temperature ionic liquids. *Green Chem* 10:80–86
154. Lee J-M, Ruckes S, Prausnitz JM (2008) Solvent polarities and kamlet-taft parameters for ionic liquids containing a pyridinium cation. *J. Phys. Chem. B* 112:1473–1476
155. Lungwitz R, Strehmel V, Spange S (2010) The dipolarity/polarisability of 1-alkyl-3-methylimidazolium ionic liquids as function of anion structure and the alkyl chain length. *New J Chem* 34:1135–1149
156. Strehmel V, Lungwitz R, Rexhausen H, Spange S (2010) Relationship between hyperfine coupling constants of spin probes and empirical polarity parameters of some ionic liquids. *New J Chem* 34:2125–2131
157. Niedermeyer H, Ashworth C, Brandt A, Welton T, Hunt PA (2013) A step towards the a priori design of ionic liquids. *Phys Chem Chem Phys* 15:11566–11578
158. Spange S, Lungwitz R, Schade A (2014) Correlation of molecular structure and polarity of ionic liquids. *J Mol Liquids* 192:137–143
159. Lohse PW, Borsing R, Lenzer T, Oum K (2008) Exploring 12'-Apo- β -carotenoic-12'-acid as an ultrafast polarity probe for ionic liquids. *J Phys Chem B* 112:3048–3057
160. S. Zhang, Ya. Zhang, X. Ma, L. Lu, Y. He, Y. Deng (2013) Benzonitrile as a probe of local environment in ionic liquids. *J Phys Chem B* 117:2764–2772
161. Stoesser R, Herrmann W, Zehl A, Laschewsky A, Strehmel V (2006) Microviscosity and micropolarity effects of imidazolium based ionic liquids investigated by spin probes their diffusion and spin exchange. *Z Phys Chem* 220:1309–1342

162. Strehmel V (2012) Radicals in Ionic liquids. *ChemPhysChem* 13:1649–1663
163. Wakai C, Oleinikova A, Ott M, Weingärtner H (2005) *J Phys Chem B* 109:17028–17030
164. Bright FV, Baker GA (2006) Comment on “How Polar Are Ionic Liquids? Determination of the static dielectric constant of an imidazolium-based ionic liquid by microwave spectroscopy”. *J Phys Chem B* 110:5822–5823
165. Wakai C, Oleinikova A, Weingärtner H (2006) Reply to “Comment on ‘How Polar Are Ionic Liquids? Determination of the static dielectric constant of an imidazolium-based ionic liquid by microwave spectroscopy’”. *J Phys Chem B* 110:5824
166. Singh T, Kumar A (2008), Static dielectric constant of room temperature ionic liquids: internal pressure and cohesive energy density approach. *J Phys Chem B* 112:12968–12972
167. MacFarlane DR, Forsyth M, Izgorodina EI, Abbott AP, Annata G, Fraser K (2009) On the concept of ionicity in ionic liquids. *Phys Chem Chem Phys* 11:4962–4967
168. Ueno H, Tokuda M (2010) Watanabe, Ionicity in ionic liquids: correlation with ionic structure and physicochemical properties. *Phys Chem Chem Phys* 12:1649–1658

Chapter 2

Rotational and Translational Diffusion in Ionic Liquids

Joshua Sangoro, Tyler Cosby and Friedrich Kremer

Abstract Dynamic glass transition and charge transport in a variety of glass-forming aprotic ionic liquids (ILs) are investigated in wide frequency and temperature ranges by means of broadband dielectric spectroscopy (BDS), pulsed-field gradient nuclear magnetic resonance (PFG NMR), differential scanning calorimetry and dynamic mechanical spectroscopy. On the low-frequency side, the dielectric spectra exhibit electrode polarization effects, while hopping conduction in a disordered matrix dominates the spectra of ionic liquids at higher frequencies. Upon systematic variation of the molecular structure of the ionic liquids, it is observed that the absolute values of dc conductivity and viscosity span more than 11 orders of magnitude with temperature. However, quantitative agreement is found between the characteristic charge transport and the structural α -relaxation rates. These results are discussed in the context of *dynamic glass transition-assisted hopping* as the underlying mechanism of charge transport in the ionic liquids investigated. In addition, a novel approach to determine diffusion coefficients from dielectric spectra in quantitative agreement with PFG NMR is proposed. This makes it possible to separately determine the effective number densities and mobilities of the charge carriers and the type of their temperature dependence. The observed Vogel–Fulcher–Tammann (VFT) dependence of the dc conductivity is shown to be due to a similar temperature dependence of the mobility while Arrhenius type of thermal activation is found for the number density.

J. Sangoro (✉) · T. Cosby
Department of Chemical and Biomolecular Engineering, University of Tennessee,
1512 Middle Drive, Knoxville, TN 37932, USA
e-mail: jsangoro@utk.edu

T. Cosby
e-mail: jcosby3@vols.utk.edu

F. Kremer
Institute of Experimental Physics I, University of Leipzig, Linnestr. 5,
04103 Leipzig, Germany
e-mail: kremer@physik.uni-leipzig.de

Keywords Ionic liquids · Diffusion · Charge transport rate · DC conductivity · Einstein–Smoluchowski relations · Green–Kubo relations · Effective number density · Random barrier model

2.1 Introduction

Fruitful and exciting periods of scientific and technological research often ensue the discovery of a novel material. As succinctly stated by Yves Chauvin in his 2005 Nobel address: “*If you want to find something new, look for something new!*” [1]. New breakthroughs offer possibilities to critically re-examine old problems as well as to pose new ones. This is the case with ionic liquids, liquids consisting entirely of cations and anions with melting points below 100 °C. Ionic liquids are interesting for both fundamental as well as technological applications. Depending on the composition and chemical characteristics of the constituent molecular moieties comprising the ionic liquids, they may be classified into two main categories, namely aprotic and protic ionic liquids. This chapter focuses on studies of aprotic ionic liquids. Although no single ionic liquid possesses all these characteristics, aprotic ionic liquids in general show a rich mix of outstanding properties such as low melting temperatures, high ionic conductivity, negligible vapour pressures, wide liquidus ranges, high thermal and electrochemical stability and tunability. Despite reports dating back to Paul Walden’s work in 1914 [2, 3], there has been a heightened interest in ionic liquids during the last two decades due to their unique properties which make them especially attractive for use in reaction media, as electrolytes in electrochemical energy technologies, among many others. Some of the significant areas of applications of ionic liquids are illustrated in Fig. 2.1.

From a fundamental point of view, the fact that ionic liquids can be easily supercooled makes them interesting materials to use as platforms for investigating the interplay between the dynamic glass transition and charge transport in amorphous liquids. In a sense, this involves re-examination of basic relations put forward by Einstein [4], Smoluchowski [5, 6], Maxwell [7, 8], Langevin [9] and Debye [10] concerning rotational and translational diffusion in (conducting) liquids. Although the different terminologies are employed today, certain aspects of the topics addressed by these scientists still remain unsolved. For instance, there is no general quantitative theory of dynamic glass transition (treated by Debye as rotational Brownian motion based on Einstein’s ideas) which is able to reproduce all the observed experimental results to date, notwithstanding the significant advances achieved so far from experimental and theoretical studies. Another outstanding example is Einstein’s work on Brownian motion in which he derived the link between translational diffusion (or charge transport) and viscosity (related to rotational diffusion). One of the objectives of the current chapter is to verify how well these classical relations hold in glass-forming ionic liquids.

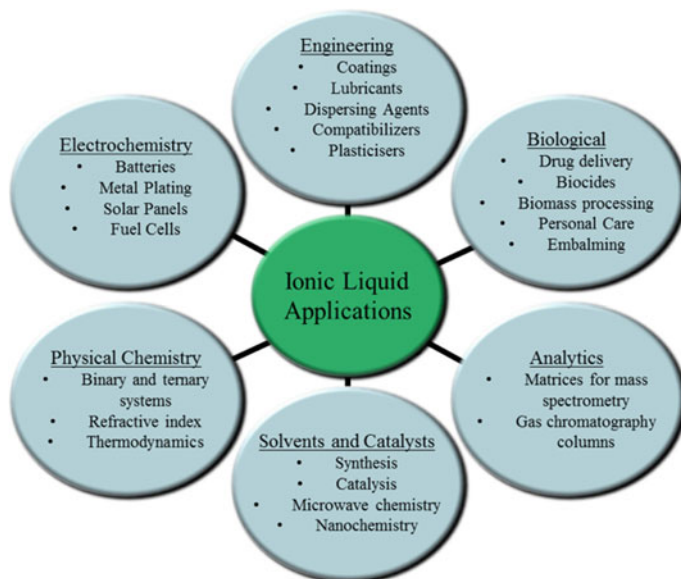


Fig. 2.1 Some possible applications of ionic liquids

Since it measures the complex dielectric function (and consequently, the complex conductivity) over many orders of magnitude in frequency and in a wide temperature interval, broadband dielectric spectroscopy (BDS) has proved to be an ideal experimental tool for addressing basic questions regarding the correlation between ion conduction (translational diffusion) and the dynamic glass transition (rotational diffusion) in broad length- and timescales as well as localized molecular fluctuations (secondary relaxations) [11–32]. Detailed knowledge of diffusion in ionic liquids, provided by this technique, is instructive for their optimal utilization in a wide range of scientific and technological applications.

It is estimated that it may be possible to synthesize approximately 10^{18} different ionic liquids based on the combinations of cations and anions available [20, 33]. This high degree of tunability has its challenges as well. Use of a trial-and-error approach in the synthesis of ionic liquids in search of one exhibiting particular physical and chemical properties is therefore not viable. Thus, it is imperative that more general relationships between the desirable properties such as high conductivities and the nature as well as structure of anions and cations be established. Molecular dynamics simulations are being conducted to make quantitative predictions of the physical properties of ionic liquids. In this chapter, it is shown that characteristic hopping lengths (determined from a combination of broadband dielectric spectroscopy and pulsed-field gradient nuclear magnetic resonance) in a selected series of ionic liquids increase with the molecular volume obtained from quantum chemical simulations.

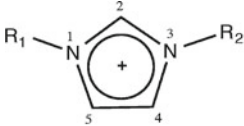
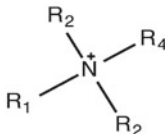
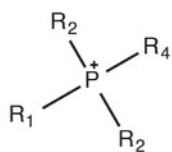
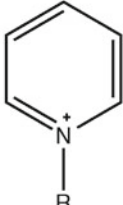
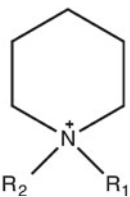
2.2 Experimental Details

The ionic liquids investigated in this study (1-hexyl-3-methylimidazolium chloride—[HMIM] [Cl], 1-hexyl-3-methylimidazolium bromide—[HMIM] [Br], 1-hexyl-3-methylimidazolium iodide—[HMIM] [I], 1-hexyl-3-methylimidazolium tetrafluoroborate—[HMIM] [BF₄], 1-hexyl-3-methylimidazolium hexafluorophosphate—[HMIM] [PF₆], 1-(2-hydroxyethyl)-3-methylimidazolium tetrafluoroborate—[HEMIM] [BF₄], 1-methyl-3-octylimidazolium tetrafluoroborate—[MOIM] [BF₄], 1-butyl-3-methylimidazolium tetrafluoroborate—[BMIM] [BF₄], 1,3-dimethylimidazolium dimethylphosphate—[MMIM] [Me₂PO₄], 1-ethyl-3-methyl-pyridinium ethylsulfate—[3-MEP] [EtSO₄], Trioctylmethylammonium bis(trifluoromethylsulfonyl)imide—[OMA] [BTA] and Tetrabutylphosphonium bromide—[TBP] [Br]) were purchased from Solvent Innovation GmbH and Iolitec GmbH. Tributylmethylphosphonium trifluoromethanesulfonate—[TBOP] [OTf] was provided by Prof. Dr. Katsuhiko Tsunashima, National Institute of Technology, Wakayama College. (1-propyl-3-methylimidazolium bis(trifluoromethylsulfonyl)imide—[PrMIM] [NTf₂], 1-butyl-3-methylimidazolium bis(trifluoromethylsulfonyl)imide—[BMIM] [NTf₂], 1-hexyl-3-methylimidazolium bis(trifluoromethylsulfonyl)imide—[HMIM] [NTf₂], 1-octyl-3-methylimidazolium bis(trifluoromethylsulfonyl)imide—[OMIM] [NTf₂], 1-decyl-3-methylimidazolium bis(trifluoromethylsulfonyl)imide—[DMIM] [NTf₂], 1-pentyl-3-vinylimidazolium bis(trifluoromethylsulfonyl)—[PVIM] [NTf₂], 1-octyl-3-vinylimidazolium bis(trifluoromethylsulfonyl)—[OVIM] [NTf₂]) were prepared by Prof. Dr. Veronika Strehmel, Hochschule Niederrhein University of Applied Sciences. The chemical structures of the cations and anions investigated are shown in Tables 2.1 and 2.2, respectively. The dielectric measurements were performed between 0.01 Hz and 1.8 GHz using a novocontrol high-resolution alpha analyzer (0.01 Hz–10 MHz) and an HP impedance analyzer (1 MHz–1.8 GHz). The analyzers were assisted by Quatro Temperature Controllers using pure nitrogen as heating agent and assuring a temperature stability better than 0.2 K. An ARES (Advanced Rheometric Expansion System) rheometer from TA Instruments was employed for Dynamic Mechanical Spectroscopy (DMS) measurements. A 400 MHz NMR spectrometer with a home-built gradient device was used to obtain the self-diffusivities at different temperatures.

2.3 Results and Discussion

In this chapter, the dielectric properties of ionic liquids are investigated in broad frequency and temperature ranges. Emphasis is placed on quantitative understanding of the underlying mechanisms as well as the interplay between charge transport and glassy dynamics in these materials. Quantum chemical calculations of molecular volumes of ionic liquids are performed using MOPAC2009 package in

Table 2.1 Chemical structures of typical cations in ionic liquids

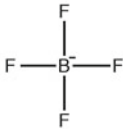
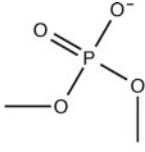
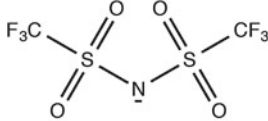
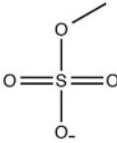
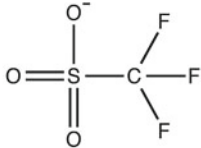
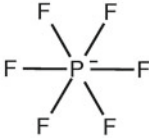
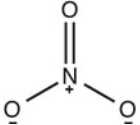
1 - alkyl - 3 - methylimidazolium	Tetra-alkyl-ammonium
	
Tetra-alkyl-phosphonium	N-alkyl-pyridinium
	
N-alkyl-N- methylpiperidinium	Symbol key
	$R_{1,2,3,4} = \text{CH}_3(\text{CH}_2)_n$, ($n = 1,3,5,7,9$), aryl, etc...

order to re-examine the predictions of Einstein concerning the dependence of the diffusion coefficient on molecular sizes. The following techniques are employed: broadband dielectric spectroscopy, pulsed-field gradient nuclear magnetic resonance, differential scanning calorimetry and dynamic mechanical spectroscopy.

2.3.1 Charge Transport and Dynamic Glass Transition in Ionic Liquids

Broadband dielectric spectroscopy (BDS) measures the complex dielectric function, ϵ^* , which is equivalent to the complex conductivity function, σ^* . This is expressed as

Table 2.2 Chemical structures of some of the anions comprising the ionic liquids investigated

$[\text{BF}_4]^-$	$[\text{Me}_2\text{PO}_4]^-$
	
$[\text{NTf}_2]^-$	[ethyl sulfate] $^-$
	
$[\text{OTf}]^-$	$[\text{PF}_6]^-$
	
$[\text{NO}_3]^-$	[halides] $^-$
	$\text{Cl}^-, \text{Br}^-, \text{I}^-$

$\sigma^*(\omega, T) = i\varepsilon_0\omega\varepsilon^*(\omega, T)$, implying that $\sigma' = \varepsilon_0\omega\varepsilon''$ and $\sigma'' = \varepsilon_0\omega\varepsilon'$ (ε_0 being the vacuum permittivity and ω the radial frequency) [32]. The dielectric spectra of the ionic liquid [HMIM] [Cl] are presented in Fig. 2.2. The real part of the complex conductivity σ' is characterized on the low-frequency side by a plateau (the value of which directly yields the long range ionic conductivity, σ_0), and the characteristic rate, ω_c , at which dispersion sets in and turns into a power law at higher frequencies. On the other hand, the real part of the complex dielectric function ε' turns from the high frequency limit to the static value ε_s at the characteristic rate ω_c . At lower frequencies, it is observed that σ' decreases from σ_0 value and this is due to electrode polarization that results from slowing down of charge carriers at the electrodes.

Rescaled with respect to ω_c and σ_0 , the dielectric spectra—as measured over wide temperature ranges—coincide (see Fig. 2.3), thus proving the uniqueness of

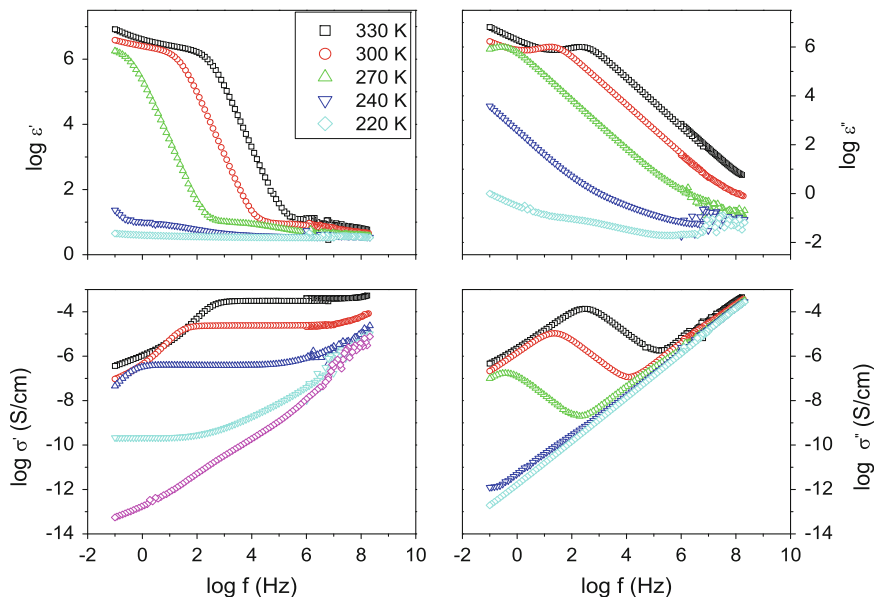


Fig. 2.2 Complex dielectric function ($\epsilon^* = \epsilon' - i\epsilon''$) and complex conductivity function ($\sigma^* = \sigma' + i\sigma''$) of the ionic liquid 1-hexyl-3-methylimidazolium chloride—[HMIM] [Cl] at different temperatures as indicated. The error bars are comparable to the size of the symbols, if not explicitly indicated otherwise. The logarithm is to base 10

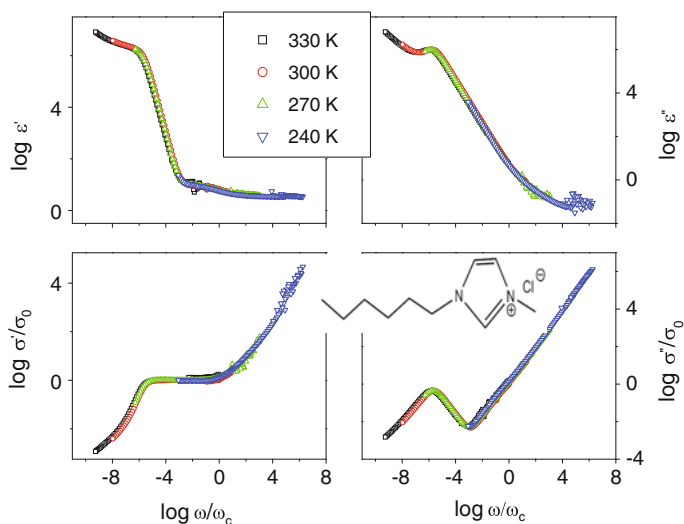


Fig. 2.3 Scaling of the complex dielectric function ($\epsilon^* = \epsilon' - i\epsilon''$) and complex conductivity function ($\sigma^* = \sigma' + i\sigma''$) with respect to ω_c and σ_0 for the ionic liquid 1-hexyl-3-methylimidazolium chloride—[HMIM] [Cl] at different temperatures

the mechanism of charge transport. It can be concluded that the underlying processes in the spectral and temperature ranges probed exhibit identical thermal activation [22, 23, 34–36].

Charge transport in many amorphous ion-conducting systems is reasonably well described by random barrier model developed by Dyre [37]. In the context of this model, ions hop in a random spatially distributed potential landscape. The ion transport is determined by the ability of the charge carriers to hop over the random energy barriers. The success of the ions in surmounting the highest barrier determines long range or dc conductivity σ_0 [38]. The time corresponding to the attempt rate to overcome the highest barrier is denoted by τ_e . The analytical solution for the complex dielectric function, obtained within the continuous-time-random walk approximation, is expressed as

$$\varepsilon^*(\omega) = \frac{\sigma_0 \tau_e}{\varepsilon_0 \ln(1 + i\omega \tau_e)}. \quad (2.1)$$

It has been demonstrated that the approximate form of the random barrier model given in Eq. 2.1 describes the dielectric spectra of many different ion-conducting systems qualitatively well. However, a close examination of the fits of the dielectric spectra of ionic liquids reveals the existence of additional ‘relaxation-like’ process. This contribution is particularly dominant in the real part of the complex dielectric function. Apparently, this additional process was neglected in many earlier dielectric studies of ionic liquids but its possible origin is fairly obvious. From a physical point of view, a successful ionic jump must be accompanied by structural reorganization of the ionic atmosphere, leading to a relaxation-like contribution not only to the imaginary part, but also to the real part of the dielectric function. This reorganization accompanying successful ion jumps causes additional fluctuations in the polarization, resulting in a relaxation process with characteristic timescales similar to that of ionic motion.

From the definition of polarization \mathbf{P} in terms of the complex dielectric function $\varepsilon^*(\omega)$, Debye employed the Lorentz field and substituted the static permittivity with the dynamic permittivity obtaining

$$\mathbf{P} = \varepsilon_0(\varepsilon^*(\omega) - 1)\mathbf{E} = N_1 \left[\alpha_\infty + \frac{\mu^2}{3kT(1 + i\omega\tau_D)} \right] \frac{\varepsilon^*(\omega) + 2}{3} \mathbf{E} \quad (2.2)$$

where α_∞ and N_1 denote the polarizability and number of dipoles per unit volume, respectively, and τ_D is the Debye macroscopic relaxation time. Defining ε_s and ε_∞ as the unrelaxed and relaxed values of the dielectric permittivity, respectively, Eq. 2.2 can be rearranged as

$$\frac{\varepsilon^*(\omega) - \varepsilon_\infty}{\varepsilon_s - \varepsilon_\infty} = \frac{1}{1 + i\omega\tau_D} \quad (2.3)$$

The Debye equations of dielectric permittivity can also be derived by considering the first-order kinetics of rise or decay of the dipolar polarization. Further details can be found in [32, 39].

It should be recalled that although the Debye theory of dielectric relaxation resulted from rigorous treatment of rotational Brownian motion, Debye-like relaxations are only observed in rare cases in glass-forming systems. The usual dielectric spectra are much broader than predicted by Debye's approach. Thus, a number of phenomenological descriptions aimed at obtaining better fits to experimental data like the Cole-Cole, Cole- Davidson and Havriliak-Negami functions have been proposed. The empirical Havriliak-Negami function is the most commonly used form to fit the spectra of many materials exhibiting dielectric relaxations. Within this approach, the complex dielectric function is given by

$$\epsilon_{\text{HN}}^* = \epsilon_\infty + \frac{\Delta\epsilon}{\left(1 + (i\omega\tau_{\text{HN}})^\beta\right)^\gamma} \quad (2.4)$$

where $\Delta\epsilon = \epsilon_s - \epsilon_\infty$ is the dielectric relaxation strength or intensity with $\epsilon_s = \lim_{\omega\tau_{\text{HN}} \geq 1} \epsilon'(\omega)$ and $\epsilon_\infty = \lim_{\omega\tau_{\text{HN}} \leq 1} \epsilon'(\omega)$. The shape parameters β and γ describe symmetric and asymmetric broadening of the complex dielectric function. The position of maximal loss ω_p depends on the characteristic time obtained from Eq. 2.4

as well as the shape parameters according to $\omega_p = \frac{1}{\tau_{\text{HN}}} \left[\sin \frac{\beta\pi}{2+2\gamma} \right]^{\frac{1}{\beta}} \left[\sin \frac{\beta\gamma\pi}{2+2\gamma} \right]^{-\frac{1}{\beta}}$. It should be noted that the real and imaginary parts of the complex dielectric function are related by the Kramers-Kronig relations [32, 40].

Thus, to account for ionic motion and the accompanying structural reorganization, the complex dielectric function should be described by Eq. 2.5:

$$\epsilon^*(\omega) = \frac{\sigma_0\tau_e}{\epsilon_0 \ln(1 + i\omega\tau_e)} + \frac{\Delta\epsilon}{\left(1 + (i\omega\tau_{\text{HN}})^\beta\right)^\gamma} + \epsilon_\infty \quad (2.5)$$

where ϵ_∞ is the (high frequency) relaxed value of ϵ' . As shown in Fig. 2.4 for [TBOP] [OTf], Eq. 2.5 yields a quantitative fit to the part of the experimental spectra dominated by charge transport.

The dielectric spectra of ionic disordered materials can also be presented in terms of the electrical modulus M^* , where $M^* = 1/\epsilon^*$. Although the three formalisms (complex dielectric, conductivity and modulus functions) are equivalent, they emphasize different aspects of the underlying mechanisms of charge transport and molecular dynamics. The first two forms—the complex dielectric and conductivity functions—have traditionally been used in studies of (dipolar) relaxations and charge transport, respectively. Maxwell's equations, which describe the interaction of electromagnetic waves with matter, make direct reference to and indicate equivalence of these approaches. At higher frequencies, secondary relaxations

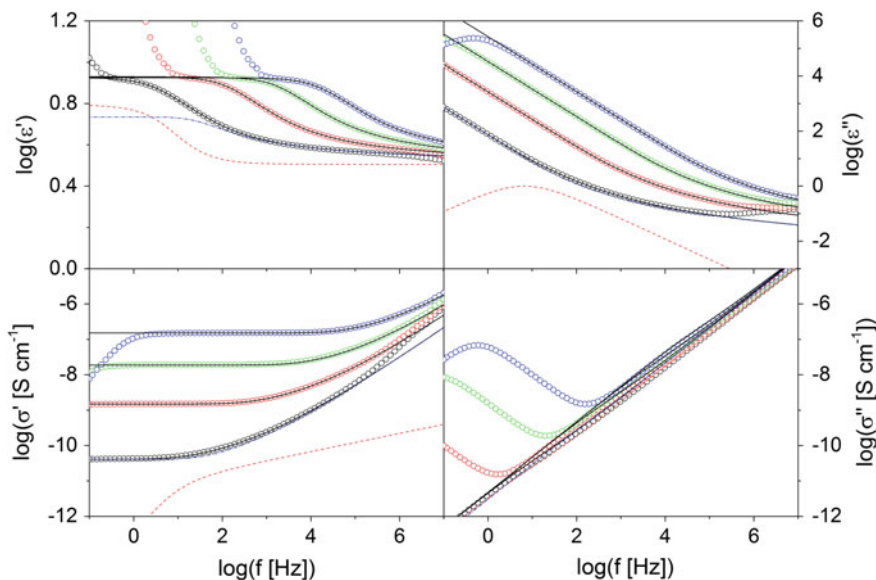


Fig. 2.4 The dielectric and conductivity functions for [TBOP] [OTf] versus frequency at different temperatures, as indicated. The fits are made using Eq. 2.5. The spectra are shown at temperatures from 210 to 240 K (10 K increments). The *continuous solid lines* denote the combination of the Havriliak–Negami (*red*) and random barrier model (*blue*) functions. The error bars are comparable to the size of the symbols, if not specified otherwise

(denoted by rate ω_β) are observed. We recently showed that these dipolar processes are due to librations of the cations [23, 41].

In the intermediate frequency ranges, the dielectric properties are governed by motion of the charge carriers in the bulk. This contribution represents the (translational) diffusion of the ions. This regime of the dielectric spectra can be used to obtain important molecular parameters characterizing translational diffusion of the charge carriers. Electrode polarization dominates the spectra at lower frequencies.

Empirically, $\omega_c \cong \omega_M \cong 1/\tau_e$ as shown in Fig. 2.5, where ω_M is the radial frequency corresponding to the peak in the imaginary part of the electrical modulus and $\omega_e = (1/\tau_e)$ is a characteristic time that defines the attempt rate of the charge carriers to overcome the highest energy barrier (limiting the σ_0), thereby enabling the physical interpretation of ω_c within the random barrier model [32, 37].

To find out the impact of molecular structure and composition on charge transport and dynamics of these systems, ionic liquids based on the HMIM cation are systematically investigated upon variation of the anions. The thermal activation of σ_0 and ω_c —the central quantities describing ion transport—are studied. It is clear that systematic changes of the anions while keeping the same [HMIM] cation result in substantial differences in the charge transport parameters. These differences become more significant as the temperature is lowered towards the calorimetric glass transition temperature of the ionic liquid under study. In order to find out the

Fig. 2.5 Activation plot for characteristic electrical rates ω_M (as obtained from the peak frequency of M''), ω_e and ω_p as taken from the fit using Eq. 2.5 for TBOP OTf. The error bars are smaller than the size of the symbols, if not explicitly stated otherwise. The logarithm is to base 10

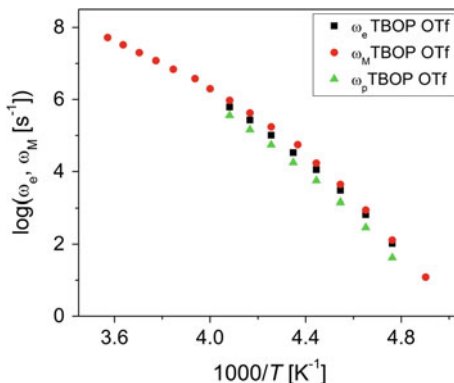
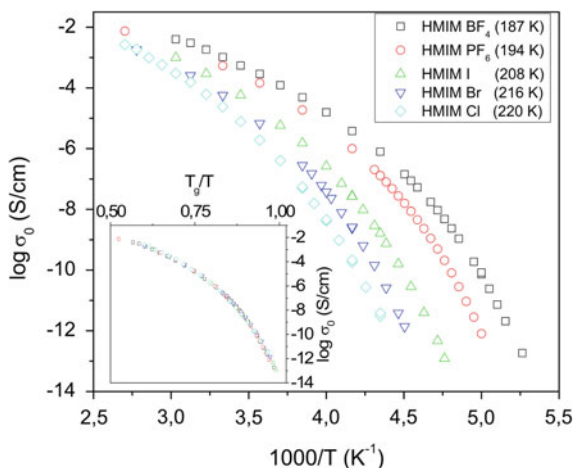


Fig. 2.6 Temperature dependence of σ_0 for the selected ionic liquids is shown. *Inset* Scaling with respect to the calorimetric glass transition temperature (values given in the legend) determined by differential scanning calorimetry. Reproduced from Ref. [34] with permission from the PCCP Owner Societies



impact of the dynamic glass transition on charge transport in ionic liquids, dc conductivity and viscosity measurements were performed for a systematic series of ionic liquids, upon variation of the anions. Figure 2.6 presents the temperature dependence of σ_0 for the selected ionic liquids.

Systematic variation of the chemical structure leads to remarkable differences exceeding six orders of magnitude in σ_0 (between the tetrafluoroborate and chloride anions) at lower temperatures. However, upon scaling with the calorimetric glass transition temperature, all the data coincide for the anions examined. This experimental finding highlights the important role played by dynamic glass transition in charge transport in ionic liquids. In addition, viscosity, η ,—well known to be directly related to the dynamic glass transition in liquids—also exhibits a similar thermal activation. The significant changes in the viscosity and ω_e upon systematic variation of the anions is also worth pointing out as presented in Fig. 2.7.

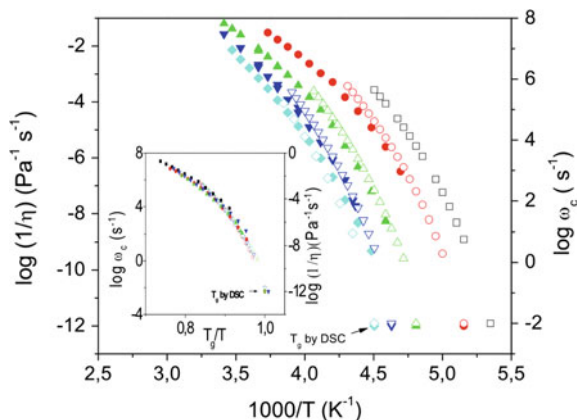
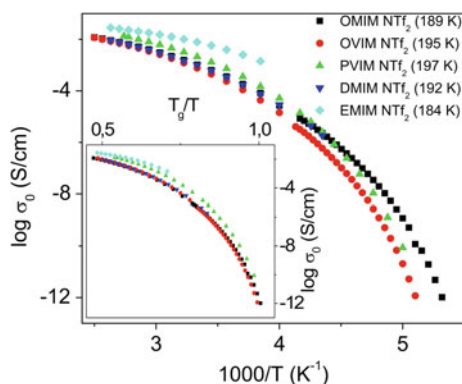


Fig. 2.7 Thermal activation of the fluidity (inverse viscosity) $1/\eta(T)$ and $\omega_c(T)$ for the series of imidazolium-based ionic liquids upon variation of the anions. *Inset* Scaling with respect to the calorimetric glass transition temperature obtained by differential scanning calorimetry (see legend of Fig. 2.6). The symbols are identical to those in Fig. 2.6 with $1/\eta(T)$ and $\omega_c(T)$ represented by *full* and *open symbols*, respectively. Reproduced from Ref. [34] with permission from the PCCP Owner Societies

Fig. 2.8 Temperature dependence of $\sigma_0(T)$. *Inset* Scaling with respect to the calorimetric glass transition temperature (as shown) measured by differential scanning calorimetry) for selected bis (trifluoromethylsulfonyl) imide-based ionic liquids



Extrapolating ω_c to the timescale corresponding to 100 s, agreement with the measured calorimetric glass transition temperature T_g within margins of ± 2 K is found. Scaling of $\sigma_0(T)$, $\omega_c(T)$, and $1/\eta(T)$ with respect to T_g using the approach proposed by Angell [42–45], coinciding plots for all the investigated ionic liquids are found as shown in Figs. 2.6 and 2.7. On the other hand, upon varying the cation and maintaining the same anion, deviations can be observed in the scaled plot of $\sigma_0(T)$. This is illustrated for the bis(trifluoromethylsulfonyl)imide-based ionic liquids in Fig. 2.8. Our conjecture is that since the size of the cation in ionic liquids is larger than that of the anion, the cations play a more pronounced role in determining the viscosity and structural relaxation (and consequently charge transport). It should be

recalled that electrostatic interactions, which control the dynamic glass transition in these materials, are strongly influenced by both the charge as well as the distance of separation between the interacting ions.

Using the Einstein and Einstein–Smoluchowski equations together with the definition of dc conductivity, one obtains [23, 34]:

$$\sigma_0(T) = q\mu(T)n(T) = n(T) \frac{q^2 D(T)}{kT} = n(T) \frac{q^2 \lambda^2 \omega_c(T)}{6kT} \quad (2.6)$$

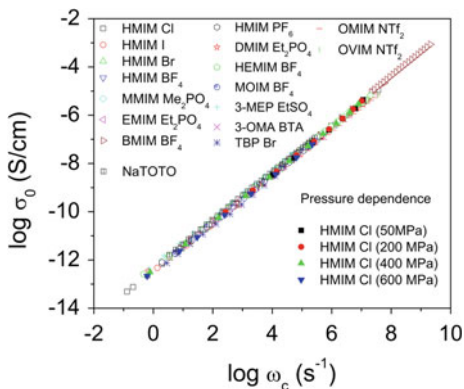
where n denotes the effective number density of charge carriers contributing to ion transport at the timescale of ω_c , λ refers to the characteristic diffusion length in this timescale, also taken characterizing the cross-over from non-random diffusion to random diffusion [46], D is the diffusion coefficient, μ is the mobility, q is the elementary charge and k denotes the Boltzmann constant. Therefore, $\sigma_0 \propto \omega_c$ as implied by the empirical BNN relation and in full agreement with the results presented in Fig. 2.9. It is noteworthy that the data coincide for all the ionic liquids investigated despite variations of the absolute values of both the dc conductivity and the characteristic rates spanning more than 11 decades upon changes in the temperature, pressure as well as composition.

In his paper on Brownian motion, Einstein [4] derived the first form of what is currently known as the fluctuation–dissipation theorem, linking position fluctuations to a dissipation (viscosity). This relation forms the basis of the linear response theory emphasized by Kubo [47] and is of direct relevance in the current studies. Einstein showed that

$$\langle x^2 \rangle_t = 2Dt = \frac{RT}{N} \frac{t}{3\pi\eta a} \quad (2.7)$$

where $\langle x^2 \rangle_t$ denote the position fluctuations (completely identical to λ^2 employed in Eq. 2.6), t is a measure of the timescale (equivalent to $1/\omega_c$ in the current work), R the gas constant, N the Avogadro number and a the Stoke’s radius. Upon

Fig. 2.9 The dc conductivity, σ_0 , versus the characteristic charge transport rate, ω_c , for different ionic liquids as indicated. The data for all ionic liquids are obtained from dielectric measurements at ambient pressure except for the HMIM Cl, for which the transport quantities are also measured at different pressures as indicated



rearranging Eq. 2.7, it is clear that the observed universality of charge transport in ionic liquids as displayed in Fig. 2.9 is due to identical thermal activation of the charge transport rate and the viscosity, i.e., the product $\eta(T)\omega_c(T)/T$ exhibits negligible temperature and pressure dependence. This embodies the link between charge transport and structural relaxation in the ionic liquids studied.

Further insight into the correlation between charge transport and dynamic glass transition can be gained by comparison of viscosity obtained from dynamic mechanical spectroscopy (DMS) and the charge transport rate ω_c . Due to technical reasons, DMS only covers a spectral range spanning about 3–4 decades. This is about nine orders of magnitude less than the range accessible by broadband dielectric spectroscopy. To circumvent this difficulty and compare dielectric and DMS results over many decades, the structural relaxation rate ω_η can be approximated using Maxwell relation, $\omega_\eta = \frac{G_\infty}{\eta}$, assuming a temperature independent instantaneous shear modulus (typically 0.1 GPa) and position fluctuations (typically 0.2 nm). Based on Einstein–Smoluchowski, Stokes–Einstein and Maxwell relations one can easily show that $\omega_c = P\omega_\eta$, where $P = kT/(3\pi G_\infty a\lambda^2)$. Figure 2.10 demonstrates that $\omega_c \cong \omega_\eta$ over 6 decades and P is a constant of order one within experimental accuracy. These two rates can be compared more directly by making dielectric and DMS measurements at temperatures just above the calorimetric glass transition as shown Fig. 2.10. The rate ω_η obtained from the peak in G'' is observed to be in quantitative agreement with the charge transport rate ω_c determined from the dielectric spectra. It is therefore experimentally established that ω_c is ω_η in

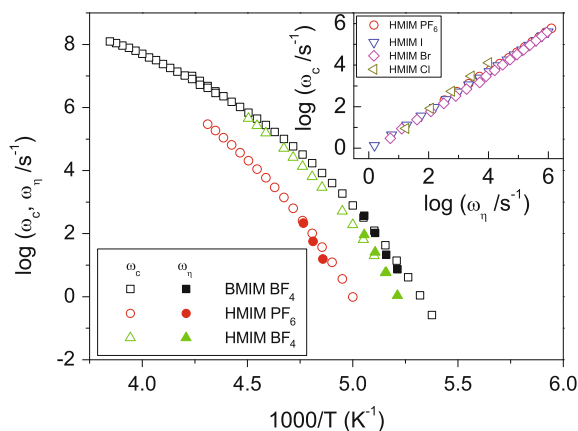


Fig. 2.10 The temperature dependence of the characteristic charge transport rate ω_c as well as the structural relaxation rate, ω_η , determined from dynamic mechanical spectroscopy (DMS) measurements for selected ionic liquids as shown. The two characteristic rates practically coincide within the spectral range measured. *Inset* The characteristic charge transport rate ω_c versus the structural relaxation rate, ω_η , determined from viscosity by applying the Maxwell relation given by $\omega_\eta = \frac{G_\infty}{\eta}$. Reprinted with permission from (*Acc. Chem. Res.*, 2012, 45 (4), pp. 525–532). Copyright (2012) American Chemical Society

glass-forming ionic liquids. The observed universality is thus understood based on Einstein's predictions as already discussed.

According to Eq. 2.6, the measured σ_0 is a product of the mobility and the effective number density of charge carriers contributing to ionic transport. It is essential to identify which of the two quantities gives the dc conductivity its characteristic VFT-type temperature dependence. In addition, it is helpful to find out whether one of the two quantities has greater influence on the ionic conductivity. For electronic conductors, *Hall Effect* measurements provide a means of disentangling the contributions of n and μ to the measured electrical conductivity, but the Hall voltages associated with ionic transport are at the nano-volt levels and are therefore too small to be determined with sufficient accuracy using state-of-the-art equipment. In addition, the validity of Hall measurements on ionic conductors is still in doubt [48].

Estimative determinations of the diffusion coefficients can be made by applying Eq. 2.6 and taking for the hopping length, values in the order of the Pauling diameter [49], i.e. $\lambda = 0.17$ nm and $\lambda = 0.19$ nm for [BMIM] [BF₄] and [MMIM] [Me₂PO₄], respectively. Independent results from PFG NMR together with the diffusion coefficients obtained from dielectric measurements are shown in Fig. 2.11. This simple method yields diffusion coefficients in agreement with those obtained by PFG NMR [22, 23]. Additionally, these experimentally determined diffusivities have been shown to coincide with those found from computations involving the Green–Kubo and Einstein relations as shown for [BMIM] [Br] in Fig. 2.12. These estimates make it possible to disentangle (using Eq. 2.6) the influence of n , the

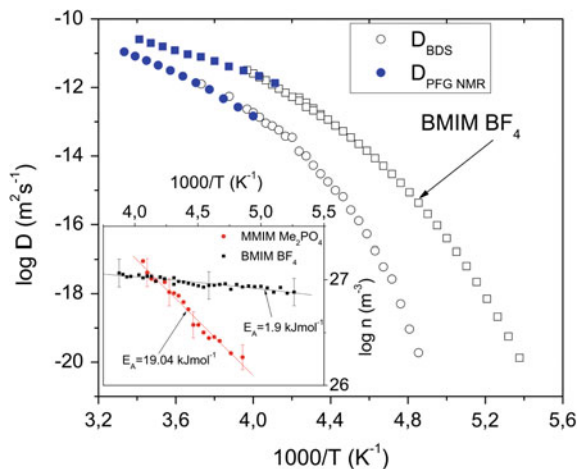


Fig. 2.11 Diffusion coefficient determined by the novel approach involving application of the Einstein–Smolukowski equation (using ω_c as hopping rate and with λ equal to the Pauling diameter of the ions as hopping length [49]), compared with the diffusion coefficient measured by PFG NMR (blue colour) for two ionic liquids: BMIM BF₄ and MMIM Me₂PO₄ [22, 23]. *Inset* Effective number of charge carriers as a function of inverse temperature (the respective activation energies are as indicated). The error bars are comparable to the size of the symbols, if not specified otherwise. Log is used to refer to logarithm to base 10

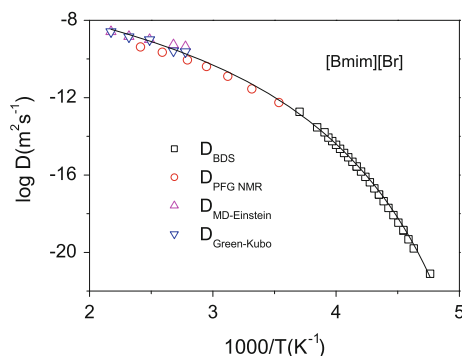


Fig. 2.12 Diffusion coefficients obtained from the dielectric spectra by application of the Einstein–Smoluchowski relation as well as those measured by PFG NMR for the ionic liquid [BMIM] [Br]. In addition, diffusion coefficients determined computationally by Einstein and Green-Kubo equations from quantum mechanical simulations are presented as well. Reprinted with permission from (*Acc. Chem. Res.*, 2012, 45 (4), pp. 525–532). Copyright (2012) American Chemical Society

effective number density, from that of the electrical mobility, μ . It is found that the VFT-type of thermal activation of the ionic conductivity originates exclusively from a similar dependence of the diffusion coefficient. In contrast, the effective number density of the ions exhibits Arrhenius type of temperature dependence (inset of Fig. 2.11). By extrapolating the effective number density to room temperature, one obtains $2.9 \times 10^{27} \text{ m}^{-3}$ for [BMIM] [BF₄], close to $3.4 \times 10^{27} \text{ m}^{-3}$, which is the stoichiometric number of ions in the system. Therefore, around 85 % of the available charge carriers participate in ionic transport at room temperature. This result agrees with recent reports suggesting that only a fraction of the available charge carriers actually participate in the conduction process [12–14]. We have demonstrated that the approach to determine diffusion coefficient from dielectric spectra holds for other glass-forming systems as well [35]. Thus, this approach enables the determination of diffusion coefficient spanning many orders of magnitude by broadband dielectric spectroscopy.

2.3.2 *Elucidating the Correlation Between Characteristic Hopping Lengths and Molecular Volumes of Ionic Liquids*

There is a concerted effort aimed at understanding the physico-chemical properties of ionic liquids (ILs). In general, they exhibit a unique mix of interesting properties such as high conductivities, wide electrochemical windows, thermal stability, negligible vapour pressures, wide liquid ranges and low melting points, which makes them promising for use in power sources for electric vehicles, hybrid cars,

electronic and power storage devices [22, 23, 34, 50, 51]. It is estimated that it is possible to synthesize up to about 10^{18} different ILs based on the combinations of cations and anions available [20, 33]. Thus, it is imperative that more general relationships between the desirable properties such as high conductivities and the nature of anions and cations be established. Previous attempts to make quantitative predictions of the physical properties of ILs using quantitative structure–property relationships and molecular mechanics simulations have had some success [20]. The major drawbacks of these approaches include the need for large experimental datasets to derive correlations, time consuming computational methods or at least some experimental data from the IL under study. In this section, the hopping lengths characterizing charge transport are investigated with respect to ionic volumes determined by quantum chemical calculations.

Quantum chemical calculations of molecular volumes of the ionic liquids were carried out using MOPAC2009 [52]. Semi-empirical quantum chemical calculations have been performed using MOPAC2009 and the PM6 [53] Hamiltonian for geometry optimization. The COSMO technique was applied to account for solvent effects [54]. The typical value of the static dielectric permittivity for many imidazolium-based ILs is $\epsilon_s = 15$, so this value was assumed in the calculations [15, 25]. Because the molecular diameter is strongly dependent on the conformation of the molecule various conformers were considered (e.g. 56 conformers for [DMIM]⁺). Molecular volumes, V , were obtained by modelling the molecule as a series of intersecting spheres, whose radii are determined by the atom type (as implemented in MOPAC2009 [52] by the COSMO [54] solvation model). By taking the longest distance between two atoms and adding the van der Waals radii of the atoms, the maximum molecular diameters, D , were determined. The van der Waals radii reported by Bondi [55] were assumed for the calculation of the volume V as well as the diameter D . The ranges of molecular dimensions obtained are presented in Table 2.3. The technique described has been shown to reproduce the well-established ionic volumes of many common ions [56]. The values obtained in our studies are systematically lower than volumes determined from crystal structures but they exhibit the same trends [20]. The volumes corresponding to those of the crystal structures could only be reproduced by choosing different van der Waals radii.

Table 2.3 Range of molecular volumes, V , and maximum diameters, D , for different conformations of the ions constituting the ionic liquids

Ion	V/nm^3	D/pm
[MVIM]	0.1205–0.1208	966–1018
[PropMIM]	0.1492–0.1524	989–1131
[PVIM]	0.2601–0.2722	1084–1522
[OVIM]	0.1694–0.1738	1118–1905
[OMIM]	0.2483–0.2619	1030–1768
[DMIM]	0.2899–0.3139	1053–2021
[(CF ₃ SO ₂) ₂ N] (or [NTf ₂])	0.1693–0.1748	1000–1027

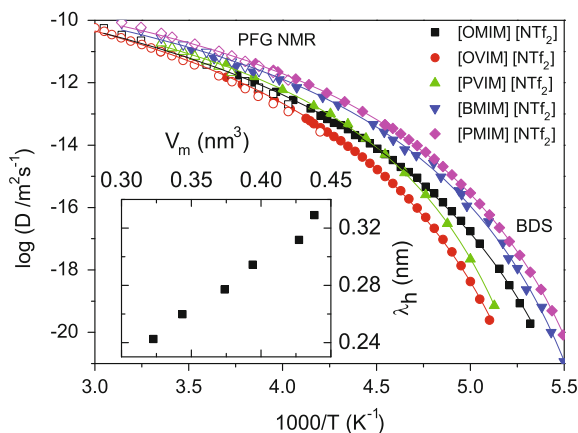


Fig. 2.13 Diffusion coefficients determined from broadband dielectric spectra (*filled symbols*) by applying the Einstein–Smoluchowski relation, using ω_c as the characteristic hopping rate for a series of ionic liquids based on the bis(trifluoromethylsulfonyl)imide anion as a function of inverse temperature. The diffusion coefficient measured by PFG NMR (*open symbols*) versus inverse temperature. *Inset* The mean hopping lengths λ_c (determined by the Einstein–Smoluchowski equation ($D = \lambda^2 \omega_c / 6$) using ω_c obtained from BDS as the characteristic hopping rate and diffusion coefficient D measured by PFG NMR) versus the sum of molecular volumes of anions and cations from quantum chemical calculations for the different ionic liquids based on the same bis(trifluoromethylsulfonyl)imides anion. The calculation is carried out in the temperature ranges accessible to both techniques. Reprinted with permission from (*Acc. Chem. Res.*, 2012, 45 (4), pp. 525–532). Copyright (2012) American Chemical Society

Using a combination of PFG NMR and dielectric measurements, it is possible to calculate the characteristic hopping length λ_h , from diffusion coefficients and rates in the temperature range where the two techniques coincide. Based on Eq. 2.7, one can expect only a weak temperature dependence (if any) of λ_h given the universality of charge transport in ionic liquids as already discussed. The values of λ_h obtained are then used to determine diffusion coefficients from dielectric spectra of a series of ionic liquids as presented in Fig. 2.13. By that, it becomes possible to extend the range of diffusion coefficients measured by PFG NMR from about 4 to over 11 decades by employing dielectric spectroscopy. Consequently, electrical mobilities and effective number densities as well as their type of temperature dependence can be determined. The latter shows a weak Arrhenius-type dependence and is practically independent of the cation whereas the former exhibits a VFT—type behaviour and shows a pronounced dependence on the nature of the cation (especially at lower temperatures).

Central to the concept of diffusion within the linear response regime is the magnitude of the position fluctuations (also referred to as hopping lengths in the current chapter) λ of molecules in thermal equilibrium. Based on Einstein’s [4] theory, the direct link to the diffusion coefficient was established. According to Eq. 2.7, molecular size has a direct influence on λ . The molecular volume of an IL

is a measure of its size and is more physically meaningful than the radius (or diameter). Based on quantum chemical calculations, it is possible to compute the molecular volumes of ionic liquids. Table 2.3 presents the results obtained for the series of ILs investigated. These are then compared with the values of λ obtained from diffusion measurements. It is observed that λ increases with the volume of the cation (see inset of Fig. 2.13). This can be interpreted in terms of the increase in the average distance between the ions for larger cations. One can expect that larger position fluctuations are only possible if adequate space is available. It has been shown that the knowledge of volumes of ILs can be used to successfully predict their physical properties [20].

Diffusion in dilute electrolytes comprised of multiple ionic species is often described by the Nernst–Hartley approach which neglects the contributions arising from ion–ion cross-correlation effects [57]. However, a general analytical expression of the diffusion coefficient for concentrated systems incorporating the contributions from the ion–correlation is yet to be found. It is therefore instructive to investigate the deviation from the predictions of the Nernst–Hartley equation and employ it as a means of quantifying the interaction of ionic species in ionic liquids. In two-component monovalent electrolytes, the effective diffusion coefficient within this framework is given by the Nernst-Hartley diffusion coefficient, D_{NH} , expressed as [57]:

$$D_{\text{NH}} = \frac{2D_{\text{A}}D_{\text{C}}}{D_{\text{A}} + D_{\text{C}}} \quad (2.8)$$

where D_{A} and D_{C} denote the diffusion coefficients of the anion and cation, respectively. Based on Einstein–Smoluchowski relation, the effective characteristic diffusion (hopping) length, λ_{h} [in the timescale of the characteristic diffusion (charge transport) rate, ω_{c} , (described in Sect. 2.3.1)] can be defined with respect to the corresponding hopping lengths of the anions and cations given by λ_{A} and λ_{C} , respectively. If a single diffusion rate is further assumed, then the effective hopping length λ_{h} can be expressed as

$$\lambda_{\text{h}} = \sqrt{\frac{2\lambda_{\text{A}}^2\lambda_{\text{C}}^2}{\lambda_{\text{A}}^2 + \lambda_{\text{C}}^2}} \quad (2.9)$$

As experimentally established in Sect. 2.3.1 of the current chapter, the diffusion rate, ω_{c} and the structural α -relaxation rate are identical. Given that the molecules experience mean displacements comparable to their diameters [58], it is worthwhile to estimate the average hopping lengths using Eq. 2.9 and diameters of anions as well as cations obtained from quantum chemical calculations. Based on the data in Table 2.3 as well as Eq. 2.9, this consideration yields effective hopping lengths of the order of 5 Å in contrast to the typical 2–3 Å determined experimentally for the

ionic liquids investigated. This disparity is indicative of the role of the cation–anion correlation in ionic liquids. Thus, the cross-correlation terms in ionic liquids are shown to be non-negligible. An adequate theory capable of describing diffusion coefficients in highly concentrated electrolytes such as ionic liquids is yet to be obtained. The Nernst–Hartley approach overestimates the diffusion coefficients because it does not consider the interaction between the anions and cations.

2.4 Conclusions

Because of the ease with which they can be supercooled, ionic liquids offer new opportunities to investigate long-standing problems regarding the nature of dynamic glass transition as well as its impact on charge transport. Despite the significant progress achieved so far from experimental and theoretical studies, no generally accepted quantitative theory of dynamic glass transition capable of reproducing all the experimentally observed features exists to date. In this chapter, we discuss recent studies on the interplay between charge transport and glassy dynamics in ionic liquids as investigated by a combination of several experimental techniques. Using Einstein–Smoluchowski relations, we suggest a simple approach to determine diffusion coefficients in a broad range spanning more than ten orders of magnitude from dielectric spectra of ionic liquids in quantitative agreement with independent pulsed-field gradient nuclear magnetic resonance measurements. This provides a new possibility to separately determine the electrical mobility and effective number density of charge carriers from the measured dc conductivity. The origin of the remarkable universality of charge transport in different classes of glass-forming ionic liquids is also unravelled.

Acknowledgments J. S. and T. C. acknowledge the National Science Foundation for financial support through the award number DMR-1508394. The authors gratefully acknowledge financial support from the Deutsche Forschungsgemeinschaft under the DFG SPP 1191 Priority Program on Ionic Liquids.

References

1. Chauvin Y (2006) Olefin metathesis: the early days (nobel lecture). *Angew Chem Int Ed* 45:3740–3747
2. Walden P (1914) Molecular weights and electrical conductivity of several fused salts. *Acad Sci St. Petersburg* 8:405–422
3. Plechkova NV, Seddon KR (2008) Applications of ionic liquids in the chemical industry. *Chem Soc Rev* 37(1):123–150
4. Einstein A (1905) Über die von der molekularkinetischen Theorie der Wärme geforderte Bewegung von in ruhenden Flüssigkeiten suspendierten Teilchen. *Ann d Physik* 17:549–560
5. Smoluchowski M (1906) Zur kinetischen Theorie der Brownschen Molekularbewegung und der Suspensionen. *Ann d Physik* 21:755–780

6. Smoluchowski, M (1906) On the mean path of molecules of gas and its relationship to the theory of diffusion. *Bullet Intern Acad Cracovie*: 202–213
7. Maxwell JC (1866) On the viscosity or internal friction of air and other gases. *Philos Trans R Soc Lond* 156:249–268
8. Maxwell JC (1867) On the dynamical theory of gases. *Phil Trans Royal Soc London A* 157:49–88
9. Langevin P (1908) Sur la théorie du mouvement brownien. *C R Acad Sci (Paris)* 146:530–533
10. Debye P, Hueckel E (1923) Zur Theorie der Elektrolyte I. Gefrierpunktserniedrigung und verwandte Erscheinungen. *Physik. Z.* 24:185–206
11. Xu W, Angell CA (2003) Solvent-free electrolytes with aqueous solution-like conductivities. *Science* 302(5644):422–425
12. Tokuda H, Hayamizu K, Ishii K, Susan H, Watanabe M (2005) Physicochemical properties and structures of room temperature ionic liquids. 2. Variation of alkyl chain length in imidazolium cation. *J Phys Chem B* 109(13):6103–6110
13. Tokuda H, Tsuzuki S, Susan H, Hayamizu K, Watanabe M (2006) How ionic are room-temperature ionic liquids? An indicator of the physicochemical properties. *J Phys Chem B* 110(39):19593–19600
14. Tokuda H, Ishii K, Susan H, Tsuzuki S, Hayamizu K, Watanabe M (2006) Physicochemical properties and structures of room-temperature ionic liquids. 3. Variation of cationic structures. *J Phys Chem B* 110(6):2833–2839
15. Weingaertner H (2006) The static dielectric constant of ionic liquids. *Z Phys Chem* 220:1395–1405
16. Ito N, Huang W, Richert R (2006) Dynamics of a supercooled ionic liquid studied by optical and dielectric spectroscopy. *J Phys Chem B* 110(9):4371–4377
17. Rivera A, Roessler EA (2006) Evidence of secondary relaxations in the dielectric spectra of ionic liquids. *Phys Rev B* 73(21):212201–212204
18. Ito N, Richert R (2007) Solvation dynamics and electric field relaxation in an imidazolium-pf6 ionic liquid: from room temperature to the glass transition. *J Phys Chem B* 111(18):5016–5022
19. Rivera A, Brodin A, Pugachev A, Roessler EA (2007) Orientational and translational dynamics in room temperature ionic liquids. *J Chem Phys* 126(11):114503–114507
20. Slattery JM, Daguene C, Dyson PJ, Schubert TJS, Krossing I (2007) How to predict the physical properties of ionic liquids: a volume-based approach. *Angew Chem Int Ed* 46:5384–5388
21. Leys J, Wuebbenhorst M, Menon CP, Rajesh R, Thoen J, Glorieux C, Nockemann P, Thijs B, Binnemans K, Longuemart S (2008) Temperature dependence of the electrical conductivity of imidazolium ionic liquids. *J Chem Phys* 128(6):064509
22. Sangoro J, Iacob I, Serghei A, Naumov S, Galvosas P, Kaerger J, Wespe C, Bordusa F, Kremer F (2008) Charge transport and mass transport in imidazolium-based ionic liquids. *Phys Rev E* 77(5 Pt 1):051202
23. Sangoro J, Iacob I, Serghei A, Naumov S, Galvosas P, Kaerger J, Wespe C, Bordusa F, Stoppa A, Hunger J, Buchner R, Kremer F (2008) Electrical conductivity and translational diffusion in the 1-butyl-3-methylimidazolium tetrafluoroborate ionic liquid. *J Chem Phys* 128(21):214509
24. Turton DA, Hunger J, Stoppa A, Hefter G, Thoman A, Walther M, Buchner R, Wynne K (2009) Dynamics of imidazolium ionic liquids from a combined dielectric relaxation and optical kerr effect study: evidence for mesoscopic aggregation. *J Am Chem Soc* 131(31):11140–11146
25. Hunger J, Stoppa A, Schroedle S, Hefter G, Buchner R (2009) Temperature dependence of the dielectric properties and dynamics of ionic liquids. *Chem Phys Chem* 10(4):723–733
26. Sidebottom DL (2009) Colloquium: understanding ion motion in disordered solids from impedance spectroscopy scaling. *Rev Mod Phys* 81(3):999
27. Krause C, Sangoro JR, Iacob C, Kremer F (2010) Charge transport and dipolar relaxations in imidazolium-based ionic liquids. *J Phys Chem B* 114(1):382–386

28. Sangoro JR, Iacob C, Naumov S, Valiullin R, Rexhausen H, Hunger J, Buchner R, Strehmel V, Karger J, Kremer F (2011) Diffusion in ionic liquids: the interplay between molecular structure and dynamics. *Soft Matter* 7:1678–1681
29. Sangoro JR, Kremer F (2012) Charge transport and glassy dynamics in ionic liquids. *Acc Chem Res* 45(4):525–532
30. Hensel-Bielowka S, Wojnarowska Z, Dzida M, Zor ebski E, Zorebski M, Geppert-Rybczyńska M, Peppel T, Grzybowska K, Wang Y, Sokolov AP, Paluch M (2015) Heterogeneous nature of relaxation dynamics of room-temperature ionic liquids (emim)2[co(ncs)4] and (bmim)2[co(ncs)4]. *J Phys Chem C* 119(35):20363–20368
31. Paluch M, Wojnarowska Z, Goodrich P, Jacquemin J, Pionteck J, Hensel-Bielowka S (2015) Can the scaling behavior of electric conductivity be used to probe the self-organizational changes in solution with respect to the ionic liquid structure? The case of [c8mim][ntf2]. *Soft Matter* 11:6520–6526
32. Kremer F, Schoenhals A (eds) (2003) *Broadband dielectric spectroscopy*. Springer, Berlin
33. Katritzky AR, Jain R, Lomaka A, Petrukhin R, Karelson M, Visser AE, Rogers RD (2002) Correlation of the melting points of potential ionic liquids (imidazolium bromides and benzimidazolium bromides) using the codessa program. *J Chem Inf Comput Sci* 42:225–231
34. Sangoro JR, Iacob C, Serghei A, Friedrich C, Kremer F (2009) Universal scaling of charge transport in glass-forming ionic liquids. *Phys Chem Chem Phys* 11(6):913–916
35. Sangoro JP, Turky G, Abdel Rehim M, Iacob C, Naumov S, Ghoneim A, Kaerger J, Kremer F (2009) Charge transport and dipolar relaxations in hyperbranched polyamide amines. *Macromolecules* 42(5):1648–1651
36. Iacob C, Sangoro JR, Serghei A, Naumov S, Korth Y, Kaerger J, Friedrich C, Kremer F (2008) Charge transport and glassy dynamics in imidazole-based liquids. *J Chem Phys* 129(23):234511
37. Dyre JC (1988) Unified formalism for excess current noise in random-walk models. *Phys Rev B* 37(17):10143–10149
38. Boettger H, Bryksin VV (1985) *Hopping conduction in solids*. Akademie-Verlag, Berlin
39. Riande E, Díaz-Calleja R (2004) *Electrical properties of polymers*. Marcel Dekker, New York
40. Boettcher CJF, Bordewijk P (1978) *Theory of electric polarization (vol II)*. Elsevier Academic Press, Amsterdam
41. Krause C, Sangoro JR, Iacob C, Kremer F (2009, Oct) Charge transport and dipolar relaxations in imidazolium-based ionic liquids. *J Phys Chem B* 114(1):382–386. doi:10.1021/jp908519u
42. Angell CA (1985) Strong and fragile liquids. In: Ngai KL, Wright GB (eds) *Relaxations in complex systems*. U.S. GPO, Washington, DC
43. Angell CA (1995) Formation of glasses from liquids and biopolymers. *Science* 267(5206):1924–1935
44. Martínez LM, Angell CA (2001) A thermodynamic connection to the fragility of glass-forming liquids. *Nature* 410(6829):663–667
45. Dyre JC (2006) Colloquium: the glass transition and elastic models of glass-forming liquids. *Rev Mod Phys* 78(3):953
46. Roling B, Martiny C, Murugavel S (2001) Ionic conduction in glass: new information on the interrelation between the “jonscher behavior” and the “nearly constant-loss behavior” from broadband conductivity spectra. *Phys Rev Lett* 87(8):085901
47. Kubo R (1986) Brownian motion and nonequilibrium statistical mechanics. *Science* 233(4761):330–334
48. Bruce P (ed) (1995) *Chemistry of solid state materials: solid state electrochemistry*. Cambridge University Press
49. Pauling L (1960) *The nature of the chemical bond*, 3rd edn. Cornell University Press, Ithaca, New York
50. Wasserscheid P, Welton W (eds) (2002) *Ionic liquids in synthesis*. Wiley-VCH Verlag, Weinheim

51. Welton T (1999) Room-temperature ionic liquids. Solvents for synthesis and catalysis. *Chem Rev* 99(8):2071–2084
52. Stewart JJP (2009) MOPAC2009: the next generation quantum chemistry tool for property prediction. A molecular dynamics simulation software
53. Stewart JJP (2007) Optimization of parameters for semi-empirical methods V: modification of NDDO approximations and application to 70 elements. *J Mol Mod* 13:1173–1213
54. Klamt A, Schuurmann G (1993) Cosmo: a new approach to dielectric screening in solvents with explicit expressions for the screening energy and its gradient. *J Chem Soc Perkin Trans* 2:799–805
55. Bondi A (1964) van der Waals volumes and radii. *J Phys Chem* 68(3):441–451
56. Marcus Y (1997) Ion properties. Marcel Dekker, New York
57. Turq T, Barthel J, Chemla M (1992) Lecture notes in chemistry (57): transport, relaxation, and kinetic processes in electrolyte solutions. Springer, Heidelberg
58. Larini L, Ottochian A, De Michele C, Leporini D (2008) Universal scaling between structural relaxation and vibrational dynamics in glass-forming liquids and polymers. *Nat Phys* 4(1):42–45

Chapter 3

Femto- to Nanosecond Dynamics in Ionic Liquids: From Single Molecules to Collective Motions

Johannes Hunger and Richard Buchner

Abstract The dynamics of room temperature ionic liquids (RTILs) have been intensively studied within the last decades as these are of high relevance for the solvation of solutes in applications of RTILs as reaction media. Broadband dielectric spectroscopy (DS) can readily cover any dynamics ranging from seconds to femtoseconds and is thus a widely applied technique to elucidate RTIL dynamics. As DS probes all dynamics that go along with a change in the macroscopic polarization, DS is excellently suited to study such compounds, where the motions of its charged and dipolar ions inevitably modulate sample polarization. However, interactions in RTILs are not only governed by long-ranged Coulombic forces. Also hydrogen bonding, pi-pi stacking and dispersion forces contribute significantly to the local potential energy landscape, making RTIL dynamics extremely complex. To fully correlate the dynamical information from dielectric spectra to molecular dynamics, the combination of DS with other techniques exploring liquid-state dynamics is advantageous as such a combination allows unraveling the wealth of information present in dielectric spectra and provides detailed molecular level insights. In this chapter we summarize recent advances in understanding the femto- to nanosecond dynamics of RTILs, which could only be obtained using combined experimental and theoretical efforts.

J. Hunger (✉)

Department for Molecular Spectroscopy, Max Planck Institute for Polymer Research,
Ackermannweg 10, 55128 Mainz, Germany
e-mail: hunger@mpip-mainz.mpg.de

R. Buchner

Institute of Physical and Theoretical Chemistry, University of Regensburg,
Universitätsstr. 31, 93040 Regensburg, Germany
e-mail: richard.buchner@chemie.uni-regensburg.de

3.1 Introduction

After the first report on air and water stable imidazolium based room temperature ionic liquids (RTILs) in 1992 [1] and the subsequent discussion of their potential use as reaction media [2] the scientific community started to realize the enormous possibilities in using RTILs as substitutes for conventional solvents. Even after more than two decades of intensive research the performance of ionic liquids as reaction media, in particular when fast photochemical reactions are conducted therein, has remained somewhat elusive [3]. More specifically, the reaction rates for some fast—presumably diffusion controlled—photochemical reactions have been reported to proceed much faster than expected from the macroscopic properties of the RTILs, e.g. their viscosity [3]. This has been later on related to the specific structure of RTILs and it was concluded that not only the nature of the RTIL itself, but also the nature and size of the reacting molecule determine reactivity [4]. The latter fact can be understood from the peculiar structure of RTILs: despite being seemingly simply composed of only the constituting cations and anions, the amphiphilic nature of the cations (and to some extent anions) makes RTILs heterogeneous on a molecular level [3, 5–7]. This mesoscopic heterogeneity has been evidenced using both computational [8, 9] and experimental techniques [10].

The structural heterogeneities in turn provide evidence that the interaction of a cation with its immediate environment is very anisotropic: charged groups are predominantly in contact with other ionic moieties due to strong Coulombic forces [11] and hydrogen bonds [11, 12] whereas simultaneously hydrophobic domains are formed by aggregating apolar alkyl side chains, which interact mainly through weak dispersion forces. These complex intermolecular interactions result in rather complicated dynamics on a molecular level [5, 13, 14]. For many RTILs molecular motions span timescales ranging from femto- to nanoseconds at ambient temperatures. As this molecular level dynamics is intimately connected to the solvation of reactants also reactions performed in ionic liquids are affected on these timescales. Thus, RTIL dynamics critically influence their performance as solvents [15]. To understand ionic liquids as reaction media it is therefore of paramount importance to understand their molecular motions on these timescales.

Dielectric relaxation spectroscopy is excellently suited to study the molecular dynamics in ionic liquids [16–20]. This technique probes the polarization of a sample as response to an externally applied oscillating field. As RTILs consist of ions, which are generally anisotropic and thus of dipolar nature any kind of molecular motions inevitably goes along with a change in macroscopic polarization. Moreover, due to recent technological advances, dielectric spectra are readily accessible at frequencies ranging from Hertz to several tens of Terahertz. Thus, as discussed in more detail below, for RTILs at ambient conditions, the relevant time scales ranging from nanoseconds to femtoseconds can be readily accessed with this experimental technique. A—in our opinion only apparent—drawback of DS is that it probes fluctuations of the macroscopic sample polarization and thus collective dynamics, which may be dominated by cross correlations of motions. For this

reason the straight forward assignment of features appearing in the spectrum to specific motions of individual molecules or ions is often not possible. However, other techniques, like computer simulations or time-resolved ultrafast infrared spectroscopy do provide such information, whereas at the same token liquid-state dynamics is generally highly collective. Thus, by combining DS with other methods its apparent disadvantage of yielding only collective dynamics actually becomes a bonus as by such an approach the full dynamical information on ionic liquids becomes available. In this chapter, we summarize our recent efforts in combining dielectric spectroscopy with other methods to exploit the full potential of DS. We restrict this overview to neat ionic liquids at ambient temperature and pressure.

3.2 Broadband Dielectric Spectra of Ionic Liquids

Despite the unique opportunities to study the fundamental dynamics of RTILs using DS, the first studies using this technique were reported more than a decade after the advent of RTILs as a novel class of electrolytes. While these early reports initially focused on extrapolating the ‘static dielectric constants’ from frequency dependent measurements [21, 22], much progress has been made within the last decades extracting also dynamical information from broadband dielectric measurements of neat ionic liquids [18, 23–26]. In this section, we discuss the experimental approaches and the general features of the dielectric spectra of prototypical ionic liquids.

In general, dielectric spectroscopy records the total polarization, $\vec{P}(t)$, as a response of a sample to a time-dependent externally applied electric field, $\vec{E}(t)$. The response is typically presented in the frequency domain as a function of field frequency, ν . The sample polarization is typically expressed in terms of the frequency dependent complex permittivity:

$$\hat{\epsilon}(\nu) = \epsilon'(\nu) - i\epsilon''(\nu) \quad (3.1)$$

where the relative permittivity, $\epsilon'(\nu)$, represents the in-phase polarization components of the sample and the dielectric loss, $\epsilon''(\nu)$, corresponds to the energy dissipation due to the out-of-phase polarization components in the sample ($i^2 = -1$). For a sample containing a single species of uncorrelated molecular dipoles, $\epsilon'(\nu)$ exhibits a dispersion from the static value at low frequencies, ϵ , to the limiting high frequency value, ϵ_∞ . The latter subsumes polarization responses faster than dipolar reorientations, and is typically dominated by electronic polarizability or resonant contribution due to charge displacement in molecular oscillators. The dispersion in $\epsilon'(\nu)$ is accompanied by a corresponding peak in the dielectric loss, $\epsilon''(\nu)$, and for liquid samples at ambient temperature such relaxation processes associated with

molecular level motion are predominantly centered at several hundreds of MHz to a few tens of GHz.

It is important to note that for many samples in addition to dipole rotation, which dominates the response of a dipolar liquid, additionally charge translations (conductivity) and magnetic polarizations may contribute to the recorded dielectric response. All these contributions are intrinsically interconnected. While most ionic liquids ions do not have intrinsic magnetic moments and thus contributions due to magnetization can be neglected, their ionic nature implies additional polarization due to translational motions that appears in the measured dielectric spectrum. Here it is convenient to distinguish dc conductivity, κ , which is an equilibrium property *not* depending on frequency (time), from those translational components that explicitly depend on frequency (time). Thus, the experimentally accessible generalized complex permittivity, $\hat{\eta}(\nu)$ [27], can be written as

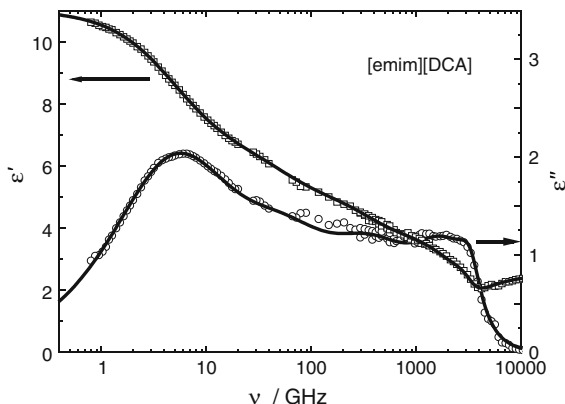
$$\hat{\eta}(\nu) = \varepsilon'(\nu) - i\varepsilon''(\nu) - i\kappa/2\pi\nu\varepsilon_0 \quad (3.2)$$

with ε_0 being the permittivity of free space, so that the thus extracted dielectric permittivity spectra, $\hat{\varepsilon}(\nu)$, contain *all* frequency dependent dynamics irrespective of their translational or rotational nature [27]. These contributions are discussed in more detail in the next section. Note that even for simple electrolyte solutions continuum theories predict coupling of ion transport and solvent reorientation leading to a decrease of both the permittivity and the conductivity from the ideal static value that would be expected in the absence of such correlations [28, 29].

As mentioned above, DS is probably the only technique enabling to study dynamics over the exceptionally broad frequency range of milli- to terahertz, i.e. timescales ranging from femtoseconds to hours. However, to cover such a wide frequency window various experimental setups have to be combined. At frequencies below a few hundred megahertz traditional parallel plate capacitance methods can be routinely used [16, 30–33]. Coaxial reflection techniques allow covering frequencies from hundreds of MHz up to several tens of GHz [20, 34, 35]. It should be noted, that virtually all coaxial reflection techniques provide only relative measurements and thus rely on accurate calibrations [34, 35]. In the gigahertz range waveguide methods are often preferable despite their limited frequency coverage [36, 37]. These methods extract the dielectric response using an incremental increase of the sample thickness in a transmission experiment and thus do not require any calibration. At frequencies ranging from a few hundred GHz to several THz, optical methods based on ultrashort laser pulses are now routinely used to extract the dielectric response from transmission or reflection experiments [35, 38, 39]. In particular for ionic liquids the observed dynamics extend beyond several THz and for accurate determination also the far-infrared range needs to be covered. This is achieved by recording far-infrared absorption spectra and using the Kramers-Kronig relation to extract dispersive components [39].

In Fig. 3.1 we show the broadband dielectric spectrum for 1-methyl-3-ethylimidazolium dicyanamide ([emim][DCA]) obtained by such combination of methods ($\nu \leq 50$ GHz: coaxial reflection, 26–89 GHz: waveguide transmission, 0.3–1.5 THz:

Fig. 3.1 Dielectric permittivity, $\epsilon'(\nu)$ (squares), and loss, $\epsilon''(\nu)$ (circles), spectra of 1-ethyl-3-methylimidazolium dicyanamide ([emim][DCA]) at 25 °C. Symbols represent experimental data, lines correspond to a fit using a dielectric relaxation model (for details see Ref. [40])



time-domain transmission and, 1–3 THz: reflection, 2–10 THz: far-IR absorption). As it is apparent from the experimental data shown in Fig. 3.1, the data obtained using these different experimental methodologies are in excellent agreement and the resulting spectra show continuous dispersion. One general, qualitative feature of the experimental spectrum is a marked dispersion in $\epsilon'(\nu)$ along with a pronounced peak in $\epsilon''(\nu)$ observed at a few gigahertz (~ 7 GHz for [emim][DCA], Fig. 3.1). This feature is typical for many different RTILs [41–43] and there is evidence that this lower frequency relaxation in imidazolium ionic liquids is dominated by the rotational relaxations of the dipolar ions [44]. At higher frequencies the dielectric loss remains rather featureless and constant until it abruptly drops at ~ 8 THz. These high frequency features have been attributed to intermolecular and intramolecular vibrations (i.e. are of translational nature) [11, 41, 44–46].

In Fig. 3.2 we show the effect of varying the nature of the different ions for a series of dicyanamide and tetrafluoroborate salts. As it is apparent from the dielectric loss spectra (Fig. 3.2b, d), the onset of the dielectric loss at ~ 8 THz is virtually unaffected upon varying the length of the alkylchain of the imidazolium cation from 1-ethyl-3methyl-imidazolium to 1-hexyl-3methyl-imidazolium. This is consistent with the view that these high-frequency contributions are dominated by intermolecular vibrations and these vibrations (i.e., the local intermolecular interaction) do not significantly depend on the alkyl side chain. As intermolecular vibrations involving interionic interactions have a large transition dipole, this observation suggests that the association of the ionic fragments of the RTILs is hardly influenced by the size of the hydrophobic molecular fragments, in line with the reported nanoscale segregation of ionic liquids [6].

On the other hand, the dominating relaxation at gigahertz frequencies is shifted to lower frequencies as the length of the alkyl chain is increasing. For tetrafluoroborate ionic liquids the maximum in the dielectric loss peak is red-shifted from ~ 5 GHz for [emim][BF₄] to ~ 800 MHz for [bmim][BF₄] to frequencies as low as ~ 200 MHz for [hmim][BF₄]. For the dicyanamide salts the loss peaks are

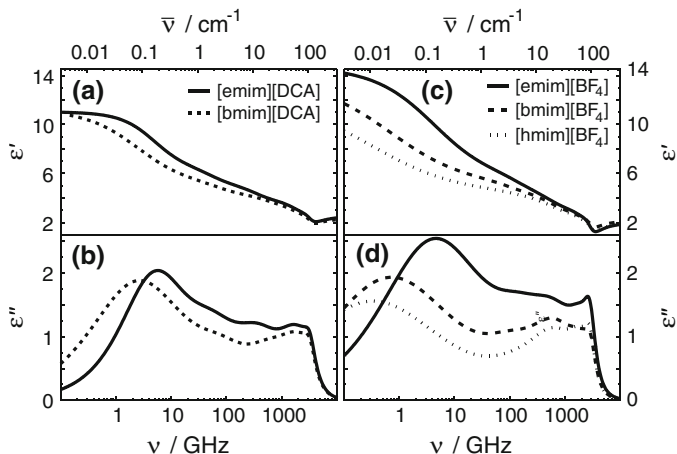


Fig. 3.2 Dielectric permittivity, $\epsilon'(\nu)$ (a), and loss, $\epsilon''(\nu)$ (b), spectra of [emim][DCA] (solid lines) and [bmim][DCA] (dashed lines) at 25 °C. In the right panels the dielectric permittivity (c) and loss (d) for a series of tetrafluoroborate ionic liquids are shown ([emim][BF₄]: solid lines; [bmim][BF₄]: dashed lines; [hmim][BF₄]: dotted lines). For visual clarity the experimental data are omitted. The experimental data are reported in Ref. [40]

centered at ~ 10 GHz for [emim][DCA] and ~ 2 GHz for [bmim][DCA]. For a given cation this relaxation is located at higher frequencies for the dicyanamide salts, compared to the tetrafluoroborates. This is consistent with the lower frequency relaxation being dominated by hydrodynamically controlled molecular level dynamics [43]. However, while such qualitative observation give indications for the molecular level nature of the observed relaxations, only the combinations with other methods provides a detailed insight into the underlying dynamics, as we will discuss in the following sections.

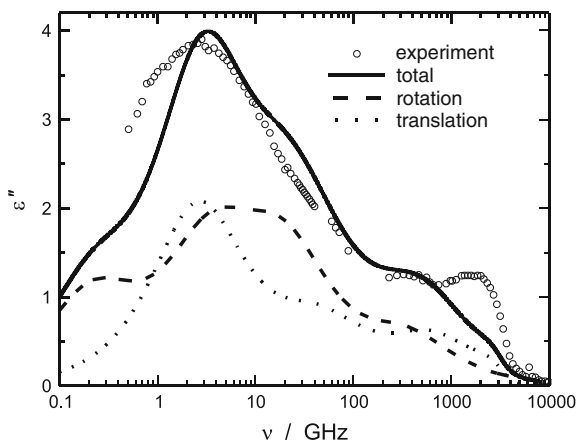
3.3 Translation or Rotation—Comparison to Computational Results

As discussed above, it is challenging to discriminate between translational or rotational contributions based on only DS. In particular the origin of the lower frequency relaxation modes observed at a few hundreds of MHz to several GHz has been controversially debated: On the one hand experimental data show that the relaxation amplitudes of this main mode is decreasing with increasing temperature [43], which is indicative of rotational relaxation of the dipolar ions [45]. Moreover, upon dilution of ionic liquids with polar solvents the relaxation amplitudes assigned to rotational modes of the ions scale with concentration, which is consistent with

their dipolar origin [27]. On the other hand, some molecular dynamics simulations have challenged this interpretation and suggest that ionic translations govern the dynamics at MHz frequencies [47]. Other computational studies predict a less pronounced contribution of ionic translations, nevertheless, translations can certainly not be neglected even in the low GHz region [44, 48, 49]. From the discussion outlined above, it is apparent that assignment of relaxation modes to molecular level motion requires methods with molecular resolution. Despite computation of dynamics in RTILs remains challenging [9, 50, 51], only such simulations can track the motion of individual atoms or molecules and thus are indispensable for understanding dielectric spectra.

In recent years, much progress has been made in simulating the dielectric response of RTILs and the computational results approach quantitative agreement with experiments [52, 53]. As seen from the comparison of the dielectric loss spectrum for 1-ethyl-3-methyl-imidazolium trifluoromethanesulfonate ([emim][triflate]) in Fig. 3.3, the experimental and simulated loss spectra broadly agree. Deconvolution of the simulated spectrum into rotational and translational components show that over the studied frequency range both types of motion contribute, with the components from rotational polarization often dominating. In this context it is interesting to note that—in contrast to earlier studies suggesting that translational and rotational contributions contribute at markedly different frequency ranges [54]—both kinds of motion overlap over essentially the entire frequency range if the polarizability is accounted for in the simulation [52]. Also the nature of the ions that form the RTIL has pronounced effects on the relative weight of translational and rotational contributions [54]. This means that the conventional analysis of dielectric spectra in terms of sums of individual relaxation modes has to be taken with a grain of salt as no clear assignment to specific molecular motions can be made. Nevertheless, some information on the dominating contribution can be made from the temperature dependence as the amplitude of rotational (dipolar) relaxations

Fig. 3.3 Dielectric loss spectrum, $\epsilon''(\nu)$, for [emim][triflate]. Green symbols show experimental data and the solid black line shows results obtained using molecular dynamics simulations. The dashed line shows the contributions of rotational motion to the simulated spectrum, the dotted line shows translational polarization components (Figure adopted from Ref. [52])



is expected to decrease with increasing temperature, whereas that of translational contributions increase [45]. Conversely, this also means that their relative weight also depends on temperature.

3.4 Local Versus Global Dielectric Response— Comparison to Solvation Response

As introduced above, segregation into hydrophobic and ionic domains on nanometer scales is a common structural motif of many RTILs [6]. Hence, the local dynamics and polarization response within these domains could potentially be very different. Solvation dynamics experiments that probe solvent reorganization around a dissolved probe molecule allow accessing such local dynamics in solution [55–57]. In these experiments sample (i.e. solvent) polarization is induced by taking advantage of the large transition dipole moments of the electronic excitation of (predominantly Coumarin-based) dyes. This allows altering the local field exerted on the solvent on ultrafast timescales and in turn probing the reaction field by measuring the time dependent Stokes shift of the probe dye.

It has been shown recently that the overall solvation response in RTILs can be reasonably well predicted by the dc conductivity of the ionic liquids [58] indicating charge translations to dominate the temporal evolution of the Stokes shift. Such correlations provide a useful estimate for the overall dynamics in RTILs but yield no details on solvation dynamics. Generally, this process is not governed by a single time constant and the experiments clearly show processes occurring on different timescales. Typically, at least two distinctively different timescales are observed in dynamics Stokes shift experiments in ionic liquids. These have been assigned to fast inertial motion of the ions and subsequent diffusive reorganization of the RTIL structure [59]. The timescales of these two contributions are in qualitative agreement with the two maxima at THz and at GHz frequencies in the dielectric loss spectra (Figs. 3.1 and 3.2).

Using continuum theories to predict solvation dynamics Maroncelli et al. recently showed that the experimental time-dependent Stokes shift, which reflects the local RTIL dynamics, is in good agreement with what would be expected from the macroscopic dynamics as measured with DS [59]. The continuum-model prediction from DS data and measured local response differed by only a factor of ~ 2 , which was assigned to fundamental differences in the experiments, rather than to intrinsic properties of the RTIL. Hence, comparison between solvation dynamics and DS experiments provides strong evidence that the local dynamics around a solute does not differ significantly from those observed on a macroscopic level probed by DS, at least on length scales that are accessible using dyes as probe molecules. Notably, even for mixtures of ionic liquids with water, where one may expect a pronounced heterogeneous molecular structure due to the amphiphilic nature of the RTIL cations, the solvation response seems to be reasonably well

predicted from the macroscopic dielectric function [60]. The same is true for mixtures with less polar solvents, like acetonitrile [61], though some deviations have been observed at very low RTIL concentrations. Altogether, the comparison of DS experiments to solvation dynamics using dipolar probe molecules do not provide evidence for the RTIL solvation response to depend substantially on the length scale.

3.5 Balanced Sensitivities—Comparison to Optical Kerr Effect Spectroscopy

To better resolve the broadly overlapping modes observed in the dielectric spectra, their comparison to spectra from optical heterodyne-detected Raman-induced Kerr effect spectroscopy (OKE) offers a valuable tool. While DS is sensitive to dynamics that go along with the macroscopic polarization of the sample, OKE monitors molecular motions that affect anisotropic components in the polarizability tensor. OKE is routinely applied to measure the vibrational response at THz frequencies and several groups have studied these for RTILs, see, e.g. [13, 62–71] but also times as long as nanoseconds can be accessed [26, 41, 72, 73].

In principle, OKE and DS monitor similar dynamics with, however, different sensitivities [74, 75]. In the particular case of diffusive rotational motions, the experimental symmetry results in 3 times faster dynamics in OKE experiments compared to DS [39, 76]. This makes the combination of DS and OKE a very powerful combination [26, 41, 72, 73, 77] as it provides information on whether observed rotational dynamics are of diffusive nature or, e.g. proceeds through large-angle jumps. Also, it may bring contributions to RTIL dynamics forward, which would have remained hidden when using only a single spectroscopic method. Besides yielding a much more robust description of the high frequency part of ionic liquids (e.g. the THz range in Fig. 3.2), combination of DS and OKE allowed in identifying a particular low frequency mode in imidazolium-based ionic liquids [41]. From the comparison of both spectra, it became apparent that this low frequency relaxation contributes to both spectra. This sub- α mode is centered at lower frequencies than the dominant main relaxation in imidazolium ILs and has large amplitudes in the OKE spectra, while it only weakly contributes to the DS spectra. This implies that the underlying molecular level dynamics, occurring on a timescale of a few hundred picoseconds, go along with a large change in the polarizability tensor, while the macroscopic dipole moment is only little affected. Based on this fact the sub- α mode has been related to a relaxation in large scale clusters, which may be understood from the nanoscale formation of aggregates: A symmetric “breathing” motion within ionic aggregates would be consistent with the observed intensities [41]. Recent molecular dynamics simulations indicate a similar interionic polarization mechanism, with the correlated motions of the cations in the field of the counterion cage being the dominant contribution [52].

A particular example that demonstrates the strength of combining Kerr effect spectroscopy with dielectric spectroscopy is the investigation of nitrate containing ionic liquids, with ethylammonium nitrate being the presumably most prominent RTIL [78]. The centro-symmetry of the nitrate anion and the resulting absence of a permanent electrical dipole moment makes the rotational motion of the nitrate anion to be absent in the dielectric spectra. In turn, the planar geometry together with its π electrons make the polarizability of the nitrate anion very anisotropic, which results in large amplitudes in the OKE spectra. Conversely, the prolate ellipsoidal structure of the ethylammonium ion, with the charge localized at the ammonium group results in a large electrical dipole moment when taking the center of the ellipsoid as center of rotation. At the same time its polarizability anisotropy is small [43, 72, 73]. Thus, for uncorrelated rotational diffusion of the ethylammonium cations large amplitude modes due to cation rotation are expected in the dielectric spectra. Thus, OKE and DS are complementary in sensing the rotation of anions and cations. As seen from the OKE spectra and the dielectric loss spectra in Fig. 3.4, the main relaxation mode in both spectra is centered at ~ 2 GHz, indicating that the modes associated with the cation and the anion relaxations are observed on similar timescales [73]. Note that for diffusive rotation of the identical individual ions the peak frequencies in both experiments would be expected to differ by a factor of 3 [41]. The similarity of both relaxation times together with the observation that both the OKE and the DS relaxation time are decoupled from viscosity shows that the molecular level motion of the ions in ethylammonium nitrate cannot be explained by hydrodynamically controlled motion of individual ions [72, 73]. It rather evidences that the strong intermolecular interaction between the ions—being it Coulombic, hydrogen bonds

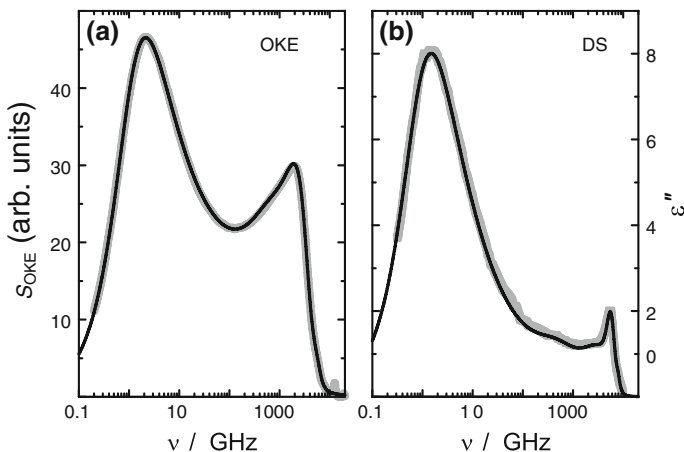


Fig. 3.4 Optical Kerr effect spectrum, S_{OKE} , **a** and dielectric loss spectrum, $\varepsilon''(\nu)$, **b** for ethylammonium nitrate at 25 °C. Grey lines are (interpolated for DS) experimental data, lines show fits using a relaxation model. The main relaxation at low frequencies was assigned to the cooperative relaxation of the anions and cations in the OKE and DS spectra, respectively (for details see Ref. [72], from where the figure has been adopted from)

or dispersion forces—result in highly concerted dynamics with the observed loss peaks resulting from collective structural relaxation of the RTIL. Hence, in addition to the coupling between translational and rotational motions as discussed in Sect. 3.3, also the motions of cations and anions are evidently correlated.

3.6 Adding Molecular Specificity—Comparison to Ultrafast Infrared Spectroscopy

As detailed above, the combination of OKE with DS allows probing different sub-ensembles of the complex three-dimensional structure of RTILs. However, both techniques probe collective dynamics. It is thus challenging to unambiguously relate the observed relaxations to the dynamics of single molecules. Time and polarization-resolved femtosecond infrared spectroscopy (fs-IR) in turn can access single-molecule rotational dynamics with molecular specificity through an appropriate infrared-active vibrational transition [79–84]. This is achieved via excitation of a molecular vibration using an intense femtosecond infrared laser pulse and subsequent monitoring of the temporal evolution of the excitation via the transient infrared absorption changes measured with delayed probe laser pulses. Due to the polarized nature of the infrared excitation pulse, the excitation is anisotropic and the anisotropy can be measured by rotating the polarization of the infrared probe pulse. The thus determined time-dependent anisotropy parameter is a measure of the orientational memory of the sample on the initial excitation polarization. The anisotropy decay corresponds in principle to a second order molecular rotational correlation function provided the measured transient signal originates from the vibrationally excited state. In reality, finite vibrational lifetimes of the studied vibrations lead to a dissipation of the absorbed energy, which will eventually assume thermal distribution, i.e. the sample is heated. This effect very often limits the accessible time window to probe rotational dynamics to ~ 10 times the vibrational lifetime of the excited state. Hence, the first fs-IR experiments have focused on studying small (mobile) molecules in RTILs, e.g. water [85–87].

It is however also possible to study the dynamics of neat RTILs. In the particular case of ethylammonium nitrate the transient signals remained anisotropic over an exceptionally long time (~ 500 times the vibrational lifetime) [88], when studying the dynamics of the cation's ammonium group. This long-lived orientational memory can be rationalized by the fact that thermal transport in ethylammonium nitrate is very slow. Thus, the excess energy, even though having nearly equilibrium distribution, is dissipated very locally and thus any transient modulation due to thermal heating predominantly affects the initially excited oscillator. Hence, the orientational memory persists on timescales that are much longer than the timescale where the vibrationally excited state contributes to the signal. Thus, long-time dynamics—relevant to the rather slow motion of the ionic liquids ions—can be readily studied, providing detailed insight into the single molecule motion of the ions.

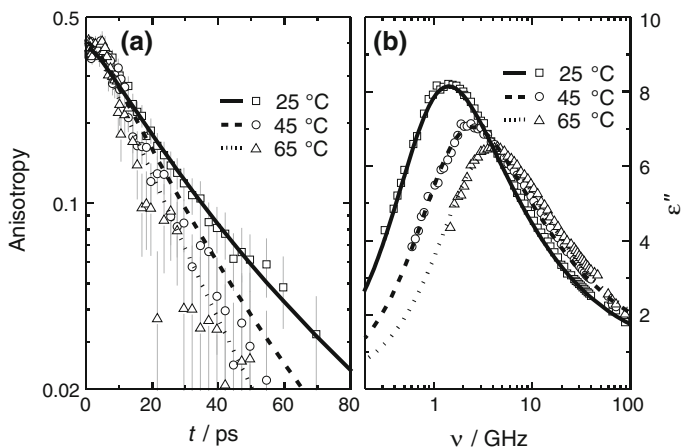


Fig. 3.5 **a** Decay of the excitation anisotropy after excitation of the N-D stretching vibration in isotopically labelled ethylammonium nitrate ($[\text{C}_2\text{H}_5\text{NH}_{2.94}\text{D}_{0.06}][\text{NO}_3]$) at temperatures ranging from 25 to 65 °C. Due to the short vibrational lifetime the decay of the anisotropy contains contributions due to rotation of the $[\text{C}_2\text{H}_5\text{NH}_2\text{D}]^+$ cations and thermal diffusion of the excess energy from initially excited to non-excited cations. The *lines* show fits using a model that takes both decay mechanisms into account (for details see Ref. [88]). **b** Dielectric loss spectrum of ethylammonium nitrate at temperatures ranging from 25 to 65 °C. The main dielectric loss peak originates from the structural relaxation of the three-dimensional structure of the ionic liquid (for details see Ref. [88])

In Fig. 3.5a, we show the measured anisotropy decays using the N-D stretching vibration as a local probe for the cation dynamics. As seen from Fig. 3.5a, the measured excitation anisotropy for diluted $[\text{C}_2\text{H}_5\text{NH}_2\text{D}]^+$ cations decays on a ~ 20 ps timescale for ethylammonium nitrate at 25 °C (average isotopic composition $[\text{C}_2\text{H}_5\text{NH}_{2.94}\text{D}_{0.06}][\text{NO}_3]$). With increasing temperature these decays are sped up, indicative of accelerated molecular dynamics. As apparent from the considerations above, the measured anisotropies are however largely determined by local heating of the initially excited oscillators, and thus thermal diffusion from locally heated cations to the bath (that contains randomly oriented cations) is an important decay mechanism for the excitation anisotropy. In order to reliably extract rotation times, it is important to study different isotopic concentrations. This allows extrapolating the decay of the anisotropy to infinitely diluted $[\text{C}_2\text{H}_5\text{NH}_2\text{D}]^+$ cations, where thermal diffusion does not contribute. Using such an extrapolation, we obtained a single-molecule rotation time for the ethylammonium cation of ~ 80 ps for ethylammonium nitrate at 25 °C, which is reduced to ~ 30 ps at 65 °C. The peak maximum of the dielectric loss spectrum (Fig. 3.5b) on the other hand corresponds to dielectric relaxation times ranging from ~ 110 ps at 25 °C to ~ 40 ps at 65 °C. Keeping in mind that both experiments probe different correlation times (first order collective rotational correlation time of DS versus second order single molecule rotation time for fs-IR) this broad agreement provides evidence for both

experiments measuring the same molecular level dynamics. This is supported by the observation that the thermal activation energies of the dielectric relaxation time and the fs-IR rotation time are the same within the experimental error [88]. Hence, comparison between fs-IR and DS confirms that the main dielectric relaxation peak for ethylammonium nitrate is dominated by the rotational relaxation of the ethylammonium cations, which one may have intuitively concluded from the symmetry and thus resulting dipole moments of the cation and the absence of a permanent dipole moment of the nitrate anion (see previous section).

Quantitative comparison of the dielectric relaxation time and the fs-IR rotation time further showed that both time constants differ by a factor of ~ 1.4 , which, as already mentioned in the previous section, is indicative of non-diffusive dynamics in ethylammonium nitrate. Taking into account that the cation and the anion in ethylammonium nitrate are strong hydrogen-bond donors and acceptors, respectively, the difference between the time constants measured in both experiments, can be rationalized by the high directionality of the interionic interaction and thus resulting jump-like reorientation dynamics [88].

It is interesting to note that the local heating induced by vibrational excitation and subsequent relaxation results not only in very local energy dissipation but the 'heating' ionic liquid also occurs on a (sub-) picosecond timescale, which is much faster than the intrinsic structural relaxation of the ionic liquids. Hence, the fast temperature rise induces structural relaxation, which leads to an (on average) increase of inter molecular distances. This structural relaxation, which typically occurs on a timescale of ~ 10 ps for alkylammonium ionic liquids at ambient conditions can be specifically probed for the ionic molecular fragments (N-H of N-D stretching vibrations) and the hydrophobic molecular fragments (C-H stretching vibration) [89]. These thermal equilibration dynamics have been found to be ca. twofold faster for the C-H groups compared to the N-H (or N-D) groups. This observation provides evidence that the nanoscale heterogeneities in RTILs also result in heterogeneous dynamics within the hydrophobic and ionic domains [89]. More importantly, it also shows that not only the strong intermolecular interactions in ionic liquids lead to highly collective molecular level motion, but also dynamics of an individual ion are determined by a highly anisotropic distribution of ions in the immediate vicinity, which leads to a remarkably inhomogeneous potential landscape experienced by the ions.

3.7 Conclusions

In summary, DS in combination with other experiments has provided unprecedented insight into the molecular dynamics of ionic liquids and has advanced our understanding on how RTILs solvate reactants. The picture that emerged within the

last decade shows that RTILs can stabilize reacting solutes at both very short (femtosecond) timescales while full equilibration typically exceeds several tens to hundreds of picoseconds at ambient conditions: While translations on short length scales are fast, full relaxation of the three-dimensional structure of ionic liquids involve motions that take much longer. Combination of DS with both polarization resolved femtosecond infrared spectroscopy and molecular dynamics simulations provide evidence for molecular rotation making up a significant portion of these slower dynamics.

These extremely wide spread of timescales for the molecular motion in RTILs is a result of the wealth of specific intermolecular interactions, which make molecular motion highly collective. Combining DS with OKE spectroscopy and computational techniques shows that all conceivable molecular motions are not independent of each other: ion rotation is correlated with ion translation and an ion cannot translate or rotate without a concerted motion of the corresponding counterion. Such long-range interactions likely result in the correlation of the pico- to nanosecond dynamics in RTIL to macroscopic transport properties (e.g., viscosity), despite measured dynamics are inconsistent with a truly diffusive nature. This is even true for ionic liquids consisting of small ions—like ethylammonium nitrate—where one may expect from the small size of the hydrophobic fragments that the nanoscale segregation in ionic liquids is of minor importance.

Nevertheless, even for the weakly amphiphilic ethylammonium cation, femtosecond infrared experiments show that dynamics within the hydrophobic molecular fragments are substantially faster than in the ionic molecular fragments. Thus, dynamics are heterogeneous on short length scales (a few Ångströms). In turn, the solvation response as interrogated using dye molecules suggests that these dynamical heterogeneities are smeared out on the (few nanometers) length scales probed by these dyes.

Albeit most of discussed features of RTIL dynamics are common to many ionic liquids studied to date, the exact details of these dynamics are highly specific to the specific identity of the anion and the cation. Based on the current understanding it is though not yet possible to predict the dynamical properties of novel ionic liquids or of ionic liquid mixtures (being it a mixture with a RTIL or with a dipolar component). As the latter mixtures are highly relevant to technological applications using RTILs as solvents, both more experimental and computational efforts are required to achieve such knowledge.

Acknowledgments We are indebted to all our academic collaborations, whose names occur frequently in the list of references below. Without their contribution not a single combined study, as summarized in this chapter, would have been possible. We are also grateful to all co-workers, students and colleagues whose enthusiasm and permanent availability for discussion was crucial for the work presented herein. We also thank the Deutsche Forschungsgemeinschaft for funding within the priority program SPP 1191.

References

1. Wilkes JS, Zaworotko MJ (1992) Air and water stable 1-ethyl-3-methylimidazolium based ionic liquids. *J Chem Soc Chem Commun* 965–967. doi:[10.1039/c39920000965](https://doi.org/10.1039/c39920000965)
2. Freemantle M (1998) Designer solvents. *Chem Eng News* 76:32–37. doi:[10.1021/cen-v076n013.p032](https://doi.org/10.1021/cen-v076n013.p032)
3. Castner EW, Margulis CJ, Maroncelli M, Wishart JF (2011) Ionic liquids: structure and photochemical reactions. *Annu Rev Phys Chem* 62:85–105. doi:[10.1146/annurev-physchem-032210-103421](https://doi.org/10.1146/annurev-physchem-032210-103421)
4. Araque JC, Hettige JJ, Margulis CJ (2015) Modern room temperature ionic liquids, a simple guide to understanding their structure and how it may relate to dynamics. *J Phys Chem B* 119:12727–12740. doi:[10.1021/acs.jpcc.5b05506](https://doi.org/10.1021/acs.jpcc.5b05506)
5. Weingärtner H (2008) Understanding ionic liquids at the molecular level: facts, problems, and controversies. *Angew Chem Int Ed Engl* 47:654–670. doi:[10.1002/anie.200604951](https://doi.org/10.1002/anie.200604951)
6. Hayes R, Warr GG, Atkin R (2015) Structure and nanostructure in ionic liquids. *Chem Rev* 115:6357–6426. doi:[10.1021/cr500411q](https://doi.org/10.1021/cr500411q)
7. Greaves TL, Drummond CJ (2013) Solvent nanostructure, the solvophobic effect and amphiphile self-assembly in ionic liquids. *Chem Soc Rev* 42:1096–1120. doi:[10.1039/C2CS35339C](https://doi.org/10.1039/C2CS35339C)
8. Maginn EJ (2009) Molecular simulation of ionic liquids: current status and future opportunities. *J Phys Condens Matter* 21:373101. doi:[10.1088/0953-8984/21/37/373101](https://doi.org/10.1088/0953-8984/21/37/373101)
9. Dommert F, Wendler K, Berger R et al (2012) Force fields for studying the structure and dynamics of ionic liquids: a critical review of recent developments. *ChemPhysChem* 13:1625–1637. doi:[10.1002/cphc.201100997](https://doi.org/10.1002/cphc.201100997)
10. Russina O, Triolo A, Gontrani L, Caminiti R (2012) Mesoscopic structural heterogeneities in room-temperature ionic liquids. *J Phys Chem Lett* 3:27–33. doi:[10.1021/jz201349z](https://doi.org/10.1021/jz201349z)
11. Fumino K, Reimann S, Ludwig R (2014) Probing molecular interaction in ionic liquids by low frequency spectroscopy: Coulomb energy, hydrogen bonding and dispersion forces. *Phys Chem Chem Phys* 16:21903–21929. doi:[10.1039/C4CP01476F](https://doi.org/10.1039/C4CP01476F)
12. Hunt PA, Ashworth CR, Matthews RP (2015) Hydrogen bonding in ionic liquids. *Chem Soc Rev* 44:1257–1288. doi:[10.1039/C4CS00278D](https://doi.org/10.1039/C4CS00278D)
13. Castner EW, Wishart JF, Shirota H (2007) Intermolecular dynamics, interactions, and solvation in ionic liquids. *Acc Chem Res* 40:1217–1227. doi:[10.1021/ar700169g](https://doi.org/10.1021/ar700169g)
14. Tsuzuki S (2012) Factors controlling the diffusion of ions in ionic liquids. *ChemPhysChem* 13:1664–1670. doi:[10.1002/cphc.201100870](https://doi.org/10.1002/cphc.201100870)
15. Marcus RA (1993) Electron transfer reactions in chemistry. Theory and experiment. *Rev Mod Phys* 65:599–610. doi:[10.1103/RevModPhys.65.599](https://doi.org/10.1103/RevModPhys.65.599)
16. Kremer F, Schönhal A (2003) *Broadband dielectric spectroscopy*. Springer, Berlin
17. Kaatze U (2013) Measuring the dielectric properties of materials. Ninety-year development from low-frequency techniques to broadband spectroscopy and high-frequency imaging. *Meas Sci Technol* 24:12005. doi:[10.1088/0957-0233/24/1/012005](https://doi.org/10.1088/0957-0233/24/1/012005)
18. Weingärtner H (2014) Dielectric properties of ionic liquids: achievements so far and challenges remaining. In: *Ionic liquids further UnCOILed*. Wiley, Hoboken, NJ, USA, pp 235–258
19. Buchner R, Hefter G (2009) Interactions and dynamics in electrolyte solutions by dielectric spectroscopy. *Phys Chem Chem Phys* 11:8984–8999. doi:[10.1039/b906555p](https://doi.org/10.1039/b906555p)
20. Gregory AP, Clarke RN (2006) A review of RF and microwave techniques for dielectric measurements on polar liquids. *IEEE Trans Dielectr Electr Insul* 13:727–743. doi:[10.1109/TDEI.2006.1667730](https://doi.org/10.1109/TDEI.2006.1667730)
21. Wakai C, Oleinikova A, Ott M, Weingärtner H (2005) How polar are ionic liquids? Determination of the static dielectric constant of an imidazolium-based ionic liquid by microwave dielectric spectroscopy. *J Phys Chem B* 109:17028–17030. doi:[10.1021/jp053946+](https://doi.org/10.1021/jp053946+)

22. Weingärtner H (2006) The static dielectric constant of ionic liquids. *Zeitschrift für Phys Chemie* 220:1395–1405. doi:[10.1524/zpch.2006.220.10.1395](https://doi.org/10.1524/zpch.2006.220.10.1395)
23. Sangoro JR, Kremer F (2012) Charge transport and glassy dynamics in ionic liquids. *Acc Chem Res* 45:525–532. doi:[10.1021/ar2001809](https://doi.org/10.1021/ar2001809)
24. Hensel-Bielowka S, Wojnarowska Z, Dzida M et al (2015) Heterogeneous nature of relaxation dynamics of room-temperature ionic liquids (EMIm)₂ [Co(NCS)₄] and (BMIm)₂[Co(NCS)₄]. *J Phys Chem C* 119:20363–20368. doi:[10.1021/acs.jpcc.5b07123](https://doi.org/10.1021/acs.jpcc.5b07123)
25. Sippel P, Lunkenheimer P, Krohns S et al (2015) Importance of liquid fragility for energy applications of ionic liquids. *Sci Rep* 5:13922. doi:[10.1038/srep13922](https://doi.org/10.1038/srep13922)
26. Sonnleitner T, Turton DA, Waselikowski S et al (2014) Dynamics of RTILs: A comparative dielectric and OKE study. *J Mol Liq* 192:19–25. doi:[10.1016/j.molliq.2013.09.019](https://doi.org/10.1016/j.molliq.2013.09.019)
27. Hunger J, Stoppa A, Buchner R, Hefter G (2008) From ionic liquid to electrolyte solution: dynamics of 1-N-butyl-3-N-methylimidazolium tetrafluoroborate/dichloromethane mixtures. *J Phys Chem B* 112:12913–12919. doi:[10.1021/jp8045627](https://doi.org/10.1021/jp8045627)
28. Hubbard JB, Onsager L, van Beek WM, Mandel M (1977) Kinetic polarization deficiency in electrolyte solutions. *Proc Natl Acad Sci USA* 74:401–404. doi:[10.1073/pnas.74.2.401](https://doi.org/10.1073/pnas.74.2.401)
29. Ottosson N, Hunger J, Bakker HJ (2014) Effect of cations on the hydrated proton. *J Am Chem Soc* 136:12808–12811. doi:[10.1021/ja503635j](https://doi.org/10.1021/ja503635j)
30. Sangoro J, Jacob C, Sergei A et al (2008) Electrical conductivity and translational diffusion in the 1-butyl-3-methylimidazolium tetrafluoroborate ionic liquid. *J Chem Phys* 128:214509. doi:[10.1063/1.2921796](https://doi.org/10.1063/1.2921796)
31. Zech O, Hunger J, Sangoro JR et al (2010) Correlation between polarity parameters and dielectric properties of [Na][TOTO]—a sodium ionic liquid. *Phys Chem Chem Phys* 12:14341–14350. doi:[10.1039/c0cp00840k](https://doi.org/10.1039/c0cp00840k)
32. Krause C, Sangoro JR, Jacob C, Kremer F (2010) Charge transport and dipolar relaxations in imidazolium-based ionic liquids. *J Phys Chem B* 114:382–386. doi:[10.1021/jp908519u](https://doi.org/10.1021/jp908519u)
33. Sangoro JR, Jacob C, Naumov S et al (2011) Diffusion in ionic liquids: the interplay between molecular structure and dynamics. *Soft Matter* 7:1678–1681. doi:[10.1039/c0sm01404d](https://doi.org/10.1039/c0sm01404d)
34. Buchner R, Hefter GT, May PM (1999) Dielectric relaxation of aqueous NaCl solutions. *J Phys Chem A* 103:1–9. doi:[10.1021/jp982977k](https://doi.org/10.1021/jp982977k)
35. Ensing W, Hunger J, Ottosson N, Bakker HJ (2013) On the orientational mobility of water molecules in proton and sodium terminated nafion membranes. *J Phys Chem C* 117:12930–12935. doi:[10.1021/jp312623p](https://doi.org/10.1021/jp312623p)
36. Hunger J, Cerjak I, Schoenmaker H et al (2011) Precision waveguide system for measurement of complex permittivity of liquids at frequencies from 60 to 90 GHz. *Rev Sci Instrum* 82:104703
37. Barthel J, Buchner R, Eberspächer P-N et al (1998) Dielectric relaxation spectroscopy of electrolyte solutions. Recent developments and prospects. *J Mol Liq* 78:83–109. doi:[10.1016/S0167-7322\(98\)00085-3](https://doi.org/10.1016/S0167-7322(98)00085-3)
38. Ulbricht R, Hendry E, Shan J et al (2011) Carrier dynamics in semiconductors studied with time-resolved terahertz spectroscopy. *Rev Mod Phys* 83:543–586. doi:[10.1103/RevModPhys.83.543](https://doi.org/10.1103/RevModPhys.83.543)
39. Hunger J, Stoppa A, Thoman A et al (2009) Broadband dielectric response of dichloromethane. *Chem Phys Lett* 471:85–91. doi:[10.1016/j.cplett.2009.02.024](https://doi.org/10.1016/j.cplett.2009.02.024)
40. Hunger J (2009) Effects of polar compounds on the dynamics and dielectric properties of room-temperature ionic liquids. Ph.D. Thesis, University of Regensburg
41. Turton DA, Hunger J, Stoppa A et al (2009) Dynamics of imidazolium ionic liquids from a combined dielectric relaxation and optical Kerr effect study: evidence for mesoscopic aggregation. *J Am Chem Soc* 131:11140–11146. doi:[10.1021/ja903315v](https://doi.org/10.1021/ja903315v)
42. Stoppa A, Hunger J, Buchner R et al (2008) Interactions and dynamics in ionic liquids. *J Phys Chem B* 112:4854–4858. doi:[10.1021/jp800852z](https://doi.org/10.1021/jp800852z)
43. Hunger J, Stoppa A, Schrödle S et al (2009) Temperature dependence of the dielectric properties and dynamics of ionic liquids. *ChemPhysChem* 10:723–733. doi:[10.1002/cphc.200800483](https://doi.org/10.1002/cphc.200800483)

44. Schröder C, Steinhauser O (2009) On the dielectric conductivity of molecular ionic liquids. *J Chem Phys* 131:114504. doi:[10.1063/1.3220069](https://doi.org/10.1063/1.3220069)
45. Shim Y, Kim HJ (2013) Dielectric relaxation and solvation dynamics in a room-temperature ionic liquid: temperature dependence. *J Phys Chem B* 117:11743–11752. doi:[10.1021/jp406353j](https://doi.org/10.1021/jp406353j)
46. Fumino K, Wulf A, Ludwig R (2008) The cation-anion interaction in ionic liquids probed by far-infrared spectroscopy. *Angew Chem Int Ed Engl* 47:3830–3834. doi:[10.1002/anie.200705736](https://doi.org/10.1002/anie.200705736)
47. Yamaguchi T, Koda S (2010) Mode-coupling theoretical analysis of transport and relaxation properties of liquid dimethylimidazolium chloride. *J Chem Phys* 132:114502. doi:[10.1063/1.3354117](https://doi.org/10.1063/1.3354117)
48. Schröder C, Wakai C, Weingärtner H et al (2007) Collective rotational dynamics in ionic liquids: a computational and experimental study of 1-butyl-3-methyl-imidazolium tetrafluoroborate. *J Chem Phys* 126:084511. doi:[10.1063/1.2464057](https://doi.org/10.1063/1.2464057)
49. Schröder C, Rudas T, Steinhauser O (2006) Simulation studies of ionic liquids: orientational correlations and static dielectric properties. *J Chem Phys* 125:244506. doi:[10.1063/1.2404674](https://doi.org/10.1063/1.2404674)
50. Kirchner B (2010) Ionic liquids from theoretical investigations. *Top Curr Chem* 290:213–262. doi:[10.1007/128_2008_36](https://doi.org/10.1007/128_2008_36)
51. Gabl S, Schröder C, Steinhauser O (2012) Computational studies of ionic liquids: size does matter and time too. *J Chem Phys* 137:094501. doi:[10.1063/1.4748352](https://doi.org/10.1063/1.4748352)
52. Schröder C, Sonnleitner T, Buchner R, Steinhauser O (2011) The influence of polarizability on the dielectric spectrum of the ionic liquid 1-ethyl-3-methylimidazolium triflate. *Phys Chem Chem Phys* 13:12240–12248. doi:[10.1039/c1cp20559e](https://doi.org/10.1039/c1cp20559e)
53. Schröder C, Steinhauser O (2010) Computational dielectric spectroscopy of charged, dipolar systems. In: *Computational spectroscopy*. Wiley-VCH Verlag GmbH & Co. KGaA, Weinheim, Germany, pp 279–321. doi:[10.1002/9783527633272.ch10](https://doi.org/10.1002/9783527633272.ch10)
54. Schröder C, Haberler M, Steinhauser O (2008) On the computation and contribution of conductivity in molecular ionic liquids. *J Chem Phys* 128:134501. doi:[10.1063/1.2868752](https://doi.org/10.1063/1.2868752)
55. Horng ML, Gardecki JA, Papazyan A, Maroncelli M (1995) Subpicosecond measurements of polar solvation dynamics: coumarin 153 revisited. *J Phys Chem* 99:17311–17337. doi:[10.1021/j100048a004](https://doi.org/10.1021/j100048a004)
56. Bagchi B (1989) Dynamics of solvation and charge transfer reactions in dipolar liquids. *Annu Rev Phys Chem* 40:115–141. doi:[10.1146/annurev.pc.40.100189.000555](https://doi.org/10.1146/annurev.pc.40.100189.000555)
57. Samanta A (2010) Solvation dynamics in ionic liquids: what we have learned from the dynamic fluorescence Stokes shift studies. *J Phys Chem Lett* 1:1557–1562. doi:[10.1021/jz100273b](https://doi.org/10.1021/jz100273b)
58. Zhang X-X, Liang M, Ernsting NP, Maroncelli M (2013) Conductivity and solvation dynamics in ionic liquids. *J Phys Chem Lett* 4:1205–1210. doi:[10.1021/jz400359r](https://doi.org/10.1021/jz400359r)
59. Zhang X-X, Liang M, Ernsting NP, Maroncelli M (2013) Complete solvation response of coumarin 153 in ionic liquids. *J Phys Chem B* 117:4291–4304. doi:[10.1021/jp305430a](https://doi.org/10.1021/jp305430a)
60. Zhang X, Liang M, Hunger J et al (2013) Dielectric relaxation and solvation dynamics in a prototypical ionic liquid + dipolar protic liquid mixture: 1-butyl-3-methylimidazolium tetrafluoroborate + water. *J Phys Chem B* 117:15356–15368. doi:[10.1021/jp4043528](https://doi.org/10.1021/jp4043528)
61. Lohse PW, Bartels N, Stoppa A et al (2012) Dielectric relaxation and ultrafast transient absorption spectroscopy of $[\text{C}_6\text{mim}]^+[\text{TF}_2\text{N}]^-/\text{acetonitrile}$ mixtures. *Phys Chem Chem Phys* 14:3596–3603. doi:[10.1039/c2cp23704k](https://doi.org/10.1039/c2cp23704k)
62. Fayer MD (2014) Dynamics and structure of room temperature ionic liquids. *Chem Phys Lett* 616–617:259–274. doi:[10.1016/j.cplett.2014.09.062](https://doi.org/10.1016/j.cplett.2014.09.062)
63. Li J, Wang I, Fruchey K, Fayer MD (2006) Dynamics in supercooled ionic organic liquids and mode coupling theory analysis. *J Phys Chem A* 110:10384–10391. doi:[10.1021/jp0637476](https://doi.org/10.1021/jp0637476)
64. Hunt NT, Jaye AA, Meech SR (2007) Ultrafast dynamics in complex fluids observed through the ultrafast optically-heterodyne-detected optical-Kerr-effect (OHD-OKE). *Phys Chem Chem Phys* 9:2167–2180. doi:[10.1039/b616078f](https://doi.org/10.1039/b616078f)

65. Giraud G, Gordon CM, Dunkin IR, Wynne K (2003) The effects of anion and cation substitution on the ultrafast solvent dynamics of ionic liquids: A time-resolved optical Kerr-effect spectroscopic study. *J Chem Phys* 119:464–477. doi:[10.1063/1.1578056](https://doi.org/10.1063/1.1578056)
66. Xiao D, Hines LG, Li S et al (2009) Effect of cation symmetry and alkyl chain length on the structure and intermolecular dynamics of 1,3-dialkylimidazolium bis(trifluoromethanesulfonyl)amide ionic liquids. *J Phys Chem B* 113:6426–6433. doi:[10.1021/jp8102595](https://doi.org/10.1021/jp8102595)
67. Xue L, Tamas G, Gurung E, Quitevis EL (2014) Probing the interplay between electrostatic and dispersion interactions in the solvation of nonpolar nonaromatic solute molecules in ionic liquids: An OKE spectroscopic study of CS₂/[C_nC₁im][NTf₂] mixtures (n = 1 – 4). *J Chem Phys* 140:164512. doi:[10.1063/1.4872038](https://doi.org/10.1063/1.4872038)
68. Xiao D, Hines LG, Holtz MW et al (2010) Effect of cation symmetry on the low-frequency spectra of imidazolium ionic liquids: OKE and Raman spectroscopic measurements and DFT calculations. *Chem Phys Lett* 497:37–42. doi:[10.1016/j.cplett.2010.07.085](https://doi.org/10.1016/j.cplett.2010.07.085)
69. Shirota H (2012) Comparison of low-frequency spectra between aromatic and nonaromatic cation based ionic liquids using femtosecond raman-induced Kerr effect spectroscopy. *ChemPhysChem* 13:1638–1648. doi:[10.1002/cphc.201100731](https://doi.org/10.1002/cphc.201100731)
70. Ishida T, Shirota H (2013) Dicationic versus monocationic ionic liquids: distinctive ionic dynamics and dynamical heterogeneity. *J Phys Chem B* 117:1136–1150. doi:[10.1021/jp3110425](https://doi.org/10.1021/jp3110425)
71. Shirota H, Kakinuma S (2015) Temperature dependence of low-frequency spectra in molten bis(trifluoromethylsulfonyl)amide salts of imidazolium cations studied by femtosecond raman-induced Kerr effect spectroscopy. *J Phys Chem B* 119:9835–9846. doi:[10.1021/acs.jpcc.5b01776](https://doi.org/10.1021/acs.jpcc.5b01776)
72. Sonnleitner T, Turton DA, Hefter G et al (2015) Ultra-broadband dielectric and optical Kerr-effect study of the ionic liquids ethyl and propylammonium nitrate. *J Phys Chem B* 119:8826–8841. doi:[10.1021/jp502935t](https://doi.org/10.1021/jp502935t)
73. Turton DA, Sonnleitner T, Ortner A et al (2012) Structure and dynamics in protic ionic liquids: A combined optical Kerr-effect and dielectric relaxation spectroscopy study. *Faraday Discuss* 154:145–153. doi:[10.1039/c1fd00054c](https://doi.org/10.1039/c1fd00054c)
74. Giraud G, Wynne K (2003) A comparison of the low-frequency vibrational spectra of liquids obtained through infrared and Raman spectroscopies. *J Chem Phys* 119:11753. doi:[10.1063/1.1623747](https://doi.org/10.1063/1.1623747)
75. Fukasawa T, Sato T, Watanabe J et al (2005) Relation between dielectric and low-frequency Raman spectra of hydrogen-bond liquids. *Phys Rev Lett* 95:197802. doi:[10.1103/PhysRevLett.95.197802](https://doi.org/10.1103/PhysRevLett.95.197802)
76. Turton DA, Hunger J, Hefter G et al (2008) Glasslike behavior in aqueous electrolyte solutions. *J Chem Phys* 128:161102. doi:[10.1063/1.2906132](https://doi.org/10.1063/1.2906132)
77. Turton DA, Hunger J, Stoppa A et al (2011) Rattling the cage: Micro- to mesoscopic structure in liquids as simple as argon and as complicated as water. *J Mol Liq* 159:2–8. doi:[10.1016/j.molliq.2010.04.005](https://doi.org/10.1016/j.molliq.2010.04.005)
78. Greaves TL, Drummond CJ (2015) Protic ionic liquids: evolving structure–property relationships and expanding applications. *Chem Rev* 115:11379–11448. doi:[10.1021/acs.chemrev.5b00158](https://doi.org/10.1021/acs.chemrev.5b00158)
79. Nibbering ETJ, Fidler H, Pines E (2005) Ultrafast chemistry: using time-resolved vibrational spectroscopy for interrogation of structural dynamics. *Annu Rev Phys Chem* 56:337–367. doi:[10.1146/annurev.physchem.56.092503.141314](https://doi.org/10.1146/annurev.physchem.56.092503.141314)
80. Bakker HJ, Skinner JL (2010) Vibrational spectroscopy as a probe of structure and dynamics in liquid water. *Chem Rev* 110:1498–1517. doi:[10.1021/cr9001879](https://doi.org/10.1021/cr9001879)
81. Zheng J, Kwak K, Fayer MD (2007) Ultrafast 2D IR vibrational echo spectroscopy. *Acc Chem Res* 40:75–83. doi:[10.1021/ar068010d](https://doi.org/10.1021/ar068010d)
82. Olschewski M, Knop S, Lindner J, Vöhringer P (2013) From single hydrogen bonds to extended hydrogen-bond wires: low-dimensional model systems for vibrational spectroscopy of associated liquids. *Angew Chemie Int Ed* 52:9634–9654. doi:[10.1002/anie.201210009](https://doi.org/10.1002/anie.201210009)

83. Hamm P, Zanni M (2011) Concepts and methods of 2D infrared spectroscopy. Cambridge University Press, Oxford, UK
84. Tan H-S, Piletic IR, Fayer MD (2005) Polarization selective spectroscopy experiments: methodology and pitfalls. *J Opt Soc Am B* 22:2009–2017. doi:[10.1364/JOSAB.22.002009](https://doi.org/10.1364/JOSAB.22.002009)
85. Kramer PL, Giammanco CH, Fayer MD (2015) Dynamics of water, methanol, and ethanol in a room temperature ionic liquid. *J Chem Phys* 142:212408. doi:[10.1063/1.4914156](https://doi.org/10.1063/1.4914156)
86. Wong DB, Giammanco CH, Fenn EE, Fayer MD (2013) Dynamics of isolated water molecules in a sea of ions in a room temperature ionic liquid. *J Phys Chem B* 117:623–635. doi:[10.1021/jp310086s](https://doi.org/10.1021/jp310086s)
87. Sturlaugson AL, Fruchey KS, Fayer MD (2012) Orientational dynamics of room temperature ionic liquid/water mixtures: water-induced structure. *J Phys Chem B* 116:1777–1787. doi:[10.1021/jp209942r](https://doi.org/10.1021/jp209942r)
88. Hunger J, Sonnleitner T, Liu L et al (2012) Hydrogen-bond dynamics in a protic ionic liquid: evidence of large-angle jumps. *J Phys Chem Lett* 3:3034–3038. doi:[10.1021/jz301334j](https://doi.org/10.1021/jz301334j)
89. Zheng Z-P, Fan W, Roy S et al (2014) Ionic liquids: not only structurally but also dynamically heterogeneous. *Angew Chem Int Ed Engl* 54:687–690. doi:[10.1002/anie.201409136](https://doi.org/10.1002/anie.201409136)

Chapter 4

High-Pressure Dielectric Spectroscopy for Studying the Charge Transfer in Ionic Liquids and Solids

Z. Wojnarowska and M. Paluch

Abstract In this chapter, the dielectric properties of ionic systems under conditions of high compression are thoroughly discussed. At the beginning the technical details on the high-pressure dielectric measurements are provided. Then we examine the pressure sensitivity of various ionic systems (protic, aprotic ionic liquids, inorganic conductors, as well as ionic polymers) that is reflected in activation volume parameter ΔV and dT_g/dP coefficient. On the other hand, the volume dependence of isothermal and isobaric conductivity data collected for a number of ionic materials enable us to separate the contributions of density and thermal effects to the ion dynamics near T_g as well as to verify the validity of the thermodynamic scaling concept for these compounds. The next part of this chapter is dedicated to relation between charge transport and structural relaxation in various ionic glass-forming systems. Therein, we show that at $\sigma_{dc} \gg 10^{-15} \text{ S cm}^{-1}$ the pressure dependence of dc-conductivity recorded for some protic conductors, inorganic salts and polymerized ionic liquids reveals the characteristic crossover (from VFT to Arrhenius-like behavior) that reflects the time scale separation (so-called decoupling) between charge diffusion and structural/segmental dynamics. Herein, the physical origin of such phenomenon is discussed in the context of charge transport mechanism. We explain in detail the methods used to quantify decoupling phenomenon as well as the physical and chemical factors affecting time scale speciation

Z. Wojnarowska (✉) · M. Paluch
Institute of Physics, University of Silesia, Uniwersytecka 4,
40-007 Katowice, Poland
e-mail: zaneta.wojnarowska@us.edu.pl

Z. Wojnarowska · M. Paluch
Silesian Center for Education and Interdisciplinary Research,
75 Pulku Piechoty 1A, 41-500 Chorzow, Poland

between charge and mass diffusion. The procedure used to recognize the charge transport mechanism based on the ambient and high-pressure dielectric measurements is also described.

4.1 Conductivity Measurements Under High-Pressure Conditions. How to Exert Pressure on the Sample?

To perform the high-pressure dielectric measurements, one needs an experimental setup containing of three modules:

- capacitor connected to the appropriate impedance analyzer which measures capacitance (C) and resistance (R) of the sample;
- equipment in which pressure is exerted on the studied material;
- thermostatic bath that provides the stable temperature conditions during the experiment.

High-pressure dielectric capacitors are usually of the variable types depending on the examined system and applied pressure generator, i.e., hydraulic press or gas compressor. However, in each case they consist of two stainless steel or gold-covered parallel plates electrically separated by Teflon or quartz spacers and equipped with wires providing the electrical contact with the impedance analyzer. If the liquid is measured, the best is to place the capacitor with the silica spacers inside the Teflon capsule that has been previously filled with a tested sample. To make sure that the examined material is in contact only with stainless steel and spacers, the capsule has to be closed with metal clamp. On the other hand, to investigate the dielectric properties of solid conductors under high-pressure conditions the capacitor with the tested material are usually tightly wrapped by means of Teflon tape. A representative illustration is shown in Fig. 4.1.

To exert pressure on the sample the capacitor is next placed in the chamber and compressed using the pressure-transmitting medium (liquid or gas). The transmitting fluid must be nonpolar, noncorrosive to electrical connections, and maintain a low viscosity at low temperatures and high pressures. Silicon oil is a popular choice (e.g., Fluorinert). It can be mixed with alkanes such as heptane to decrease its freezing point and thus allow measurements at lower temperatures, in the range of 180–200 K. The only potential danger of such equipment is that during the course of an experiment, with continual changes of temperature and pressure, the tested system may be contaminated by the pressure-transmitting fluid. To avoid such situation, the sample cell has to be precisely closed before the measurements. On the other hand the gas compressor with helium as pressure-transmitting medium can be employed. High-pressure chamber working with pressurizing fluid, presented in Fig. 4.2, is suitable for measurements in the pressure range from 0.1 MPa to 1 GPa. However, to compress the sample more a different construction of the pressure chamber has to be used. In this set up, the cylindrical Teflon capsule filled with the

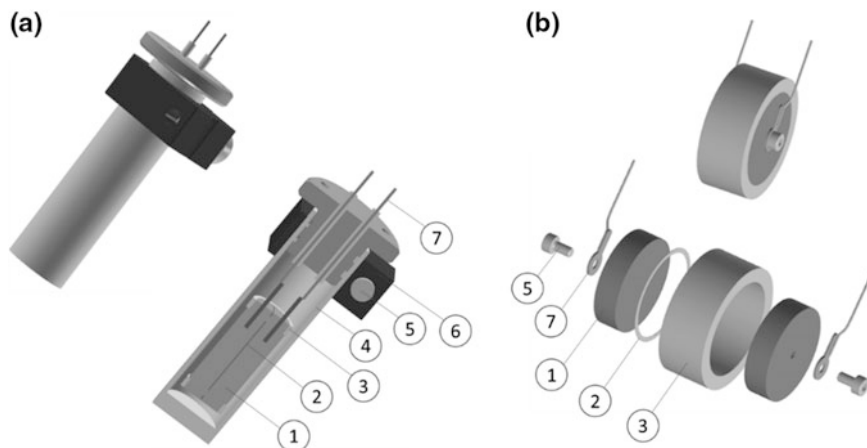


Fig. 4.1 High-pressure capacitor commonly used to investigate ionic liquids (a) and solids (b). 1 capacitor plate, 2 spacer, 3 Teflon ring, 4 Teflon capsule, 5 screw, 6 metal clamp, 7 wires

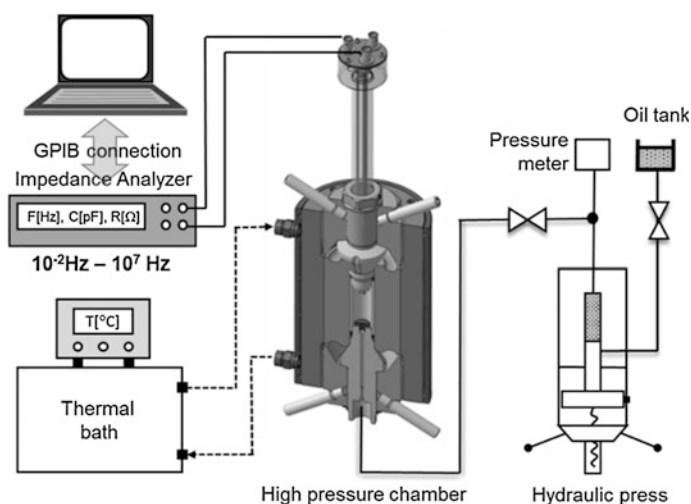
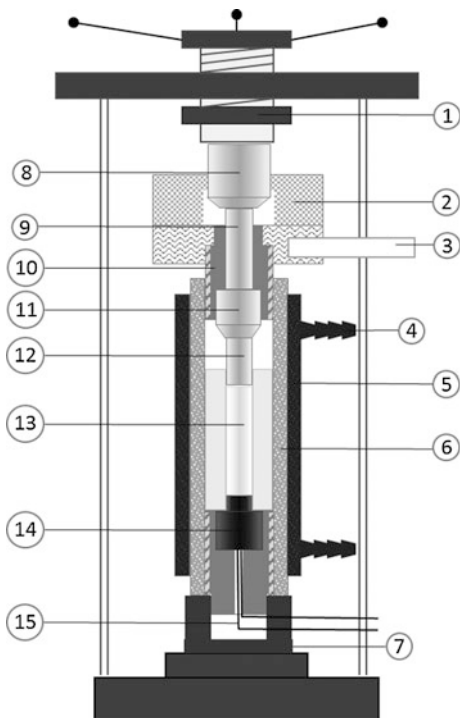


Fig. 4.2 High-pressure chamber suitable for measurements up to 1 GPa using the fluid as a pressure-transmitting medium

sample is squeezed by pistons in conjunction with a hydraulic press (see Fig. 4.3). Thus, in this system the sample serves as its own pressure-transmitting fluid. With this equipment even 2 GPa can be achieved. However, there are some limitations of this approach. Namely, only liquid materials above their glass transition temperature can be compressed. This is because solid samples can no exert hydrostatic stress. Another potential problem is friction between the cylinder and pistons occurring when the axial force is applied to the sample. This difficulty does not

Fig. 4.3 High-pressure chamber suitable for measurements up to 2 GPa. 1 hydraulic press, 2 crown, 3 arm, 4 thermal bath connector, 5 thermostatic coat, 6 high-pressure chamber, 7 holder, 8 pusher, 9 piston, 10 scroll, 11 anvil, 12 pin, 13 Teflon capsule, 14 sample holder, 15 electrical connection with impedance analyzer



exist in the case of oil chambers in which the sample is compressed from all sides at the same time.

To control both temperature and pressure during the measurements, one need thermostatic bath or other temperature controller connected to the high-pressure chamber.

The described above high-pressure setups connected to the appropriate impedance analyzer enable us to monitor the charge carrier's migration in the presence of an electrical field at various T - P thermodynamic conditions. Formalisms, the most frequently used to present the dielectric data of conducting materials, are the real part of complex electric conductivity $\sigma^*(\omega) = \varepsilon_0/Z^*(\omega)C_0$ and the imaginary part of complex electric modulus $M^*(\omega) = i\omega C_0 Z^*(\omega)$ [1]. As depicted in Fig. 4.4, $M''(f)$ function takes the form of well-resolved peak with the maximum defining the conductivity relaxation time $\tau_\sigma = 1/2\pi f_{\max}$. On the other hand, the frequency independent region of $\sigma'(f)$ function gives us information about the dc-conductivity value σ_{dc} that is inversely related to τ_σ of the given compound. Herein, it should be noted that in contrast to ambient pressure dielectric measurements, that can be performed over 16 decades of frequency ($10^{-4} < f(\text{Hz}) < 10^{12}$), the high-pressure dielectric technique is usually limited to 10^7 Hz.

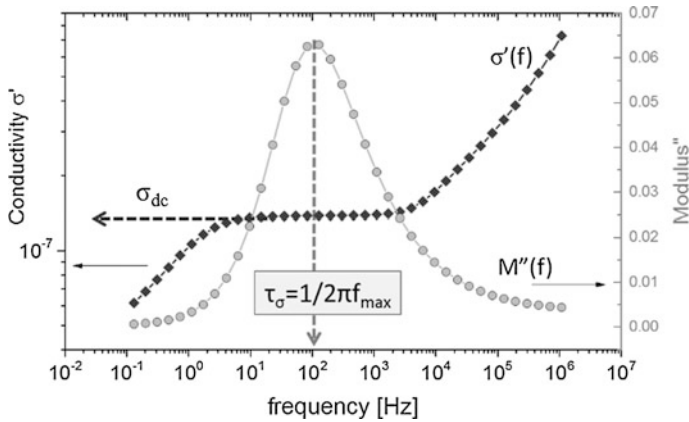


Fig. 4.4 The dielectric relaxation spectrum presented in two equivalent formalisms, i.e., the imaginary part of complex modulus function $M''(f)$ and the real part of electric conductivity $\sigma'(f)$

4.2 Pressure Sensitivity of Ion Dynamics. How Much Pressure Do We Need to “Supercool” Ionic System?

Basically, the isothermal compression brings about the same effect on the ion dynamics as isobaric cooling. Namely, during squeezing the mobility of charge carriers enormously slows down, resulting in dramatic decrease of ionic conductivity (see Fig. 4.5). What is more with elevating pressure ionic liquid can be transformed into the disordered solid (glass). Then the dc-conductivity usually changes in more than 12 decades achieving values of approximately 10^{-15} [S cm $^{-1}$] in the vicinity of the glass transition temperature (T_g) [2]. However, to affect the mobility of ions so significantly the pressure of the order of hundreds of MPa is required.

To evaluate the effect of pressure on the ion dynamics first the values of σ_{dc} under various T - P conditions have to be determined. For most electrolytes compressed in the normal liquid state logarithmic variation in dc-conductivity $\log \sigma_{dc}$ as a function of pressure at constant temperature forms the straight line that can be well parameterized by means of the pressure version of the Arrhenius law (see Fig. 4.6):

$$\log \sigma_{dc}(P) = \log \sigma_0 + \frac{\log(e)P\Delta V^\#}{RT} \quad (4.1)$$

where $\log \sigma_0$ is the value of dc-conductivity at atmospheric pressure, R is the universal gas constant and $\Delta V^\#$ is an apparent activation volume commonly related to the local volume expansion required for ionic transport [4, 5].

On the other hand, it has been experimentally recognized that ionic transport of most electrolytes compressed in the vicinity of the glass transition temperature

Fig. 4.5 Electrical conductivity as a function of frequency recorded during the isothermal squeezing of $[C_8MIM][NTf_2]$ at $T = 213$ K. Data were taken from Ref. [3]

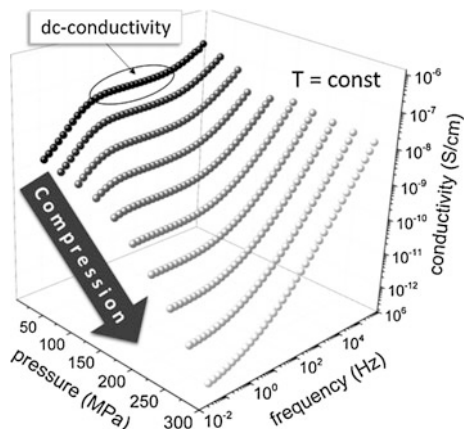
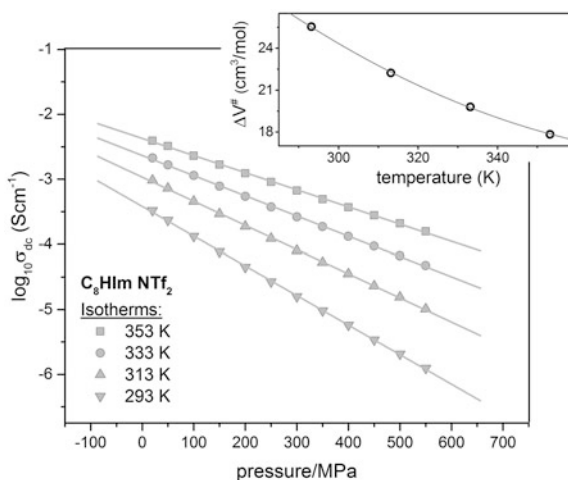


Fig. 4.6 Pressure dependence of dc-conductivity determined at several temperatures for protic ionic liquid $[C_8HIM][NTf_2]$. In the *inset* the variation of activation volume with temperature for the same compound is depicted



follows a Vogel–Fulcher–Tammann (VFT) type behavior rather than a classical Arrhenius type law.

$$\log \sigma_{dc}(P) = \log \sigma_0 + \frac{CP}{P_0 - P} \log e \quad (4.2)$$

Similar to the volume activated equation, the pressure counterpart of VFT function includes two fitting parameters: C and P_0 . The third coefficient, pre-exponential factor $\log \sigma_0$, refers to the value of σ_{dc} recorded at ambient pressure and therefore it can be easily determined directly from an experiment. An example illustrating the pressure dependence of dc-conductivity recorded in the supercooled state of $[C_8MIM][NTf_2]$, portrayed by Eq. 4.2 is depicted in Fig. 4.7a.

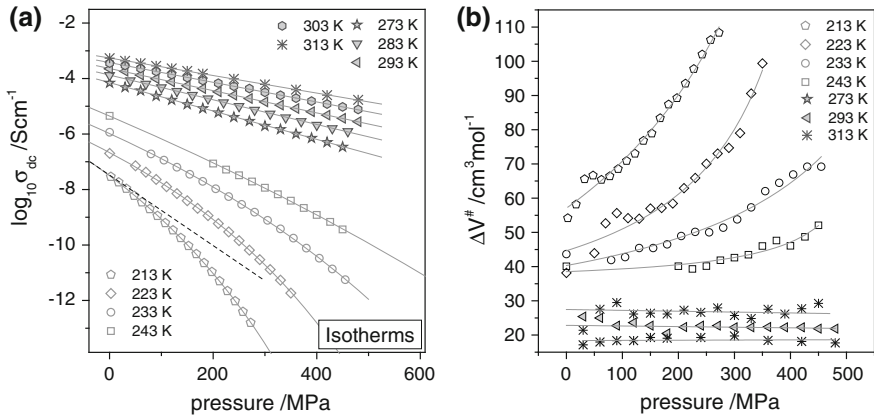


Fig. 4.7 Panel (a) The dc-conductivity data of $[\text{C}_8\text{MIM}][\text{NTf}_2]$ measured under various isothermal conditions. *Solid lines* are fits of Eqs. 4.1 and 4.2 to the experimental data. Panel (b) activation volume as a function of pressure calculated for the isothermal $\log \sigma_{\text{dc}}(P)$ data presented in panel a

The nonlinear character of the $\log \sigma_{\text{dc}}(P)$ curves recorded in the supercooled liquid state indicates that this time the pressure dependence of apparent activation volume is not constant but it increases with the similar fashion like the conductivity data do (see Fig. 4.7b). This is in analogy to the activation energy that starts to dramatically raise when the glass transition is achieved by isobaric cooling. The reason of such behavior lies in the simple relation between two physical quantities, namely $\Delta V^\#$ and σ_{dc} :

$$\Delta V^\# = 2.303RT \left(\frac{d \log \sigma_{\text{dc}}}{dP} \right) \quad (4.3)$$

From Eq. 4.3 it becomes obvious that the higher is the $\Delta V^\#$ value the greater change in σ_{dc} with squeezing is observed. Therefore, the activation volume parameter can be successfully treated as a measure of pressure sensitivity of the given ionic system. However, it should be stressed that to compare the pressure sensitivity of several samples the dielectric measurements for the same initial value of conductivity need to be performed. This is due to the general strong temperature dependence of activation volume as depicted in the inset to Fig. 4.6.

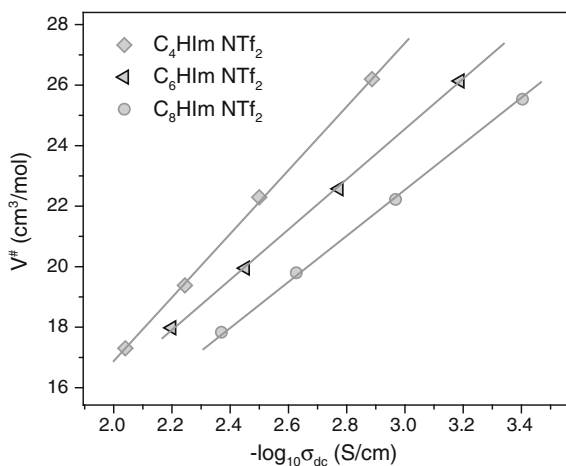
Generally, the activation volume is a very useful parameter describing the relaxation processes in glass-forming liquids. It has been experimentally verified that in the case of van der Waals systems the size of the mobile units have an influence on the value of $\Delta V^\#$ —roughly speaking, the larger particle the higher activation volume. As an example, the correspondence between the molecular and apparent activation volumes was found for polyalcohol series: glycerol, threitol, xylitol, and sorbitol [6]. Nevertheless, in the case of ionic conductors the relation between the size of charge carrying units and $\Delta V^\#$ parameter is not so obvious and

requires consideration of many additional factors. One of them is the competition between van der Waals and Coulombic interactions existing in many conducting systems. It is easily to understand when the transport properties of ILs with various lengths of alkyl side chains in the cation are considered. It has been demonstrated that longer alkyl chains induce a nanometer-scale segregation between regions of high charge density (the imidazolium head-groups and the anions) and low charge density (the nonpolar alkyl side chains) [7]. Therefore, as self-organization is more pronounced the dominant character of van der Waals interactions, when compared to the Coulomb terms, occurs. This results in lower pressure sensitivity of ILs with longer side chains and consequently smaller values of ΔV^\ddagger at the same conductivity (see Fig. 4.8).

Among these intermolecular aspects also the conformational flexibility of ions, the strength of H-bonds as well as the conductivity mechanism were found to affect the ΔV^\ddagger value of ionic systems. Namely, ΔV^\ddagger parameter determined for protic ionic systems, usually characterized by well-expanded H-bonded network, is generally lower than that of aprotic materials. It is well visualized in Fig. 4.9, where the ion dynamics of two ILs, protic one—[C₄Him][HSO₄] and aprotic [C₄C₁Im][NTf₂], is compared. Consequently, ΔV^\ddagger coefficient can be used to assess the ability of ionic system to H-bonds formation.

Another important aspect is the sensitivity of apparent activation volume on the type of charge carrying units. From the high-pressure studies of various ionic systems it was found that if the ionic conduction process is dominated by the smallest charge carriers (protons), the value of ΔV^\ddagger significantly decreases [8]. As an example one can recall carvedilol salts with the activation volume two times lower when the anion is changed from hydrochloride (131 cm³/mol) to phosphate (62 cm³/mol). Interestingly, when the proton hopping is involved in charge transfer the activation volume can be even negative. It means that the electrical conductivity increases with elevating pressure. Such result were found for two strongly hydrated

Fig. 4.8 The activation volume of three protic ionic liquids with 4, 6 and 8 carbons in alkyl side chain, respectively, plotted as a function of dc-conductivity



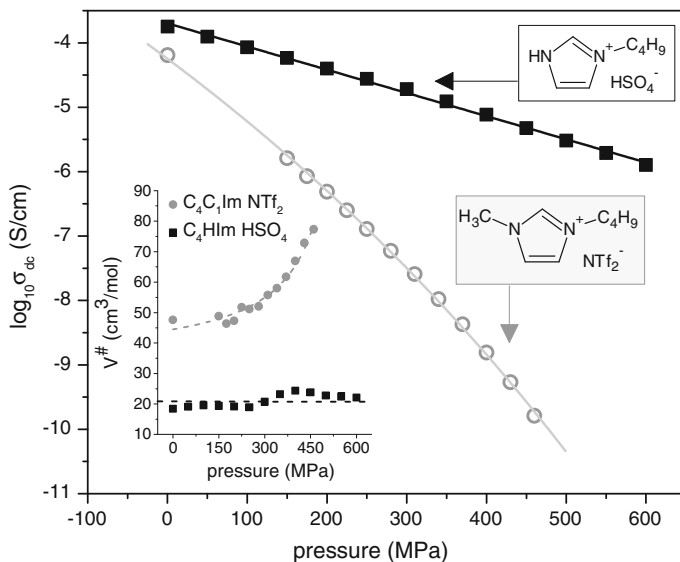


Fig. 4.9 The pressure dependence of dc-conductivity for two ionic liquids protic one—[C₄HIm][HSO₄] and aprotic [C₄C₁Im][NTf₂]. In the *inset* $\Delta V^\#(P)$ for these two compounds is illustrated

materials, i.e., dilute sulfuric acid and Nafion membranes containing more than 10 water molecules per sulfonate [9]. It is relatively straightforward to devise a conductivity mechanism that gives rise to a negative activation volume. As it was explained in Ref. [9], the activation volume for ion motion represents the volume change occurring when a diffusing species transform from a “normal” to an “activated” position. For this mechanism “normal” state consists of two parts, H₃O⁺ and a water molecule. On the other hand, the “activated” state contains two water molecules sharing a proton. Because of the sharing the activated state would be expected to have a smaller volume than the normal state. This gives rise to the negative volume of activation. Having this idea in mind, one can expect that the dynamics of hydrated ionic materials should be characterized with activation volume lower than that determined for anhydrous samples. The high-pressure experimental results obtained for popular ionic anesthetic agent lidocaine HCl and its monohydrate form confirm this statement [10, 11].

Among the activation volume concept in the literature, one can find another method commonly employed to determine the pressure sensitivity of glass-forming systems. This idea is based on the pressure coefficient of the glass transition temperature dT_g/dP determined as the first derivative of $T_g(P_g)$ dependence in the limit of ambient pressure. Since the value of $dT_g/dP|_{P=0.1 \text{ MPa}}$ is material constant it is very convenient to describe the pressure sensitivity of given material by means of this approach [12]. The only thing one needs to know is the pressure variation of the glass transition temperature.

Generally, there are several experimental methods that can be used to define T_g at ambient and elevated pressure. Among others the most popular are dilatometric and heat capacity measurements in which the volume V and enthalpy H of a glass-forming liquid as a function of temperature are, respectively, determined. Since $V(T)$ and $H(T)$ curves recorded at constant P reveal the same pattern of behavior (see Fig. 4.10a) the procedure of T_g estimation is the same in both cases and it involves the analysis of crossover point between two linear regimes that directly provides T_g value. Alternatively, the glass transition temperature can be determined from the derivatives of $V(T)$ and $H(T)$, i.e., from thermal expansion coefficient $\alpha_p = V^{-1}(\partial \ln V / \partial T)_p$ and the heat capacity $C_p = (\partial H / \partial T)_p$, respectively, that are the largest in the supercooled state and drop down on approaching T_g (see Fig. 4.10b).

Herein, it is worth noting that in both described above thermodynamic techniques the procedure of T_g determination is universal, i.e., it does not depend on the chemical structure of studied material as well as on the interactions occurring between the molecules (van der Waals or coulombic forces). This is in contrast with dielectric spectroscopy where these properties should be taken into account during the data analysis. In the case of ionic liquids and solids the charge transfer mechanism is of particular importance. In general two different procedures for defining the liquid–glass transition of ionic conductors can be distinguished. The first one refers to aprotic materials in which the charge transfer is achieved through the translational diffusion of large molecular species and therefore the conductivity is completely controlled by the viscosity. In such scenario the pressure variation of dc-conductivity can be well parameterized in the whole measured range by means of the pVFT or Arrhenius equation and the glass transition pressure (or glass transition temperature for isobaric data) is determined from an isochronal definition, i.e., P_g (or T_g) = P (or T) ($\sigma_{dc} \approx 10^{-15}$ S cm $^{-1}$ or $\tau_\sigma \approx 10^3$ s). Since, the dielectric measurements below the frequency 10^{-2} Hz are time-consuming it is a standard practice to extrapolate the data to obtain the P_g value. Alternatively, one can define

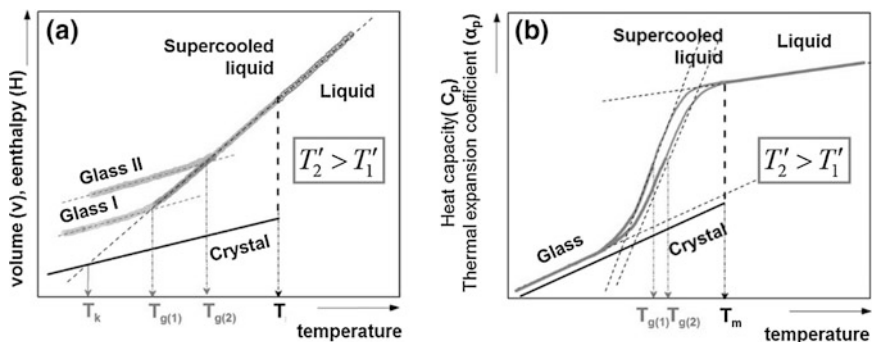


Fig. 4.10 Panel (a) the volume V and enthalpy H of a glass-forming liquid as a function of temperature. $T_{g(1)}$ is achieved when the slower cooling rate T'_1 is applied. Panel (b) jump in the thermal expansion coefficient α_p and the heat capacity C_p with temperature

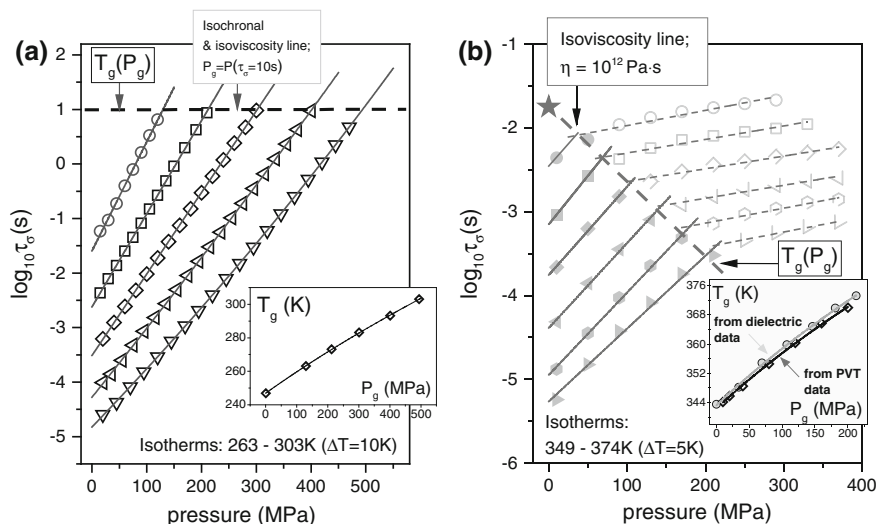


Fig. 4.11 The isothermal dielectric measurements of conductivity relaxation time of lidocaine docusate (a) and carvedilol dihydrogen phosphate (b). The insets present the pressure dependence of the T_g temperature for these compounds. Data were taken from Refs. [8, 13]

P_g as pressure at which σ_{dc} and τ_σ are respectively, a little bit higher and lower than required (see Fig. 4.11a). Nevertheless, it should be still the isochronal value of P_g .

On the other hand, if the charge transfer is faster than the species controlling the structural relaxation $\sigma_{dc}(P)$ (as well as $\tau_\sigma(P)$) dependence flexes in relatively high values of dc-conductivity (or short conductivity relaxation times), i.e., above 10^{-15} S cm $^{-1}$ (or below 10^3 s). As already pointed out in many literature reports, in such cases the value of P_g can be found directly as a crossover point of isothermal data [14–16]. Importantly, if the charge transfer is faster than the species controlling structural relaxation then $\sigma_{dc}(P_g)$ (as well as $\tau_\sigma(P_g)$) is not constant but it is changing with pressure (see Fig. 4.11b). However, it was demonstrated that the kinks of the isothermal $\sigma_{dc}(P)$ (as well as $\tau_\sigma(P)$) curves mark the isoviscosity line very well. Moreover, $T_g(P_g)$ dependence assessed from high-pressure dielectric experiments perfectly corresponds to values of T_g and P_g determined directly from dilatometric measurements. Such a comparison is presented in the inset to Fig. 4.11b. Note, that the coupling/decoupling phenomenon in ionic conductors will be discussed in details in the next paragraph of this chapter.

According to the literature reports the experimentally determined T_g rises with squeezing for all glass-formers, including ionic systems. This behavior is attributed to an increase in molecular packing induced by compression. Moreover, the $T_g(P)$ dependence usually displays a nonlinear character well reconstructed by means of second-order polynomial or an empirical relation proposed by Andersson and Andersson:

$$T_g = k_1 \left(1 + \frac{k_2}{k_3} P \right)^{1/k_2} \quad (4.4)$$

with k_1 , k_2 , and k_3 being material constants. Thus, the pressure coefficient of the glass transition temperature at ambient conditions, $dT_g/dP|_{P=0.1 \text{ MPa}}$ can be easily calculated as the ratio of k_1/k_3 . It is well known that the value of dT_g/dP in the limit of ambient pressure depends strongly on the material and it usually falls in the range 30–300 K/GPa. The low value of this coefficient reflects the high resistance of T_g on the pressure changes and it is typical for hydrogen-bonded systems and metallic glasses [17–19]. At the opposite extreme, there are van der Waals liquids with quite strong pressure sensitivity of molecular dynamics and thus high values of dT_g/dP parameter [20–22]. On the other hand, the group of ionic materials is quite diversified. The data collected in Table 4.1 indicate that the pressure sensitivity of T_g raises beginning with inorganic glasses to typical ionic liquids and finishing with protic materials.

Herein, it should be stressed that in the literature one can find the correlation between both coefficients defining the pressure sensitivity of glass-forming liquids. This relationship was derived by Paluch et al. in the following form:

$$\frac{\Delta V^\#}{dT_g/dP} = 2.303R \cdot m_P \quad (4.5)$$

where $m_P \equiv d \log(x)/d(T_g/T)_P|_{T=T_g}$, called isobaric fragility, is material-specific property that describes the deviation of x (τ_σ , σ_{dc} , τ_α or η) from the Arrhenius behavior when the T_g is approached. According to the recent paper of Lunkenheimer et al. [32] among the ionic systems there are materials characterized by small as well as high value of steepness index m_P , i.e., those with weak and significant deviation of $\sigma_{dc}(T)$ from the linear dependence, respectively. In the first group, commonly known as strong glass-formers one can find e.g., $C_{10}C_1\text{Im BF}_4$ ($m_P = 55$) [33] or $C_1C_4\text{Im SCN}$ ($m_P = 56$) [34]. On the other hand, 1,5-Bis(3-benzyl-2-methylimidazolium)pentane di-bis(trifluoromethanesulfonyl)imide or 1,5-Bis(3-methyl-2-phenylimidazolium)pentane di-bis(trifluoromethanesulfonyl)imide with $m_P = 173$ and 168, respectively, belong to fragile systems [35]. The difference between the conductivity behavior of strong and fragile ionic glasses becomes particularly evident when σ_{dc} or τ_σ are plotted as a function of T_g/T . Such prepared graph, usually called T_g -normalized Arrhenius plot, is presented in Fig. 4.12. Although fragility of ionic glass-formers is usually measured at ambient conditions, the pressure behavior of m_P index has been also reported [36]. Similarly as for van der Waals liquids the high-pressure results available for ionic compounds reveal a drop in steepness index at elevated pressure.

Coming back to the relation between dT_g/dP and $\Delta V^\#$ expressed by Eq. 4.5 one have to note that it has been derived for the viscosity data. Since in accordance with the fractional Walden rule the electric conductivity is controlled by fluidity,

Table 4.1 The values of T_g and dT_g/dP determined for various ionic glass-formers

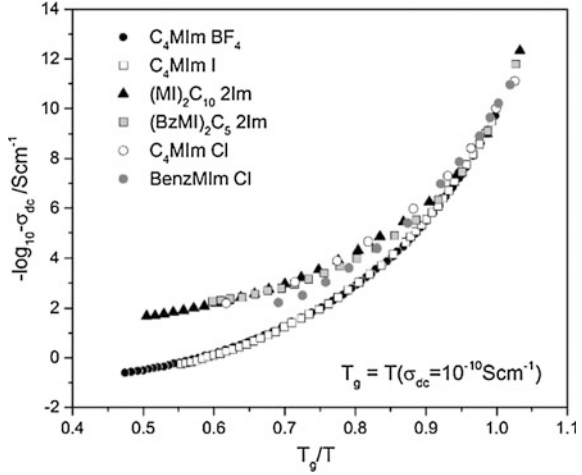
Material	$T_g(K)$ at 0.1 MPa	$dT_g/dP _{P=0.1 \text{ MPa}}$ (K/GPa)	Method	Reference
<i>Inorganic salts</i>				
$\text{Ca}(\text{NO}_3)_2 \cdot 4\text{H}_2\text{O}$	215.7	43	DTA	[23]
$\text{Ca}(\text{NO}_3)_2 \cdot 8\text{H}_2\text{O}$	181.2	36		[23]
$\text{Mg}(\text{OAc})_2 \cdot 4\text{H}_2\text{O}$	259	44		[23]
$\text{Li}(\text{OAc}) \cdot 6\text{H}_2\text{O}$	178	8.3		[23]
$\text{Na}(\text{OAc}) \cdot 10\text{H}_2\text{O}$	174	4.8		[23]
$\text{LiCl} \cdot R = 10$	139	40		[24]
$\text{LiCl} \cdot R = 3$	162	56		[24]
$\text{AgCl}_3 \cdot R = 30$	141	50		[24]
CKN	335	66		[38]
<i>Aprotic ionic systems</i>				
$\text{C}_4\text{C}_1\text{Im} \cdot \text{NTf}_2$	182*	115	BDS	[25]
$\text{C}_8\text{C}_1\text{Im} \cdot \text{NTf}_2$	185*	116		[3]
BMP-BOB	228	125		[26]
SiMIm BF_4	215	109		[27]
Lidocaine docusate	299*	132		[13]
<i>Protic ionic systems</i>				
Lidocaine hemisuccinate	274*	127	BDS	[13]
Sumatriptan hemisuccinate	309.6*	144		[28]
Procainamide HCl	316	150		[14]
Carvedilol HCl	330	152		[8]
Carvedilol H_2PO_4	346	170		[8]
Lidocaine HCl anhydrous	311*	170		[10]
Verapamil HCl	328	208		[29]
<i>Conducting polymers</i>				
PPG+ NaCF_3SO_3	219	196	N/A	[30]
PEG+ NaCF_3SO_3	204	90	N/A	[30]
Poly-BuVIm $\cdot\text{NTf}_2$	317	90	BDS	[31]

The T_g values marked with (*) were determined by means of DSC technique

$\sigma_{\text{dc}} \cdot \eta^{-k} = \text{const}$, [37] formally, Eq. 4.5 can be also implemented for studies of ionic systems. However, in practice three different cases should be considered.

The first one concerns ionic systems for which the exponent k is equal to unity and it does not depend on thermodynamic variables, T - P . Then by differentiating the logarithmic form of Walden rule with respect to T_g/T and taking into account Eq. 4.5 supplemented by definition of m_p the straightforward relation is obtained:

Fig. 4.12 T_g -normalized Arrhenius plot of selected ionic liquids. To avoid the data extrapolation T_g was defined as temperature at which σ_{dc} reaches 10^{-10} S cm^{-1} . Data were taken from Ref. [32]



$$\frac{\Delta V_{\sigma}^{\#}}{\Delta V_{\eta}^{\#}} = \frac{m_p^{\sigma}}{m_p^{\eta}} = k \quad (4.6)$$

According to this formula if $k = 1$ and $k \neq f(T, P)$, there is no difference between the apparent activation volume and isobaric fragility portraying both structural and ion dynamics. As a consequence, the relation between dT_g/dP and $\Delta V^{\#}$ parameters is satisfied. Such scenario occurs for ionic materials for that the charge diffusion fully mimics to viscosity behavior (pure vehicle mechanism). The second picture refers to ionic glass-formers characterized by the exponent k lower than one but still being insensitive to temperature and pressure changes. It means that $\sigma_{dc}(T, P)$ and $\eta(T, P)$ are decoupled from each other, however the separation between the time scale of charge and mass diffusion is constant regardless of T - P conditions. As a result Eq. 4.5 is valid despite the fact that physical parameters describing $\eta(T, P)$ dependence are higher than those determined from conductivity measurements. An example of ionic system that fulfills this rule is $[\text{Ca}(\text{NO}_3)_2]_{0.4}[\text{KNO}_3]_{0.6}$ commonly known as CKN [38]. On the other hand, the third group includes materials characterized by the fractional and pressure dependent value of the exponent k . Consequently, $\sigma_{dc}(T, P)$ dependence does not mimic $\eta(T, P)$ data and the liquid-glass transition of given ionic material is no longer isochronal, i.e., T_g (or P_g) = T or P ($\sigma_{dc} \neq \text{const}$). Since, the isochronal definition of glass transition temperature/pressure was a fundamental assumption of Eq. 4.5 this formula as well as Eq. 4.6 are not satisfied for conductivity data. Simultaneously, the conductivity activation volume $\Delta V_{\sigma}^{\#}$ is considerably lower than $\Delta V_{\eta}^{\#}$ determined at the same T - P conditions and $\Delta V_{\sigma}^{\#}/\Delta V_{\eta}^{\#} \neq k$. The case described herein involves ionic systems in which the charge transfer is governed by the Grotthuss mechanism (fast proton hopping). An experimental verification of above statements comes from

high-pressure studies of carvedilol dihydrogen phosphate, for which $\Delta V_{\sigma}^{\#}(T_g)$, $\Delta V_{\eta}^{\#}(T_g)$ and k were found to be equal 486, 85 and 0.6, respectively [8].

4.3 Thermal and Density Fluctuations to the Temperature Dependence of σ_{dc} at Ambient and Elevated Pressure

As already mentioned, many of ILs show a remarkable tendency of supercooling and consequently glass formation. It gives an opportunity to study the temperature evolution of the ionic dc-conductivity in an extraordinary wide range. On cooling toward the glass transition, the dc-conductivity decreases from values of order 10^{-2} [$\Omega^{-1} \text{ cm}^{-1}$] that are characteristic for the normal liquid state of typical IL to values of 10^{-15} [$\Omega^{-1} \text{ cm}^{-1}$] (conventionally taken as a hallmark of the liquid–glass transition), over a temperature range of a few tens of K. This enormous and continuous drop of σ_{dc} is accompanied by the dramatic slowing down of the mobility/diffusion of ions. It is well known that temperature can control the ions diffusion through two different mechanisms: changing both kinetic energy (thermal energy) and the packing density of ions. Consequently, in recent years, some efforts have been made to clarify the role played by the density and thermal effects [3, 39, 40]. In order to separate the contributions of these effects it is necessary to measure both temperature and pressure dependence of ionic conductivity [12].

According to previous discussion, there are a numerous examples that the temperature dependence of ionic conductivity significantly deviates from the Arrhenius behavior upon approaching the glass transition. Although all ILs reveal basically the same pattern of the behavior, the degree of the deviation from the Arrhenius law is not the same for each material [32]. An intriguing aspect of this behavior is also understanding whether or not the packing density of ions affect the deviation from the Arrhenius law? If yes, then to what extent?

There are two simple approaches that are generally used to asses qualitatively the contributions of thermal and density fluctuations to the temperature dependence of σ_{dc} at ambient pressure. The first one is based on the comparison of isobaric and isothermal data by plotting σ_{dc} against density or alternatively specific volume. An example of such comparison for ionic liquid $[\text{C}_8\text{MIM}][\text{NTf}_2]$ is depicted in Fig. 4.13.

It can be easily noted that the increment of conductivity for the same volume change is radically different at isobaric and isothermal conditions. The decrease of the specific volume from 0.76 to 0.705 leads to the decrease of σ_{dc} about 9 and 1 decades at constant pressure and temperature, respectively, indicating that the thermal effect is more dominating in this case. In fact, as will be discussed below, such behavior seems to be a common feature of all ILs.

A second approach for estimating the relative importance of thermal and density effects requires comparison between isobaric and isochoric data as shown in Fig. 4.14.

Fig. 4.13 Isothermal and isobaric data for [C₈MIM][NTf₂] plotted as a function of volume. Data taken from Ref. [3]

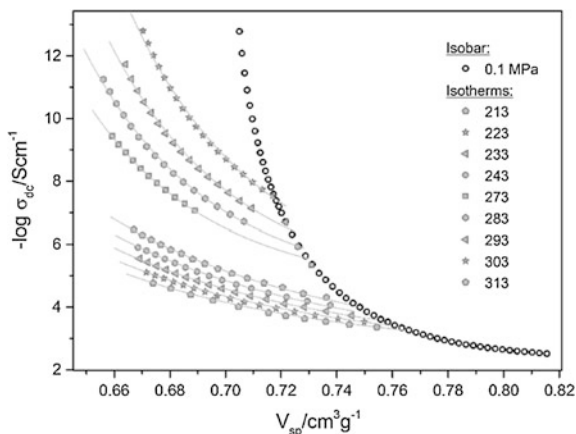
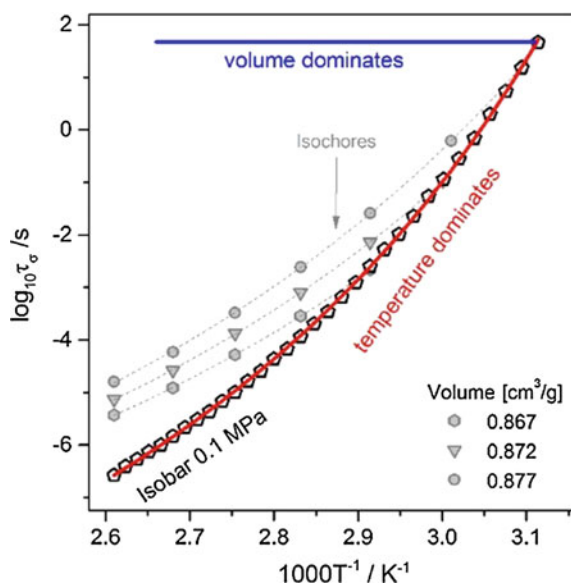


Fig. 4.14 The temperature dependence of conductivity relaxation times at constant volume condition. The *open symbols* represent the dependence of relaxation times at ambient pressure. Data taken from Ref. [36]



In addition to the experimental data denoted by symbols, we also plotted two isochoric curves (solid lines) corresponding to two limiting cases, i.e., when ion diffusion is controlled solely by (1) thermal energy fluctuations (red line) or (2) local density fluctuations (blue line). In the first case, isobaric and isochoric data should collapse onto a single line and such result would be a rigorous confirmation that the purely thermally activated models are valid. The second limiting case, manifested by the lack of any temperature dependence of σ_{dc} at constant volume, would mean that free volume models are suitable. There is no doubt that the experimental data for [C₈MIM][NTf₂] do not support fully any of these two

discussed limiting cases. However, it can be only concluded that ion mobility is much more sensitive to changes in the thermal energy than changes in density, indicating that the energy barriers for ion jumps are only slightly modified by compression. Moreover it is obvious from Fig. 4.14 that the dependence of $\log \sigma_{dc}$ on $1/T$ shows a very pronounced curvature at isochoric conditions. Thus, the non-Arrhenius behavior can occur even if the ion packing density remains unchanged.

In the above-mentioned two cases, we needed to know explicitly how the ionic conductivity depends on volume, $\sigma_{dc}(V)$. Unfortunately, $\sigma_{dc}(V)$ cannot be determined from a single experiment. Instead of this one has to perform two different types of experiments: the high-pressure dielectric studies to determine $\sigma_{dc}(T, P)$ and dilatometry measurements of the temperature–pressure dependence of the specific volume (PVT data). Having both these sets of data, it is possible to analyze the ionic conductivity at all thermodynamic states. Since the temperature and pressure ranges covered by these two experiments usually differ from each other, it becomes necessary to interpolate and/or extrapolate PVT data using an equation of state (EOS). The most popular one used for this purpose is the empirical equation of Tait. More recently, a new equation of state has been formulated by Grzybowski et al. [41] which has been experimentally verified for a wide variety of liquids.

$$V(T, P) = V(T, P_0) \left[1 + \frac{\gamma_{EOS}}{B_T(P_0)} (P - P_0) \right]^{-1/\gamma_{EOS}} \quad (4.7)$$

$$B_T(P_0) = B_T(T, P_0) = b_0 \exp(-b_2(T - T_0)) \quad (4.8)$$

$$V_0 = V(T, P_0) = \sum_{l=0}^k A_l (T - T_0)^l \quad (4.9)$$

where $b_0 = B_{T_0}(P_0)$, $b_2 = b_2(P_0) = -\partial \ln B_T(T, P_0) / \partial T|_{T=T_0}$, $A_0 = V(T_0, P_0)$, and $A_l = (1/l!) \partial^l V(T, P_0) / \partial T^l|_{T=T_0}$ for $l = 1, 2, \dots$, and the reference temperature T_0 and pressure P_0 are arbitrarily chosen. Its fundamental advantage relies on its derivation from the effective intermolecular potential [42]

$$V(r) = \frac{A}{r^{3\gamma_{EOS}}} - B \quad (4.10)$$

where A and B are constant. Above equation is limited to the density range where the isothermal bulk modulus $B_T(P)$ linearly depends on pressure. However, this limitation can be removed if the exponent γ_{EOS} is replaced by a density dependent function, $\gamma_{EOS}(\rho)$ as suggested by the General Density Scaling Law [43].

Obviously, a more quantitative assessment of the relative importance of different thermodynamics variables is needed if we want to catch any differences among various ILs. It is possible by analyzing the data from Fig. 4.14 in terms of the

apparent enthalpy, H_P , at constant pressure and the apparent activation energy, E_V , at constant volume [44]:

$$H_P = R \left(\frac{\partial \ln \sigma}{\partial T^{-1}} \right)_P \quad (4.11)$$

$$E_V = R \left(\frac{\partial \ln \sigma}{\partial T^{-1}} \right)_V \quad (4.12)$$

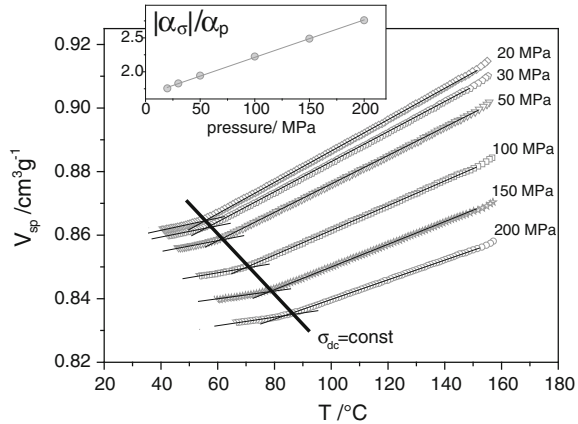
where R is the gas constant. As discussed by Naoki et al. [45], the relative dominance of thermal and volume effects is reflected in the ratio of E_V to H_P which can vary from 0 to 1. Note that values 0 and 1 correspond to two limiting cases (2) and (1), respectively, from Fig. 4.14. This ratio should be determined at the point where isobaric and isochoric curves meet together. For $[\text{C}_{80}\text{MIM}][\text{NTf}_2]$ at temperatures close to T_g the value of the ratio E_V/H_P is nearly constant and equal to 0.79 ± 0.02 . Similar but not the same values were also reported for other ILs. Thus, it is evident that the temperature is the dominant control parameter in the vicinity of glass transition temperature for ILs.

It will be value at this stage to review briefly the results of E_V/H_P obtained for various types of materials [12, 46]. Literature data for van der Waals liquids shows that the ratio E_V/H_P lies usually in the range 0.4–0.6, indicating that the effects of thermal and volume fluctuations are comparable. This is in contrast to associated liquids which have values of the ratio E_V/H_P frequently close to unity. It means that pure temperature effects on molecular rearrangements are dominant. The reason is that the associated liquids usually form extensive hydrogen-bonded structures with strong hydrogen-bonding interactions. And consequently, the thermal fluctuations provide necessary energy to break H-bonds and to facilitate the molecular diffusion across the sample. Thus, clear pictures emerge that the magnitude of the ratio E_V/H_P reflects the degree and type of intermolecular interactions (van der Waals, H-bonded, Coulombic).

Another interesting aspect worth to be mentioned is pressure dependence of the ratio E_V/H_P . In a few cases it was found the ratio slightly increases with compression indicating the growing role of the thermal fluctuations [3].

For the completeness of the discussion on methods for assessing the relative contributions of the thermal and volume fluctuation in the temperature dependence of ionic conduction, we should also mention the method proposed by Ferrer et al. [47]. This requires calculating the coefficient of isobaric expansivity, $\alpha_P = V^{-1}(\partial V/\partial T)_P$ and the coefficient of isochronal (i.e., constant viscosity η or structural relaxation time, τ_α) expansivity, $\alpha_\eta = V^{-1}(\partial V/\partial T)_\eta$. The second one can be also determined at constant value of σ_{dc} provided that the fractional DSE law is satisfied at considered T and P range. As pointed out by Ferrer et al. the ratio of $\alpha_\eta/\alpha_P \gg 1$ means that the ion transport is governed by thermal fluctuations and the energy barrier for ion hopping does not change with compression. On the other hand, the ratio of α_η/α_P approaches to zero when volume fluctuations alone control

Fig. 4.15 The temperature dependence of specific volume V_{sp} in the pressure range of 20–200 MPa for verapamil hydrochloride. In the *inset panel* the pressure dependence of α_σ/α_P for the same compound is depicted



ion transport. Figure 4.15 illustrates the changes of the specific volume against temperature at constant pressure that can be easily used to determine the pressure dependences of α_P and α_σ for given ionic liquid.

From this type of data, it is very simple to calculate the value of the ratio of α_σ/α_P for considered IL at various pressure conditions (see inset to Fig. 4.15). However, one should add that there is an analytical expression that relates E_V/H_P and of α_η/α_P [48]:

$$\frac{E_V}{H_P} = \left(1 - \frac{\alpha_P}{\alpha_\eta}\right)^{-1} \quad (4.13)$$

Since these two ratios provide exactly the same information about the relative contributions of the thermal and volume fluctuations they can be treated equally.

4.4 Density Scaling of Ionic Systems

In the previous section, we demonstrated that by converting both isobaric and isothermal ionic conductivity data to specific volume representation, it is possible to assess in qualitative way the role played by thermal and density fluctuations in the charge transport process. In this section, we will introduce a simple model which can be used for the quantitative analysis of the volume dependent ionic conductivity data. This model was originally proposed by Avramov to describe the temperature and pressure dependence of various transport properties (e.g., viscosity) of glass-forming liquids [49] and later on adopted by Casalini and Roland [50] to account of the volume effects. The main underlining assumptions of the model are that (1) ion motion is thermally activated process with a jump frequency related to the energy barrier and temperature through the exponential relation:

$$v = v_0 \exp\left(-\frac{E_i}{kT}\right) \quad (4.14)$$

and (2) the maximal energy barrier E_{\max} changes with system density according to the power law [26]:

$$E_m = E_r \left(\frac{V_r}{V}\right)^{\gamma_{\text{EOS}}} \quad (4.15)$$

Since the charge transport takes place in structurally disordered systems, therefore, there is a distribution of energy barrier heights $P(E, \delta)$. The mean jump frequency—reflecting average charge carrier mobility—is defined as

$$\langle v \rangle = \int_0^{E_m} \sigma(E) P(E) dE \quad (4.16)$$

From the mean jump frequency being proportional to the average charge carrier mobility $\langle \mu \rangle$ one can calculate the dc-conductivity:

$$\langle v \rangle \approx \langle \mu \rangle \approx \sigma_{\text{dc}} \quad (4.17)$$

It has been argued that a choice of a truncated Poisson probability distribution function to represent the energy distribution for real systems is a quite rational approach

$$P(E) = \left[\delta - \delta \exp\left(-\frac{E_m}{\delta}\right) \right]^{-1} \exp\left[\frac{(E - E_m)}{\delta}\right] \quad (4.18)$$

where δ is the variance of the probability distribution function. One of the advantage of such choice is that Eq. 4.16 can be solved analytically. For $RT \ll \delta < E_{\max}$ its solution takes a simple exponential form:

$$\langle v \rangle = v_0 \exp\left(-\frac{E_m(V)}{\delta}\right) \quad (4.19)$$

As demonstrated by the Avramov [51], the variance of distribution function of barrier heights is directly connected to the total entropy of system through the relation:

$$S - S_r \approx -\frac{RZ}{2} \ln \frac{\delta}{\delta_r} \quad (4.20)$$

where δ_r and S_r denotes the variance and entropy of system at some reference state, respectively, while Z is the degeneracy of system and can be interpreted as the

number of escape channels available for each charge carrier. Above equation was derived from a more general rule that establishes a relationship between the entropy of system and the distribution function of barrier heights:

$$S - S_r = -\frac{RZ}{2} \int_0^{E_m} P(E) \ln P(E) dE \quad (4.21)$$

Taking into account that the average jump frequency is proportional to ionic conductivity (Eq. 4.17) and combining Eqs. (4.19) and (4.20) we obtain the expression describing the dependence of ionic conductivity on the total entropy of system:

$$\sigma_{dc} = \sigma_0 \exp \left\{ -E_m(V) \exp \left[\frac{2(S - S_r)}{ZR} \right] \right\} \quad (4.22)$$

The final step in derivation of the equation for volume dependence of ionic conductivity is the recalling the relationship between the total entropy of system and volume (Eq. 4.23), established by Casalini and Roland [52] for supercooled liquids

$$S - S_r = -C_V \ln[(V_r/V)^{\gamma_G} T_r/T] \quad (4.23)$$

When Eq. 4.23 is inserted into Eq. 4.22, we finally arrive at

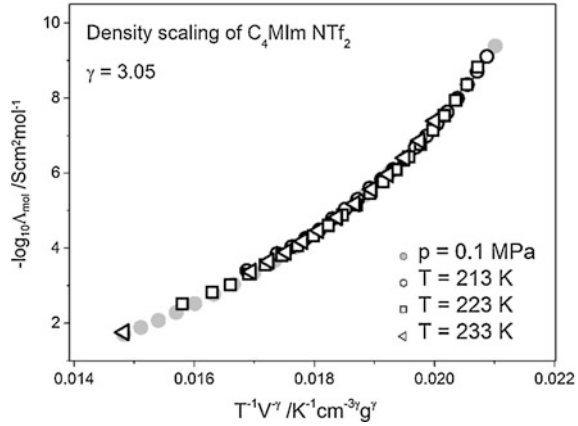
$$\log \sigma_{dc}(T, V) = \log \sigma_0 - \left(\frac{B}{TV^\gamma} \right)^D \quad (4.24)$$

Above equation was shown to provide a good description of the electric conductivity data spanning many decades [3, 25, 26, 53]. In this context, it is also worth mentioning that the Eq. 4.28 does a good job of representing the viscosity data of various ionic liquids [53–55]. However, a key feature of this equation is a prediction of the scaling behavior both for conductivity and viscosity data. It implies that isobaric and isothermal data could be collapsed on the single master curve if they are plotted as a function of new generalized variable: TV^γ . Such scaling, often called density scaling, is indeed possible as shown in Fig. 4.16 for $[C_4MIM][NTf_2]$.

The exponent γ is a material constant which is related to the Grüneisen parameter γ_G and the exponent γ_{EOS} characterizing the repulsive part of the intermolecular potential [26, 56]:

$$\gamma = \frac{\gamma_{EOS}}{D} + \gamma_G \quad (4.25)$$

Fig. 4.16 The density scaling versus the quantity $T^{-1}V^{-\gamma}$ for ionic liquid $[C_4MIM][NTf_2]$. Data taken from Ref. [25]



And thus it becomes obvious that there is a direct connection between intermolecular potential, thermodynamics and ionic charge transport. The validity of the relationship was confirmed by comparing the values of γ_g calculated from Eq. 4.24 and determined directly from its thermodynamic definition [26]:

$$\gamma_G = \frac{C_p/C_v - 1}{T\alpha_P} \tag{4.26}$$

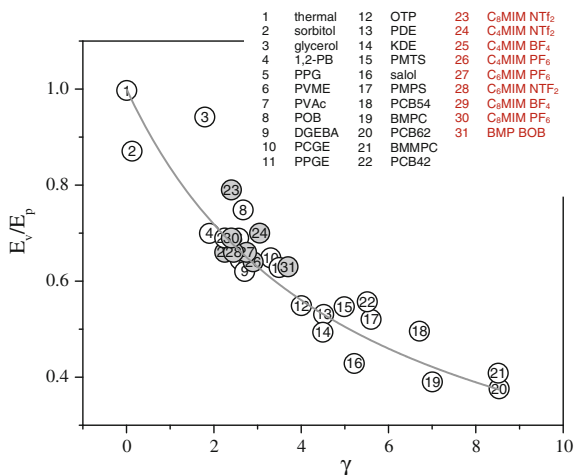
A more important aspect of the density scaling is that the scaling exponent γ can be also related to the ratio of the E_v/E_P according to [46]:

$$\frac{E_v}{E_P} = \frac{1}{1 + \gamma \alpha_P T_g} \tag{4.27}$$

As depicted in Fig. 4.17, a strong correlation between these two quantities was experimentally found for various types of glass-forming liquids including ionic liquids. The experimental fact is that the product αT_g takes almost the same values for analyzed materials, let us consider γ as an alternative measure of the relative degree to which temperature and density control the molecular transport.

It is easy to note that for $E_v/E_P = 1$ the exponent γ is equal 0 and correspond to the case when charge transport is solely controlled by the thermal fluctuations. On the other hand, if E_v/E_P approach to zero, then γ tends to infinity and intermolecular free volume governs the ions mobility. The typical values of the scaling exponent found for various ionic liquids are collected in Table 4.2.

Another benefit arising from the density scaling approach is that for given ionic liquid the same value of the exponent γ can be used to rescale electric conductivity and viscosity data. However, it is only true if there is no decoupling between these two transport properties. This case was nicely presented by Lopez et al. [53]. The authors analyzed the behavior of the electric conductivity data of six ionic liquids: $[C_4C_1IM][BF_4]$, $[C_8C_1IM][BF_4]$, $[C_4C_1IM][PF_6]$, $[C_6C_1IM][PF_6]$, $[C_8C_1IM][PF_6]$,

Fig. 4.17 E_v/E_p as a function of γ coefficient**Table 4.2** The values of the scaling exponent found for various ionic liquids

Compound	γ_σ	γ_η	Ref.
(BMP-BOB)		3.7	[26]
[C ₈ MIM][NTf ₂]	2.4	2.4	[3, 7]
[C ₄ MIM]BF ₄		2.25	[7]
[C ₄ MIM]PF ₆		2.9	[7]
[C ₄ MIM]NTf ₂	3.05	2.85	[25]
[C ₆ MIM]PF ₆		2.75	[7]
[C ₆ MIM]NTf ₂		2.45	
[C ₈ MIM]BF ₄		2.25	
[C ₈ MIM]PF ₆		2.4	
Verapamil HCl	2.45		[36]
Carvedilol HCl	2.13	2.42	[8]
Carvedilol dihydrogen phosphate	1.18	2.46	[8]
Lidocaine HCl anhydrous	2.4		[10]
Lidocaine HCl monohydrate	2.69		[11]

[N(C₄H₉)₄][B(C₄H₉)₄] for which high-pressure viscosity data were available. As a result they found that the scaling exponents obtained from electric conductivity are quite close to those obtained from viscosities. On the other hand, two different values of the scaling exponent are needed if electric conductivity is decoupled from viscosity. In addition, one can observe a clear relation between the values of exponent k in DSE relation and the ratio $\gamma_\sigma/\gamma_\eta$,

$$\gamma_\sigma/\gamma_\eta \approx k^{\text{SE}} \quad (4.28)$$

Such correlation was found to be quite well satisfied in the case of protic ionic liquids. According to data presented in Table 4.2 the ratio $\gamma_\sigma/\gamma_\eta$ is equal to 0.88 and 0.48 for hydrochloride and phosphate salts of carvedilol, respectively. On the other hand, the values of k for these compounds were found to be equal to 0.77 and 0.6, respectively. Thus, one can state that the ratio $\gamma_\sigma/\gamma_\eta$ could be a useful measure of the decoupling phenomenon.

The analysis of both viscosity and electric conductivity data in terms of the density scaling also revealed that the value of scaling exponent γ significantly depends on the molecular architecture of ions [53]. A quite general trend was observed by various investigators when they studied how the γ changes with an increase in the alkyl chain length on the imidazolium cation $[\text{C}_n\text{C}_1\text{IM}]$ for the same anion. The scaling exponent has a tendency to decrease with an increase of n . It has been suggested that this experimentally observed dependence of γ on n can be related to the fact that the imidazolium-based ILs exhibit strong nanostructural organizations [3]. Molecular Dynamics simulations performed for $[\text{C}_n\text{C}_1\text{IM}][\text{PF}_6]$ with $n = 2, 4, 6, 8$ and 12 provided an evidence for formation of nonpolar domains which became larger and more connected as the alkyl chain was elongated [57]. Consequently, it is postulated that the scaling exponent may reflect the degree of self-organization evolving with the change of the alkyl side-chain length in some ILs [3].

4.5 Relation Between Ion Dynamics and Structural Relaxation at Ambient and Elevated Pressure

4.5.1 *Are the Stokes–Einstein and Walden Laws Always Satisfied?*

According to the classical Walden (or Stokes–Einstein) theory, ion transport in electrolytes is controlled by their viscosity $\Lambda_{\text{mol}} \cdot \eta = \text{const}$, i.e., molecular entities involved in structural relaxation are also the ions transporting the electrical charges. As a consequence, the temperature dependences of both molar conductivity and structural relaxation are expected to be the same and then the $\log \Lambda_{\text{mol}}$ plotted versus $\log(\eta^{-1})$ form a straight line with the slope close to unity. A number of theoretical and experimental studies performed in the past clearly indicate that such scenario holds reasonably well for most aprotic ionic liquids (see Fig. 4.18a) [58–60]. However, if the transport properties of another sets ionic materials are considered some deviations from this general rule can be observed. As presented in Fig. 4.18b, the slope of Λ_{mol} versus η^{-1} dependence determined experimentally for some protic ionic conductors, inorganic glasses as well as ionic polymers is lower than one [61]. Consequently, the Walden relation takes the fractional form $\Lambda_{\text{mol}} \cdot \eta^{-k} = \text{const}$. Moreover, ionic samples classified as exceptions from Walden rule usually fall above the “ideal line”, i.e., in the so-called superionic region. It

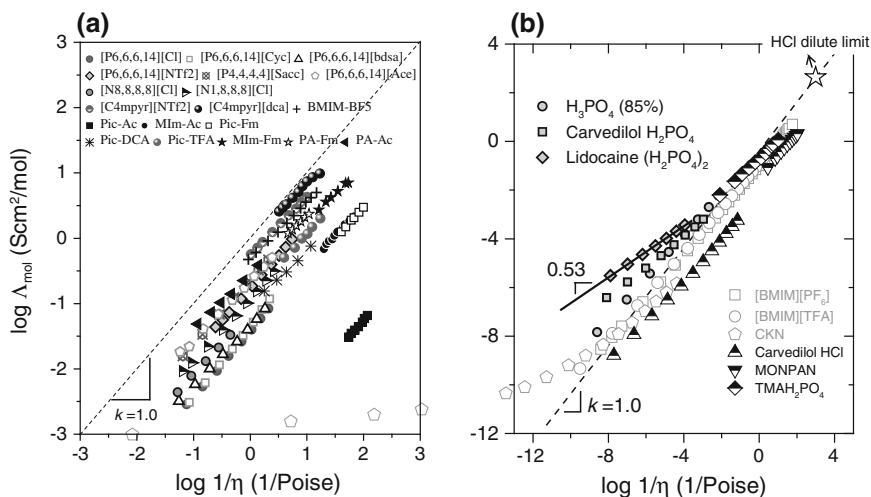


Fig. 4.18 Walden plots constructed for various aprotic and protic ionic conductors. Data were taken from [58–62]. The dashed line with the slope equal to unity was determined for the dilute HCl solution

means that they are characterized by the abnormally high mobility of charge carrying species, strongly decoupled from mass diffusion.

In the last years, a lot of effort has been devoted to recognizing the origin of excess conductivity of some ionic liquids and glasses. Generally, there are two concepts that explain this phenomenon. The first one involves a fast proton transfer through the system within so-called Grotthuss picture. Alternatively, the motions of species larger than protons that can slip through the structure via channels are also regarded.

In the Grotthuss mechanism the protonic defect is moved from one electrode to another while a given proton is transferred only between two neighboring molecules [63–65]. This is in contrast with classical proton hopping idea when the same proton is sequentially transferred within hydrogen bonds from one ion/molecule to the other (see Fig. 4.19). It has been found that the proton motions within the Grotthuss picture, originally proposed to explain high conductivity of water, gives rise to superprotonic behavior of many other compounds. As an example, phosphoric acid turned out to be almost ideal proton conductor [66]. In Fig. 4.18b H_3PO_4 clearly appears in the superionic regime of Walden plot in the entire studied temperature range. The highly efficient Grotthuss mechanism was also reported for nonionic heterocycles incorporating both proton donor and acceptor groups [67, 68] as well as hydrated imidazolium-based acidic polymers with H^+ transport realized mainly through the water molecules [69] (see Fig. 4.19). Interestingly, it was found that some protic salt systems, usually regarded as poor ionic materials, can be also characterized by efficient proton conductivity. Among others, the large decoupling between conductivity relaxation and structural dynamics was reported for carvedilol

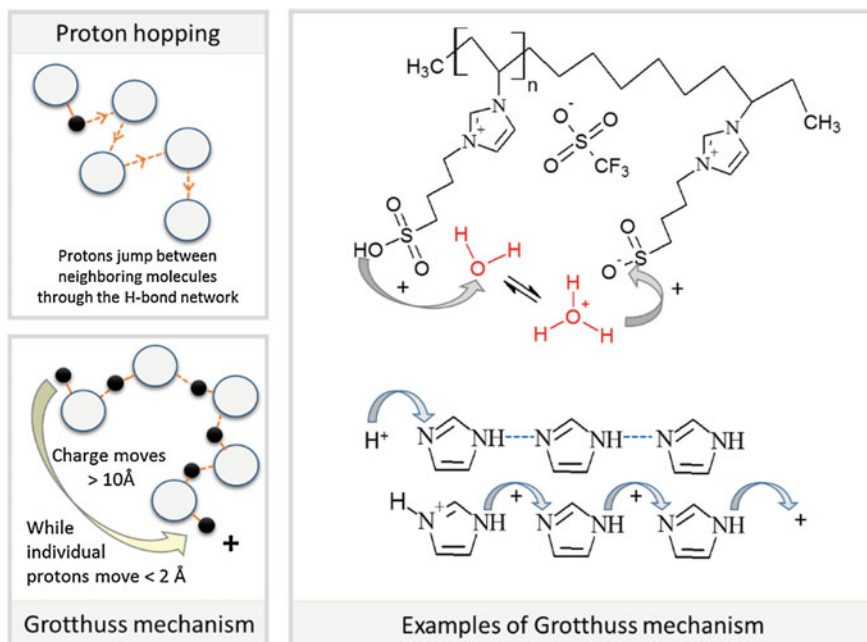


Fig. 4.19 Conductivity mechanism in protic ionic systems. Examples of proton transfer through the hydrated poly-[HSO₃-BVIIm][OTf] membrane and imidazole molecules are presented

dihydrogen phosphate [70] and succinate salt of sumatriptan [28]. However, up to now the PIL revealing the strongest time scale separation between the charge transport and mass diffusion is lidocaine di-dihydrogen phosphate with relatively low exponent k in fractional Walden rule [61] (see Fig. 4.19). Herein, it should be noted that the common feature of superprotic systems is their significant deviation from ideal KCl line at low temperatures. On the other hand, the opposite behavior is observed much above the liquid–glass transition region. This is because with increasing temperature the Grotthuss conduction is progressively dominated by vehicle-type mechanism.

The second concept of superionic conductors concerns the decoupled aprotic systems. Despite the lack of proton transfer the difference in the time scale of conductivity relaxation and structural dynamics occurs in these materials. Such observation was reported for various inorganic glasses (silver oxyhalide [71], sodium silicate [72] or KNO₃-Ca(NO₃)₂, commonly known as KKN [73]), some deep eutectic solvents (like binary mixture of acetamide+LiNO₃) [74], or various polymerized ionic liquids based on polyvinylimidazole chain [75–78]. As an origin of excess conductivity of these materials the motions of species larger than protons that can slip through the structure via channels are usually regarded. Since the charge migration is accompanied by translational diffusion of ions, such mechanism can be called vehicle-type conduction. However, in contrast to the classical

vehicular transfer, the cations and anions give different contributions to ionic conductivity and structural dynamics. The difference between these two mechanisms is visualized schematically in Fig. 4.20.

As it was reported in literature to recognize the physical origin of excess conductivity in various ionic liquids and glasses the pulsed field gradient (PFG) NMR spectroscopy is usually employed. This is due to its ability to describe the diffusion of cations, anions and protons separately. However, recently it has been demonstrated that the high-pressure dielectric spectroscopy can be also successfully applied to identify the nature of transport properties in ionic systems [79].

It has been found that in the case of ionic samples characterized by classical vehicle conduction the dielectric experimental data do not exhibit any specific features, i.e., the temperature variation of conductivity relaxation times or dc-conductivity reveal usually the non-Arrhenius curvature satisfactorily parameterized by means of the VFT equation. On the other hand, $\log \tau_{\sigma}(P)$ points form straight line or slightly deviate from linear behavior (see Fig. 4.21a and b). Since in the case of classical vehicle mechanism the conductivity relaxation mimics the structural dynamics $\tau_{\sigma}(T)$ and $\tau_{\sigma}(P)$ data can be successfully applied to determine the glass transition temperature T_g and glass transition pressure P_g , of the given ionic liquid using the typical definition of T_g (or P_g) for which τ_{σ} reaches 1000 s. As a consequence of isoviscosity and isochronal character of $T_g(P_g)$ line the electrical conductivity (or conductivity relaxation times) measured at different temperature and pressure conditions falls on one curve with the slope close to unity when

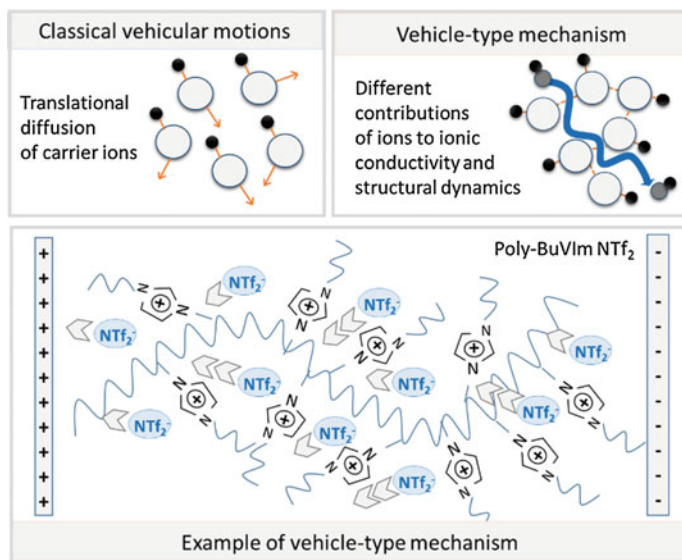


Fig. 4.20 In the *upper panels* the difference between classical vehicle conduction and vehicle-type mechanism is visualized. Below the example of vehicle-type transport through polymerized ionic liquid poly-BuVIm NTF₂ is presented

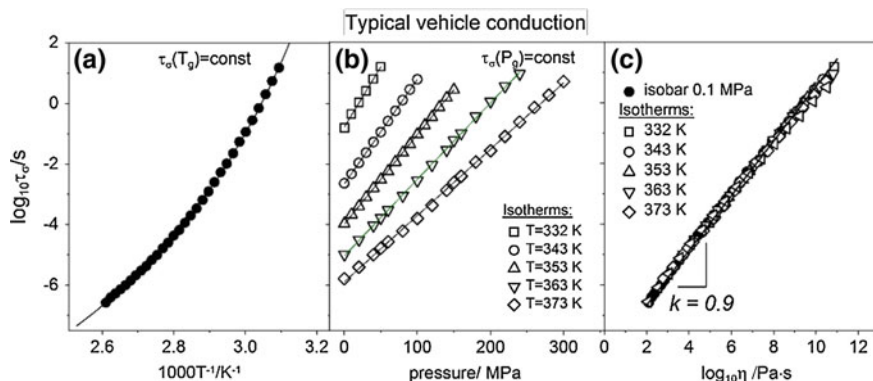


Fig. 4.21 The temperature (a) and pressure (b) dependences of conductivity relaxation times measured for verapamil hydrochloride. Panel (c) presents the Stokes–Einstein plot for the same compound. The data were taken from Refs. [8, 36]

plotted against the fluidity. It means that the Walden law as well as the Stokes–Einstein relation are satisfied under high-pressure if the conductivity of ionic system is controlled by the classical vehicle mechanism (see Fig. 4.21c). Ionic systems that fulfill these rules are aprotic ionic liquids in general [80, 81] as well as some protic salts like verapamil HCl [8] or lidocaine docusate [13].

The second picture refers to vehicle mechanism in which the counterions give different contribution to dc-conductivity and structural dynamics. As a result, the time scale separation between the charge transfer and structural relaxation takes place. At ambient pressure the decoupling between τ_σ and τ_α is always manifested by the crossover of $\tau_\sigma(T)$ plot that occurs at conductivity relaxation times shorter than 1000 s and which indicates T_g of given ionic system. However, when such a system is compressed isothermally two different patterns of $\tau_\sigma(P)$ behavior can be observed. In the first case, typical for inorganic salts composed of cations and anions with different ionic charge, the kink of $\tau_\sigma(P)$ dependences occurs at the same conductivity relaxation time as at ambient conditions [38]. Thus, the decoupling between τ_σ and τ_α is independent of T – P conditions (see Fig. 4.22b). In such scenario the exponent k in Walden rule is lower than one and it is pressure independent (see Fig. 4.22c). On the other hand, the isothermal compression of polymerized aprotic ionic liquids markedly reduces the decoupling between τ_σ and τ_α , i.e., the crossover of $\tau_\sigma(P)$ dependence moves toward longer conductivity relaxation times as pressure increases (see Fig. 4.22e). Consequently, the $T_g(P_g)$ line is no longer isochronal and Walden rule is no longer valid. In such scenario, the isothermal and isobaric conductivity data cannot collapse into single curve when plotted against viscosity. Moreover, as schematically illustrated in Fig. 4.22f, the exponent k in Walden rule is expected to be higher at elevated pressure. The described pattern of conductivity behavior has been recently reported for aprotic polycationic system poly-1-vinyl-3-butylimidazolium bis(trifluoromethylsulfonyl) imide [PBuVIm][NTf₂] [31]. The decrease in the time scale separation of charge

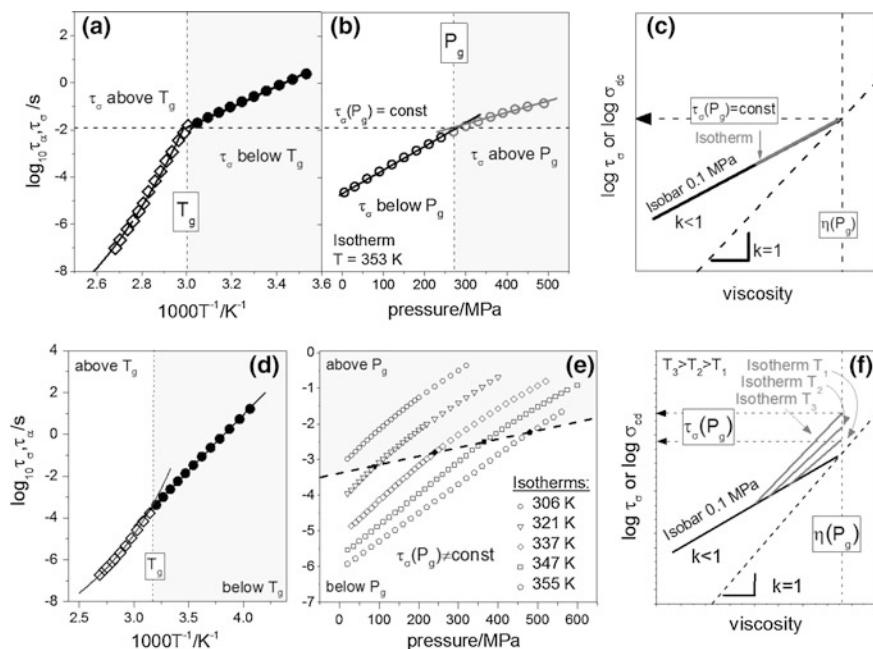


Fig. 4.22 The temperature and pressure dependences of conductivity relaxation times of inorganic conductor CKN (panels **a** and **b**) and polymerized ionic liquid poly-BuVIm NTf₂ (panels **d** and **e**). Panels **(c)** and **(f)** present schematically the Stokes–Einstein plot for both these compounds. The data were taken from Refs. [15, 31]

transport and segmental relaxation under pressure was explained in this case by the lower free volume in polymer matrix that result in slowing down of anions diffusion.

Another behavior pattern for $\tau_{\sigma}(P)$ experimental data was found for protic ionic liquids and solids with the charge transfer governed by the Grotthuss mechanism. In these materials, the temperature dependence of the conductivity relaxation time recorded at ambient pressure conditions reveals a well-defined kink from non-Arrhenius to Arrhenius-like behavior at $\tau_{\sigma} < 100$ s that indicates the time scale separation between proton transfer and mass diffusion (see Fig. 4.23a). However, in contrast to the vehicle-type conduction the addition of pressure as an external thermodynamic variable significantly enhances the decoupling between τ_{σ} and τ_{α} in the case of ionic systems with fast proton hopping. It means that the characteristic crossover of $\tau_{\sigma}(P)$ dependence is observed at shorter conductivity relaxation times under pressure (see Fig. 4.23b). The physical explanation of such observations lies in reduced interionic distances as well as strongly reinforced H-bonded structure that together provide new pathways for fast proton transfer. Since with increasing pressure the viscosity at T_g remains constant while $\tau_{\sigma}(T_g)$ progressively decreases the fractional Stokes–Einstein and Walden relations are expected to be broken for

protic ionic conductors. As presented in Fig. 4.23c, the isothermal and isobaric conductivity data of protic ionic system with the fast proton transfer indeed do not superimpose each other, as opposed to the previously described classical vehicle conduction. Additionally, the exponent in the Walden relation is in general pressure dependent—it is getting lower at elevated pressure.

As illustrated above to recognize the conductivity mechanism in ionic systems at least one isothermal $\tau_\sigma(P)$ curve, in addition to ambient pressure data, is required. However, to precisely examine the Walden law under high-pressure conditions the viscosity behavior as a function of pressure needs to be determined in addition to T – P conductivity data. Since such experiment is technically complicated the analysis of $\tau_\sigma(T, P)$ data in terms of high-pressure Walden rule is rarely performed and it is limited to normal liquid state. Therefore, recently a novel procedure based on the density scaling concept and the T – V version of the Avramov entropic model has been proposed for this purpose. The details regarding density scaling idea and entropic models will be provided in the next paragraphs of this chapter. To determine the viscosity behavior under desired T – P conditions the results of ambient pressure rheological measurements and high-pressure dilatometric experiments are required. The first step of discussed procedure involves the parameterization of $V_{sp}(T)$ data recorded above the glass transition temperature of given system by means of the equation of state. For this purpose the Tait formula can be employed [82].

$$V(T, P) = V(T, 0) \left[1 - C \ln \left(1 + \frac{P}{B(T)} \right) \right] \quad (4.29)$$

where $V(T, 0) = V_0 + V_1T$; C is a universal constant equal to 0.0894; $B(T) = b_0 \exp(-b_1T)$; T is the temperature in degrees Celsius and P is the pressure in MPa. The next part of the analysis is based on the density scaling concept. Briefly speaking, this idea relies on the experimental finding that the σ_{dc} , τ_σ , τ_α and η data of various glass-forming systems, measured as a function of both temperature and pressure, can be superimposed by plotting versus the quantity $T^{-1}V^{-\gamma}$, with γ being a material constant. Herein, it should be noted that the scaling parameter can be determined directly from the PVT experiment as the slope of $T_g(V_g)$ dependence. Note that in the case of ionic conductors with the charge transfer governed by fast proton hopping the value of γ estimated in such way can be applied only for viscosity scaling. Therefore, it is denoted as γ_η . Having the scaling exponent one can easily convert the ambient pressure $\eta(T)$ data into $\eta(TV^{\gamma})^{-1}$ representation and describe it by means of the Avramov entropic model. These are last requirements that have to be satisfied to generate isothermal $\eta(P)$ dependences. The parameters determined during described fitting procedures can be next applied to simulate the viscosity behavior of any ionic conductor and under any T – P conditions. The schematic description of such a method is illustrated in Fig. 4.24.

Here, it should be stressed that the results of such a procedure (solid gray lines in Fig. 4.23c) correspond well with the experimentally determined points (open

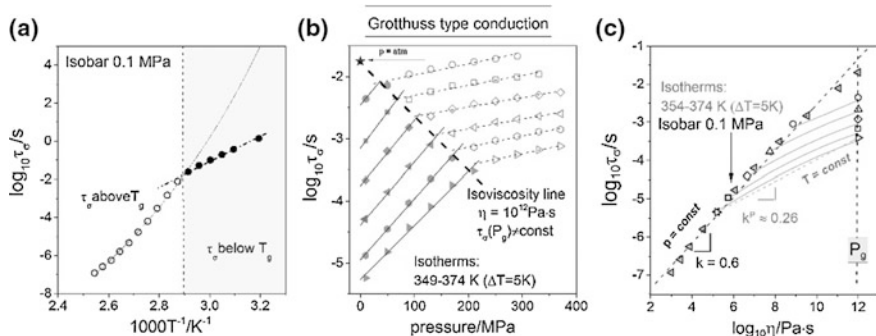


Fig. 4.23 The temperature (a) and pressure (b) dependences of conductivity relaxation times of protic ionic liquid carvedilol dihydrogen phosphate. Panel (c) presents the Stokes–Einstein plot for this compound. The data were taken from Ref. [8]

symbols in Fig. 4.23c), i.e., with the values of η measured at 0.1 MPa and estimated at P_g (it is widely accepted that η at T_g (or P_g) is in the order of 10^{12} Pa s).

4.5.2 How to Quantify Decoupling Between the Charge Transfer and Structural/Segmental Relaxation in Ionic Conductors?

As it appeared in preceding section the exponent k in Stokes–Einstein (or Walden) relation can be successfully applied to quantify the decoupling of charge transfer and structural/segmental relaxation in ionic conductors. However, it is not the only possibility. An alternative way to evaluate the interplay between charge transport and the structural dynamics is to calculate the decoupling index defined as the ratio of the electrical relaxation time τ_σ and the structural relaxation time τ_α at T_g .

$$R_\tau(T_g) \equiv \log[\tau_\alpha(T_g)/\tau_\sigma(T_g)] \quad (4.30)$$

To determine $\tau_\alpha(T)$, and consequently to calculate precisely the decoupling index, the rheological experiment can be performed in addition to conductivity measurements. An alternative experimental method that can be employed to determine $\tau_\alpha(T)$ is temperature-modulated differential scanning calorimetry (TMDSC). However, if we assume that τ_α at T_g is equal to 10^2 s Eq. 4.30 can be simplified to the following form:

$$R_\tau(T_g) \equiv 2 - \log[\tau_\sigma(T_g)] \quad (4.31)$$

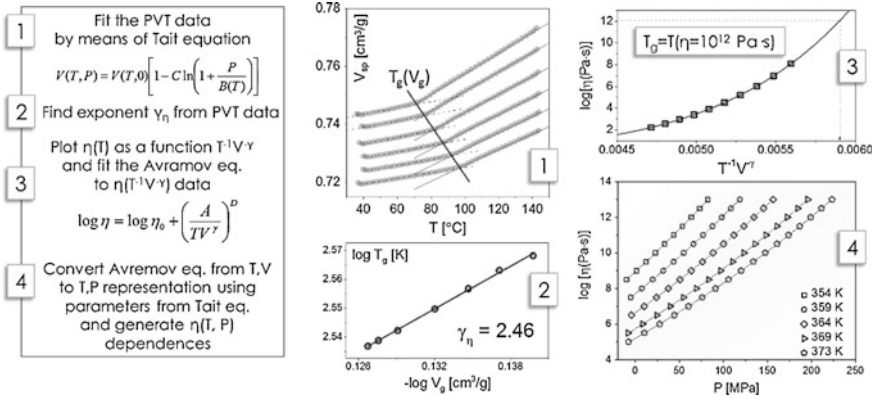


Fig. 4.24 The procedure used for determination of $\eta(T, P)$ dependence close to the liquid–glass transition

Consequently, one can calculate the decoupling index having only the experimentally determined $\tau_\sigma(T)$ dependence.

In the case of fully coupled systems for which dc-conductivity mimics, the structural dynamics, $R_\tau(T_g)$, is equal to zero. However, for strongly decoupled conductors characterized by the time scale of charge transfer much shorter than that of the mass diffusion the decoupling index is higher than one. This is because the value of τ_σ at T_g can be markedly lower than hundreds or thousands of seconds as reported for conventional ionic and molecular glass-forming liquids. The difference between the time scale of charge diffusion and structural dynamics is well visible when the τ_σ and τ_α are plotted together as a function of temperature (see Fig. 4.25).

The values of decoupling index determined for a number of ionic materials are collected in Fig. 4.26. From the examples presented in this plot it becomes obvious that there is a relation between the Stokes–Einstein coefficient (k) and $R_\tau(T_g)$. Namely, k as well as $R_\tau(T_g)$ are close to unity in the case of fully coupled systems, i.e., when the conductivity is associated with the translational diffusion of ions (like in the case of lidocaine acetate (No. 2) or lidocaine docusate (No. 3)). On the other hand, as the separation between τ_σ and τ_α increases (i.e., $R_\tau(T_g)$ is getting higher) the exponent k becomes lower.

As it was demonstrated in previous section squeezing of ionic system can be used to control the degree of decoupling effectively. Thus, it is important to introduce a new parameter which will determine the pressure sensitivity of the decoupling index in the limit of ambient pressure. It is defined as the derivative of $\log R_\tau$ with respect to pressure. Since the structural relaxation time at T_g is pressure independent, the following expression has been obtained:

$$d \log R_\tau / dP = -d \log \tau_{cross} / dP \tag{4.32}$$

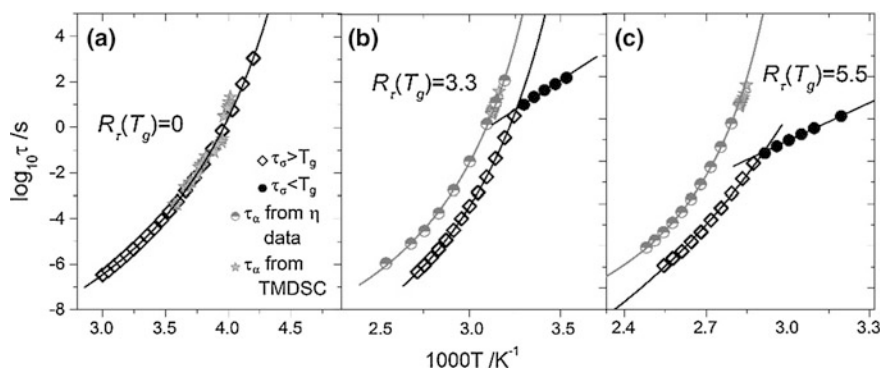


Fig. 4.25 The temperature dependences of conductivity and structural relaxation times for three different protic ionic systems: **a** lidocaine docusate, **b** procainamide HCl, **c** carvedilol H_2PO_4 . The rheological τ_α is evaluated from the Maxwell relation $\tau_\alpha = \eta/g\omega$, by using the measured viscosity and τ_α from TMDSC. Experimental data were taken from Refs. [13, 14, 70]

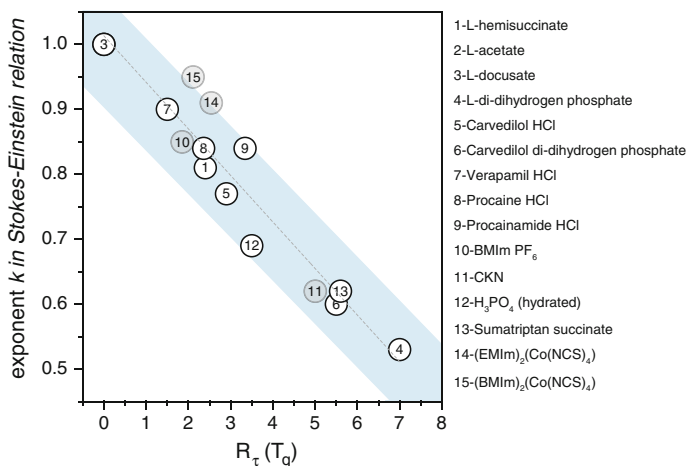


Fig. 4.26 The relation between the Stokes–Einstein coefficient (k) and decoupling index $Rr(T_g)$. *Closed circles* indicate aprotic ionic conductors while *open ones* protic materials. L = lidocaine. Data were taken from Refs. [8, 13, 14, 16, 28, 79, 83]

To visualize the differences in the pressure sensitivity of the decoupling index between various ionic systems the $\log \tau_{\text{cross}}$ has been plotted as a function of pressure in Fig. 4.27. In order to determine the value of $d \log R_r/dP$ coefficient, the linear regression analysis of data presented in Fig. 4.27 has to be performed. Interestingly, the slope of $\log \tau_{\text{cross}}(P)$ dependence of lidocaine hemisuccinate, carvedilol HCl and sumatriptan succinate is practically the same. Therefore, these protic ionic systems are characterized by similar values of $d \log R_r/dP$ coefficient ($\approx 0.003 \text{ M Pa}^{-1}$). On the other hand, more than

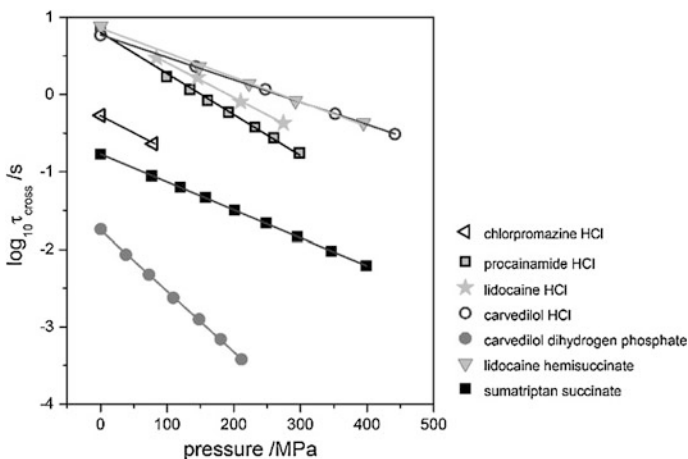


Fig. 4.27 The values of conductivity relaxation times at glass transition pressures determined for various protic ionic systems. Experimental data were taken from Ref. [79]

two times higher $d \log R_c/dP$ parameter (0.0079 M P^{-1}) characterizes the mobility of charge carriers in carvedilol dihydrogen phosphate.

4.5.3 How to Control the Time Scale Separation Between Charge and Mass Diffusion?

As it was explained in preceding sections there are two main reasons why the time scale separation between charge transfer and structural dynamics occurs in ionic systems. Namely,

- the significant contribution of proton hopping to dc-conductivity,
- different contribution of cations and anions to ionic conductivity and structural dynamics.

It is generally known that ionic systems with enhanced proton conductivity are widely viewed as promising electrolytes in fuel cells and batteries. Nevertheless, a major limitation toward their commercialization lies in the factors controlling the fast proton hopping in anhydrous conditions [84]. Despite a number of papers dealing with this issue a lot of problems still require clarification. Below the most important factors that were found to influence the enhanced proton conductivity in anhydrous ionic materials are highlighted.

An important aspect that should be taken into account when discussing the factors affecting the proton conduction is the ionization degree of given system. It is reflected in the value of ΔpK_a defined as the difference between pK_a of base and acid that were mixed together to prepare protic ionic material [85]. It is well known

that if a PIL is synthesized using strong acid and a strong base, the proton is fixed very tightly to the base and the possibility of the reverse process toward uncharged components is negligible. Then, the value of ΔpK_a is large. However, depending on the reacting compounds, the proton transfer may be less than complete and then the obtained liquid is a mixture of ions (BH^+ and A^-) and neutral species (HA and B) with relatively low value of ΔpK_a parameter (~ 1).



As postulated by Angell et al. [86] and McFarlane et al. [87] the value of ΔpK_a parameter should be high enough to meet the criteria of IL. However, as indicated in a number of literature reports, it cannot be too exaggerated since nonconductive species fulfill the role of efficient H^+ -carriers. This is the reason why in the group of protic ionic liquids one can find a number of incompletely ionized materials that can be classified as superprotic liquids and glasses, especially in the condition of high compression. An example illustrating the abovementioned idea is an enhanced proton conductivity of imidazolium bis(trifluoromethylsulfonyl)imide ([Im][TFSI]) observed only when the sample is prepared with a threefold excess of imidazole [88].

However, one should note that not every chemical compound works as effective proton transmitter. Among others the proton acceptor/donor capability of acid/base taken to prepare PIL is of great importance. As an example one can recall acetate anion. Generally, it readily accepts proton and acquires the form of energetically preferred neutral acetic acid that is characterized by poor donor capability. As a consequence, at ambient and elevated pressure conditions the conductivity of acetate salts should be governed by translational diffusion of large molecular species and therefore τ_α and τ_σ are expected to be fully coupled. To confirm this statement, the perfect agreement between dielectric and calorimetric data of lidocaine acetate is illustrated in Fig. 4.23. Considerably different conductivity trace occurs if cation/anion possesses the moieties actively involved in charge transfer (e.g., hydroxyl groups) and it readily accepts and releases protons. In the light of existing theoretical and experimental data, one can state that at least two proton active moieties in the anion are required to enhance the Grotthuss conduction through the ionic system. However, the more proton donors in chemical structure, the more efficient charge transfer is expected. Therefore, as an effective proton mediator one can classify for example succinate, citrate or phosphate structures [13]. Surprisingly, the PILs containing sulfonate groups, frequently regarded as a source of high proton conductivity of polymer electrolyte membranes, are usually characterized by the less pronounced decoupling between charge and mass diffusion. This is because the hemisulfate salts, just like hydrochlorides or hydrobromides, are composed solely of ions ($\Delta pK_a > 13$) with strongly reduced affinity of system to deionization.

Interestingly, among the protic ionic systems studied so far the largest separation between charge transfer and structural diffusion (around 7 decades) was found in the case of lidocaine di(dihydrogen phosphate) (see Fig. 4.28).

The origin of such huge excess proton conductivity in this ionic glass-former is twofold. The first one involves the unique chemical structure of lidocaine cation. It was found that this molecule very easily undergoes an internal bond rearrangement and thus facilitates the proton transfer within the Grotthuss mechanism (see Fig. 4.29a). According to the density functional theory (DFT) calculations, such ionic amide-imidic acid conversion is able to reduce the energy required for charge transfer between cations and anions by even four times. On the other hand, the phosphate molecules on their own were found to form a crown-like layered, self-assembled arrangement which looks like a promising route of proton transfer with possibly a lower activation energy due to already partial deprotonation and strong dislocation of protons (see Fig. 4.29b). All these factors together with highly expanded H-bonded make the phosphate salt of lidocaine highly efficient proton conductor.

In the discussion presented above, the factors influencing the decoupling phenomenon in low-molecular protic ionic liquids were considered. However, this paragraph will be dedicated to “decoupled” aprotic polymerized ionic liquids. As it was mentioned previously in the case of macromolecular ionic systems, the contribution of cations and anions to the global dynamics and dc-conductivity can be totally different that is manifested by the crossed $\tau_\sigma(T)$ dependence. This is completely understandable when we take into account that cations or anions are covalently bound to the polymer chain. However, to understand the factors governing decoupling phenomenon the architecture of polymeric system should be considered. As illustrated in Fig. 4.30 in the group of polymerized ionic liquid with NTf₂ anion, the largest decoupling index $R_{\sigma dc}(T_g)$ is observed when short side groups are clipped to the polymer chain. On the other hand, in the case of polyIL

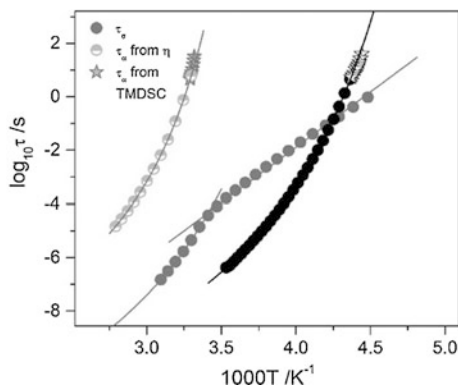


Fig. 4.28 Temperature dependence of structural and conductivity relaxation times for two PILs, lidocaine di-(dihydrogen phosphate) *gray symbols*, and lidocaine acetate (*black symbols*). *Filled circles*: conductivity relaxation time τ_σ recorded by means of a dielectric setup. *Stars*: structural relaxation time τ_α from TMDSC measurements. *Half-filled symbols*: structural relaxation time τ_α from viscosity measurements, calculated according to the Maxwell relation: $\tau_\alpha = \eta/G$. The data were taken from Ref. [13]

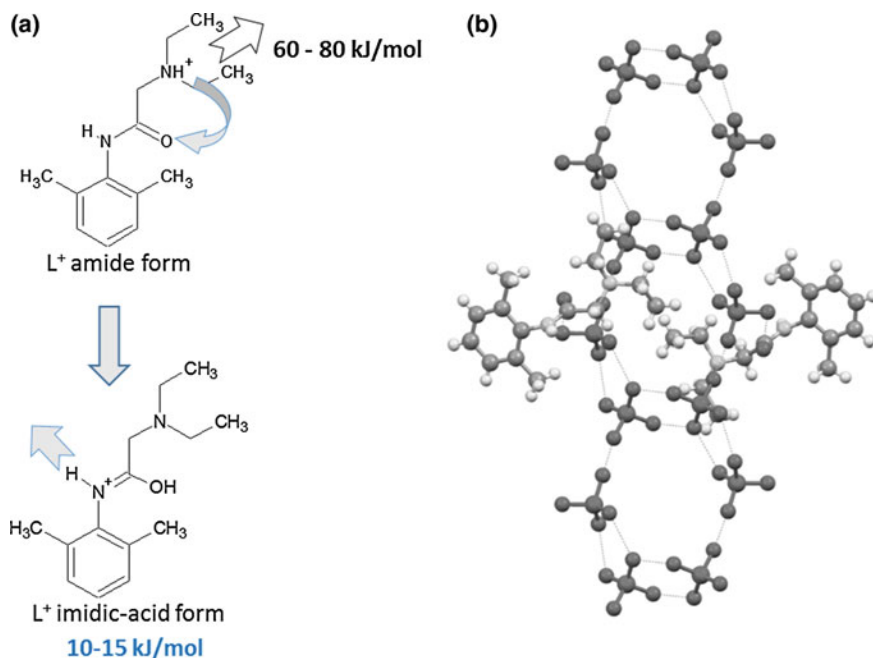


Fig. 4.29 **a** Intramolecular proton transfer within the lidocaine structure; **b** crown cluster motifs of phosphate molecules along c axis with exemplar amide "bridges" of lidocaine molecules

with long ionomers the segmental dynamics and charge transfer are fully coupled. Additionally, one can notice that the simpler is the chemical structure of anion the more enhanced is the diffusion of negative charge in polycationic system. Thus, to increase the decoupling of dc-conductivity and segmental dynamics the polymerized ionic systems with relatively short side chains and small counterions should be synthesized.

4.6 Conclusions and Perspectives

As it has been demonstrated in this chapter high-pressure conductivity measurements provide a valuable inside into ion dynamics of various ionic glass-formers. From $\sigma_{dc}(T, P, V)$ dependences we are able to:

- describe the pressure sensitivity of given IL,
- assess the ability of ionic system to H-bonds formation,
- identify the conductivity mechanism in ionic conductors,
- estimate the contribution of thermal and density fluctuations to the ions mobility.

Fig. 4.30 The decoupling index $R_{\sigma_{dc}}(T_g)$ calculated for several polymerized ionic liquids. Data were taken from Ref. [75]

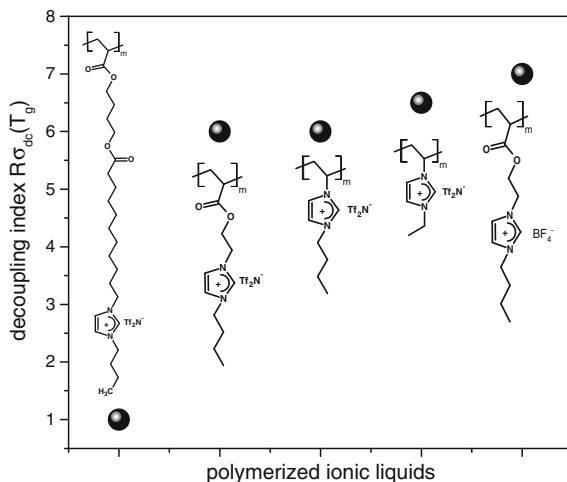
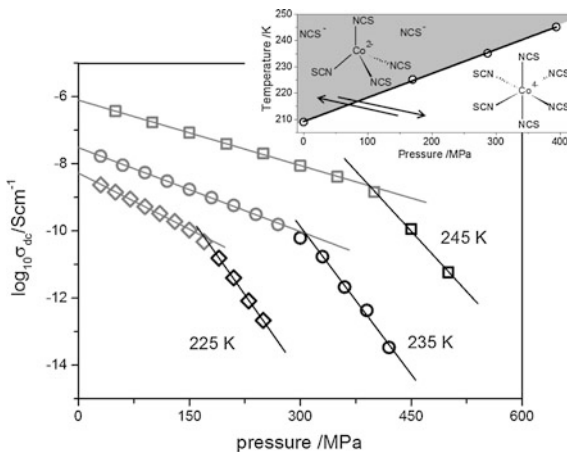


Fig. 4.31 The effects of pressure on dc-conductivity behavior of $[P_{6,6,6,14}][SCN] + Co(SCN)_2$ (10:1). Data were taken from Ref. [89]



However, recently it has been demonstrated that switching in cobalt coordination from tetrahedral to octahedral in phosphonium based ionic liquid is accompanied by the conductivity changes, and therefore it can be easily monitored at ambient as well as elevated pressure by means of dielectric spectroscopy. Moreover, it was found that such coordination changes can be induced not only by isobaric cooling but also during the isothermal compression. This is clearly reflected in pressure dependence of dc-conductivity presented in Fig. 4.31 [89].

Acknowledgement Z.W. and M.P. are deeply grateful for the financial support by the National Science Centre within the framework of the Opus 8 project (Grant No. DEC-2014/15/B/ST3/04246).

References

1. Kremer F, Schoenhals A (2003) *Broadband dielectric spectroscopy*. Springer, Berlin
2. Mizuno F, Belieres JP, Kuwata N, Pradel A, Ribes M, Angell CA (2006) *J Non-Cryst Solids* 352:5147–5155
3. Paluch M, Wojnarowska Z, Goodrich P, Jacquemin J, Pionteck J, Hensel-Bielowka S (2015) *Soft Matter* 11:6520
4. Guggenheim EA (1937) *Trans Faraday Soc* 33:607
5. Paluch M, Grzybowska K, Grzybowski A (2007) *J Phys Condens Matter* 19:205117
6. Williams G (1964) *Trans Faraday Soc* 60:1548
7. Pensado AS, Padua AAH, Comunas MJP, Fernandez J (2008) *J Phys Chem B* 112:5563–5574
8. Wojnarowska Z, Wang Y, Pionteck J, Grzybowska K, Sokolov AP, Paluch M (2013) *Phys Rev Lett* 111:225703
9. Fontanella JJ, Edmondson CA, Wintersgill MC, Wu Y, Greenbaum SG (1996) *Macromolecules* 29(14):4944–4951
10. Swiety-Pospiech A, Wojnarowska Z, Hensel-Bielowka S, Pionteck J, Paluch M (2013) *J Chem Phys* 138:204502
11. Swiety-Pospiech A, Wojnarowska Z, Pionteck J, Pawlus S, Grzybowski A, Hensel-Bielowka S, Grzybowska K, Szulc A, Paluch M (2012) *J Chem Phys* 136:224501
12. Floudas G, Paluch M, Grzybowski A, Ngai KL (2011) *Molecular dynamics of glass-forming systems—effect of pressure*. Springer, Berlin, Heidelberg
13. Wojnarowska Z, Paluch KJ, Shoifet E, Schick C, Tajber L, Knapik J, Włodarczyk P, Grzybowska K, Hensel-Bielowka S, Verevkin SP, Paluch M (2015) *J Am Chem Soc* 137:1157–1164
14. Wojnarowska Z, Roland CM, Swiety-Pospiech A, Grzybowska K, Paluch M (2012) *Phys Rev Lett* 108:015701
15. Pimenov A, Lunkenheimer P, Rall H, Kohlhaas R, Loidl A, Bohmer R (1996) *Phys Rev E* 54:676
16. Wojnarowska Z, Kołodziejczyk K, Paluch K, Tajber L, Grzybowska K, Ngai KL, Paluch M (2013) *Phys Chem Chem Phys* 15:9205–9211
17. Roland CM, Psurek T, Pawlus S, Paluch M (2003) *J Polym Sci Part B Polym Phys* 41:3047–3052
18. Hensel-Bielowka S, Paluch M, Ziolo J, Roland CM (2002) *J Phys Chem B* 106:12459–12463
19. Roland CM, Hensel-Bielowka S, Paluch M, Casalini R (2005) *Rep Prog Phys* 68:1405
20. Casalini R, Paluch M, Roland CM (2003) *J Phys Cond Matter* 15:859
21. Roland CM (2011) *Viscoelastic behavior of rubbery materials*. Oxford Scholarship Print ISBN-13: 9780199571574
22. Patkowski A, Gapinski J, Meier G (2004) *Colloid Polym Sci* 282:874–881
23. Williams E, Angell CA (1977) *J Phys Chem* 81:3
24. MacFarlane D, Scheirer J, Smedley SI (1986) *J Phys Chem* 90:10
25. Wojnarowska Z, Jarosz G, Grzybowski A, Pionteck J, Jacquemin J, Paluch M (2014) *Phys Chem Chem Phys* 16:20444
26. Paluch M, Haracz S, Grzybowski A, Mierzwa M, Pionteck J, Rivera-Calzada A, Leon C (2010) *J Phys Chem Lett* 1:987
27. Jarosz G, Mierzwa M, Ziolo J, Paluch M (2011) *J Phys Chem B* 115:12709–12716
28. Wojnarowska Z, Knapik J, Rams-Baron M, Jedrzejowska A, Paczkowska M, Krause A, Cielecka-Piontek J, Jaworska M, Lodowski P, Paluch M (2015) *Mol. Pharmaceutics*. doi:10.1021/acs.molpharmaceut.5b00911
29. Wojnarowska Z, Grzybowska K, Grzybowski A, Paluch M, Kaminski K, Włodarczyk P, Adrjanowicz K, Pionteck J (2010) *J Chem Phys* 132:094506
30. Bendler JT, Fontanella JJ, Shlesinger MF, Wintersgill MC, (2001) *Electrochimica Acta* 46:10–11, 15, 1615–1621

31. Wojnarowska Z, Knapik J, Jacquemin J, Berdzinski S, Strehmel V, Sangoro JR (2015) Paluch M. doi:[10.1021/acs.macromol.5b02130](https://doi.org/10.1021/acs.macromol.5b02130)
32. Sippel P, Lunkenheimer P, Krohns S, Thoms E, Loidl A (2015) *Sci. Rep.* 5:13922
33. Leys J et al (2008) *J Chem Phys* 128:064509
34. Leys J et al (2010) *J Chem Phys* 133:034503
35. Pitawala J et al (2009) *J Phys Chem B* 113:10607–10610
36. Wojnarowska Z, Paluch M, Grzybowski A, Adrjanowicz K, Grzybowska K, Kaminski K, Wlodarczyk P, Pionteck J (2009) *J Chem Phys* 131:104505
37. Pinkert A, Ang KL, Marsh KN, Panga S (2011) *Phys Chem Chem Phys* 13:5136–5143
38. Wojnarowska Z, Ngai KL, Paluch M (2014) *Phys Rev E* 90:062315
39. Pensado AS, Padua AAH, Comunas MJP, Fernandez J (2008) *J Phys Chem B* 112:5563
40. Paluch M (2014) *Phys Chem Chem Phys* 16:20444
41. Grzybowski A, Grzybowska K, Paluch M, Swiety A, Koperwas K (2011) *Phys Rev E* 83:041505
42. Grzybowski A, Haracz S, Paluch M, Grzybowska K (2010) *J Phys Chem B* 114:11544
43. Grzybowski A, Koperwas K, Paluch M (2014) *J Chem Phys* 140:044502
44. Paluch M, Casalini R, Roland CM (2002) *Phys Rev B* 66:092202
45. Naoki M, Endou H, Matsumoto K (1987) *J Phys Chem* 91:4169
46. Roland CM, Hensel-Bielowka S, Paluch M, Casalini R (2006) *Rep Prog Phys* 68:1405
47. Ferrer ML, Lawrence C, Demirjin BG, Kivelson D, Alba-Simonesco C (1998) *G. Tarjus. J Chem Phys* 109:8010
48. Casalini R, Roland CM (2003) *J Chem Phys* 119:4052
49. Avramov I, Non-Cryst J (2000) *Solids* 262:258
50. Casalini R, Mohanty U, Roland CM (2006) *J Chem Phys* 125:014505
51. Avramov I, Milchev A, Non-Cryst J (1988) *Solids* 104:253
52. Casalini R, Mohanty U, Roland CM (2006) *J Chem Phys* 125:014505
53. Lopez ER, Pensado AS, Comunas MJP, Padua AAH, Fernandez J, Harris KR (2011) *J Chem Phys* 134:144507
54. Roland CM, Bair S, Casalini R (2006) *J Chem Phys* 125:124508
55. Pensado AS, Padua AAH, Comunas MJP, Fernandez J (2008) *J Phys Chem B* 112:5563
56. Grzybowski A, Paluch M, Grzybowska K, Haracz S (2010) *J Chem Phys* 133:161101
57. Canongia Lopes JNA, Padua AAH (2006) *J Phys Chem B* 110:3330
58. Yoshizawa M, Xu W, Angell CA (2003) *J Am Chem Soc* 125:15411
59. Walden P (1914) *Bull Acad Imp Sci* 1800:405–422
60. Angell CA, Byrne N, Belieres JP (2007) *Acc Chem Res* 40:1228
61. Wojnarowska Z, Wang Y, Paluch KJ, Sokolov AP, Paluch M (2014) *Phys Chem Chem Phys* 16:9123
62. Wang Y et al (2013) *J Phys Chem B* 117:8003–8009
63. Agmon N (1995) The grothhuss mechanism. *Chem Phys Lett* 244:456–462
64. Marx D (2006) *Chem Phys Chem* 7:1848–1870
65. Mangiatordi GF, Laage D, Adamo C (2013) *Mater Chem A* 1:7751–7759
66. Dippel Th, Kreuer KD, Lassègues JC, Rodriguez D (1993) *Solid State Ionics* 61:41–46
67. Kreuer KD, Fuchs A, Ise M, Spaeth M, Maier J (1998) *Electrochim Acta* 43:1281–1288
68. Mangiatordi GF, Butera V, Russo N, Laage D, Adamo C (2012) *Phys Chem Chem Phys* 21:10910–10918
69. Wojnarowska Z, Knapik J, Diaz M, Ortiz A, Ortiz I, Paluch M (2014) *Macromolecules* 47:4056–4065
70. Wojnarowska Z, Roland CM, Kolodziejczyk K, Swiety-Pospiech A, Grzybowska K, Paluch M (2012) *J Phys Chem Lett* 3:1238
71. Angell CA (1983) *Solid State Ionics* 9–10:3–16
72. Angell CA (1986) *Solid State Ionics* 18–19:72–88
73. Paluch M, Wojnarowska Z, Hensel-Bielowka S (2013) *Phys Rev Lett* 110:1
74. Guchhait B, Daschakraborty S, Biswas R (2012) *J Chem Phys* 136:174503

75. Choi U H, Ye Y, Salas de la Cruz, D, Liu W, Winey KI, Elabd YA, Runt J, Colby RH (2014) *Macromolecules* 47(2):777–790
76. Nakamura K, Fukao K, Inoue T (2012) *Macromolecules* 2012(45):3850–3858
77. Nakamura K, Fukao K (2013) *Polymer* 54:3306–3313
78. Sangoro JR, Iacob C, Agapov AL, Wang Y, Berdzinski S, Rexhausen H, Strehmel V, Friedrich C, Sokolov AP, Kremer F (2014) *Soft Matter* 10:3536–3540
79. Wojnarowska Z, Paluch M (2015) *J Phys Condens Matter* 27:073202
80. Harris K, Kanakubo M (2012) *Faraday Discuss* 154:425–438
81. Harris KR, Woolf LA, Kanakubo M (2005) *J Chem Eng Data* 50:1777
82. Schlosser H, Ferrante J (1989) *J Phys Condens Matter* 1:2727
83. Hensel-Bielowka S, Wojnarowska Z, Dzida M, Zorębski E, Zorębski M, Geppert-Rybczyńska M, Peppel T, Grzybowska K, Wang Y, Sokolov AP, Paluch M (2015) *J Phys Chem C* 119:20363–20368
84. Armand M, Endres F, MacFarlane DR, Ohno H, Scrosati B (2009) *Nat Mater* 8:621–629
85. Miran MS, Kinoshita H, Yasuda T, Susan MA, Watanabe M (2012) *Phys Chem Chem Phys* 14:5178–5186
86. Beleieres JP, Angell CA (2007) *J Phys Chem B* 111:4926–4937
87. MacFarlane DR, Forsyth M, Izgorodina EI, Abbott AP, Annat G, Fraser K (2009) *Phys Chem Chem Phys* 11:4962
88. Hoarfrost ML, Tyagi M, Segalman RA, Reimer JA (2012) *J Phys Chem B* 116:8201–8209
89. McCourt E, Wojnarowska Z, Jacquemin J, Nockemann P, Manyara HG, Hawelek L, Paluch M (2016) *J Chem Phys C* doi:[10.1021/acs.jpcc.6b01325](https://doi.org/10.1021/acs.jpcc.6b01325)

Chapter 5

Glassy Dynamics and Charge Transport in Polymeric Ionic Liquids

Falk Frenzel, Wolfgang H. Binder, Joshua Rume Sangoro
and Friedrich Kremer

Abstract While glassy dynamics and (ionic) charge transport coincide in low-molecular weight ionic liquids (ILs), they are widely decoupled in corresponding polymeric systems. This is studied by means of broadband dielectric spectroscopy (BDS) for monovalent and bivalent telechelic polyisobutylene (PIB) carrying the Ionic Liquid (IL)-like cationic headgroup (N,N,N-triethylammonium or 1-methylpyrrolidinium) with Br, NTf₂, OTf or pTOS as anions, as well as for neat and polymerized 1-vinyl-3-pentylimidazolium bis-(trifluoromethylsulfonyl) imide (PVIM NTf₂). The former shows a wealth of dielectrically active fluctuations in contrast to the latter, where only the dynamic glass transition is observed. Additionally a conductivity relaxation originating from charge transport in the IL-like moieties and a weak electrode polarization caused by the accumulation of mobile charge carriers at the metal interfaces is found. In both systems molecular fluctuations and charge transport are well separated from each other thereby enabling accurate description of the net conductivity within the framework of the effective medium approximation for the PIB-based systems.

5.1 Introduction

Ionic liquids (ILs), defined as molten salts below temperatures of 100 °C, have attracted significant interest over the last 20–30 years due to their exceptional

F. Frenzel (✉) · F. Kremer
Institute of Experimental Physics I, Leipzig University, Linnéstrasse 5,
04103 Leipzig, Germany
e-mail: falk.frenzel@physik.uni-leipzig.de

W.H. Binder
Institute of Chemistry, Macromolecular Chemistry, Martin-Luther-University
Halle-Wittenberg, Von-Danckelmann-Platz 4, 06120 Halle, Germany

J.R. Sangoro
Department of Chemical and Biomolecular Engineering, University of Tennessee,
Knoxville, TN 37996-2200, USA

features as high ion conductivity, wide electrochemical and thermal stability, negligible vapor pressure, non-flammability, and interesting properties as solvents [1–6]. Their versatile application areas already comprise a continuously accumulating billion dollar market [7, 8], most notable in fields as analytics [9], solvents [4, 10, 11] and catalysts [12, 13], electro- and biochemistry [14–16], engineering [17, 18]; but also medicine [19, 20], aeronautics [21] and space technology [22, 23]. The physical, chemical, and engineering properties of low-molecular weight ILs are well explored due to a multitude of experimental studies based on broadband dielectric spectroscopy [24–33], differential scanning and AC calorimetry [34, 35], ellipsometry [36], infrared and fluorescence spectroscopy [37–40], nuclear magnetic resonance [41, 42], neutron and X-ray scattering [43–46], atomic force and electron microscopy [47–50]. For several applications the liquid-like character of low-molecular weight ILs is an essential disadvantage; this led to the development of polymeric ionic liquids (PIL), synthesized by either polymerizing neat ILs or incorporating IL-headgroups into classical polymers. In this chapter representatives of both synthetic routes are analyzed concerning their fundamental properties such as molecular dynamics, charge transport, and mesoscopic structure and compared with their low-molecular weight counterparts. This will lead to a new level of understanding of the properties of PILs paving the way for novel applications, e.g., gas and liquid separator membranes, fuel cell membranes or as cheap and innovative polyelectrolyte for a new generation of batteries or super capacitors.

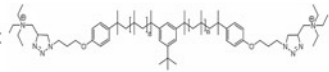
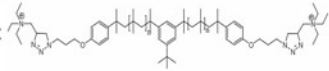
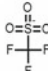
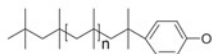

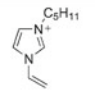
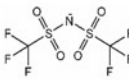
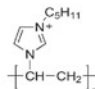
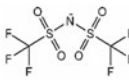
5.2 Experimental Details

Polyisobutylene-based PILs (Scheme 5.1) were synthesized as described in reference [51–56]; PVIM NTf₂ and its polymeric equivalent (Scheme 5.1) as specified in [57, 58].

Broadband dielectric spectroscopy (BDS) measurements were carried out using a high-resolution Novocontrol Alpha-analyzer in combination with a Quatro temperature controller ensuring absolute thermal stability of ≤ 1 K by using pure nitrogen as heating agent within a frequency window of 10^{-2} – 10^7 Hz and a temperature range from 200 to 400 K.

Rheology analysis was performed for (Poly)NTf₂ using a TA Instruments Advanced Rheometric Expansion System (ARES). Dynamic frequency sweep measurements to determine zero shear viscosity η_0 in an 8 mm parallel-plate geometry (thickness of 1 mm) were applied at constant deformation in a radial frequency range of 0.01–100 rad/s. By extrapolating the dynamic viscosity to the low frequency limit the zero shear viscosity was determined.

Differential scanning calorimetry (DSC) measurements were conducted using a Q100 DSC from TA Instruments for monomeric and polymeric PVIM NTf₂, and by a Netzsch 204 F1 phoenix 240-120-0142-L instrument for the PIB-PILs; both with heating/cooling rates of 10 K/min. The calorimetric glass transition temperature was taken as a midpoint of a heat capacity change from the glassy to the liquid state.

cationic unit	counteranion	T_g
BVNEt ₃ : 	Br: Br [⊖]	209K
BVNEt ₃ : 	OTf: 	209K
PIB-N ₃ : 	-----	204K
Py-IL: 	Br: Br [⊖]	216K
PVIM: 	NTf ₂ : 	197K
poly PVIM: 	NTf ₂ : 	329K

Scheme 5.1 Chemical structures

Transmission electron microscopy (TEM) measurements with PIB-PILs were recorded using a LEO 912 Omega from Zeiss with 120 kV. This technique involves the preparation of ultra-thin (800 nm) cryo-cut (-60°C) slices. The measurements were performed without using contrast agents.

5.3 Results and Discussion

Based on the Maxwell's equations, BDS measures both, charge transport (of mobile charge carriers) and polarization of dipoles (chemically bound partial charges); additionally it is a sensitive tool to study macroscopic polarization phenomena, like electrode polarization. With these features BDS is ideally suited to analyze and to compare the dielectric properties of low-molecular weight and polymeric ILs. While the former were in the scientific focus over the last 10–15 years, the new class of polymeric ILs or polymerized ILs is much less explored. The synthesis of PILs is either achieved by polymerizing neat ILs (e.g., Poly PVIM NTf₂) or functionalizing polymers with IL-like head groups (e.g., PIB-PILs). Representatives of both approaches will be analyzed in the course of this chapter.

Electrode polarization (I) is caused by the accumulation of immobilized mobile charge carriers at the interface between sample material and metal electrodes [28]. One of the key dielectric signatures of electrode polarization (EP) is the steep

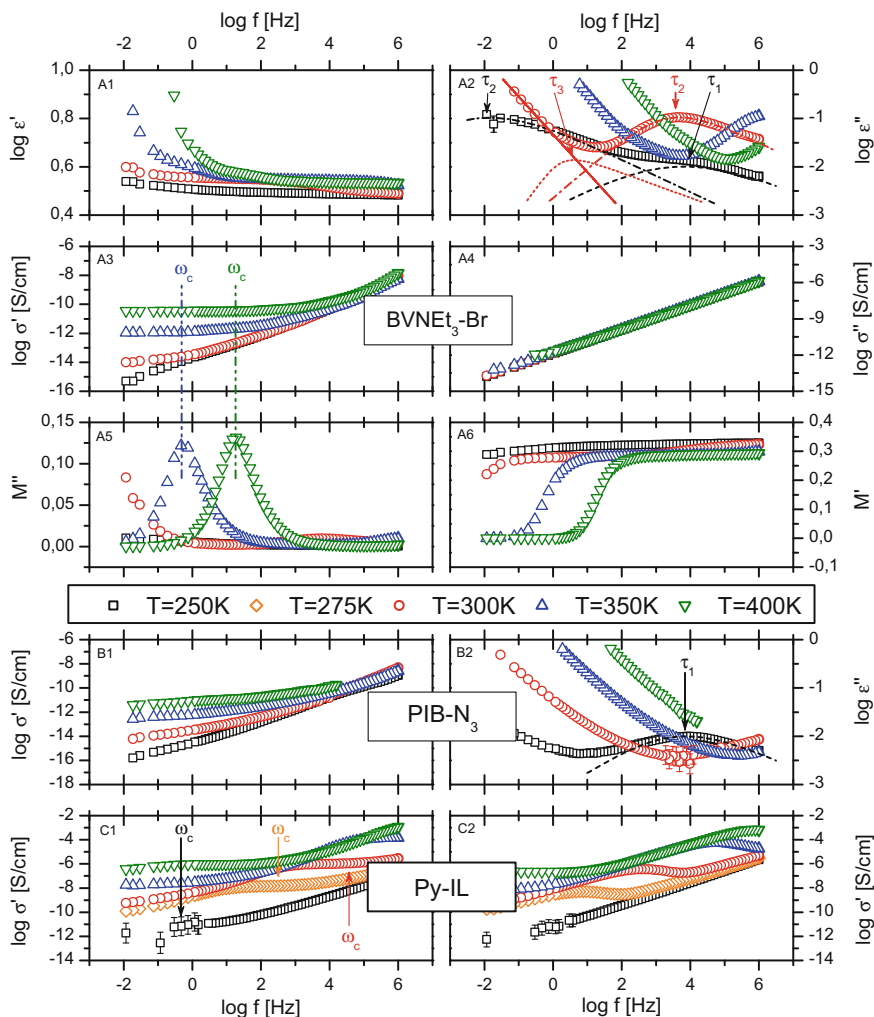


Fig. 5.1 Real and imaginary part of the complex dielectric function ($\epsilon^* = \epsilon' - i\epsilon''$), complex conductivity ($\sigma^* = \sigma' + i\sigma''$) and complex modulus ($M^* = M' + iM''$) versus frequency of the sample BVNEt₃-Br (A) and, in addition, $\sigma'(f)$ and $\epsilon''(f)$ for the polymeric backbone PIB-N₃ (B) and the neat IL-like moiety Py-IL (C) at four different temperatures as indicated. **A1** The increase on the low frequency side is caused by electrode polarization. **A2** The dielectric spectrum exhibits a conductivity contribution (*straight line*) and three separated molecular relaxation processes. The latter are described by Havriliak-Negami-fits (*dotted, dashed-dotted, dashed line*) with relaxation times τ_1, τ_2, τ_3 respectively. **A3** Subtracting the relaxation processes exposes the dc-conductivity plateaus σ_0 as well as the critical frequencies ω_c , which mark the onset of the power law dependence $\sigma' : \omega^x$. **B1** and **C1** Comparison between the polymeric- and IL-like moieties demonstrates the investigated PILs as a composition of two contrasting components with widely varying conductivities. **B2** The relaxation process proves to be identical with τ_1 in **A2**. The error bars are smaller than the symbols, unless otherwise indicated. The logarithm is to base 10

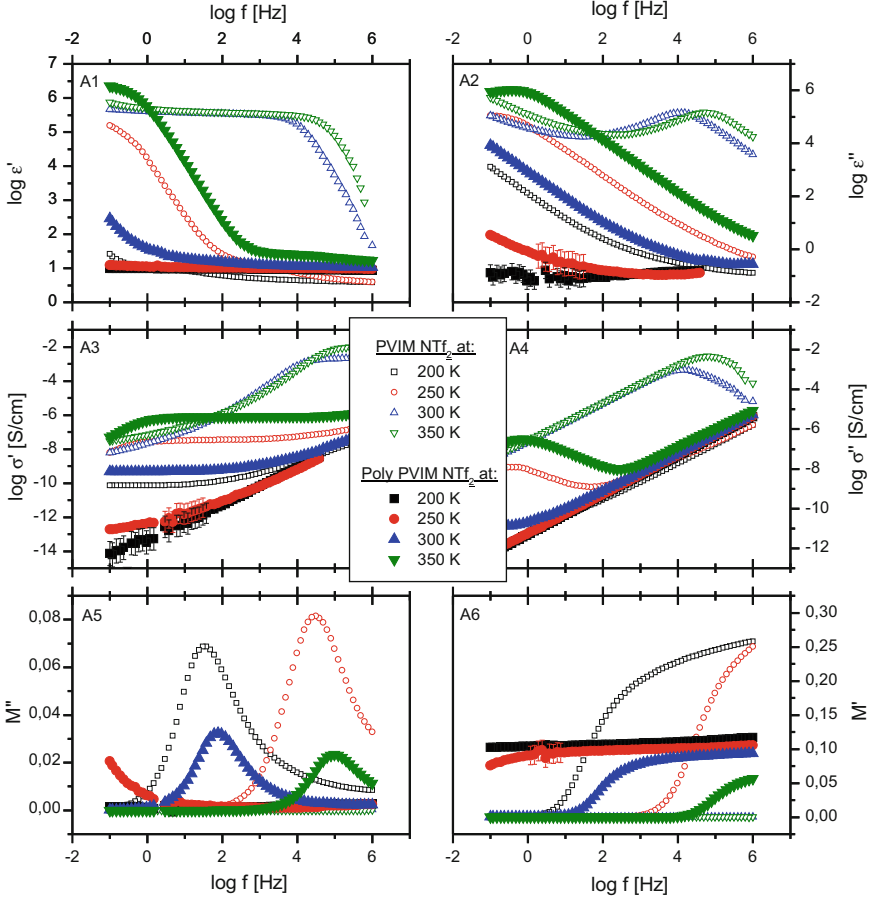


Fig. 5.2 Real and imaginary part of the complex dielectric function ($\epsilon^* = \epsilon' - i\epsilon''$), complex conductivity ($\sigma^* = \sigma' - i\sigma''$) and complex modulus ($M^* = M' - iM''$) versus frequency of the sample PVIM NTf₂ (open symbols) and its polymeric equivalent Poly PVIM NTf₂ (filled symbols) at four different temperatures as indicated. The error bars are smaller than the symbols, unless otherwise indicated. The logarithm is to base 10

increase in $\epsilon'(\omega, T)$ versus frequency (Figs. 5.1A1 and 5.2A1) at lower frequencies and elevated temperatures and as a distinct peak on the low frequency side of $\sigma''(\omega, T)$ versus frequency (Figs. 5.1A4 and 5.2A4) [28]. It is remarkable that although EP shows up for both PIL-systems, it is by decades more pronounced for the polymerized PVIM NTf₂. This is explained by the low IL-volume fraction of 6.5 % for PIB-PILs and consequently, lower ionic conductivity. Charge transport (II) shows up in the dc-conductivity plateau σ_0 on the intermediate frequency regime in $\sigma'(\omega, T)$ versus frequency (Figs. 5.1A3 and 5.2A3) or as distinct slope at elevated temperatures in $\epsilon''(\omega, T)$ versus frequency (Figs. 5.1A2 and 5.2A2). From the frequency dependence of $\sigma'(\omega, T)$ the characteristic hopping rate ω_c of the charge

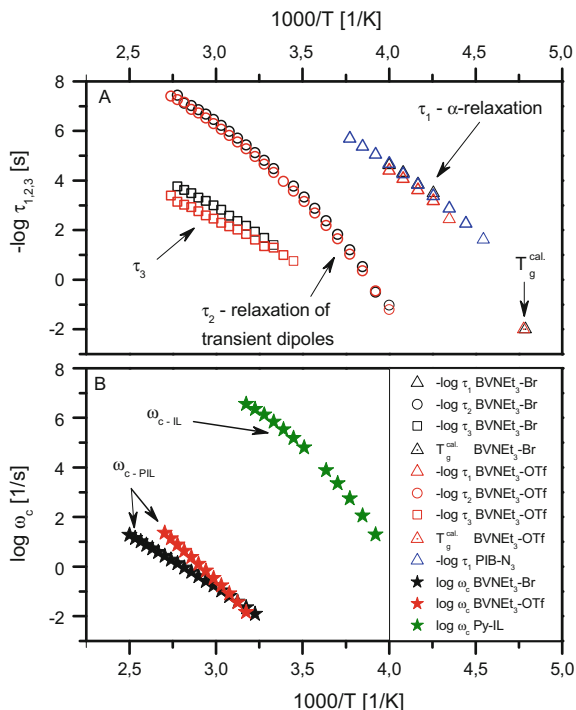


Fig. 5.3 Activation plot of the structural fluctuations of the samples BVNET₃-Br (black) and BVNET₃-OTf (red) and the polymeric counterpart without IL-like functionalization (PIL-N₃—blue) (A), as well as the conductivity relaxations of the former and the neat IL Py-IL (green) (B). Compared are the α -relaxations τ_1 of the two PILs with the sole structural relaxation of the PIB-N₃ (triangles) and the calorimetrically measured glass transition temperature T_g^{cal} , the fluctuations of the IL-like moieties τ_2 (circles) with the charge transport relaxation of the Py-IL ω_{c-IL} , as well as the latter with conductivity relaxation of both PILs ω_{c-PIL} (star)

carriers can be deduced as given by the onset of the power law dependence $\sigma' \sim \omega^\chi$ ($\chi \leq 1$). Molecular relaxation processes (III) are best analyzed in $\epsilon''(\omega, T)$ versus frequency representation (Figs. 5.1A2 and 5.2A2). For the series of PIB-PILs three well-separated processes can be quantitatively analyzed by Havriliak–Negami functions. To determine their molecular origin, the PIB-PIL-subunits PIB-N₃ (polymeric moiety—Fig. 5.1B) and Py-IL (IL-like functionalization—Fig. 5.1C) are measured in comparison. The first is characterized by one α -relaxation, being assigned to the dynamic glass transition (DGT) of the polymer, the latter is typical for low-molecular weight ILs, particularly by the more than 4 decades higher dc-conductivity σ_0 compared to the PIL BVNET₃ – Br (Fig. 5.1A3 vs. C1).

The thermal activations for both, the molecular and conductivity relaxation processes, are presented in Fig. 5.3 (PIB-PILs) and Fig. 5.4 (Poly PVIM NTf₂). The first system reveals three molecular fluctuations. The τ_1 -relaxation is VFT-like and identical for all PIB-PILs under study, as well as for the polymeric moiety

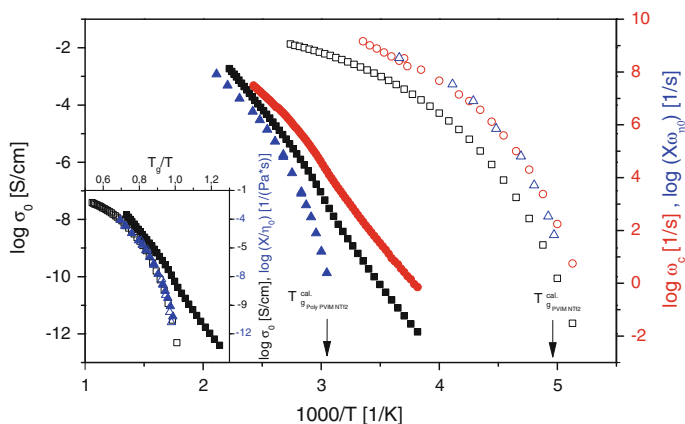


Fig. 5.4 Activation-plot of the dc-conductivity σ_0 (black squares), the charge carrier hopping rate ω_c (red circles) and inverse shear viscosity hopping rate ω_{η_0} (blue triangles) of the low-molecular weight ILPVIM NTF₂ (open symbols) and its polymeric equivalent Poly PVIM NTF₂ (filled symbols). For the neat IL the charge carrier hopping rate and the viscosimetrically measured dynamic glass transition coincide and scale with the calorimetrically determined glass transition temperature T_g^{cal} . This is in pronounced contrast to the polymeric counterpart. *Inset*: Activation plot of the dc-conductivity σ_0 and inverse shear viscosity $\frac{1}{\eta_0}$ for the same samples; rescaled to T_g^{cal} . The constant X (with values 1 and $10^{4.43}$ for the IL and PIL due to different molecular weights) is employed for direct comparison of the temperature dependence of $\frac{1}{\eta_0}$

PIB-N₃. Its extrapolation agrees well with the calorimetrically measured glass transition temperature. Thus, this process is assigned to the dynamic glass transition (DGT) and denoted α -relaxation. The second relaxation process τ_2 shows a VFT-like behavior as well. It is assigned to the fluctuation of transient dipoles by the following four facts: (i) compared to the α -relaxation, this process is slowed down by typical 6–7 decades, which indicates its origin to bigger molecular units than the benzene-oxygen group of the τ_1 -relaxation; (ii) the conductivity relaxation of the IL-like moiety is nearly identical with the τ_2 -relaxation of the PIL; (iii) this relaxation correlates linearly to the dc-conductivity σ_0 (inset Fig. 5.5); and (iv) its spectral position strongly depends on the anion–cation composition [56]. Besides these two processes a third relaxation τ_3 is found; it is tentatively assigned to fluctuations of IL-like aggregations. Comparing Poly PVIM NTF₂ to the PIB-PILs, the former exhibits only one relaxation process, which is measured as zero shear viscosity relaxation by rheology. This process has a VFT-like thermal activation for the monovalent as well as for the polymeric PVIM NTF₂; their ω_{η_0} deviate by typically 10 decades. Both relaxations scale approximately with the DSC-measured glass transition temperature T_g^{cal} ; for Poly PVIM NTF₂ the factor X is 1, the extrapolated $T_g(0.01\text{Hz}) = 312$ K compared to the calorimetric glass transition temperature $T_g^{\text{cal}} = 329$ K; for PVIM NTF₂ the factor X is $10^{4.43}$, the extrapolated

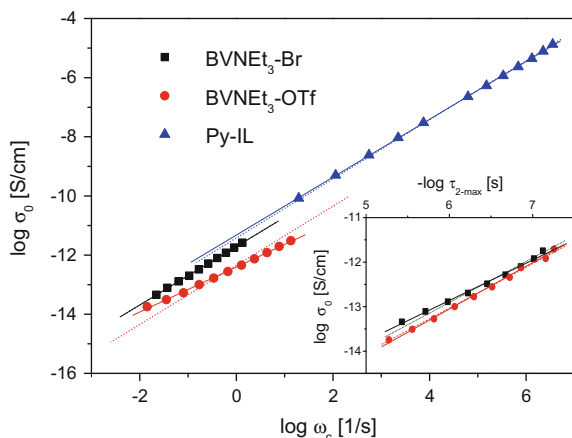


Fig. 5.5 Barton–Namikawa–Nakajima relation $\sigma_0 \sim \omega_c$ between the dc-conductivity σ_0 and the charge carrier relaxation ω_c for the samples BVNET₃-Br (*black*) and BVNET₃-OTf (*red*), as well as for Py-IL. The *inset* shows the correlation of σ_0 with the structural fluctuation τ_{2-max} of transient dipole dynamics in the IL-like PIL-moiety. The *straight lines* describe a linear fit, the *dotted lines* indicate slope 1

$T_g^{\text{cal.}}(0.01 \text{ Hz}) = 188 \text{ K}$ compared to the calorimetric glass transition temperature $T_g^{\text{cal.}} = 197 \text{ K}$ (Figs. 5.4).

The charge transport as observed in the sample PVIM NTf₂ fulfills the Barton–Namikawa–Nakajima (BNN)-relation $\sigma_0 \sim \omega_c$ over 9 decades as expected for a low-molecular weight IL (Fig. 5.6). This is also confirmed for its polymeric equivalent, which points towards the same underlying charge transport mechanism in both

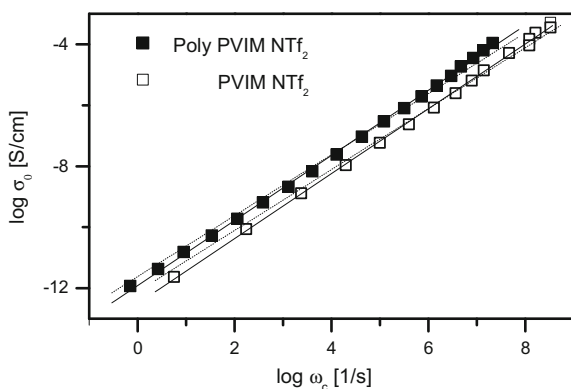


Fig. 5.6 Barton–Namikawa–Nakajima relation $\sigma_0 \sim \omega_c$ between the dc-conductivity σ_0 and the charge carrier relaxation ω_c for the samples PVIM NTf₂ (*open squares*) and Poly PVIM NTf₂ (*filled squares*). The *straight lines* describe a linear fit, the *dotted lines* indicate slope 1

systems. It is remarkable that despite this similarity the conductivity relaxation ω_c of the IL is VFT-like over its whole activation range, while for the PIL ω_c is VFT-like for temperatures above T_g and becomes Arrhenius-like below (Fig. 5.4). Comparing the dc-conductivities σ_0 and the inverse zero shear viscosity η_0 with respect to T_g one observes the strong decoupling of charge transport from glassy dynamics below the calorimetric glass transition temperature as well (inset Fig. 5.4). It is exceptional that rescaled to T_g , the dc-conductivity σ_0 is consistently higher for the polymeric PVIM NTf₂; it reaches a 10^4 higher value at T_g . This demonstrates that by decreasing the temperature to T_g , where the segmental dynamics is dramatically slowed down, the charge transport mechanism remains effective. Therefore, it must be decoupled from glassy dynamics. To obtain a deeper insight to the charge transport mechanism one can initially assume that all ions of the sample contribute equally to the dc-conductivity, i.e., $\sigma_0 = \sigma_{\text{cation}} + \sigma_{\text{anion}}$. For the current PIL the diffusivity of the cations could be measured by pulsed field gradient (PFG) ¹H-NMR due to its molecular structure. At 400 K the diffusion coefficient was measured as $D = 1.5 \pm 0.3 \cdot 10^{-13} \text{ m}^2\text{s}^{-1}$. Assuming that all cations would contribute in their stoichiometric number density $n = 2 \cdot 10^{25} \text{ m}^{-3}$ to the charge transport, the highest possible conductivity value would result in $\sigma = n \cdot q \cdot \mu = \frac{n \cdot q^2 \cdot D}{k_B \cdot T} \approx 1.4 \cdot 10^{-7} \text{ S/cm}$, which is more than 500 times lower than the dc-conductivity measured by BDS. This implies, that the cations contribute much less to the overall conductivity, which agrees well with the physical picture, that the polymeric backbones form a more or less rigid, but porous-like matrix, where the anions diffuse through free volume channels [58]. While the so far discussed PIL Poly PVIM NTf₂ is quite conductive with a σ_0 -value of $\approx 7.5 \cdot 10^{-5} \text{ S/cm}$ at 400 K, PIB-PILs deliver typical values of $\sigma_0 \approx 10^{-10} - 10^{-11} \text{ S/cm}$ in this temperature range (Fig. 5.1A3). Although the BNN-relation holds for this system over many decades too, a decoupling between glassy dynamics and charge transport is already indicated by the about 6 decades faster relaxation rate of the polymeric moiety compared to the IL-like headgroup of the PILs. To describe the net conductivity of such an heterogeneous material, an effective medium approximation (EMA) is used. For that the Bruggeman equation

$$\frac{\sigma_{\text{EMA}}^* - \sigma_{\text{IL}}^*}{\sigma_{\text{pol.}}^* - \sigma_{\text{IL}}^*} \left(\frac{\sigma_{\text{pol.}}^*}{\sigma_{\text{EMA}}^*} \right)^{\frac{1}{3}} = 1 - \phi \quad (5.1)$$

is employed, to take into account the phase-separation between spherical micelles consisting of IL-like headgroups having a high electrical conductivity embedded in an insulating polymeric matrix. σ_{EMA}^* is thereby the complex net conductivity of the effective medium, σ_{IL}^* the complex conductivity of the IL-like micelles, $\sigma_{\text{pol.}}^*$ the complex conductivity of the polymeric matrix and ϕ the micelle volume fraction, which is about 6.5 %. This formula solved for the complex net conductivity reads as follows:

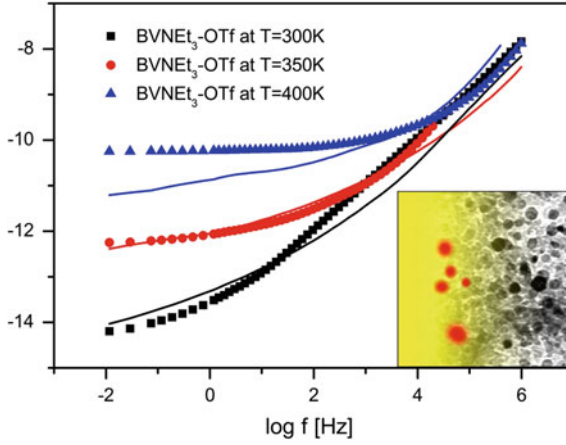


Fig. 5.7 Real part of the complex conductivity σ' versus frequency for BVNEt₃-OTf at three different temperatures as indicated. The *straight lines* represent fits within the Effective Medium Approximation (EMA) using the Bruggeman formula. *Inset* TEM image for NEt₃-Br with illustration of the Bruggeman theory according to Eq. (5.1). The *yellow area* displays the polymeric matrix, *red circles* the spherical IL-like micelles

$$\sigma_{\text{EMA}}^* = \frac{\left[\frac{1}{3} \left(\frac{(1-\phi)(\sigma_{\text{pol}}^* - \sigma_{\text{IL}}^*)}{\sigma_{\text{pol}}^{\frac{1}{3}}} \right)^3 \right]^{\frac{1}{3}}}{\left[9 \left(\frac{(1-\phi)(\sigma_{\text{pol}}^* - \sigma_{\text{IL}}^*)}{\sigma_{\text{pol}}^{\frac{1}{3}}} \right) \sigma_{\text{IL}}^* + 3^{\frac{1}{2}} \left[27 \left(\frac{(1-\phi)(\sigma_{\text{pol}}^* - \sigma_{\text{IL}}^*)}{\sigma_{\text{pol}}^{\frac{1}{3}}} \right)^6 \sigma_{\text{IL}}^{*2} - 4 \left(\frac{(1-\phi)(\sigma_{\text{pol}}^* - \sigma_{\text{IL}}^*)}{\sigma_{\text{pol}}^{\frac{1}{3}}} \right)^9 \right]^{\frac{1}{3}} \right]^{\frac{1}{3}} + \frac{\left[9 \left(\frac{(1-\phi)(\sigma_{\text{pol}}^* - \sigma_{\text{IL}}^*)}{\sigma_{\text{pol}}^{\frac{1}{3}}} \right) \sigma_{\text{IL}}^* + 3^{\frac{1}{2}} \left[27 \left(\frac{(1-\phi)(\sigma_{\text{pol}}^* - \sigma_{\text{IL}}^*)}{\sigma_{\text{pol}}^{\frac{1}{3}}} \right)^6 \sigma_{\text{IL}}^{*2} - 4 \left(\frac{(1-\phi)(\sigma_{\text{pol}}^* - \sigma_{\text{IL}}^*)}{\sigma_{\text{pol}}^{\frac{1}{3}}} \right)^9 \right]^{\frac{1}{3}} \right]^{\frac{1}{3}}}{2^{\frac{1}{3}} \cdot 3^{\frac{2}{3}}} + \sigma_{\text{IL}}^* \quad (5.2)$$

For $\sigma_{\text{IL}}^* \gg \sigma_{\text{pol}}^*$ it can be approximated as:

$$\sigma^* = \frac{\sigma_{\text{pol}}^*}{(1-\phi)^3}. \quad (5.3)$$

This equation displays a good agreement with the BDS-measured data as shown in Fig. 5.7; deviations in the low frequency range are caused by the influence of electrode polarization.

Aware of the mesoscopic morphology, which is additionally proven to be phase separated by TEM (inset Fig. 5.7), one can estimate the length-scale on which charge transport takes place. Due to the strongly decoupled dynamics between polymeric and IL-like moieties and the sharp contours in the TEM image, it is

possible to treat the IL-headgroups as an assembly of neat ILs, that diffuse through the polymeric matrix. Using the well known diffusion constants D for low-molecular weight ILs from the literature [25, 26] and the time span t of the applied electrical field, it is possible to calculate the diffusion length S of the IL assemblies through the polymeric matrix $S = \sqrt{6 \cdot D \cdot t} \approx 7 - 12$ nm. These values are in the range of the micelle diameter ($S \approx 13$ nm), but much smaller than the mean separation ($S \approx 40$ nm) between two of them. Additionally one has to consider that the IL-like moieties are covalently bound to the polymeric units, which will decrease the mobility and S further. In summary, it is expected, that charge transport takes primarily place within the IL-like micelles, whilst the glassy dynamics is determined by relaxations of the polymeric matrix.

While low-molecular weight ILs are usually homogeneous materials, a variety of publications report different PILs as nanophase separated. Yuan, Mecerreyes and Antonietti [59] discuss this segregation into IL-like micelles or nanoworms for samples like poly (3-alkyl-1-vinylimidazolium bromide) as an effect of the chemistry between hydrophilic IL-like moieties and hydrophobic polymeric mainchains. Ye et al. [55] investigated the separation phenomena as a weak effect for PIL-block-copolymers like poly (MMA-b-MEBIm-NTf₂) and Koebe et al. [60] for a series of crosslinked ILs, in addition to the PIB-PILs under study. These structural inhomogeneities might be the origin of the decoupling of charge transport and molecular dynamics, which is observed for many PIL representatives. Wojnarowska et al. [61] demonstrated the decoupling effect below the calorimetric glass transition temperature T_g for PBuVIm-NTf₂ by increasing pressure up to 400 MPa (and therefore shifting T_g) and for [HSO₃ – BVIm]⁺ OTf⁻ [62] under the systematic influence of an increasing water content, whereas the charge transport is proven to be in accord with the Grotthuss mechanism. Choi et al. [63] observed the decoupling between dc-conductivity σ_0 and molecular relaxation ω_α below T_g for PILs, by varying the linker length between polymeric backbone and IL-headgroup; Shiro Seki et al. [64] for PMMA network polymers with dissolved EMIm-NTf₂ and Agapov et al. [65] even determined a decoupling coefficient between ionic conductivity and structural relaxation for classical polyelectrolytes (e.g., P2VP, PMMA, PVC, PEO), which are no PILs but belong to a very similar class of materials. In summary, one has to conclude that in contrast to low-molecular weight ILs, a segregation into nanophases between IL-like and polymeric parts is observed for a wide variety of different PILs. While this effect is weak for the sample MMA-b-MEBIm-NTf₂ [55] it dominates the physical properties in the PIB-PILs under study due to huge differences in the volume fraction between the polymeric and IL-like moieties ($\phi_{V-IL} = 6.5\%$, $\phi_{V-pol.} = 93.5\%$). It seems to be self-evident to conclude, that according to this phase-separation, charge transport and molecular dynamics do no longer coincide for the PIB-PILs. This effect for most of the systems specified above is observed below the calorimetric glass transition temperature T_g . That can be explained by the physical picture that the polymeric backbones and their IL-like headgroups are essentially frozen below T_g , while the counterions diffuse further through free volume channels. Exceptions for this rule

are again the PIB-PILs, which are so strongly decoupled, that the relaxation processes for both, the polymeric chain and the IL-like headgroup, are well observable in the dielectric spectra by a separation of typically 6 decades, as well as the charge carrier hopping rates ω_c , which differ by about 9 decades and show different thermal activations.

5.4 Conclusion

In summary, two different systems from the same class of materials are analyzed concerning their physical properties of molecular dynamics, charge transport and mesoscopic structure. By means of broadband dielectric spectroscopy, rheology, nuclear magnetic resonance, and transmission electron microscopy, it is possible to get a deep insight into polymeric ionic liquids, its subunits and monomeric equivalents. It is remarkable—that compared to low-molecular weight ILs and according to the literature glassy dynamics and charge transport are strongly decoupled in PILs due to their mesoscopic phase-separated structure, which can be quantitatively described within a frame work of the effective medium approximation.

Acknowledgments FF and FK are grateful for the financial support from the Deutsche Forschungsgesellschaft under the DFG-project “Neue Polymermaterialien auf der Basis von funktionalisierten ionischen Flüssigkeiten für Anwendungen in Membranen ‘Erkenntnistransfer-Projekt’” (KR 1138/24-1). WHB thanks the SFB TR 102, project A3; and FK within the project B08, for financial support. FK gratefully acknowledges financial support from the Deutsche Forschungsgemeinschaft under the DFG SPP 1191 Priority Program on Ionic Liquids. JRS acknowledges the National Science Foundation for financial support through the award number DMR-1508394. The authors gratefully acknowledge Sylvia Goerlitz for TEM investigations, Clement Appiah for DSC measurements, Jörg Kärger and Rustem Vallulin for PFG NMR measurements on the PVIM NTf₂ and its polymeric equivalent.

References

1. Ghandi K (2014) A review of ionic liquids, their limits and applications. *Green Sustain Chem* 4
2. Aparicio S, Atilhan M, Karadas F (2010) Thermophysical properties of pure ionic liquids: review of present situation. *Ind Eng Chem Res* 49:9580–9595
3. Wang X, Chi Y, Mu T (2014) A review on the transport properties of ionic liquids. *J Mol Liq* 193:262–266
4. Rogers RD, Seddon KR (2003) Ionic liquids-solvents of the future? *Science* 302:792–793
5. Armand M, Endres F, MacFarlane DR, Ohno H, Scrosati B (2009) Ionic-liquid materials for the electrochemical challenges of the future. *Nat Mater* 8:621–629
6. Jessop PG, Heldebrandt DJ, Li X, Eckert CA, Liotta CL (2005) Green chemistry: Reversible nonpolar-to-polar solvent. *Nature* 436:1102

7. Ionic Liquid Technologies, Markets, Applications, Companies and Developments Worldwide 2012 to 2020 by years and 2030; 2015
8. Dámaso JFF (2011) Recovery of ionic liquids from aqueous solution by nanofiltration. Ph.D. thesis, Universität Bremen
9. Tholey A, Heinzle E (2006) Ionic (liquid) matrices for matrix-assisted laser desorption/ionization mass spectrometry-applications and perspectives. *Anal Bioanal Chem* 386:24–37
10. Chiappe C, Pieraccini D (2005) Ionic liquids: solvent properties and organic reactivity. *J Phys Org Chem* 18:275–297
11. Cull S, Holbrey J, Vargas-Mora V, Seddon K, Lye G (2000) Room-temperature ionic liquids as replacements for organic solvents in multiphase bioprocess operations. *Biotechnol Bioeng* 69:227–233
12. Wilkes JS (2004) Properties of ionic liquid solvents for catalysis. *J Mol Catal A: Chem* 214:11–17 (Ionic Liquids as promising alternative media for organic synthesis and catalysis)
13. Wasserscheid P, Keim W (2000) Ionic Liquids—new “solutions” for transition metal catalysis. *Angew Chem Int Ed* 39:3772–3789
14. Ohno H (2011) *Electrochemical aspects of ionic liquids*. Wiley
15. Galiński M, Lewandowski A, Stepniak I (2006) Ionic liquids as electrolytes. *Electrochim Acta* 51:5567–5580
16. Fukaya Y, Iizuka Y, Sekikawa K, Ohno H (2007) Bio ionic liquids: room temperature ionic liquids composed wholly of biomaterials. *Green Chem* 9:1155–1157
17. Seddon KR (1997) Ionic liquids for clean technology. *J Chem Technol Biotechnol* 68:351–356
18. Zhao H (2006) Innovative applications of ionic liquids as “Green” engineering liquids. *Chem Eng Commun* 193:1660–1677
19. Smiglak M, Pringle J, Lu X, Han L, Zhang S, Gao H, MacFarlane D, Rogers R (2014) Ionic liquids for energy, materials, and medicine. *Chem Commun* 50:9228–9250
20. Hough WL, Smiglak M, Rodriguez H, Swatloski RP, Spear SK, Daly DT, Pernak J, Grisel JE, Carliss RD, Soutullo MD et al (2007) The third evolution of ionic liquids: active pharmaceutical ingredients. *New J Chem* 31:1429–1436
21. Gao H, Joo Y-H, Twamley B, Zhou Z, Shreeve J (2009) Hypergolic ionic liquids with the 2,2-dialkyltriazanium cation. *Angew Chem* 121:2830–2833
22. Schneider S, Hawkins T, Ahmed Y, Rosander M, Hudgens L, Mills J (2011) Green bipropellants: hydrogen-rich ionic liquids that are hypergolic with hydrogen peroxide. *Angew Chem Int Ed* 50:5886–5888
23. Singh RP, Verma RD, Meshri DT, Shreeve JM (2006) Energetic nitrogen-rich salts and ionic liquids. *Angew Chem Int Ed* 45:3584–3601
24. Sangoro JR, Serghei A, Naumov S, Galvosas P, Kärger J, Wespe C, Bordusa F, Kremer F (2008) Charge transport and mass transport in imidazolium-based ionic liquids. *Phys Rev E* 77
25. Sangoro JR, Iacob C, Naumov S, Valiullin R, Rexhausen H, Hunger J, Buchner R, Strehmel V, Karger J, Kremer F (2011) Diffusion in ionic liquids: the interplay between molecular structure and dynamics. *Soft Matter* 7:1678–1681
26. Sangoro JR, Kremer F (2012) Charge transport and glassy dynamics in ionic liquids. *Acc Chem Res* 45:525–532
27. Sangoro JR, Mierzwa M, Iacob C, Paluch M, Kremer F (2012) Brownian dynamics determine universality of charge transport in ionic liquids. *RSC Adv* 2:5047–5050
28. Serghei A, Tress M, Sangoro JR, Kremer F (2009) Electrode polarization and charge transport at solid interfaces. *Phys Rev B* 80:184301
29. Krause C, Sangoro JR, Iacob C, Kremer F (2010) Charge transport and dipolar relaxations in imidazolium-based ionic liquids. *J Phys Chem B* 114:382–386
30. Wojnarowska Z, Wang Y, Pionteck J, Grzybowska K, Sokolov AP, Paluch M (2013) High pressure as a key factor to identify the conductivity mechanism in protic ionic liquids. *Phys Rev Lett* 111:225703

31. Wojnarowska Z, Kolodziejczyk K, Paluch KJ, Tajber L, Grzybowska K, Ngai KL, Paluch M (2013) Decoupling of conductivity relaxation from structural relaxation in protic ionic liquids and general properties. *Phys Chem Chem Phys* 15:9205–9211
32. Jarosz G, Mierzwa M, Ziolo J, Paluch M, Shiota H, Ngai KL (2011) Glass transition dynamics of room-temperature ionic liquid 1-methyl-3-trimethylsilylmethylimidazolium tetrafluoroborate. *J Phys Chem B* 115:12709–12716
33. Sippel P, Lunkenheimer P, Krohns S, Thoms E, Loidl A (2015) Importance of liquid fragility for energy applications of ionic liquids. *Sci Rep*
34. Holbrey JD, Seddon KR (1999) The phase behaviour of 1-alkyl-3-methylimidazolium tetrafluoroborates; ionic liquids and ionic liquid crystals. *J Chem Soc Dalton Trans* 2133–2140
35. Kuang D, Wang P, Ito S, Zakeeruddin SM, Grätzel M (2006) Stable mesoscopic dye-sensitized solar cells based on tetracyanoborate ionic liquid electrolyte. *J Am Chem Soc* 128:7732–7733
36. Nishi N, Kasuya K, Kakiuchi T (2012) Surface structure of a hydrophobic ionic liquid probed by spectroscopic ellipsometry. *J Phys Chem C* 116:5097–5102
37. Cammarata L, Kazarian S, Salter P, Welton T (2001) Molecular states of water in room temperature ionic liquids. *Phys Chem Chem Phys* 3:5192–5200
38. Fumino K, Wulf A, Ludwig R (2008) The cation—Anion interaction in ionic liquids probed by far-infrared spectroscopy. *Angew Chem Int Ed* 47:3830–3834
39. Werner JH, Baker SN, Baker GA (2003) Fluorescence correlation spectroscopic studies of diffusion within the ionic liquid 1-butyl-3-methylimidazolium hexafluorophosphate. *Analyst* 128:786–789
40. Yang Z, Pan W (2005) Ionic liquids: green solvents for nonaqueous biocatalysis. *Enzyme Microbial Technol* 37:19–28
41. Remsing RC, Swatloski RP, Rogers RD, Moyna G (2006) Mechanism of cellulose dissolution in the ionic liquid 1-n-butyl-3-methylimidazolium chloride: a ¹³C and ^{35/37}Cl NMR relaxation study on model systems. *Chem Commun* 1271–1273
42. Akihiro Noda MW (2001) Kikuko Hayamizu Pulsed-Gradient Spin-Echo ¹H and ¹⁹F NMR ionic diffusion coefficient, viscosity, and ionic conductivity of non-chloroaluminate room-temperature ionic liquids. *J Phys Chem B* 105:4603–4610
43. Hardacre C, Holbrey JD, Mullan CL, Youngs TGA, Bowron DT (2010) Small angle neutron scattering from 1-alkyl-3-methylimidazolium hexafluorophosphate ionic liquids ([Cnmim][PF₆], n = 4, 6, and 8). *J Chem Phys* 133
44. Hardacre C, Holbrey JD, McMath SEJ, Bowron DT, Soper AK (2003) Structure of molten 1,3-dimethylimidazolium chloride using neutron diffraction. *J Chem Phys* 118:273–278
45. Bradley AE, Holbrey CHJD, Johnston S, McMath SEJ, Nieuwenhuyzen M (2002) Small-angle X-ray scattering studies of liquid crystalline 1-Alkyl-3-methylimidazolium salts. *Chem Mater* 14:629–635
46. Katayanagi H, Hayashi S, Hamaguchi, HO, Nishikawa K (2004) Structure of an ionic liquid, 1-n-butyl-3-methylimidazolium iodide, studied by wide-angle X-ray scattering and Raman spectroscopy. *Chem Phys Lett* 392:460–464
47. Bhushan B, Palacio M, Kinzig B (2008) AFM-based nanotribological and electrical characterization of ultrathin wear-resistant ionic liquid films. *J Colloid Interface Sci* 317:275–287
48. Endres F, Borisenko N, El Abedin SZ, Hayes R, Atkin R (2012) The interface ionic liquid (s)/electrode (s): In situ STM and AFM measurements. *Faraday Discuss* 154:221–233
49. Kuwabata S, Kongkanand A, Oyamatsu D, Torimoto T (2006) Observation of Ionic liquid by scanning electron microscope. *Chem Lett* 35:600–601
50. Arimoto S, Sugimura M, Kageyama H, Torimoto T, Kuwabata S (2008) Development of new techniques for scanning electron microscope observation using ionic liquid. *Electrochimica Acta* 53:6228–6234, {ELECTRIFIED} {INTERFACES} Selection of papers from the International Conference (ICEI 2007) 24–29 June 2007, Sahoro, Hokkaido, Japan

51. Binder WH, Kunz MJ, Kluger C, Hayn G, Saf R (2004) Synthesis and Analysis of telechelic polyisobutylenes for hydrogen-bonded supramolecular pseudo-block copolymers. *Macromolecules* 37:1749–1759
52. Adekunle O, Herbst F, Hackethal K, Binder WH (2011) Synthesis of nonsymmetric chain end functionalized polyisobutylenes. *J Polym Sci, Part A: Polym Chem* 49:2931–2940
53. Hackethal K, Binder WH (2013) polyisobutylene based supramolecular networks via living carbocationic polymerization. *Macromolecular Symposia* 323:58–63
54. Morgan DL, Martinez-Castro N, Storey RF (2010) End-Quenching of TiCl₄-catalyzed Quasiliving Polyisobutylene with Alkoxybenzenes for direct chain end functionalization. *Macromolecules* 43:8724–8740
55. Ye Y, Choi J-H, Winey KI, Elabd YA (2012) Polymerized Ionic liquid block and random copolymers: effect of weak microphase separation on ion transport. *Macromolecules* 45:7027–7035
56. Frenzel F, Folikumah MY, Schulz M, Anton AM, Binder WH, Kremer F (2016) Molecular dynamics and charge transport in polymeric polyisobutylene-based ionic liquids. *Macromolecules*
57. Tan, JS, Sochor AR (1981) Chain characteristics and counterion binding of poly (N-vinylimidazole) and its protonated and quaternized salts. *Macromolecules* 14:1700–1706
58. Sangoro JR, Iacob C, Agapov AL, Wang Y, Berdzinski S, Rexhausen H, Strehmel V, Friedrich C, Sokolov AP, Kremer F (2014) Decoupling of ionic conductivity from structural dynamics in polymerized ionic liquids. *Soft Matter* 10:3536–3540
59. Yuan J, Mecerreyes D, Antonietti M (2013) Poly(ionic liquid)s: an update. *Prog Polym Sci* 38:1009–1036
60. Koebe M, Drechsler M, Weber J, Yuan J (2012) Crosslinked Poly(ionic liquid) nanoparticles: inner structure, size, and morphology. *Macromol Rapid Commun* 33:646–651
61. Wojnarowska Z, Knapik J, Diaz M, Ortiz A, Ortiz I, Paluch M (2014) conductivity mechanism in polymerized imidazolium-based protic ionic liquid [HSO₃-BVIIm][OTf]: dielectric relaxation studies. *Macromolecules* 47:4056–4065
62. Wojnarowska Z, Knapik J, Jacquemin J, Berdzinski S, Strehmel V, Sangoro JR, Paluch M (2015) Effect of pressure on decoupling of ionic conductivity from segmental dynamics in polymerized ionic liquids. *Macromolecules* 48:8660–8666
63. Choi UH, Ye Y, de la Cruz DS, Liu W, Winey KI, Elabd YA, Runt J, Colby RH (2014) Dielectric and viscoelastic responses of imidazolium-based ionomers with different counterions and side chain lengths. *Macromolecules* 47:777–790
64. Seki S, Susan MABH, Kaneko T, Tokuda H, Noda A, Watanabe M (2005) Distinct difference in ionic transport behavior in polymer electrolytes depending on the matrix polymers and incorporated salts. *J Phys Chem B* 109:3886–3892
65. Agapov AL, Sokolov AP (2011) Decoupling Ionic Conductivity from Structural relaxation: a way to solid polymer electrolytes? *Macromolecules* 44:4410–4414

Chapter 6

Ionic Transport and Dielectric Relaxation in Polymer Electrolytes

Yangyang Wang

Abstract Understanding the electrical properties of polymer electrolytes is a fundamentally and practically important problem in electrolyte science. The presence of salt not only poses challenges for the analysis of dielectric spectrum, but also leads to the emergence of new relaxation processes. In addition, the ionic transport mechanism in polymers remains poorly understood. Here we present a brief review of the methods for analysis of the dielectric spectra as well as an account of the phenomenology of ionic transport and dielectric relaxation in polymer electrolytes.

6.1 Introduction

Solid polymer electrolytes have continuously attracted much attention, because of the many significant advantages they promise to bring forth for battery technologies [1]. Despite tremendous efforts in the past several decades, this type of electrolytes still suffers from low ionic conductivities. Room temperature ionic liquids, because of their many unique physiochemical properties, have the potential to offer an elegant solution to this conundrum. It has been demonstrated that the addition of room temperature ionic liquids to conventional solid polymer electrolytes leads to dramatic improvements of properties [2]. Furthermore, incorporating ionic liquid structure into either the backbone or side groups of polymers gives rise to a new type of functional materials, polymerized ionic liquids, which present an opportunity to combine the intrinsic high ionic conductivity of ionic liquids and superior mechanical property of polymers, while keeping the transference number of the counterions close to unity.

This chapter focuses on ionic transport and dielectric relaxation in conventional dry polymer electrolytes. In spite of the fact that this type of material has been

Y. Wang (✉)

Center for Nanophase Materials Sciences, Oak Ridge National Laboratory,
Oak Ridge, TN 37831, USA
e-mail: wangy@ornl.gov

extensively studied, many fundamental problems remain poorly understood. This chapter will focus on the phenomenology of ionic transport and dielectric relaxation in polymer electrolytes.

Conventional polymer electrolytes are based on salts of relatively high melting points such as LiClO_4 (lithium perchlorate) and LiTFSI (lithium bistrifluoromethanesulfonimide). Here we note that room temperature ionic liquids can be regarded as a special class of salts, which are liquids instead of solids at room temperature. Therefore, much of what being discussed in this chapter should apply to polymer and ionic liquid mixtures, although fundamental studies of such systems are still lacking. Moreover, knowledge about conventional dry polymer electrolytes is indispensable for a better understanding of emerging electrolytes such as polymerized ionic liquids.

This chapter is organized as follows. We first give a brief overview of the protocols that researchers in the field have employed to analyze the dielectric spectrum of polymer electrolytes and recent efforts to treat the electrode polarization (EP) phenomenon which is ubiquitous in ionic materials. The quantitative change of dielectric relaxation in polymers with the addition of salts will then be discussed primarily based on results from polypropylene glycols (PPGs). The focus of the last part of the chapter is placed on the relationship between ionic transport and polymer relaxation.

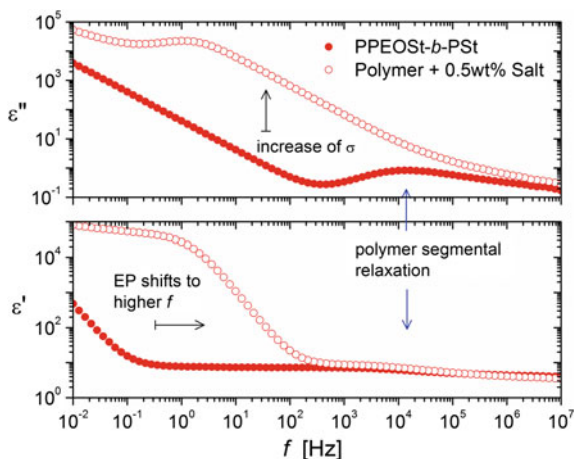
6.2 Dielectric Relaxation in Polymer Electrolytes

6.2.1 Analysis of Dielectric Spectra of Polymer Electrolytes

Analysis of dielectric spectra of polymer electrolytes is a challenging task. The presence of ionic species significantly increases the ionic conductivity in polymers and introduces additional dielectric relaxation processes. The increase of ionic conductivity brings forth two general problems for spectrum analysis. On the one hand, the dc conductivity ($\sigma/\epsilon_0\omega$) overwhelms the measured dielectric loss, making it difficult to resolve other relaxation processes. On the other hand, the EP phenomenon associated the high conductivity interferes with the analysis of the real part of permittivity as well. Moreover, when microphase separation is present, which is often the case for charged polymers, additional complications have to be considered. Therefore, analysis of the dielectric spectrum of polymer electrolytes requires extra care.

An example is given in Fig. 6.1 to illustrate the qualitative change of the dielectric spectrum of a polymer (poly(polyethylene oxide styrene)-*b*-polystyrene) after the addition of salt (LiClO_4). Because of the non-conducting nature of the parent polymer, the addition of a small amount of salt leads to dramatic increase of dc conductivity by several orders of magnitude (Fig. 6.1, upper panel). As a result of this increase of conductivity, the onset of the low-frequency EP process shifts to

Fig. 6.1 Dielectric spectra of poly(polyethylene oxide styrene)-*b*-polystyrene (PPEOST-*b*-PSt), and PPEOST-*b*-PSt with 0.5 wt% LiClO₄, at 46 °C. The addition of a small amount of salt significantly increases the contribution of dc conductivity to the dielectric loss and shifts the response due to electrode polarization (EP) to higher frequencies



higher frequencies (Fig. 6.1, lower panel). The change of polymer segmental dielectric relaxation (α relaxation) is typically small at low salt loading. However, significant changes are generally observed at high salt concentrations. Figure 6.1 also shows that even at 0.5 wt% loading of LiClO₄, the dielectric loss due to polymer segmental motion is largely buried by the dc conductivity contribution.

6.2.1.1 Spectrum Analysis Protocols

Methods for analyzing the dipolar relaxations in neutral polymers have been well established. Typically, the dielectric spectrum can be described by the superposition of ionic conductivity contribution and a few Havriliak–Negami (HN) terms:

$$\varepsilon^*(\omega) = \varepsilon' - i\varepsilon'' = \frac{\sigma}{i\varepsilon_0\omega} + \sum_j \frac{\Delta\varepsilon_j}{[1 + (i\omega\tau_j)^{\alpha_j}]^{\beta_j}} + \varepsilon_\infty, \quad (6.1)$$

where $\omega = 2\pi f$ is the angular frequency, ε_∞ represents the value of $\varepsilon'(\omega)$ at infinite frequency, $\Delta\varepsilon_j$ is the dielectric relaxation strength, $\tau_{HN,j}$ is the relaxation time, α_j , β_j are the shape parameters of process j , and σ is the dc conductivity.

In the case of polymer electrolytes, because of the high ionic conductivity, the effect of EP has to be properly considered. One of the simplest ways to take this into account is to use a power-law term to describe the effect of EP on the real part of dielectric permittivity [3, 4]:

$$\varepsilon^*(\omega) = \varepsilon' - i\varepsilon'' = \frac{\sigma}{i\varepsilon_0\omega} + \sum_j \frac{\Delta\varepsilon_j}{[1 + (i\omega\tau_j)^{\alpha_j}]^{\beta_j}} + \varepsilon_\infty + A\omega^{-n}, \quad (6.2)$$

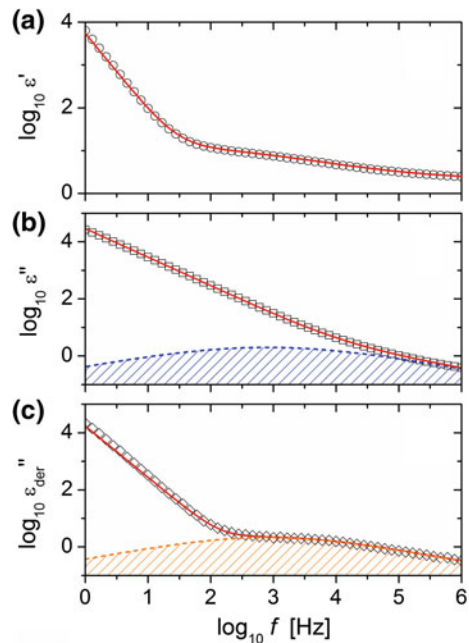
where n is related to the slope of EP's high frequency tail and A gives the amplitude of EP. This treatment relies on the fact that the frequency dependence of ϵ'' at the onset of EP does not differ too much from the relationship $\epsilon'' = \sigma'/\epsilon_0\omega$. For electrolytes, one of the key material properties is their dc conductivity. This quantity can be more conveniently extracted using the conductivity representation ($\sigma^* = i\omega\epsilon_0\epsilon^*$), where the dc conductivity appears as a plateau in the real part σ' of complex conductivity. Alternatively, the whole EP can be treated by a Debye or Cole–Cole function [5–8]:

$$\epsilon^*(\omega) = \frac{\sigma}{i\epsilon_0\omega} \left(1 - \frac{1}{1 + (i\omega\tau_{EP})^\gamma} \right) + \sum_j \frac{\Delta\epsilon_j}{[1 + (i\omega\tau_j)^{\alpha_j}]^{\beta_j}} + \epsilon_\infty, \quad (6.3)$$

where τ_{EP} is a characteristic relaxation time associated with the EP process and γ is a shape parameter. Figure 6.2 gives an example of the fitting of dielectric spectrum of polymer electrolytes by Eq. 6.2. Because of the lack of spectral features in ϵ'' and the presence of EP, it becomes important to simultaneously fit the real and imaginary parts of ϵ^* , with proper consideration of the contribution of EP.

It is well known that the real and imaginary parts of the complex permittivity for a dielectric relaxation process is interrelated according to the Kramers–Kronig relations [9]. In practice, the below relation is often used to approximate the dielectric loss without dc conductivity contribution [10]:

Fig. 6.2 Demonstration of fitting of dielectric spectrum of polymer electrolytes by Eq. 6.2. The sample is an exo-*N*-diethylene glycol-7-oxabicyclo[2.2.1]hept-5-ene-2,3-dicarboximide based polymer with 36.6 wt% of LiTFSI and the test temperature is 65 °C



$$\varepsilon''_{\text{der}} = -\frac{\pi}{2} \frac{\partial \varepsilon'}{\partial \ln \omega} \approx \varepsilon''_{\text{rel}} \quad (6.4)$$

At conditions where the dc conductivity is relatively high but the EP still occurs at relatively low frequencies, Eq. 6.4 is useful to remove the dc conductivity contribution and reveal the loss peak originally buried under the conductivity. In this case, a characteristic relaxation time can be extracted directly from the peak position of the derivative spectrum. However, when the dc conductivity is high, derivative analysis alone is still insufficient to fully resolve the dielectric relaxation concealed by conductivity and EP, and careful quantitative fitting is necessary. While Eq. 6.4 is only an approximate form of $\varepsilon''_{\text{rel}}$, the exact interconversion between real and imaginary parts of complex permittivities is not important and the derivative spectrum defined by Eq. 6.4 could be used as a check of the fit quality.

6.2.1.2 Analysis of Electrode Polarization: Ion Number Density and Diffusivity

Here we note that the EP phenomenon is a topic that deserves a separate thorough discussion. Numerous models have been proposed to describe and analyze this phenomenon [8, 11–23]. It is possible, in principle, to extract information about the free-ion number density and diffusivity from EP.

The EP phenomenon has been discussed a long time ago on the basis of the Poisson–Nernst–Planck (PNP) model, where the Poisson equation for electric potential is combined with the Nernst–Planck equation for charge transport [20]. Such a treatment allows one to obtain free-ion number density and diffusivity from the low-frequency response of an electrolytic cell. More often, the analysis of the EP is performed on the basis of simplified versions of the PNP treatment [8, 16, 24, 25], which can be described in terms of the equivalent circuit language.

For a 1-1 electrolyte solution, where the cation and the anion carry the same amount of charges, the complex dielectric function of EP in a plane capacitor can be effectively described by the Debye function:

$$\varepsilon^*(\omega) = \varepsilon_{\text{B}} + \frac{\Delta\varepsilon_{\text{EP}}}{1 + i\omega\tau_{\text{EP}}}, \quad (6.5)$$

where ε_{B} is the bulk permittivity, $\Delta\varepsilon_{\text{EP}} = (L/2L_{\text{D}} - 1) \cdot \varepsilon_{\text{B}}$, and τ_{EP} is the characteristic relaxation time of EP. τ_{EP} is defined by the bulk resistance R_{B} and the interfacial capacitance C_{EP} : $\tau_{\text{EP}} = R_{\text{B}}C_{\text{EP}}$. In the Macdonald–Trukhan model, C_{EP} is simply determined by the Debye length L_{D} and the bulk permittivity ε_{B} as:

$$C_{\text{EP}} = \varepsilon_0 \varepsilon_{\text{B}} \frac{A}{2L_{\text{D}}}, \quad (6.6)$$

with A being the surface area of the electrode. Here, the underlying assumption is that all the ions have equal diffusivity, and the sample thickness L is much larger than the Debye length L_D . An example of fit of EP by Eq. (6.5) is given in Fig. 6.3 for a solution of NaCl in the mixture of water and glycerol. The low-frequency part of the spectrum cannot be completely captured by this EP model. In this region, other interfacial properties such as molecular absorption also contribute to the total dielectric response. However, the dielectric properties at the onset of EP, e.g., f_{\max} and $(\tan \delta)_{\max}$ (Fig. 6.3b) provide sufficient information for estimation of free-ion number density and diffusivity.

To further obtain the total number density of free ions n , which is the sum of the number densities of free cations n_+ and anions n_- , one can resort to the definition of the Debye length:

$$L_D = \sqrt{\frac{\varepsilon_0 \varepsilon_B k_B T}{(n_+ + n_-) q^2}} = \sqrt{\frac{\varepsilon_0 \varepsilon_B k_B T}{n q^2}}. \quad (6.7)$$

Here, q is the amount of charges carried by an ion, and T is the absolute temperature. The ion diffusivity can subsequently be calculated from the dc conductivity and ion number density, according to the definition of conductivity and the Einstein relation:

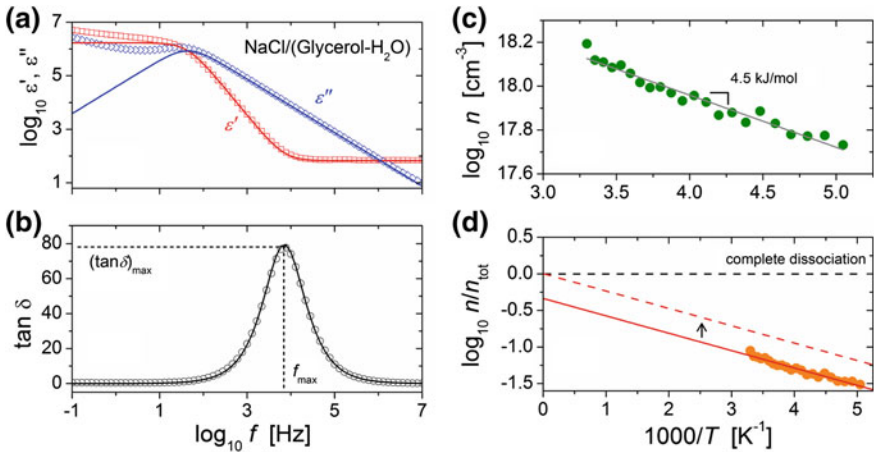


Fig. 6.3 Dielectric spectrum of NaCl/(Glycerol-H₂O) at -5 °C. **a** Complex permittivity. **b** $\tan \delta$. Here, the main “relaxation” is due to electrode polarization. *Solid lines* fits by Eq. 6.5. **c** Temperature dependence of free-ion number density determined from Eqs. 6.8 to 6.9. **d** Illustration of the correction procedure for the electrode polarization analysis. The *orange dots* are free-ion fraction determined from Eqs. 6.8 to 6.9 for NaCl/(Glycerol-H₂O). The *red line* is the Arrhenius fit of the experimental data. The *black horizontal dashed line* indicates the level of complete dissociation, i.e., $n/n_{\text{tot}} = 1$. The *red dashed line* represents the n/n_{tot} after the correction procedure

$$D = \frac{\sigma k_B T}{n q^2}. \quad (6.8)$$

In practice, it is often more convenient to use the following relation to calculate the ion diffusivity [15, 24, 25]:

$$D = \frac{2\pi f_{\max} L^2}{32(\tan \delta)_{\max}^3}, \quad (6.9)$$

where $(\tan \delta)_{\max}$ is the maximum value of $\varepsilon''/\varepsilon'$ at the onset of EP, f_{\max} is the frequency at the $\tan \delta$ maximum. In this approach the dissociation of salts is not assumed to be complete, but the dissociation-association dynamics are assumed to be much faster than the macroscopic EP. Figure 6.3c gives an example of the free-ion number density for NaCl/(glycerol–H₂O), calculated using Eqs. 6.8 and 6.9, as a function of temperature. The estimated $\log_{10} n$ exhibits a linear dependence on $1/T$, giving rise to a dissociation energy E_{dis} of 4.5 kJ/mol. This value is clearly reasonable for ionic dissociation in liquids. In fact, the dissociation energies obtained from this [21, 25] other approaches [8, 26–29] based on EP analysis all fall into a similar range.

Unfortunately, the method described above does not always yield reasonable absolute numbers for the free-ion number density and diffusivity. It is well known that a number of factors such as surface roughness and electrode chemical composition EP can strongly affect the EP behavior. However, the method outline above does not take these into consideration. Based on the observation that EP analysis typically produce reasonable dissociation energy, it has been proposed that the free-ion number density and diffusivity have to be corrected by a proportionality constant. To satisfy the complete dissociation condition at the infinitely high temperature limit, the true free-ion number density should be described by the below Arrhenius equation:

$$\tilde{n} = \frac{n_{\text{tot}}}{n_0} n = \frac{n_{\text{tot}}}{n_0} [n_0 \exp(-E_{\text{dis}}/k_B T)] = n_{\text{tot}} \exp(-E_{\text{dis}}/k_B T), \quad (6.10)$$

where \tilde{n} is the free-ion number density after correction, n is the free-ion number density before correction, n_{tot} is the total ion number density at complete dissociation, and E_{dis} is the dissociation energy from the original EP analysis. Here, we rescale the original free-ion concentration n by a factor of n_{tot}/n_0 , assuming complete dissociation at infinitely high temperature limit. Similarly, we need to correct the diffusivity by a factor of n_0/n_{tot} :

$$\tilde{D} = D \cdot \frac{n_0}{n_{\text{tot}}}, \quad (6.11)$$

with \tilde{D} being the corrected diffusivity, and D the original diffusivity from the EP analysis. Figure 6.3d gives an example for this correction procedure for

NaCl/(Glycerol–H₂O). The correction factor for the free-ion number density and diffusivity can be obtained by using the theoretically calculated n_{tot} and experimentally determined n_0 . A recent study of polymer electrolytes, ionic liquids, aqueous and non-aqueous solutions suggests that this correction procedure could yield free-ion diffusivities that are in close agreement with pulsed-field gradient NMR measurements [21].

6.2.2 Low Salt Concentration: Emergence of Ionic Mode

The presence of salt not only influences the dc conductivity and the EP behavior, but also leads to significant changes of dielectric response at high frequencies. At relatively low salt concentrations, an additional dielectric relaxation mode emerges due to the ionic fluctuations in isolated domains. This so-called ionic mode was first observed in PPG with lithium perchlorate (LiClO₄) [5]. The same process has also been found in PEO–LiClO₄ [6] and a few other systems including poly(2-vinylpyridine)–LiClO₄ [30], poly(vinyl methyl ether)–LiClO₄ [31], and polyester copolymer ionomers based on PEO [27].

Below we illustrate the presence and properties of the ionic mode in polymer electrolytes, with the recent systematic study on PPG–LiClO₄ as an example. In this study, PPGs of three different molecular weights are involved: 4000, 1000, and 425 g/mol (labeled as PPG4000, PPG1000, and PPG425). The concentration was represented by the molar ratio of ether oxygen to lithium (O:Li). Broadband dielectric measurements were performed in the frequency range of 10⁻²–10⁷ Hz, using a Novocontrol Concept 80 system, which includes an Alpha-A impedance analyzer, a ZGS active sample cell interface, and a Quatro Cryosystem temperature control unit.

In the case of neat PPG425, only one primary relaxation process (segmental relaxation) is observed. However, the presence of LiClO₄ gives rise to an additional relaxation at low frequencies in PPG425–LiClO₄ (O:Li = 1000) (Fig. 6.4a). Similar processes can also be found in PPG1000–LiClO₄ (O:Li = 1000) and PPG4000–LiClO₄ (O:Li = 1000) (Fig. 6.4b). This additional relaxation process is termed as “ionic mode” in the literature. The ionic mode cannot be clearly observed by dielectric spectroscopy for samples with O:Li ≤ 30, where other relaxation processes dominate the spectrum. The studies by Furukawa et al. [7, 32] showed that the strength of the ionic mode increased with increasing salt concentration in the range of 100 ≤ O:Li ≤ 1000. In addition, Fig. 6.5 reveals that the relaxation times of the ionic mode in PPG425 (O:Li = 1000), PPG1000 (O:Li = 1000), and PPG4000 (O:Li = 1000) closely follow one another and the relaxation strengths exhibit weak molecular dependence but essentially independent of temperature.

As will be discussed below, the slow and fast relaxations originate from the segmental relaxations in ion-rich and ion-depleted domains, respectively. Since the ionic mode is slower than the fast segmental relaxation, but faster than the slow

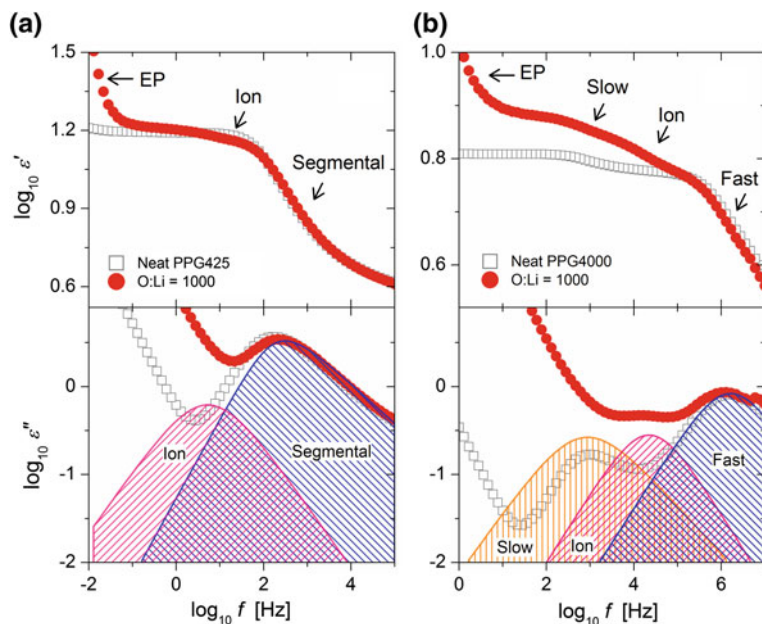
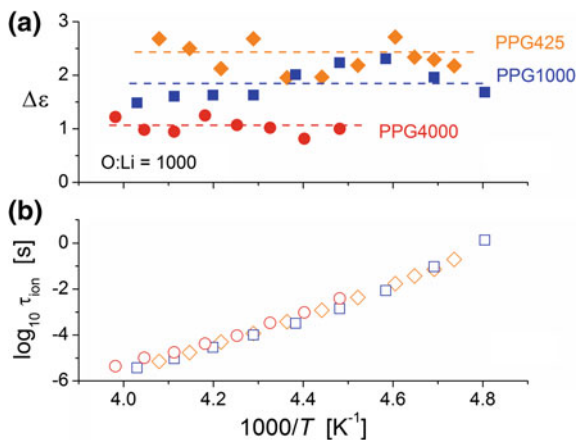


Fig. 6.4 Comparison of the dielectric spectra of PPG **a** 425 and **b** 4000 g/mol at O:Li = 1000 (low salt concentration). The *open squares* present the spectra of neat polymers and the *closed circles* present the spectra of PPG–LiClO₄. The peaks represent different relaxation processes from the fitting of PPG–LiClO₄ spectra. The increase of ϵ' at low frequencies is due to the electrode polarization effect (EP). The figure is reproduced from Ref. [4]

Fig. 6.5 Temperature dependence of **a** the relaxation strength and **b** relaxation time for the ionic relaxation mode. The *red circles*, *blue squares*, and *orange diamonds* correspond to PPG4000 (O:Li = 1000), PPG1000 (O:Li = 1000), and PPG425 (O:Li = 1000), respectively



segmental relaxation, it should only arise from the ion fluctuation in the ion-depleted domain.

6.2.2.1 Pressure Dependence of the Ionic Mode

While pressure is an important thermodynamic variable that strongly influences the dynamics and thermodynamics of glass-forming liquids and polymers, pressure-dependent dielectric spectroscopy studies of polymer electrolytes remain limited, with most of them focusing primarily on conductivity [33–35]. The recent dielectric spectroscopy study reveals that the nature of the ionic mode is not affected by compression in PPG with low LiClO₄ concentrations. Figure 6.6 shows the dielectric spectra of PPG425–LiClO₄ (O:Li = 1000) at ambient and high pressure (551 MPa). The strength and shape of the ionic and segmental relaxation at the two pressures are almost identical, despite a slight decoupling of ionic conductivity from the segmental relaxation at high pressure. The relaxation times of the ionic and segmental modes are presented as a function of pressure in Fig. 6.7. Similar to the effect of decrease of temperature, the increase of pressure shifts the ionic and segmental modes to lower frequencies. The inset shows the relation of the ionic relaxation to the segmental relaxation under both isothermal and isobaric conditions. The data fall onto the same line of a slope of one, indicating that the ionic and

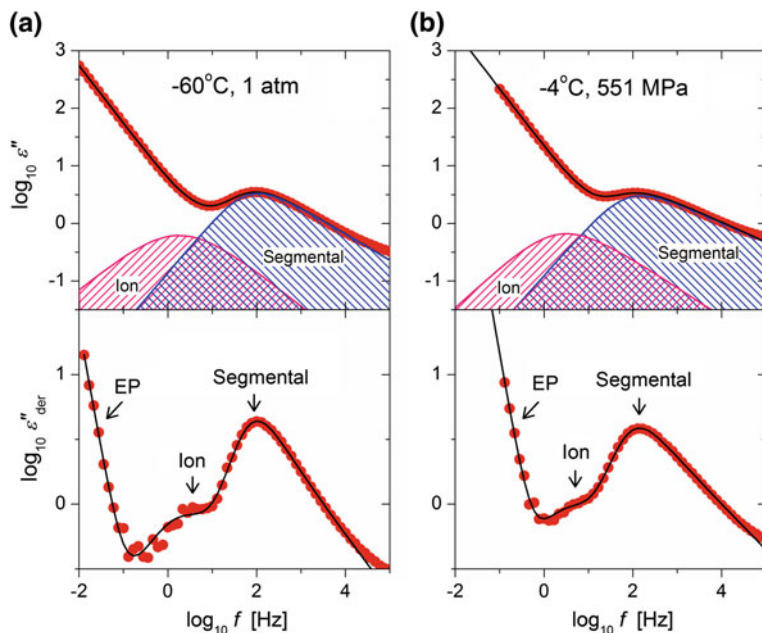
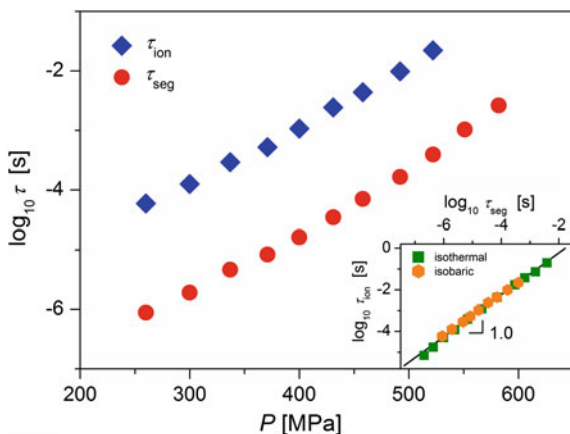


Fig. 6.6 Comparison of the spectra of PPG425–LiClO₄ (O:Li = 1000) at **a** ambient pressure (1 atm) and **b** high pressure (551 MPa). The figure is reproduced from Ref. [4]

Fig. 6.7 The relaxation time as a function of pressure for both ion mode (*diamonds*) and segmental mode (*circles*). The *inset* shows the relationship between the relaxation time of the ion mode and the segmental mode in isothermal (*squares*) and isobaric (*hexagons*) experiments



segmental modes are affected in a very similar fashion by pressure and temperature. Moreover, the inset suggests that these two modes are well coupled at the studied pressure and temperature range.

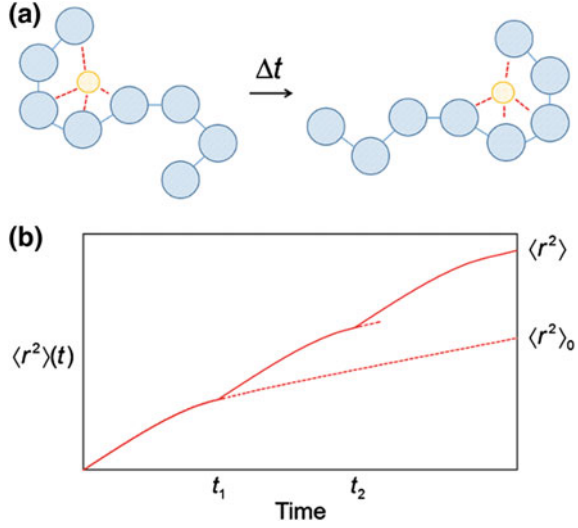
6.2.2.2 Slow Segmental Relaxation

It is worth mentioning some other spectral features in PPG4000–LiClO₄ (O:Li = 1000): a slow process appears at almost the same position as the normal mode in neat PPG4000 (Fig. 6.4b), albeit with increased relaxation strength. This mode reflects the slow segmental relaxation in PPG4000–LiClO₄, caused by the micro-phase separation in the presence of salt. While at O:Li = 1000:1, the slow segmental mode in PPG4000 appears at the frequency of normal mode in neat PPG, rheological measurements have revealed that this is not the case for other salt concentrations: the chain relaxation times from rheology and the slow segmental relaxation times from dielectric spectroscopy do not coincide in general. In PPG1000–LiClO₄ (O:Li = 1000), two processes are clearly observable. They are ionic mode and fast segmental mode. Due to the presence of the ionic mode, it is hard to resolve the slow segmental peak from the spectrum. The fast segmental processes in PPG4000–LiClO₄, PPG1000–LiClO₄ at O:Li = 1000, as well as the only segmental process in PPG425–LiClO₄ at O:Li = 1000, do not differ much from the segmental peaks in the corresponding neat PPGs, in terms of both peak frequency and shape.

6.2.2.3 Nature of the Ionic Mode

The ionic mode at low salt concentrations can be best understood in terms of the Dynamic Bond Percolation (DBP) model developed by Druger and coworkers

Fig. 6.8 **a** Illustration of ion hopping from one coordination environment to another, after Ref. [40]. **b** Schematic illustration of the renewal process for ionic transport, where the mean square displacement is shown as a function of time



[36–39]. According to the static percolation picture, below a percolation threshold value, there is no continuous pathway connecting adjacent ion-rich domains and the ionic motion is localized. However, polymers undergo rapid local structural rearrangement above their glass transition temperature, and the long-range ionic motion can be facilitated by the polymer segmental relaxation. DC ionic conductivity comes from a combination of ion hopping and structural renewal (Fig. 6.8). In the zero-frequency limit, the diffusion coefficient is related to the ionic fluctuation time τ_f and the renewal time τ_r by:

$$D \simeq \frac{\langle r^2 \rangle_0}{\tau_r + \tau_f}, \quad (6.12)$$

where $\langle r^2 \rangle_0$ is the amplitude of the ionic fluctuation. It has been shown that the frequency-dependent diffusion coefficient can be obtained by replacing the renewal rate $1/\tau_r$ with $1/\tau_r + i\omega$:

$$D^*(\omega) = \frac{1 + i\omega\tau_r}{\tau_r + \tau_f + i\omega\tau_r\tau_f} \langle r^2 \rangle_0. \quad (6.13)$$

Using the Nernst–Einstein relation: $\sigma^*(\omega) = nq^2 D^*(\omega)/k_B T$ and the interrelation between complex permittivity and conductivity: $\sigma^* = i\omega\epsilon_0\epsilon^*$ one obtains the expression of complex permittivity for the DBP model:

$$\epsilon^* = \epsilon' - i\epsilon'' = \frac{\sigma_{dc}}{i\omega\epsilon_0} + \frac{\Delta\epsilon_{ion}}{1 + i\omega\tau_{ion}}, \quad (6.14)$$

with

$$\sigma_{\text{dc}} = \frac{nq^2}{k_{\text{B}}T} \frac{\langle r^2 \rangle_0}{\tau_r + \tau_f}, \quad (6.15)$$

$$\Delta\epsilon_{\text{ion}} = \frac{nq^2}{k_{\text{B}}T} \frac{\langle r^2 \rangle_0 \tau_r^2}{(\tau_r + \tau_f)^2}, \quad (6.16)$$

$$\tau_{\text{ion}} = \frac{\tau_r \tau_f}{\tau_r + \tau_f}. \quad (6.17)$$

The second term in Eq. 6.14 describes the dielectric relaxation rising from the ionic fluctuations in the “closed” domains. This model thus offers a simple explanation for the emergence of the additional relaxation mode at relatively low salt concentration: the microphase separation in PPG–LiClO₄ leads to the formation of ion-rich and ion-depleted domains and ionic fluctuations between different domains gives rise to the ionic mode.

Here we note that the predicted ionic mode is not always reported in polymer electrolytes. As mentioned earlier, the most well-established examples are those found in polyethylene oxides (PEO) [6] and PPG [4, 5, 7, 32]. The ionic mode has also been observed in poly(vinyl methyl ether) and poly(2-vinylpyridine) containing lithium salts [30, 31]. Nevertheless, the universality of this mode in polymer electrolytes has not been established. This is partly due to the fact that the ionic mode could only be observed at relatively low salt concentrations, and with careful data analysis, while most of the studies in the field involve high salt concentrations, in which dc conductivity is the only interested quantity. Moreover, it has been argued that the presence of trapped air bubbles, which is often unavoidable in handling viscous polymeric materials, could lead to the appearance of a low-frequency Debye relaxation mode [41].

6.2.3 *Emergence of Additional Relaxation Modes at Higher Salt Concentrations*

At intermediate salt concentration, the spectra PPG4000–LiClO₄ become considerably different from those of the neat PPG4000 and PPG4000–LiClO₄ (1000:1). The split of segmental relaxation is much more pronounced (Fig. 6.9b). In addition, the ionic mode is overwhelmed by the segmental mode and can no longer be clearly resolved. With the increase of salt concentration, the relaxation strength of the slow process increases, while the strength of the fast process is reduced, and becomes unobservable when O:Li = 7 (Fig. 6.10). Moreover, the separation between slow and fast segmental relaxations also becomes larger with the increase of LiClO₄ concentration. In PPG1000–LiClO₄, as the salt content increases to O:Li = 30, the

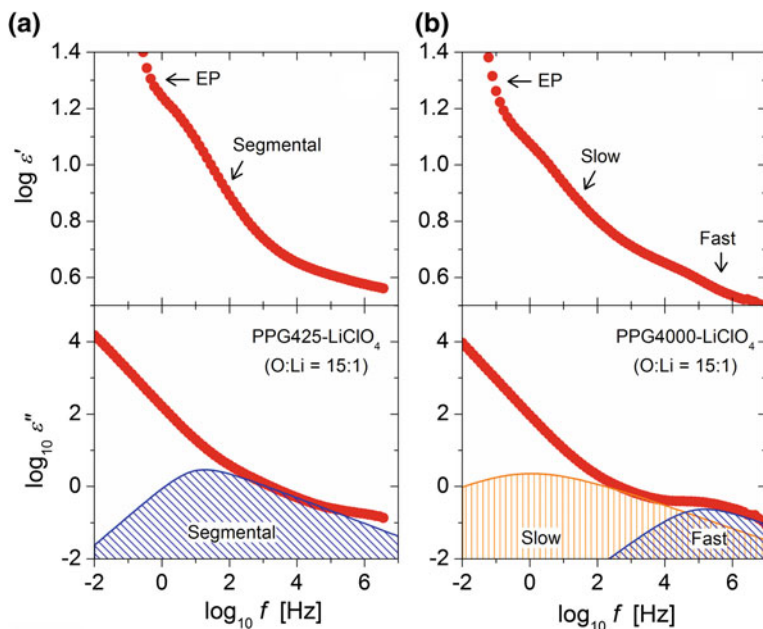


Fig. 6.9 Comparison of the dielectric spectra of PPG-LiClO₄ with molecular weight **a** 425 and **b** 4000 g/mol at O:Li = 15:1 (intermediate salt concentration). The peaks represent different relaxation processes from the fitting of the spectra

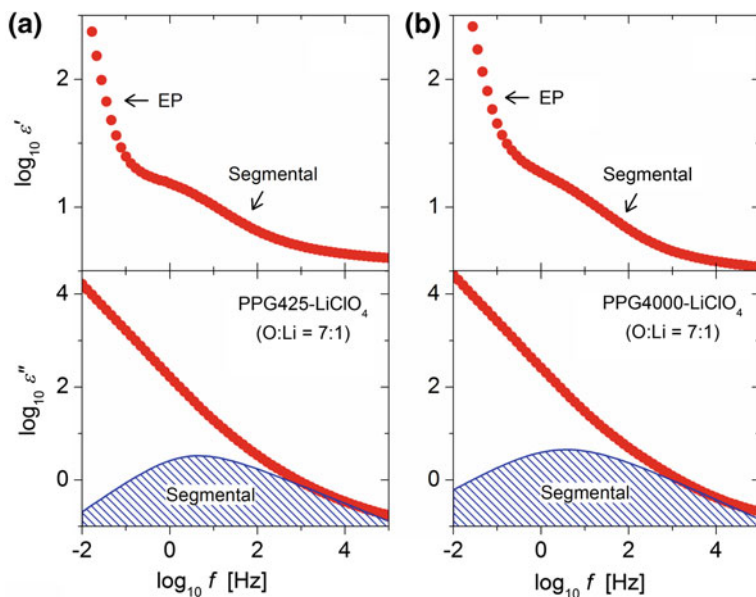


Fig. 6.10 Comparison of the dielectric spectra of PPG-LiClO₄ with molecular weight **a** 425 and **b** 4000 g/mol at O:Li = 7:1 (high salt concentration)

ionic mode disappears and the segmental relaxation splits into two separate processes, similar to the behavior of PPG4000–LiClO₄. At higher salt concentration O:Li ≤ 15, the fast segmental relaxation cannot be observed anymore. In PPG425–LiClO₄, with the increase in salt concentration the segmental relaxation process shifts to lower frequencies. No split of segmental process is found in the concentration range studied.

At high salt concentration (O:Li = 7), only a single broad relaxation process can be resolved in PPG samples (Fig. 6.10). Comparison with the results from differential calorimetry measurements confirms that this process corresponds to the polymer segmental relaxation.

6.3 Ionic Transport in Polymer Electrolytes

6.3.1 Theory of Ionic Mobility in Electrolyte Solutions

After decades of research, the mechanism of ion conduction in polymers is still not fully understood. In many polymer electrolyte systems, dielectric spectroscopy allows one to extract information about polymer segmental relaxation, dc ionic conductivity, and even free-ion number density and diffusivity via EP analysis. This allows us to explore the interplay between ionic transport and polymer structural relaxation. Polymer electrolytes could be considered as a special class of electrolyte solutions where polymers serve of solvent molecules. The traditional field of electrolyte solutions is primarily concerned with aqueous solutions and non-aqueous solutions formed by salt and small organic molecules. However, many of the fundamental principles we have learned about electrolyte solutions should apply to polymer electrolytes as well. According to the classical theory, the ionic conductivity of an electrolyte solution is determined by the number density (n), ionic mobility (μ_q), and charge (q) of all its ionic constituents (i):

$$\sigma = \sum_i n_i q_i \mu_i. \quad (6.18)$$

Among these three factors, the ionic mobility, which can vary many orders of magnitude upon change of temperature, often plays a decisive role. The ionic mobility is related to the diffusivity (D) of the ions through the Einstein relation:

$$\mu_q = \frac{Dq}{k_B T}. \quad (6.19)$$

Simple consideration of the Stokes law leads to the prediction that the ionic mobility is inversely proportional to the solution viscosity (η) and the solvent structural relaxation time (τ_s), and proportional to the structural relaxation rate (ω_s):

$$\mu_q \propto \eta^{-1} \propto \tau_s^{-1} \propto \omega_s. \quad (6.20)$$

It has been recognized that the Stokes law does not hold strictly for many ions in aqueous solutions. For example, the Stokes–Einstein relation breaks down for small cations such as Na^+ and Li^+ in water. Such an anomaly originates from the coupling between the electric field of the ion and the dielectric relaxation of the solvent. Hydrodynamic and microscopic theories have been developed to take into account the effects of dielectric friction [42–46] and ultrafast solvent dynamics [47]. Despite this known issue, the proportionality between mobility and structural relaxation rate is expected to hold to the first approximation when temperature is varied. This is supported by temperature-dependent measurements of μ_q and ω_s of molecular electrolyte solutions [48].

In the case of polymer electrolytes, the ionic diffusion is not controlled by the large-scale chain motion, but is expected to be closely coupled to the local segmental motion. In other words, while the proportionality between μ_q and $1/\eta$ no longer holds, μ_q should still be proportional to ω_s , according to the classical theory. However, a number of experimental studies have conclusively demonstrated that this is not always the case. After briefly reviewing the models for ionic transport in polymer electrolytes in Sect. 6.3.2, we will return to the experimental observations that are in support and against the classical picture.

6.3.2 Models of Ionic Transport in Polymer Electrolytes

6.3.2.1 Free-Volume Model

Empirically, the temperature dependence of ionic conductivity can be described by the Vogel–Fulcher–Tammann (VFT) equation

$$\sigma = \sigma_0 \exp\left(-\frac{B}{T - T_0}\right), \quad (6.21)$$

where σ_0 , B and T_0 are fit parameters. An example is given in Fig. 6.11: the VFT equation gives a reasonable fit of the experimental data.

The free-volume model of Turnbull and Cohen [49, 50] offers a simple way to understand such a temperature dependence [51]. According to this idea, the ionic diffusion is considered as translation of ions across the void within the cage formed by its neighboring molecules (polymer segments), which is controlled by the redistribution of the free-volume within the liquid. Following the standard argument of the free-volume model, one could arrive at the following expression for the temperature dependence for the ionic diffusivity:

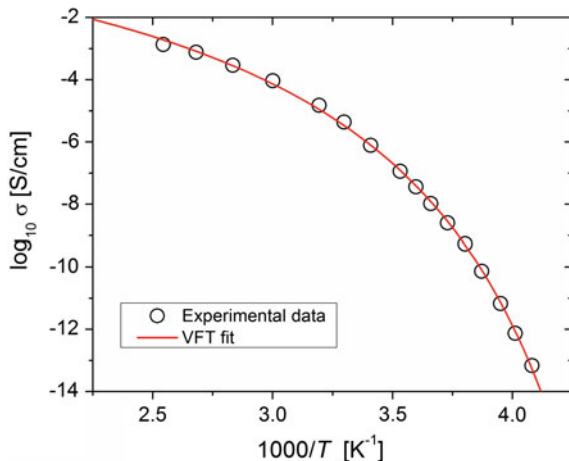


Fig. 6.11 Illustration of the typical VFT-like temperature dependence of polymer electrolytes. The experimental data is on PEG-100 K with 19 wt% LiClO₄ [6]

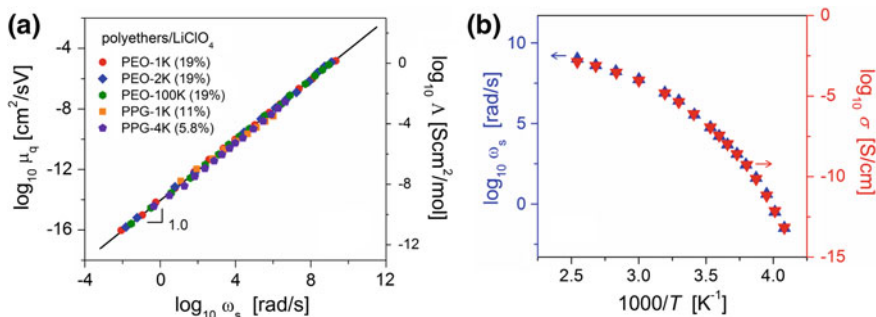


Fig. 6.12 a Relation between ionic mobility μ_q and polymer segmental (structural) relaxation frequency ω_s , molar conductivity Λ and ω_s , for polyether-based electrolytes [48, 52]. The slope of unity indicates a close coupling between ionic transport and polymer segmental dynamics. **b** Temperature dependence of segmental relaxation frequency ω_s (blue up triangles) and conductivity σ (red down triangles) in PEG-100 K with 19 wt% LiClO₄ [6]. The left and right y-axes of the inset span the same orders of magnitude

$$D = D_0 T \exp\left(-\frac{\gamma V^*}{V_g + \alpha(T - T_g)}\right). \tag{6.22}$$

where γ is a numerical factor accounting for the overlap of free volume, V^* is the critical volume for ionic diffusion, V_g is roughly the liquid volume at T_g , and α is the difference between the thermal expansion coefficients of the liquid and the glass. Combining Eq. 6.22 with the Nernst–Einstein relation, $\sigma = nq^2 D/k_B T$, leads to the VFT equation.

While the free-volume model has endured many criticisms, it provides a simple and straightforward explanation for ionic transport in many polymer electrolytes such as PEO–LiClO₄. By using the Stokes–Einstein relation in its derivation for ionic transport, it implies that the ionic conductivity is controlled by the local viscosity and thereby the polymer segmental dynamics. In other words, the local segmental motion of polymers creates a pathway for ions to move through the polymer matrix (Fig. 6.12).

Here we note that it is not unusual to analyze the temperature dependence of conductivity using other formulas. For example, Bendler and coworkers [34, 35] have argued, based on their temperature- and pressure-dependent conductivity measurements of polymer electrolytes (e.g., PPG–LiCF₃SO₃ and PEG–LiCF₃SO₃), that the temperature dependence of conductivity is better described by the following expression:

$$\sigma = \frac{A_\sigma}{T(1 - \delta)^{1/3}} \exp \left[-\frac{B \cdot T_c}{(T - T_c)^{3/2}(1 - \delta)} \right]. \quad (6.23)$$

where δ is a parameter related to the specific volume $V(T, P)/V(T, 0) = 1 - \delta(T, P)$ and T_c is the temperature at which single defects disappear in the mean field lattice gas model. The model is built on the idea that ion hopping induced by the defect flux follows a stretched exponential waiting time distribution law. Although the model seems to work pretty well in the few examples given in Refs. [34, 35], its general validity remains to be examined and explored.

6.3.2.2 Dynamic Bond Percolation Model

As discussed earlier, the DBP model developed by Nitzan, Ratner, and coworkers gives an explanation for the emergence of the ionic relaxation mode in polymer electrolytes with low salt concentration. In addition, compared to the free volume model, the DBP model provides more microscopic details for ionic motion. It recognizes that both the ionic motion in terms of jumps between neighboring sites and the structural renewal of the local coordination environment are important for the long-range ionic diffusion.

In DBP, the master equation for describing the probability P of finding an ion at site i at time t is [53]:

$$\frac{dP_i}{dt} = \sum_j (-W_{ij}P_i + W_{ji}P_j), \quad (6.24)$$

where W_{ij} is the hopping rate from site i to j . The probabilities for jumps to be permitted or forbidden are f and $1 - f$, respectively. Furthermore, the hopping rate is time-dependent in polymer electrolytes due to the polymer segmental motion. By assuming specific forms for the hopping rate, the ionic transport properties can be

computed from Eq. 6.24. When f is relatively small, the ionic transport is controlled by solvent renewal, i.e., coupled to polymer segmental relaxation. On the other hand, when f is sufficiently large, long-range ion transport is no longer limited by the renewal event and ionic conductivity is decoupled from polymer segmental dynamics. As a result, the DBP model is able to offer explanations to both coupled and decoupled conductivities that are experimentally observed.

6.3.3 *Coupling and Decoupling Between Conductivity and Polymer Relaxation*

6.3.3.1 **Observation of Decoupling in Polymer Electrolytes**

According to the classical theory, ionic transport in polymer electrolytes should be coupled to the polymer segmental dynamics. And this is indeed what has been found in polyethers such as PEO and PPGs. However, exceptions to this classical picture have also been observed. As early as in 1972, Sasabe and coworkers reported decoupled ionic conductivity in several high T_g polymers [54]. It should be pointed out that the polymers in this study did not contain added salts and the conductivity presumably originated from dissolved ionic impurities. With the advent of synthesis of polymer electrolytes, other decoupled systems such as liquid crystalline materials [55], polymerized plasticizers [56], and polymerized salts [57] have also been prepared. More recently, Wang and Sokolov, and their coworkers have analyzed and reported decoupled ionic transport in a wide variety of polymers [25, 48, 52, 58, 59]. It is shown that there might be a connection between the degree of decoupling and the fragility of the polymer segmental dynamics. Most of the fragile (rigid) polymers suffer a significant amount of frustration in chain packing [60, 61]. The loose packing structure enables the ions to move through the polymer matrix even when the segmental dynamics are slow or frozen. This idea also bears a connection to the DBP model: the enhanced free volume in fragile polymers significantly increases the probability f of successful ion hopping between neighboring sites, so that ionic transport is no longer controlled by the polymer segmental dynamics.

Figure 6.13 provides an example of decoupled dry polymer electrolytes. In poly [4-(2-methoxyethoxy)methyl styrene] (PMOEOmSt), the polymer consists of relatively rigid polystyrene backbone and 2-methoxyethoxy methyl side groups. Figure 6.13a shows that the ionic conductivity is decoupled in PMOEOmSt. The segmental relaxation frequency shifts by four and a half orders of magnitude when the temperature changes from 40 to 5 °C, whereas the decrease of conductivity is roughly two orders over the same temperature range. This difference in temperature dependence is summarized in Fig. 6.13b: the ionic resistivity has much weaker temperature dependence than the segmental relaxation time.

Fig. 6.13 a Dielectric spectra of poly[4-(2-methoxyethoxy) methyl styrene] (PMOEMSt) with 0.3 wt% LiClO_4 at 40 and 5 °C. Here, ϵ'' is the imaginary part of permittivity and f is the frequency. The *arrows* show shift of the segmental relaxation and conductivity. **b** Temperature dependence of segmental relaxation time (*circles*) and resistivity ($1/\sigma$, *diamonds*) of PMOEMSt. *Orange curve* Vogel–Fulcher–Tammann (VFT) fit of the resistivity below T_g : $(1/\sigma) = (1/\sigma_0) \exp[B/(T - T_0)]$. *Black line* Arrhenius fit of the resistivity below T_g : $(1/\sigma) = (1/\sigma_0) \exp(E_a/k_B T)$. *Pink curve* VFT fit of the segmental relaxation time: $\tau = \tau_0 \exp[B/(T - T_0)]$. The figure is reproduced from Ref. [52]

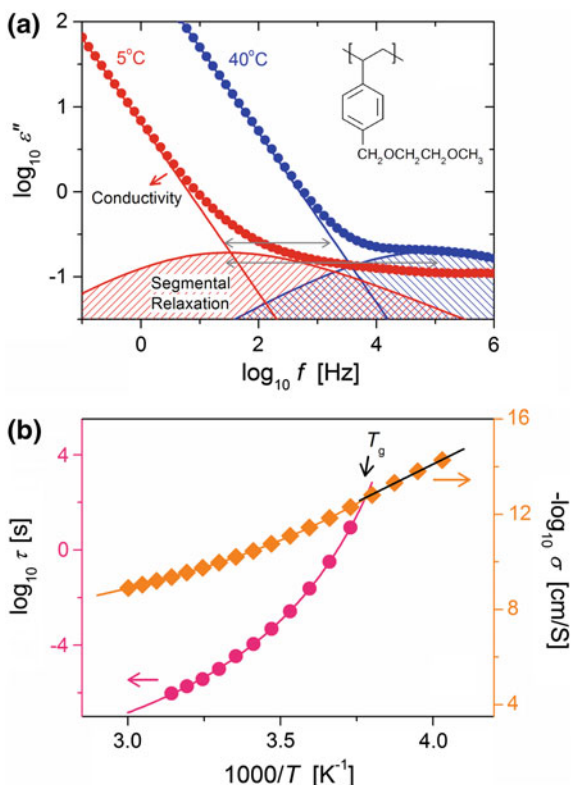


Fig. 6.14 $\sigma T \tau_S$ versus τ_S for a few different polymer electrolytes [25]. The dependence of $\sigma T \tau_S$ on τ_S near T_g can be fit by a power law (*solid lines*): $\sigma T \tau_S \sim \tau_S^\epsilon$. The exponent ϵ , which is the slope of each curve near T_g , reflects the degree of decoupling

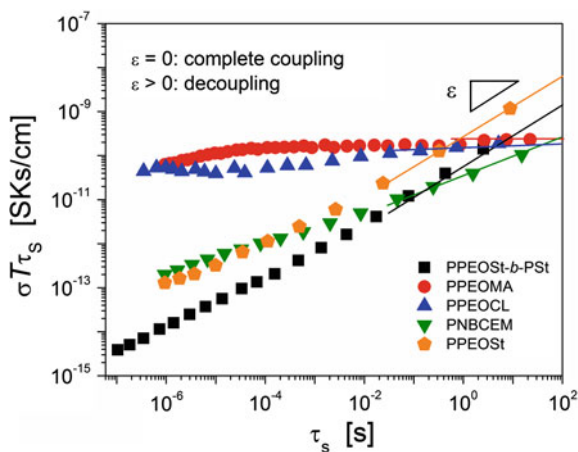
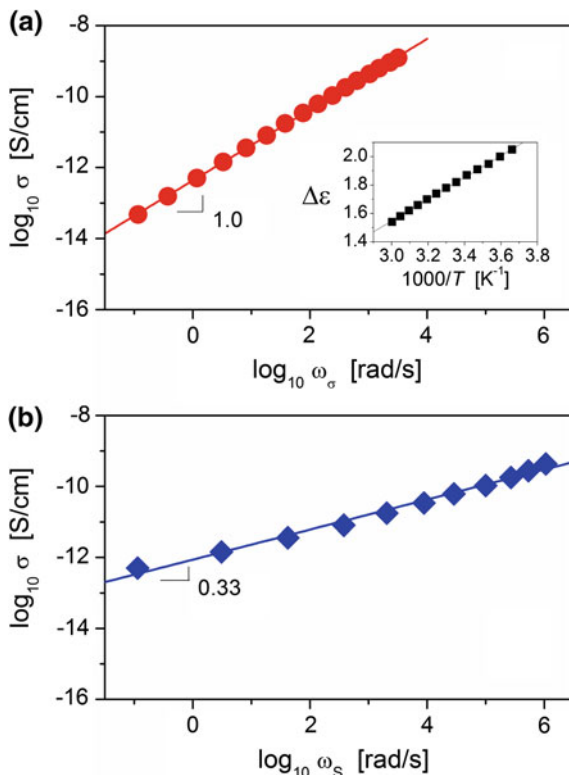


Fig. 6.15 **a** Relation between ionic conductivity (σ) and conductivity relaxation frequency (ω_σ) for PMOEMS with 0.3 % LiClO₄ [25]. *Inset* temperature dependence of strength of polymer structural relaxation. **b** Relation between σ and structural relaxation frequency (ω_S)



Another way to analyze the relation between ionic conductivity and segmental dynamics is to present $\sigma T \tau_S$ as a function of τ_S . From Eq. 6.20, we could see that when the ionic transport is completely coupled to solvent (segmental) dynamics, then conductivity should be inversely proportional to the polymer segmental viscosity η_S :

$$\sigma \propto \frac{1}{\eta_S} \propto \frac{1}{\tau_S T}. \quad (6.25)$$

The degree of decoupling can be quantified by the fractional Stokes–Einstein relation: $\sigma T \tau_S \sim \tau_S^\varepsilon$. $\sigma T \tau_S$ should be independent of τ_S when ionic transport and segmental dynamics are completely coupled. In this case, $\varepsilon = 0$. Large values of ε imply strong decoupling. Such an analysis has been performed for a number of different polymer electrolytes in Ref. [25] (Fig. 6.14). Flexible polymers such as PPEOMA and PPEOCL behave just like the classical PEO system, with $\varepsilon \approx 0$. In contrast, PPEOSt-*b*-PSt, PNBCEM, and PPEOSt exhibit different degrees of decoupling, with the highest ε found in PPEOSt-*b*-PSt and PPEOSt.

It is necessary to point out the difference between the above analysis and the so-called Barton–Nakajima–Namikawa (BNN) relation for ionic conductors [62–64].

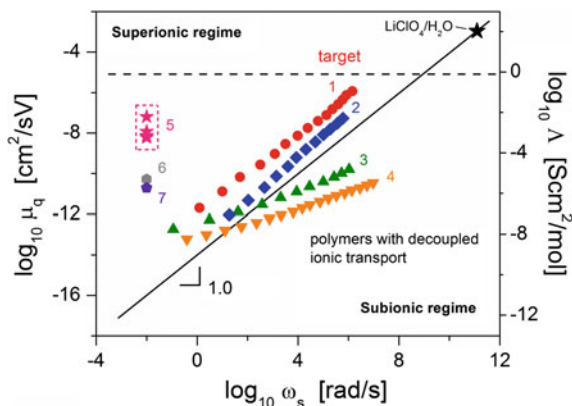


Fig. 6.16 Relation between μ_q and ω_s , Λ and ω_s , for polymers with decoupled ionic conductivity. Samples 1–7 are: 1—PVC–PPEGMEMA/LiTFSI [59], 2—PVEC–PVAc/LiTFSI [59], 3—PPEOS_t–PSt/LiClO₄ [25, 59], 4—PMOEOMS_t/LiClO₄ [25, 59], 5—liquid-crystalline polymers with LiClO₄ [55], 6—0.8(0.5LiPUS–AlCl₃)–0.2LiAlCl₄ [57], and 7—90%(50Li–30LiOAc–20LiClO₄) + 10%PPO [70]. The figure is reproduced from Ref. [48]

The BNN relation connects conductivity with dielectric loss caused by ion migration, and does not deal with the relation between ion mobility and polymer structural relaxation. It has been recently shown that for polymerized ionic liquids, the ionic transport can be strongly decoupled from polymer structural relaxation, while the BNN relation is nevertheless fulfilled [65]. To further illustrate this point, another example is given in Fig. 6.15 for PMOEOMS [25] with 0.3% LiClO₄. Here, the conductivity relaxation frequency (ω_σ) is determined from the maximum in M'' . Not surprisingly, σ is proportional to ω_σ . On the other hand, σ decouples strongly from ω_s . This strong decoupling cannot be explained by the variation of $\Delta\epsilon$, which is essentially very small.

6.3.3.2 Walden Plot Analysis

There is yet another way to analyze the relation between ionic transport and polymer segmental dynamics. It is inspired by the so-called Walden plot, which has been extensively used for ionic liquids by Angell and coworkers [66–69]. In such a plot, molar conductivity ($\Lambda = \sigma/n_{\text{tot}}$, with n_{tot} being the total number density of ions) or ionic mobility (μ_q) is presented as a function of the structural relaxation frequency (ω_s). This provides a way to calibrate the “intrinsic” conducting capability of an ionic material. A straight line of slope one, passing through a reference dilute salt aqueous solution such as KCl/H₂O and LiClO₄/H₂O (the “ideal” Walden line), divides the plane into superionic (above) and subionic (below) regimes. “Superior” ionic conductors are those that exhibit ionic mobility (or molar conductivity) much higher than the ideal line. Moreover, the degree of decoupling between conductivity

and segmental dynamics can be quantified by using the exponent α from the fractional Stokes–Einstein relation: $\mu_q = \omega_s^\alpha$ or $\Lambda = \omega_s^\alpha$; the smaller the α , the larger the degree of decoupling. $\alpha = 1$ corresponds to the case of complete coupling, while $\alpha \sim 0$ implies completely decoupled ion motions.

The original Walden plot analysis was performed in terms of fluidity ($1/\eta$), instead of structural relaxation frequency (ω_s). However, the ionic transport in polymers is controlled by microscopic rather than macroscopic viscosity. Our analyses have demonstrated that by using structural relaxation frequency, the Walden plot analysis could be successfully extended to polymer electrolytes, yielding new insights about the ionic transport mechanism in polymers [4, 48, 52, 59].

In the case of polyethers such as PEO and PPG, the ionic transport is closely coupled to their segmental relaxation. The Walden plot analysis further reveals that the ionic conductivity in polyethers falls surprisingly close to the “ideal” Walden line of aqueous solutions (Fig. 6.12) [4, 52]. This suggests that the ionic transport (friction) mechanism in polyethers is very similar to those of small-molecule liquid electrolytes. It follows that the relatively low conductivity in polyethers compared with liquid organic electrolytes is mainly a result of their sluggish segmental dynamics.

In contrast to polyethers, the ionic transport in other polymers can be strongly decoupled from their segmental dynamics. In general, two types of decoupling behavior have been observed (Fig. 6.16). In materials such as poly[poly(ethylene oxide) styrene]-polystyrene (PPEOS_t-PSt) and poly[4-(2-methoxyethoxy)methyl styrene] (PMOEMSt), ionic conductivity and polymer segmental relaxation exhibit very different temperature dependence, giving rise to prominent fractional Stokes–Einstein behavior. Although these samples fall into the subionic regime at high temperatures due to poor ion solvation, the decoupling between conductivity and segmental relaxation brings them to the superionic regime at low temperatures. A different kind of decoupling behavior is observed in polymers such as poly(vinyl carbonate)-*co*-poly[poly(ethylene glycol methyl ether methacrylate)] (PVC-PPEGMEMMA) and poly(vinyl ethylene carbonate)-*co*-poly(vinyl acetate) (PVEC-PVAc), where the relative rates of ionic transport and segmental relaxation are decoupled. These materials show up in the superionic regime at all temperatures.

The observation of decoupled conductivity in polymer electrolytes challenges the classical picture of ionic transport in polymers. Although the DBP model and the recent theoretical and experimental studies of the fragility of polymer segmental dynamics provide some rationale for the observed decoupling phenomenon, our understanding of the ionic transport mechanism in polymers is still far from complete. On the other hand, decoupling ionic conductivity from polymer segmental relaxation might provide an alternative approach to the design of highly conductive materials.

6.4 Summary

The recent advances in the field of ionic liquids have provided tremendous opportunities for many areas in science and engineering. Our understanding of ionic liquids as well as polymerized ionic liquids could benefit greatly from the development in the field of polymer electrolytes. The addition of salt to polymers gives rise to new relaxation processes. At the same time, increased ionic conductivity makes the analysis of dielectric spectrum a challenge. However, with proper treatment of EP and help from derivative analysis, the “hidden” dielectric relaxation processes can still be resolved. In addition, it is possible to extract information about free-ion number density and diffusivity from analysis of the EP phenomenon. Dielectric spectroscopy provides information on both polymer segmental dynamics and ionic conductivity, and thus allows one to examine the ion transport mechanism in polymers. While in flexible polymers such as polyethers, the ionic transport is closely coupled to polymer segmental dynamics, decoupled conductivity is found in rigid, fragile polymers.

Acknowledgments The writing of this book chapter was supported by the Oak Ridge National Laboratory’s Center for Nanophase Materials Sciences, which is a DOE Office of Science User Facility.

References

1. Di Noto V, Lavina S, Giffin GA, Negro E, Scrosati B (2011) *Electrochim Acta* 57:4–13
2. Shin J-H, Henderson WA, Passerini S (2005) *Electrochem Solid-State Lett* 8:A125–A127
3. Fragiadakis D, Dou S, Colby RH, Runt J (2008) *Macromolecules* 41:5723–5728
4. Fan F, Wang Y, Sokolov AP (2013) *Macromolecules* 46:9380–9389
5. Takeo F, Mariko I, Hiroshi Y (1997) *Jpn J Appl Phys* 36:1119
6. Yoshida K, Manabe H, Takahashi Y, Furukawa T (2011) *Electrochim Acta* 57:139–146
7. Furukawa T, Mukasa Y, Suzuki T, Kano K (2002) *J Polym Sci Part B Polym Phys* 40:613–622
8. Klein RJ, Zhang SH, Dou S, Jones BH, Colby RH, Runt J (2006) *J Chem Phys* 124:144903
9. Kremer F, Schöhal A (2002) *Broadband dielectric spectroscopy*. Springer-Verlag, Berlin
10. Wübberhorst M, van Turnhout J (2002) *J Non-Cryst Solids* 305:40–49
11. Schwab HP (1968) *Ann N Y Acad Sci* 148:191–209
12. Serghei A, Sangoro JR, Kremer F (2012) *Broadband dielectric spectroscopy on electrode polarization and its scaling*. In: Ohshima H (ed) *Electrical phenomena at interfaces and biointerfaces: fundamentals and applications in nano-, bio-, and environmental sciences*. Wiley, Hoboken, New Jersey
13. Barbero G, Scalerandi M (2012) *J Chem Phys* 136:084705
14. Macdonald JR (1973) *J Chem Phys* 58:4982–5001
15. Sørensen TS, Compañ V (1995) *J Chem Soc Faraday Trans* 91:4235–4250
16. Coelho R (1991) *J Non-Cryst Solids* 131–133:1136–1139
17. Uemura S (1972) *J Polym Sci Polym Phys Ed* 10:2155–2166
18. Sawada A, Tarumi K, Naemura S (1999) *Jpn J Appl Phys* 38:1418–1422
19. Feldman Y, Polygalov E, Ermolina I, Polevaya Y, Tsentsiper B (2001) *Meas Sci Technol* 12:1355–1364

20. Macdonald JR (1953) *Phys Rev* 92:4–17
21. Wang Y, Sun C-N, Fan F, Sangoro JR, Berman MB, Greenbaum SG, Zawodzinski TA, Sokolov AP (2013) *Phys Rev E* 87:042308
22. Sawada A (2013) *Phys Rev E* 88:032406
23. Trukhan EM (1963) *Sov Phys Solid State (Engl Transl)* 4:2560
24. Munar A, Andrio A, Iserte R, Compañ V (2011) *J Non-Cryst Solids* 357:3064–3069
25. Wang Y, Agapov AL, Fan F, Hong K, Yu X, Mays J, Sokolov AP (2012) *Phys Rev Lett* 108:088303
26. Choi UH, Mittal A, Price TL, Gibson HW, Runt J, Colby RH (2013) *Macromolecules* 46:1175–1186
27. Fragiadakis D, Dou S, Colby RH, Runt J (2009) *J Chem Phys* 130:064907
28. Tudryn GJ, Liu WJ, Wang SW, Colby RH (2011) *Macromolecules* 44:3572–3582
29. Wang SW, Liu WJ, Colby RH (2011) *Chem Mater* 23:1862–1873
30. Atornigijawat P, Runt J (2007) *J Phys Chem B* 111:13483–13490
31. Zhang S, Runt J (2004) *J Phys Chem B* 108:6295–6302
32. Kano K, Takahashi Y, Furukawa T (2001) *Jpn J Appl Phys* 40:3246–3251
33. Fontanella JJ (1999) *J Chem Phys* 111:7103–7109
34. Bendler JT, Fontanella JJ, Shlesinger MF (2001) *Phys Rev Lett* 87:195503
35. Bendler JT, Fontanella JJ, Shlesinger MF, Wintersgill MC (2003) *Electrochim Acta* 48:2267–2272
36. Druger SD, Nitzan A, Ratner MA (1983) *J Chem Phys* 79:3133–3142
37. Druger SD, Ratner MA, Nitzan A (1985) *Phys Rev B* 31:3939–3947
38. Druger SD, Ratner MA, Nitzan A (1986) *Solid State Ionics* 18–19, Part 1:106–111
39. Nitzan A, Druger SD, Ratner MA (1987) *Philos Mag Part B* 56:853–859
40. Ratner MA, Shriver DF (1988) *Chem Rev* 88:109–124
41. Richert R, Agapov A, Sokolov AP (2011) *J Chem Phys* 134:104508
42. Hubbard J, Onsager L (1977) *J Chem Phys* 67:4850–4857
43. Wolynes PG (1978) *J Chem Phys* 68:473–483
44. Wolynes PG (1980) *Ann Rev Phys Chem* 31:345–376
45. Zwanzig R (1963) *J Chem Phys* 38:1603–1605
46. Zwanzig R (1970) *J Chem Phys* 52:3625–3628
47. Biswas R, Roy S, Bagchi B (1995) *Phys Rev Lett* 75:1098–1101
48. Wang Y, Sokolov AP (2015) *Curr Opin Chem Eng* 7:113–119
49. Cohen MH, Turnbull D (1959) *J Chem Phys* 31:1164–1169
50. Turnbull D, Cohen MH (1961) *J Chem Phys* 34:120–125
51. Killis A, Le Nest JF, Gandini A, Cheradame H, Cohen-Addad JP (1984) *Solid State Ionics* 14:231–237
52. Wang Y, Fan F, Agapov AL, Yu X, Hong K, Mays J, Sokolov AP (2014) *Solid State Ionics* 262:782–784
53. Ratner MA, Johansson P, Shriver DF (2000) *MRS Bull* 25:31–37
54. Sasabe H, Saito S (1972) *Polymer J* 3:624–630
55. Imrie CT, Ingram MD, McHattie GS (1999) *Adv Mater* 11:832–834
56. Wei X, Shriver DF (1998) *Chem Mater* 10:2307–2308
57. Zhang S, Chang Z, Xu K, Angell CA (2000) *Electrochim Acta* 45:1229–1236
58. Agapov AL, Sokolov AP (2011) *Macromolecules* 44:4410–4414
59. Wang Y, Fan F, Agapov AL, Saito T, Yang J, Yu X, Hong K, Mays J, Sokolov AP (2014) *Polymer* 55:4067–4076
60. Kunal K, Robertson CG, Pawlus S, Hahn SF, Sokolov AP (2008) *Macromolecules* 41:7232–7238
61. Stukalin EB, Douglas JF, Freed KF (2009) *J Chem Phys* 131:114905
62. Barton JL (1966) *Verres Refract* 20:328
63. Nakajima T (1971) Conference on electric insulation and dielectric phenomena. Annual Report. National Academy of Sciences, Washington DC, pp 168
64. Namikawa H (1975) *J Non-Cryst Solids* 18:173–195

65. Sangoro JR, Iacob C, Agapov AL, Wang Y, Berdzinski S, Rexhausen H, Strehmel V, Friedrich C, Sokolov AP, Kremer F (2014) *Soft Matter* 10:3536–3540
66. Angell CA, Ansari Y, Zhao Z (2012) *Faraday Discuss* 154:9–27
67. Belieres J-P, Angell CA (2007) *J Phys Chem B* 111:4926–4937
68. Belieres J-P, Gervasio D, Angell CA (2006) *Chem Commun* 0:4799–4801
69. Xu W, Angell CA (2003) *Science* 302:422–425
70. Angell CA, Liu C, Sanchez E (1993) *Nature* 362:137–139

Chapter 7

Electrochemical Double Layers in Ionic Liquids Investigated by Broadband Impedance Spectroscopy and Other Complementary Experimental Techniques

Bernhard Roling, Marco Balabajew and Jens Wallauer

Abstract Ionic liquids consist of large asymmetric organic cations and of weakly coordinating anions, i.e., anions with a highly delocalized negative charge. Ionic liquids (IL) exhibit remarkable physicochemical and electrochemical properties, in particular, high thermal stability, low vapor pressure, high ionic conductivity, and broad electrochemical window (Buzzeo and Evans in *ChemPhysChem* 5:1106, 2004 [1], Endres and Zein El Abedin in *Phys Chem Chem Phys* 8:2101, 2006 [2], Galiński et al. in *Electrochim Acta* 8:2101 [3]). By changing the functional groups of cations and by varying the cation/anion combination, the properties of ionic liquids can be adjusted to particular requirements. Thus, ionic liquids are being called *designer solvents*. They are considered as promising electrolytes for different kinds of electrochemical cells, e.g., for electrosynthesis (Buzzeo and Evans in *ChemPhysChem* 5:1106, 2004 [1], Hapiot and Lagrost in *Chem Rev* 108:2238, 2008 [4]), for electroanalysis (Buzzeo and Evans in *ChemPhysChem* 5:1106, 2004 [1], Baker et al. in *Analyst* 130:800, 2005 [5]), for electrodeposition of metals (Endres and Zein El Abedin in *Phys Chem Chem Phys* 8:2101, 2006 [2], Endres et al. in *Phys Chem Chem Phys* 12:1724, 2010 [6], Endres et al. in *Angewandte Chemie (International ed. in English)* 42:3428, 2003 [7]), for energy storage in batteries and supercapacitors (Sillars et al. in *Phys Chem Chem Phys* 14:6094, 2012 [8], Simon and Gogotsi in *Nat Mater* 7:845, 2008 [9], Lewandowski and Świdorska-Mocek in *J Power Sources* 194:601, 2009 [10], Srouf et al. in 200th ECS meeting. ECS, pp 23–28, 2012 [11]), for energy conversion in dye-sensitized solar cells (Grätzel in *Acc Chem Res* 42:1788, 2009 [12]) and for double layer field-effect transistors (Yuan et al. in *Adv Funct Mater* 19:1046, 2009 [13]). For all these electrochemical applications, the structure and dynamics of the interfacial double layer between ionic liquids and electrode materials plays a crucial role, see for instance Ref. (Endres et al. in *Phys Chem Chem Phys* 12:1724, 2010 [6]). Since

B. Roling (✉) · M. Balabajew · J. Wallauer
Fachbereich Chemie, Philipps-Universität Marburg, Hans-Meerwein-Strasse 4, 35032
Marburg, Germany
e-mail: roling@staff.uni-marburg.de

ILs are highly concentrated ionic fluids, the classical STERN model for double layers in diluted electrolytes, in which the ions are treated as point charges, is not applicable. In the case of ionic liquids, the finite volume of the ions, the chemical structure of the ions, and specific interactions of the ions with the electrode surface have to be taken into account. In order to obtain information about the structure and dynamics of the double layer, various experimental techniques have been applied. Broadband impedance spectroscopy in a three-electrode setup yields electrode potential-dependent double layer capacitance values of the electrode | IL interface. Complementary information has been obtained from other techniques, such as scanning tunneling microscopy, atomic force microscopy, surface force apparatus measurements, X-ray reflectivity measurements, surface-enhanced Raman spectroscopy, and sum-frequency generation vibrational spectroscopy. In this chapter, we describe the current level of understanding of the electrode | IL interface based on the combination of the complementary techniques.

7.1 Broadband Impedance Spectroscopy

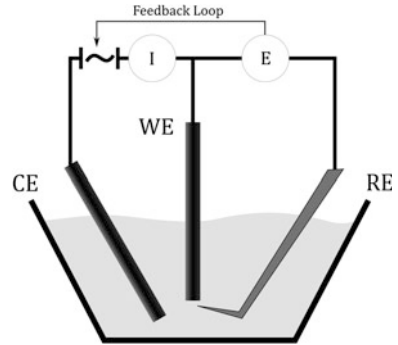
7.1.1 Introduction

The term *Impedance Spectroscopy* stems from the fact that the method probes the complex AC resistance—the impedance—of a system at different frequencies of the applied AC voltage or current. Dielectric effects, like dipole reorientation, and electrochemical processes, like charge transfer reactions or double layer charging, lead to characteristic, frequency-dependent impedance responses, and can thus be examined both qualitatively and quantitatively. With the availability of very powerful impedance spectrometers and computers, the method has developed into an important cornerstone for the characterization of dielectrics, of electrochemical materials and cells, and of many other types of systems.

In an electrochemical impedance spectroscopic (EIS) experiment, an AC voltage or current of a specific frequency is applied to an electrochemical cell, and the response signal (the AC current or voltage, respectively) is measured. The AC frequency is varied over many orders of magnitude, typically from MHz to mHz, which allows the investigation of processes taking place on different time scales. In addition to the AC excitation signal, a DC signal can be applied as well. The method has been used for characterizing different types of electrochemical cells, such as batteries [14–19], supercapacitors [20–24], fuel cells [25–27], solar cells [28–31], and cells for corrosion measurements [32–36] (see Fig. 7.1).

EIS has also been applied for studying ion transport in solid [37] and liquid electrolytes [38]. Recently, solid electrolytes for lithium batteries have attracted increasing interest, as the replacement of liquid by solid electrolytes can lead to an improved energy density and safety of batteries. However, many solid electrolytes exhibit rather low ionic conductivities and limited electrochemical stabilities in

Fig. 7.1 Schematic representation of a typical three-electrode for EIS experiments, consisting of a working (WE), a counter (CE) and a reference electrode (RE)



contact to the electrode materials [39–41]. Hence, a lot of research effort is devoted to improving the ionic conductivity as well as the electrochemical [42, 43], chemical [44, 45], and thermal [46, 47] stability of solid electrolytes. EIS measurements on solid electrolytes yield the total ionic conductivity in a straightforward manner, but allows in addition for the differentiation between different ion transport processes, for example along grains or grain boundaries [48–52].

EIS measurements can also be applied to the investigation of metal | electrolyte interfaces [53–56]. Here, the measurements give access to the differential capacitance of the double layer as a function of the electrode potential. Different types of charge storage processes taking place on different time scales can be distinguished, which is relevant, e.g., for the charge storage in supercapacitors.

7.1.2 Theory of Impedance Spectroscopy

In EIS experiments, the system is excited by the application of an AC signal. The excitation can be either an AC voltage or an AC current. In the following discussion, the excitation by an AC voltage will be considered. An equivalent discussion for the excitation by an AC current can be found in [57, 58].

The applied voltage with DC bias U_{DC} , amplitude U_0 , and angular frequency $\omega = 2\pi f$ can be written as

$$U(t) = U_{\text{DC}} + U_0 \sin(\omega t). \quad (7.1)$$

The resulting AC current can be expressed by a Taylor series around U_{DC}

$$I(t) - I_{\text{DC}} = \left(\frac{\partial I}{\partial U} \right)_{U=U_{\text{DC}}} [U(t) - U_{\text{DC}}] + \frac{1}{2} \left(\frac{\partial^2 I}{\partial U^2} \right)_{U=U_{\text{DC}}} [U(t) - U_{\text{DC}}]^2 + \dots \quad (7.2)$$

The AC current can be split into a sum of periodic functions consisting of the base frequency ω and its higher integer harmonics $2\omega, 3\omega, \dots$ by means of a Fourier analysis. The harmonics can contain additional information about the system, however, a discussion of this is beyond the scope of this chapter. In conventional EIS measurements, a small excitation amplitude is used, so that only the linear term in the Taylor series is relevant (linear response regime). In this case, the AC current can be written as

$$I(t) - I_{\text{DC}} = I_0 \sin(\omega t - \varphi) \quad (7.3)$$

Here, I_0 denotes the amplitude, while φ is a phase shift between AC voltage and AC current. The amplitudes U_0 and I_0 and the phase shift φ can be used to define a complex impedance

$$\hat{Z}(\omega) \equiv \frac{U_0}{I_0} \cdot \exp(i\varphi) = Z'(\omega) + iZ''(\omega). \quad (7.4)$$

Alternatively, the complex admittance

$$\hat{Y}(\omega) = \frac{1}{\hat{Z}(\omega)}, \quad (7.5)$$

and the complex capacitance

$$\hat{C}(\omega) = \frac{1}{i\omega\hat{Z}(\omega)} \quad (7.6)$$

can be considered.

Impedance spectra are often plotted in a Nyquist representation. In this case, $-Z''(\omega)$ is plotted versus $Z'(\omega)$. Different electrochemical processes manifest usually in different semicircles.

In order to extract quantitative information from impedance spectra, the spectra are usually fitted by suitable, parameterized model functions. The most common model functions are derived from electrical equivalent circuits consisting of typical elements given in Table 7.1. In the case of a pure resistor, the phase φ is zero, while a pure capacitor and a pure inductor cause a phase shift of -90° and $+90^\circ$, respectively.

The Warburg impedance is used to describe the diffusion of an electroactive species from the electrolyte towards a planar electrode surface or into the opposite direction. The increase of the thickness of the diffusion layer with \sqrt{t} is reflected in the increase of both real- and imaginary parts with $1/\sqrt{\omega}$. A pure Warburg element causes a phase shift of -45° . A constant phase element (CPE) is a generalized element allowing for phase shift between -90° and $+90^\circ$, depending on the value of β . CPEs have been used to describe the charging of a double layer at a rough

Table 7.1 Impedance response of common electrical and electrochemical elements

Element	Impedance response
Resistor	$\hat{Z}(\omega)_{\text{Resistor}} = R$
Capacitor	$\hat{Z}(\omega)_{\text{Capacitor}} = \frac{1}{i\omega C}$
Inductor	$\hat{Z}(\omega)_{\text{Inductor}} = i\omega L$
Constant phase element	$\hat{Z}(\omega)_{\text{CPE}} = \frac{1}{(i\omega)^{\beta} Q}$
Warburg impedance	$\hat{Z}(\omega)_{\text{Warburg}} = \frac{\sigma}{\sqrt{\omega}} - i \frac{\sigma}{\sqrt{\omega}}$

electrode [59, 60], even though newer research has shown, that the electrode roughness has no direct correlation with CPE behavior [61, 62].

EIS measurements are usually done in either two- or three-electrode configurations. In a two-electrode cell, a potentiostat applies a sinusoidal voltage with a given amplitude and frequency between two electrodes and measures the resulting AC current. In this case, the impedance of the entire cell is obtained. In a three-electrode configuration, an additional, currentless reference electrode is added. The potentiostat now varies the voltage between the working electrode and the counter electrode, until the voltage between the working electrode and the reference electrode reaches a predefined value. Since the reference electrode has a constant electrical potential, changes in the potential of the working electrode can be distinguished from changes of the potential of the counter electrode. Consequently, the impedance between the working electrode and the reference electrode is obtained.

Modern frequency response analyzers (FRA) [57, 63] perform an on-the-fly Fourier analysis of the measured current waveforms [64]. The waveforms are correlated (multiplied) with a reference signal of the same frequency as the excitation. The correlated signal is then integrated over one or multiple periods. If this is done with both a sine and a cosine reference signal, the real and imaginary parts can be extracted simultaneously. Higher harmonics can be extracted using reference signals with higher frequencies of $2\omega, 3\omega$, etc. There are other techniques for measuring the impedance, but despite the relatively high costs of FRAs, the advantages in terms of data quality, speed, and versatility made FRAs the de facto standard in modern research.

7.1.3 Practical EIS Pitfalls

Despite modern tools, there are several potential pitfalls when measuring and analyzing impedance spectra. Some of them shall be considered in the following paragraphs.

7.1.3.1 Cell Design for Three-Electrode Measurements

During an impedance measurement with three electrodes, artifacts may occur in the impedance spectra, which are related to the impedance and to the positioning of the reference electrode [65, 66]. One source of artifacts is related to the impedance of the reference electrode. If this impedance is not much smaller than the input impedance of the analyzer, a voltage divider effect occurs that can alter both the amplitude and the phase of the measured impedance.

The cell geometry, especially the positioning of the reference electrode, is a second possible cause for artifacts, as the reference electrode should probe an equipotential line in the cell [67, 68]. These equipotential lines are, however, frequency dependent, which complicates the correct positioning of the reference electrode. New cell and electrode designs need to be verified carefully to avoid these artifacts [69].

A third source of artifacts is stray capacitances between the three electrodes in the cell [70]. Often, these stray capacitances are caused by an insufficient shielding of the cables connecting the electrodes with the potentiostat. For the analysis of stray capacitance artifacts, three-terminal equivalent networks have been used [65, 70–72]. Depending on the impedance ratios of the electrodes and the values of the stray capacitances, different types of capacitive and inductive artifacts can appear in the spectra. These artifacts can be minimized by choosing short and, if possible, actively shielded cables.

7.1.3.2 Non-stationary Electrochemical Systems

The analysis of electrochemical impedance spectra by means of specific models or equivalent circuits can only be done in a reliable fashion, if the system is in an equilibrium state or in a stationary state. In electrochemical systems, it may take a considerable amount of time to reach such a state. If a measurement is started before reaching such a state, the impedance of the system changes during the recording of an impedance spectrum. These time-dependent changes lead to artifacts, in particular in the low-frequency regime. Such artifacts can be detected by means of a Kramers-Kronig test [73–76], since the measured spectra are not in accordance with the predictions of the Kramers-Kronig relations.

Consequently, it is important to allow the electrochemical system to equilibrate or to reach a stationary state, before an electrochemical impedance measurement is started. The time interval needed for this has to be determined individually for each system.

7.1.3.3 Fitting Algorithms

Once the spectra are recorded and a suitable model is chosen, the model needs to be fitted to the data [77, 78]. This is done by means of a software that employs

nonlinear curve fitting algorithms [79–82] in order to find parameter values, which minimize the discrepancy between the experimental values and the model values. More specifically, the sum of squared residuals (ESS)

$$\text{ESS} = \sum_{n=1}^N w'_n (Z'_{\text{data}} - Z'_{\text{model}})^2 + w''_n (Z''_{\text{data}} - Z''_{\text{model}})^2 \quad (7.7)$$

is minimized. Here, w'_n and w''_n are weighting factors.

The nonlinearity of the model requires the fit to be initialized with a set of parameters as a starting point for an iterative optimization. Choosing the starting parameters can be a tough problem, since the fit tends to converge into local minima of the ESS function. An additional problem is that often too complex models are chosen by the user, which causes parameters to become correlated. This means, for example, that increasing one parameter causes another to decrease, which makes it hard for the algorithm to find an unambiguous solution. As a rule of thumb, one should try to assign a physical meaning to all parameters in the model or to fix certain parameters to independently determined values.

A point to be considered is the weighting of data points via the factors w'_n and w''_n . Weighting implies that some data points contribute more to the overall ESS than others. This can help in fitting small features in the data set, but may lead to “weird” results in other cases. Reported fit results should contain information about the used weighting model.

7.1.4 Application to Metal | IL Interfaces

7.1.4.1 Introduction

As already mentioned, the classical Stern model for double layers in diluted electrolytes is not applicable to ionic liquids. In ionic liquids, the structure and dynamics of the interfacial double layer is fundamentally different [56]. This is reflected in the differential double layer capacitance ΔC_{DL} , which can be obtained by means of electrochemical impedance spectroscopy. ΔC_{DL} is defined as the derivative of the charge of the electrode q with respect to the electrode potential E at constant pressure p , temperature T , and chemical potential of the ions μ_i .

$$\Delta C_{\text{DL}} = \left. \frac{dq}{dE} \right|_{p,T,\mu_i} \quad (7.8)$$

The minimum prerequisite for describing double layers in concentrated electrolytes is to take into account the finite size of the ions. An elegant way to do this is to consider a mean-field lattice gas model [83]. In the simplest version, such a

model contains only two parameters, namely the electrode potential E and the site occupation number γ :

$$\gamma = \frac{n_{\text{occupied}}}{n_{\text{all}}} \quad (7.9)$$

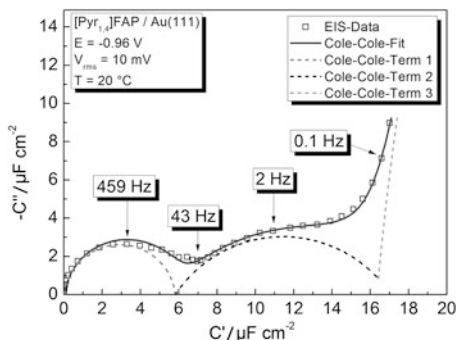
Here, n_{occupied} and n_{all} denote the number of the occupied lattice sites and the number of all lattice sites, respectively. If γ is small, charges can accumulate easily at the interface, and the differential capacitance increases with electrode potential. However, at high charge densities, the entropy loss caused by the charge accumulations becomes significant, and the differential capacitance decreases with increasing electrode potential. This effect is termed *lattice saturation*. The overall $\Delta C_{\text{DL}}(E)$ curve exhibits a camel-type shape. For γ values close to unity (highly concentrated electrolytes), lattice saturation takes place already at low charge densities, so that the differential capacitance drops continuously with increasing electrode potential (bell-shaped curve).

Experimental studies [54, 84–87] revealed that there is, in general, a much weaker dependence of ΔC_{DL} on E than predicted by the mean-field lattice gas model. Typical values for ΔC_{DL} are around 5–10 $\mu\text{F}/\text{cm}^2$. The actual shapes of the curves depend strongly on the ions that comprise the ionic liquid. This is not unexpected, since the actual shape of the ions strongly deviates from the spherical assumption. For example, IL cations are often composed of a charged core, for example an imidazolium ring, and an uncharged aliphatic side chain. Theoretical computations (DFT, MD, MC) produced results in better agreement [88–96] with experiments.

As an experimental example, measurements of the differential double layer capacitance of two ionic liquids, namely *N*-butyl-*N*-methyl-pyrrolidinium tris(pentafluoroethyl)trifluorophosphate ([Pyrr_{1,4}]FAP) and 1-ethyl-3-methylimidazolium tris(pentafluoroethyl)trifluorophosphate ([EMIm]FAP), in contact with a single-crystalline Au(111) electrode are discussed in the following. This dataset was previously published in [54].

The measurements were performed in a three-electrode cell with an Ag/AgTFSI/[EMIm]TFSI-based micro-reference electrode [97] and a platinum counter electrode. The working electrode consisted of a single-crystalline Au(111) thin film (200 nm) deposited on a mica substrate (Phasis). Ultrapure [Pyrr_{1,4}]FAP and [EMIm]FAP were dried in high vacuum conditions at elevated temperatures in order to remove residual water and other volatile impurities. The assembled cell was mounted on a Microcell HC cell stand (rhd instruments GmbH & Co. KG), which allowed for a precise control of the temperature. Starting at the open circuit potential, the electrode potential was swept in 10 mV steps in either anodic or cathodic direction. A freshly prepared working electrode and a fresh ionic liquid sample were used for each scanning direction in order to avoid irreversible processes during one sweep to affect the sweep in the opposite direction. After each potential step, the system was allowed to equilibrate for 10 min, before an impedance spectrum was recorded with an applied AC voltage of 10 mV (rms). The electrochemical measurements were performed using a POTGAL 10 V/15 A

Fig. 7.2 Capacitance spectrum of the Au (111) | [Pyrr_{1,4}]FAP interface in the complex capacitance plane (adapted from [54])



potentiostat in combination with an Alpha-A high-performance frequency analyzer (Novocontrol).

After completion of the impedance measurements, the reference electrode was calibrated by adding ~ 10 mM ferrocene to the electrolyte and measuring a cyclic voltammogram. In the following, the working electrode potentials are given with respect to the Fc^+/Fc half-wave potential.

For the data analysis, the spectra were transformed into the complex capacitance plane (CCP) and fitted using a sum of Cole-Cole-elements

$$\hat{C}(\omega) = C_\infty + \sum_i \frac{\Delta C_i}{1 + (i\omega\tau_i)^{\alpha_i}}. \quad (7.10)$$

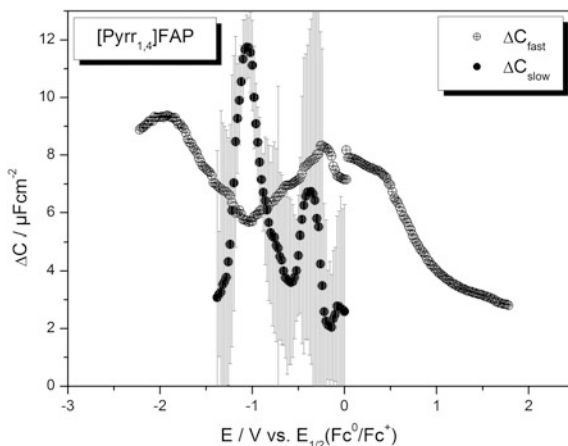
This method of analysis allows for differentiating between different capacitive processes taking place on different time scales and to determine their respective differential capacitance contribution and time scale. The fits were performed using the software RelaxIS (rhd instruments GmbH & Co. KG). The weights of the data points were chosen as the inverse squares of Z' and Z'' , respectively (*Proportional Weighting*).

A typical impedance spectrum in the CCP is shown in Fig. 7.2. The time constant for the fast capacitive process is in the millisecond regime, while the slower process takes place on the second time scale. At the lowest measured frequencies, the data rises quickly, which is most likely related to an ultraslow Faradaic process.

7.1.4.2 [Pyrr_{1,4}]FAP

Figure 7.3 shows differential capacitance curves for the pyrrolidinium-based ionic liquid [Pyrr_{1,4}]FAP. Both the differential capacitance of the fast process, ΔC_{fast} , and the differential capacitance of the slow process, ΔC_{slow} , are plotted versus the electrode potential E . The fast process is attributed to fast double layer charging governed by ion transport in bulk of the ionic liquid. The $\Delta C_{\text{fast}}(E)$ curve exhibits a more complex behavior than predicted by the mean-field lattice gas model. There is

Fig. 7.3 Differential capacitance of the fast and of the slow capacitive process, respectively, at the [Pyrr_{1,4}]FAP | Au(111) interface, plotted versus the electrode potential E (adapted from [54])



a local maximum around 0 V and an inverse square-root decrease of $\Delta C_{\text{fast}}(E)$ in the anodic regime, possibly due to a lattice saturation effect. The cathodic part, however, shows only a weak potential dependence, with a local minimum at -1 V. The differential capacitance of the slower process, ΔC_{slow} , is characterized by a sharp maximum around -1 V, where ΔC_{fast} exhibits a minimum. As will be shown in Sect. 7.2.2, this sharp maximum is related to a herringbone reconstruction of the Au(111) surface.

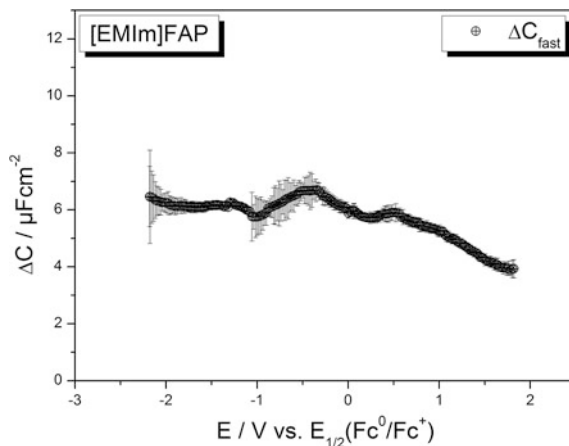
7.1.4.3 [EMIm]FAP

In order to test in what way the chemical structure of the cation influences the slow capacitive process, measurements on the ionic liquid [EMIm]FAP containing the same anion were carried out. In the case of this ionic liquid, a slow process was not detected, and the $\Delta C_{\text{fast}}(E)$ curve was more or less featureless, see Fig. 7.4. This provides strong indication that [Pyrr_{1,4}]⁺ | Au(111) interactions play an important role for the slow process. This is strongly supported by the observation that a slow process in the cathodic regime is also detectable in the case of [Pyrr_{1,4}]TFSI, but not in the case of [EMIm]TFSI [54]. More information about the slow process can be obtained when EIS is combined with STM measurements, see next section.

7.1.4.4 Conclusion

Broadband electrochemical impedance spectroscopy is capable of distinguishing fast and slow capacitive processes at the metal | IL interface and to provide values for the potential-dependent differential capacitance contributions of both processes, $\Delta C_{\text{fast}}(E)$ and $\Delta C_{\text{slow}}(E)$. The results can be compared to theoretical predictions

Fig. 7.4 Differential capacitance of the fast capacitive process at the Au (111) | [EMIm]FAP interface, plotted versus the electrode potential E (adapted from [54])



from mean-field models, DFT calculations, and simulations (MD, MC). An important prerequisite for reliable and reproducible $\Delta C_{\text{fast}}(E)$ and $\Delta C_{\text{slow}}(E)$ data is a high purity of the ionic liquids, since impurities may enrich at the metal | IL interface and influence the differential double layer capacitance.

Slow capacitive processes were mainly observed for pyrrolidinium-based ionic liquids in the cathodic regime. The slow processes appear to be related to a Herringbone reconstruction of the Au(111) surface, as observed in STM experiments (see Sect. 7.2.2).

Different methods for the analysis of complex impedance/capacitance data have been controversially discussed in the literature. We fitted the data in the complex capacitance plane using a Cole-Cole model. Other groups used constant phase elements for fitting the data in the complex impedance plane [55, 87]. Advantages and drawbacks of these approaches have been discussed in [61, 98].

7.2 Scanning Tunneling Microscopy

7.2.1 Introduction

Scanning tunneling microscopy (STM) is an imaging technique with high lateral resolution, which is based on measuring a tunneling current between a conducting sample and a sharp metallic tip. The tunneling current is very sensitive to the distance between tip and sample as well as to the density and population of electronic states in the sample and in the tip. The method was developed in 1981 by Binnig and Rohrer [99, 100], who were awarded the Nobel Prize in Physics in 1986 for their invention of, in their own words, “something which should ‘not have worked in principle’, as we were so often told” [101]. With STM, it is possible to

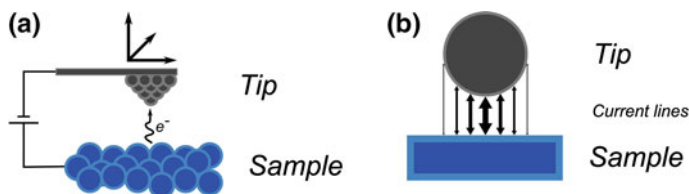


Fig. 7.5 **a** Schematic illustration of an STM with a metal tip over the metallic sample surface. **b** Illustration of the tunneling current at the very center of the tip and its exponential dependence on the distance between tip and sample

image single molecules or atoms on a sample surface. STM measurements can be carried out in air, in vacuum, and in liquids.

During an STM measurement, a metallic tip is moved towards the sample surface, and a voltage is applied between the two. The tip is comprised of, for example, tungsten metal and ideally ends in a single atom. The tip is usually vertically positioned at the tip/sample equilibrium distance, where attractive and repulsive forces cancel out. This avoids disturbances of the measurement. Using piezoelectric actuators, the tip is then precisely moved along the surface. The applied voltage causes electrons to tunnel between the tip and the sample, causing a measurable current flow. The current is exponentially dependent on the distance between tip and sample [100]. It is this fact that leads to the high lateral resolution, as the main tunneling current is related to the very center of the tip, as illustrated in Fig. 7.5b. The tunneling current is furthermore influenced by the local density of electronic states of the sample at a given position and by the density of electronic states of the metal tip. Since the density and population of states are affected by the applied voltage, by the sample composition and by the topography, a contrast in the STM images can be obtained and interpreted. The tip topography, composition, and quality can, however, not be neglected in the interpretation. This can either be a bane, if the tip quality is not high enough, but it also enables experiments where the tip is deliberately modified, e.g. by attaching specific molecules [102–104].

An STM can be used either in constant-current or constant-height mode. In constant-current mode, the height of the tip over the sample is adjusted by a feedback loop, in order to keep the current constant, giving an image of local density of states. In constant-height mode, the tip is fixed at a given height over the sample, which has the advantage that the scan rate is not limited by the feedback loop. Disadvantageous is the fact that long-term drifts of the system or large protrusions on the surface can lead to collisions between the tip and the surface.

In addition to simple imaging by lateral movement of the tip, advanced techniques are possible. In Scanning Tunneling Spectroscopy (STS), the tunneling current is recorded as a function of the applied voltage. The applied voltage affects the population of states in the sample and in the tip, and this allows for studying the local density of states (LDOS) by means of a bias scan [105]. The LDOS can be compared to density functional theory calculations.

If the imaging speed is sufficiently high—usually >1 Hz—it is possible to use the images for the so-called video-STM technique. Hereby, it is possible to record dynamic changes at the sample surface, such as diffusion phenomena or structural changes. The method can also be used for the investigation of metal | IL interfaces, as will be discussed in the next section.

7.2.2 Application to Metal | IL Interfaces

Experiments as well as simulations have shown that ionic liquids form rather complex structures when they are brought into contact with a metal electrode. One possible origin of the slow capacitive process seen in impedance spectroscopic measurements is a herringbone-type reconstruction of the metal surface. It was shown that an Au(111) surface can undergo a $22 \times \sqrt{3}$ reconstruction, where an additional gold atom is implanted into a chain of 22 atoms [106, 107]. This additional atom in the top layer leads to a local change of the crystal structure from fcc to hcp and to a bulging of the surface structure. This bulging is apparent in STM images as a characteristic, herringbone-like surface structure with well-defined atomic distances, by which it can be identified. As the surface structure changes, a restructuring in the double layer region may take place, leading to capacitive currents that are detected in the EIS experiments.

Another possible origin of slow capacitive processes is slow transitions in the structure of the ionic layers. Molecular dynamics simulations (MD) have shown that ionic liquids at metal surfaces can undergo transitions between multilayer structures with charge density oscillations and a single layer structure that compensates the full electrode charge [108]. The simulations further suggest that at very high electrode potentials, even a dual-layer structure of counter ions may exist, which, if observed from the top, resembles a herringbone-type structure.

The restructuring of the Au | IL interface was investigated for a number of ionic liquids using in situ STM. A few examples are shown and discussed below.

In 2006, Pan and Freyland [110] investigated the behavior of an Au(111) single crystal in [BMIm]PF₆ using in situ STM measurements. They reported the occurrence of a Moiré-like pattern of bright spots that is clearly visible on the flat Au (111) terraces. At moderate electrode potentials between -0.5 and $+0.5$ V, the pattern is only slightly potential-dependent. The pattern is very regular with a distance of 0.45 – 0.48 nm between the spots. The authors interpret this pattern as a compressed PF₆[−] adlayer and underline this by FFT filtering of the images. Remarkably, the formation of the adlayer is not associated with a peak in cyclic voltammetry measurements, which suggests that the initial formation of the structure is not driven by the applied potential. This correlates well with the weak dependence of the images on the applied potential. However, when the potential is driven to more negative values, the authors state that “a long-range restructuring occurs with the emergence of tiny pits, which cover all the Au(111) surface and

finally develops into a stable worm-like network” [110]. This behavior of the adlayer is an illustrative example of the complex interactions between the components of the ionic liquid and the metal electrode and provides an explanation as to why different ionic liquids can show dramatically different behavior at interfaces.

Further back in 2003, Lin [111] found a similar behavior of $[\text{BMIm}]\text{BF}_4$. The authors observed that at negative electrode potentials, a slow formation of atomic height deep pits takes place, ending up in a wormlike-pattern, similar to the one described by Pan and Freyland [110]. At low electrode potentials, Lin could not resolve a BF_4^- pattern.

Endres et al. published several papers on STM studies of metal | IL interfaces, in several cases combined with AFM studies by Atkin et al. and EIS studies by Roling et al. [53, 109]. STM allowed for detailed study of the herringbone-type reconstruction of the Au(111) surface in $[\text{Pyrr}_{1,4}]\text{FAP}$. At moderate cathodic potentials of around -0.7 V, only a fraction of the surface was covered by the herringbone structure, while at higher potentials of -1.2 V, the complete surface was covered, see Fig. 7.6. At even more negative potentials around -2 V, the herringbone structure was not detectable anymore.

In the anodic regime, no herringbone structure could be observed [112]. Instead, a more blurred out structure was found, most likely caused by disordered anion-rich layers. At high anodic potentials, the terrace steps became less clearly visible and islands almost completely disappeared, which was explained with the formation of an adsorbed anion layer.

In 2013, Buchner et al. [113] presented a paper with a demonstration how STM imaging can be combined with DFT calculations in order to distinguish between anions and cations in an image. This combination is a valuable tool for the understanding of structural features. In contrast to classical *in situ* methods, this experiment was carried out on a thin layer of the ionic liquid $[\text{Pyrr}_{1,4}]\text{TFSI}$ evaporated onto a single-crystalline silver surface in UHV. The STM images were recorded at 100 K, where the authors were able to identify different 2D structures on the surface, such as crystalline or glass-like phases. The crystalline phases contained ordered rows of dots and pairs of elongated structures. DFT calculations were performed in order to evaluate possible and likely configurations of the

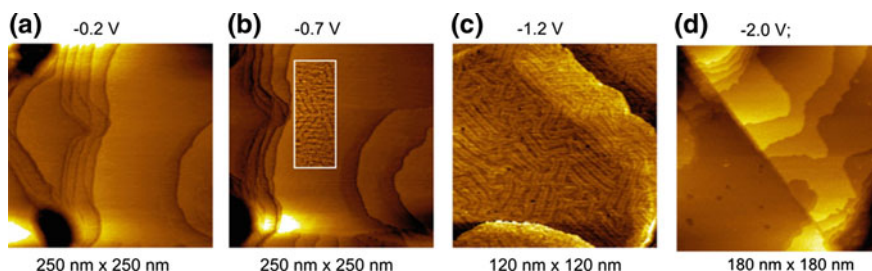


Fig. 7.6 Emergence of the herringbone-type structure on an Au(111)-surface in contact to $[\text{Pyrr}_{1,4}]\text{FAP}$ upon application of cathodic electrode potentials (adapted from [109])

molecules on the surface and to simulate STM images. The simulations were then compared with the STM images, and this comparison led to the conclusions that the dots represent the cations and the pairs of elongated structures the anions. The appearance of the anions as two entities could be related to the existence of the two terminal CF_3 groups on the TFSI anion.

A recent paper by Wen et al. [114] demonstrated the capability of in situ video-STM measurements for the imaging of dynamic changes in the structure of $\text{Au}(111) | \text{IL}$ interfaces. The results provided strong indications that dynamic changes in the surface structure are caused by reorientations of the cations. Video-STM techniques allow the recording of 10–15 images per second, corresponding to a time resolution in the 100 ms regime [115]. The cations are often comprised of a charged core, like an imidazolium ring, and a long alkyl chain connected to this core. During scanning into the cathodic regime, the tail shifts from lying on the surface to pointing into the bulk of the ionic liquid, which allows for a closer packing of the cations on the surface. This slow process should lead to a peak in $\Delta C_{\text{slow}}(E)$. As in the UHV measurements by Buchner et al. [113], the authors found a strong influence of steps between terraces on single-crystalline surfaces on the structure and dynamics of the interfacial layers. The steps appear to act as crystallization seeds facilitating the formation of crystalline 2D structures.

Overall, the high lateral and vertical resolution of the STM as well as the capability for in situ measurements make it a powerful method for identifying the structural changes responsible for slow capacitive processes.

7.3 X-Ray Reflectivity

7.3.1 Introduction

X-ray reflectivity (XRR) measurements can be used to measure the density profiles of ionic liquids at the metal interface [116]. This can provide information about the structure of the ion layers and about the fractions of cations and anions in these layers. In comparison to other techniques, like impedance spectroscopy, STM and AFM, the method has not seen widespread adoption, which may be mainly due to the experimental complexity of the measurements (see Fig. 7.7).

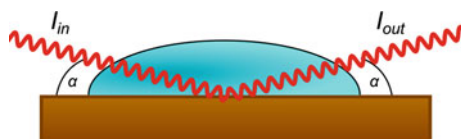


Fig. 7.7 General setup of X-ray reflectivity measurements at solid | liquid interfaces. A liquid film is deposited onto the solid sample and irradiated under small angles of incident by a high-energy X-ray beam

In XRR measurements, the sample is illuminated by a beam of X-ray radiation of a specific wavelength λ under a small angle of incident α . The wavelength and the angle of incident determine the normal momentum transfer q

$$q = \frac{4\pi}{\lambda} \sin \alpha \quad (7.11)$$

If the sample is perfectly flat, the intensity of the reflected radiation can be described by the Fresnel equations. However, if the surface is irregular or consists of multiple layers, deviations from the Fresnel equations are observed. The intensity of the reflected light is measured and usually normalized to the intensity expected from the Fresnel reflectivity. This normalized intensity $I_{\text{norm}}(q)$ is measured as a function of the normal momentum transfer q . The size of surface features d_f can be estimated from maxima in $I(q)$ at $q = q_e$ via

$$d_f \approx 2\pi/q_e. \quad (7.12)$$

To derive quantitative information from the data it is usually necessary to find a suitable, parameterized model, which can describe the expected features of the surface layers. Such a model is then fitted to the measured data.

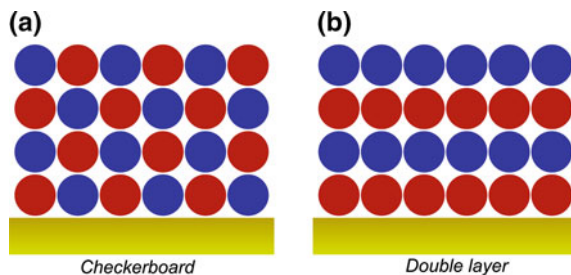
Due to the high beam energies, in particular at synchrotron beam facilities, the method can achieve a very high, submolecular resolution. The high beam energy, however, is also the main source of experimental complexity. Besides the lack of laboratory-sized synchrotron beamlines, the high energy of the radiation requires a very stable measurement setup and precautions for avoiding radiation damage of the sample by the beam. The latter can be achieved, for example, by lateral movement of the sample during the measurement [116].

Conventional so-called hard XRR measurements make use of radiation with energies in the range of 50–100 keV and cannot distinguish between atoms with different mass numbers. This makes it hard to identify the chemical species that comprise the individual layers. An alternative method is to employ soft, resonant XRR measurements [117] that probe a specific atom type using radiation around the atom's K-edge. Due to the strong energy dependence of the scattering factors around the absorption edge, which can be independently determined by NEXAFS, it is possible to derive a molecular model of the composition of the different ion layers. Since ionic liquid anions and cations often contain different atom types (e.g., fluorine in FAP^- anions), the method can distinguish anion-rich and cation-rich layers.

7.3.2 Application to Solid | IL Interfaces

Only very few X-ray based measurements on ionic liquid interfaces were conducted before 2008, when Mezger et al. [116] published an X-ray reflectivity study of three FAP^- -based ionic liquids on a sapphire surface. The measurements were conducted at a synchrotron beamline under vacuum conditions. The sample temperature could

Fig. 7.8 Different types of ion arrangements at a solid | IL interface. The ions can either be aligned in **a** a checkerboard-like arrangement or **b** in separate ion layers with alternating charge densities (double layer arrangement)



be adjusted, allowing measurements below and above the melting points of the ionic liquid. Due to the high beam energy, it was possible to achieve a normal resolution of 4.5 Å. The authors established a parameterized model for the reflectivity, which could distinguish between two specific surface structures of the anions and cations, namely a checkerboard-like pattern and a double layer-like pattern, see Fig. 7.8. The checkerboard-like pattern is expected, if cation–anion interactions are stronger than ion–metal interactions. If, on the other hand, the interaction of one type of ion with the metal surface predominates, a double layer-like pattern is expected. Fitting the models to the data then provides information about likelihood of the different patterns and about the thickness of the individual ion layers.

The results suggested that the double layer-like pattern is the better description of the layer structure. The structure is characterized by a cation-rich innermost layer with a thickness of 4–5 Å and by charge density fluctuations extending by more than 5 nm into the bulk. This result is in line with the overscreening effect at metal | IL interfaces discussed by Kornyshev [83], Bazant et al. [118] and was also observed in molecular dynamics simulations [108]. The fact that the innermost layer was mainly comprised of cations was attributed to the fact that the sapphire surface became negatively charged under X-ray illumination, leading to surface potentials between –0.5 and –1.3 V [116]. Temperature-dependent XRR measurements revealed that the spacing between the individual ion layers increases with increasing temperature, while the distance of the innermost ion layer from the surface decreases. These results illustrate very nicely the potential of the method for the characterization of solid | IL interfacial layers.

Subsequently, other groups applied the method to other solid | IL interfaces. Brkljača et al. [119] measured the XRR of the ionic liquid [EMIm]TFSI on a sapphire surface and combined the measurements with molecular dynamics simulations in order to gain insight into the structure of the double layer region on a molecular scale. The group found that, similar to the results of Mezger et al. [116], the interfacial structure can be described as a double layer arrangement with a cation-rich innermost layer and charge oscillations extending up to 50 Å into the bulk.

In order to obtain more direct information about the fractions of cations and anions in the ion layers, Mezger et al. [117] employed soft, resonant XRR. Here, X-ray radiation with an energy near the K-edge of fluorine was applied to the Au | [C₁₈MIm]FAP interface in order to obtain information about the distribution

of FAP^- anions in different interfacial ion layers. By combining the XRR measurements with energy-dependent scattering factors derived from NEXAFS measurements, the authors were able to produce a molecular-level description of both the imidazolium core of the cations and of the position of the aliphatic C_{18} chain. Based on these results, they proposed an innermost layer comprised of both anions and cations at a distance from the surface that coincides with the length of a C_{18} chain. Further ionic layers extend into the bulk, but they are separated by neutral layers comprised of the aliphatic chains. This demonstrates very nicely in what way the chemical structure of the ions influences the interfacial structure and gives hints in what way ionic liquids may be designed to achieve interfaces with specific properties.

7.4 Atomic Force Microscopy

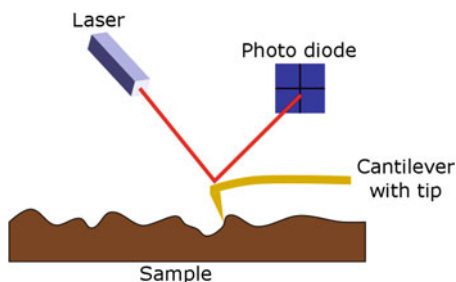
7.4.1 Introduction

Since the development of atomic force microscopy (AFM) by Binnig et al. in 1986 [120], AFM has become a widely used technique. The technique is complementary to STM, since AFM can also be used for the investigation of insulator surfaces. Binnig et al. were able to achieve a lateral resolution of 30 \AA and a vertical resolution of less than 1 \AA under atmospheric conditions [120].

In general, an AFM measures attractive or repulsive forces between a micro-fabricated tip and the sample. By scanning over a certain area of the sample in a line-by-line fashion, a topographic image of the surface is obtained. The most common method for measuring the forces between sample and tip is to monitor the deflection of a cantilever to which the tip is attached. This deflection may be measured using different methods, such as the interferometric method, the electronic tunneling method, the optical lever method, etc. [121].

Due to its easy implementation, the optical lever method (see Fig. 7.9) is the most widespread method. In this method, a laser is focused onto the backside of a reflective cantilever, and the position of the reflected laser beam is measured by means of a quartered photodiode, which is a direct measure for the deflection of the

Fig. 7.9 Schematic illustration of the optical lever method



cantilever [121]. Normally, a piezo tube actuator is used to move the sample in x-, y-, and z-direction. This allows for measuring the topography of samples under atmospheric conditions, in vacuum, and in liquids.

Classical AFM measurements are performed in contact mode, as described by Binnig et al. [120]. In this case, the tip is brought in direct contact to the sample, and repulsive forces are measured via the deflection of the cantilever. To minimize possible damages of the sample, the spring constants of cantilevers should be as low as possible [122].

In 1987, Martin et al. [123] introduced the first dynamic AFM method, namely amplitude modulation AFM (AM-AFM). For AM-AFM measurements, the cantilever is excited at or near its free resonance frequency. The interaction forces exert an influence on the oscillation amplitude, which is used as a feedback parameter for obtaining topographic information. In addition, the phase shift between the driving force and the oscillation of the cantilever gives information about material properties [124].

Another possible feedback parameter is the resonance frequency itself. This parameter is used in frequency modulation AFM (FM-AFM), which was introduced by Albrecht et al. [125] in 1991. Due to interaction forces between the tip and the sample, the resonance frequency of the cantilever shifts compared to the free cantilever, thus allowing measurements of the sample topography [124].

One of the most important parameters for dynamic AFM measurements is the so-called quality factor Q , which is an inverse measure of the damping of the oscillation and has a direct influence on force sensitivity. High Q values are desirable to increase the force resolution [126, 127]. However, high quality factors lead also to low scan speeds in AM-AFM measurements due to the influence of the quality factor on the feedback loop [125]. Since the quality factor is highest in vacuum, measurements in FM-AFM mode are often performed in vacuum, where the measurement speed is affected to a much lower extent by Q [125, 128]. The exact working principle of the feedback loops and the influence of the Q value are beyond the scope of this chapter. For further information we recommend to read the original publications [125, 128].

At this point, it should be noted that dynamic AFM methods do not measure the interaction force between the tip and the sample, but the force gradient. If the force gradient becomes higher than the spring constant of the cantilever, it is possible that the tip becomes trapped near the minimum of the interaction force. To avoid this, cantilevers with relatively high spring constants and oscillation amplitudes in the range from 1 to 100 nm are typically used [124].

Instead of a cantilever with an attached tip, it is also possible to use a piezo-electric tuning fork with a tip fixed to one of the tines [129–131]. Due to their high spring constants and high quality factors, tuning forks allow for using an oscillation amplitude of only 0.1 nm, which further improves the spatial resolution. Otherwise, the measurement is similar to FM-AFM measurements [131].

For the investigation of the structure of solid | IL interfaces, one of the most widespread types of AFM measurements is the acquisition of force-distance curves, which can be performed in two distinct ways. For measurements in static mode, the tip is ramped along the vertical axis using the z-piezo, while the force is measured via

the deflection of the cantilever [121]. These measurements are comparable to topographic imaging in contact mode without scanning over the sample. The second method uses a vibrating tip as in dynamic AFM. While ramping the tip along the vertical axis, the tip is excited at a certain frequency and the oscillation amplitude is measured (as in AM-AFM) [121, 123]. In liquids, this method suffers from low Q factors, and is therefore used to a lesser extent [121]. Both of these methods have one major problem in common. The absolute distance between tip and sample can only be determined, if adsorbed layers, which cannot be ruptured, are absent [121].

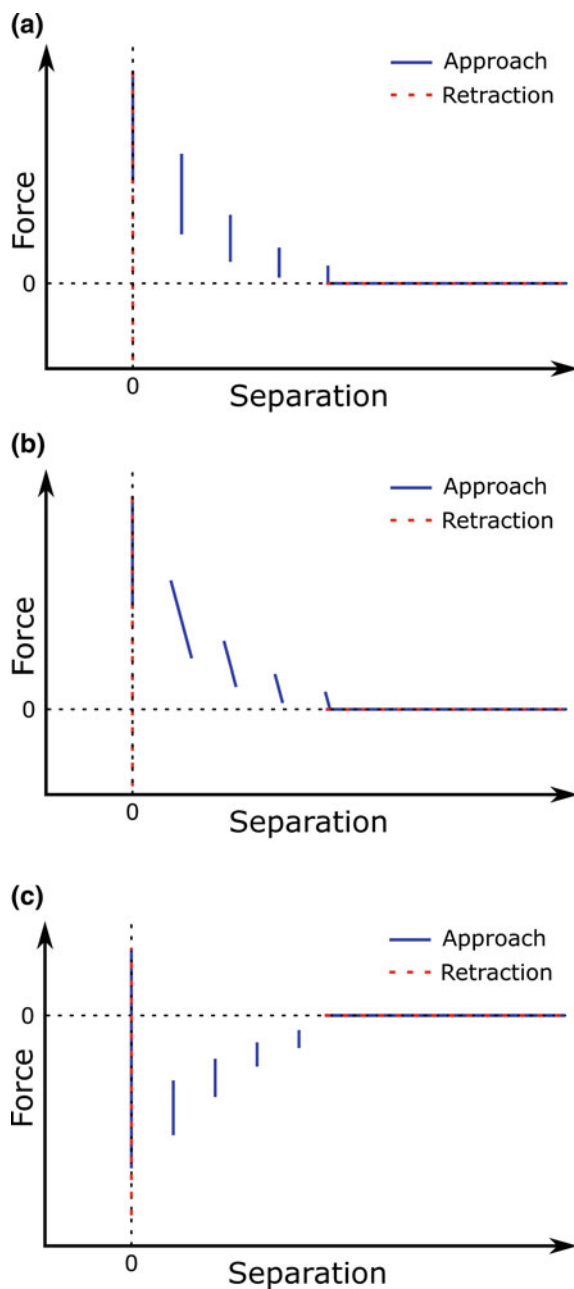
7.4.2 AFM for the Investigation of Solid | IL Interfaces

The number of AFM studies in ILs is rather limited. One of the first investigations was published in 2003 by Kubo et al. [132]. They were able to characterize the surface structure of an Au(100) crystal in EMIm tetrafluoroborate ([EMIm]BF₄) under potential control [132]. Independent of the applied potential, the surface showed a fourfold symmetry indicating a bare Au(100)-1 × 1 surface. Surface reconstructions at negative potentials, as reported in aqueous solutions [133–135], were not observed.

Subsequently, Atkin et al. investigated interfaces between solids and ILs quite extensively [6, 109, 136–146]. In 2007, they published the first study [146] examining the interface between three different ILs, namely ethylammonium nitrate (EAN), propylammonium nitrate (PAN), and EMIm acetate, and three different surfaces (mica, silica, and graphite). They measured force–distance curves that exhibit multiple *push-through events* at distinct distances from the surface (see Fig. 7.10). This provides strong indication for the existence of multiple ion layers. With decreasing distance from the solid surface, the force needed for pushing the tip through a layer increases. In case of EAN on mica, the separation distance between push-through events is about 0.5 nm, corresponding to the size of EAN ion pairs. However, for EAN on silica, a push-through event was observed at a distance of only 0.25 nm from the surface. This indicates that the innermost layer consists mainly of EA⁺ cations, which would also be expected for a negatively charged mica surface. The absence of such a push-through event at 0.25 nm for EAN on mica suggests that the innermost EA⁺ layer is very strongly bound and cannot be ruptured by the tip. This is plausible because of the higher surface charge of mica compared to silica. On retraction, there is a significant adhesion of the tip.

The force–distance curves measured at the interfaces mica | PAN and mica | EMIm acetate show one significant difference to the mica | EAN interface. The steps are not vertical, but slightly tilted (see Fig. 7.10b). This reveals the higher compressibility of the PAN and EMIm acetate ion layers as compared to EAN. Additionally, the increased size of the alkyl chain in PAN (with respect to EAN) leads to a stronger adhesion on the mica substrate and therefore to a higher force during retraction. In contrast, the adhesion in the case of EMIm acetate is even smaller than for EAN.

Fig. 7.10 Schematic AFM force–distance curves for **a**, **c** non-compressible and **b** compressible ion layers on an atomically smooth substrate; **a**, **b** without attractive forces and **c** with attractive forces between tip and substrate during approach and with adhesion during retraction



The force–distance curves obtained for EAN on graphite show characteristics very different from those obtained on mica and silica. During approach, the curve jumps to negative forces clearly showing attractive forces between the tip and the substrate.

With this extensive work, Atkin et al. demonstrated that measuring force–distance curves is a powerful tool for investigating the interface between solids and ILs and for obtaining information about properties of the ionic liquid. However, the authors mentioned one major drawback of the method. The influence of the tip chemistry on the measurements is not clear. In the studies, standard Si_3N_4 tips were used, which exhibit a low surface charge. However, different tips might yield different results.

Using the same technique, Atkin et al. showed that temperature has a strong effect on number, strength, and compressibility of ion layers by influencing their packing and H-bonding properties [145]. A lower temperature leads to fewer ion layers that are more weakly bound. Furthermore, the addition of an alcohol moiety to the alkyl chain of the cation leads to less ion layers that are more compressible. This effect can be explained by the lower solvophobic attraction and higher molecular flexibility of the cation with the alcohol moiety. Especially the solvophobic forces seem to be a significant driving force for the formation of ion layers at the interface.

Expectedly, the chemical structures of cations and anions also have a strong impact on the ion layers. Delocalization of charges leads to weaker electrostatic interaction with the surface and therefore to weaker binding of the ion layer adjacent to the surface. The force needed to rupture this layer decreases [139, 140]. The number of ion layers varies for different anions and cations due to changing H-bonding capability, solvophobic forces, mobility of moieties, etc. [139, 140, 145]. By carefully selecting the IL to tune attractive and repulsive forces, it is even possible to detect distinct anion and cation sublayers. This could be shown for the interface between mica and PA formate (PAF) [145].

In 2009, Bovio et al. used a different approach. They prepared thin IL films consisting of a few monolayers on solid substrates [147, 148]. The IL thin films rearrange, forming solid-like structures with multiple layers of ion pairs. However, it must be noted that for thin films, the interactions with the surrounding atmosphere are crucial. Since these interactions differ from the interactions with bulk IL, these studies cannot directly be compared with the studies performed by Atkin et al. One year later, Yokota et al. [149] performed a similar study using FM-AFM in bulk IL. Their results were quite similar to those of Bovio et al. They also reported one layer or multiple layers of ion pairs that are remarkably stable and therefore can be described as solid-like structures.

Due to the high damping of the cantilever oscillation, atomic resolution of mica and graphite surfaces could not be achieved by Yokota et al. This problem was overcome by Ichii et al. [150] using a quartz tuning fork sensor instead of a conventional cantilever. High-resolution topographic imaging of a mica surface could be achieved in EMIm acetate. Furthermore, in the same study, FM-AFM was used for the first time to obtain force–distance curves in an IL. These force–distance curves show oscillatory behavior with a period corresponding to the size of an ion pair, thus pointing to the existence of multiple layers, each consisting of ion pairs.

The first studies including force–distance curves at the electrified interface between an Au(111) surface and an IL, namely [Pyrr_{1,4}]FAP and [EMIm]FAP, and

therefore probing the electrochemical double layer were published in 2011 by Atkin et al. [109, 139]. By means of a three-electrode setup, the potential of an Au(111) surface acting as working electrode could be controlled. The results clearly show that a Stern model including a diffusive double layer is not suitable for the description. At the open circuit potential (OCP), the two innermost layers are thinner than the other layers. Consequently, in both systems, the innermost layer was interpreted as a cation layer followed by an anion layer.

Applying a moderate negative potential to the Au(111) surface leads to a contraction of the innermost cation layer, mostly caused by a change in the orientation of the cations from a more perpendicular to a more flat configuration. The thickness of the others layers corresponds to the diameter of the ion pair. Remarkably, at highly negative potentials, the innermost layer exhibits a thickness corresponding to the diameter of the anion. Obviously, the innermost cation layer cannot be ruptured by the tip, since it is too tightly bound. In addition, the number of detected layers increases.

At positive potentials, the thickness of the innermost layer points out a strong anion enrichment in the layer. Again, the force needed to rupture this layer increases with potential. However, as compared to the cations, the anions are less strongly bound due the delocalization of their negative charge. Apart from the innermost layer, all detected layers seem to consist of ion pairs.

Mao et al. modified AFM tips by attaching molecules with either neutral, positively charged, or negatively charged end groups [151]. The aim was to increase the force sensitivity with respect to Coulombic interaction. The application of this approach to the interface between Au(111) and 1-octyl-3-methylimidazolium hexafluorophosphate ([OMIm]PF₆) revealed a substructure in the innermost layer of ion pairs. Sublayers were detected consisting of either imidazolium rings, or octyl chains, or anions. Below the potential of zero charge (PZC), the surface is negatively charged, and cations are enriched in the innermost sublayer. The charged imidazolium rings are found adjacent to the solid surface, followed by a sublayer of octyl chains and a sublayer of anions. At potentials above the PZC, the positively charged surface attracts the anions, which form the innermost sublayer. The OMIm⁺ cations arrange with the imidazolium ring adjacent to the anions and the octyl chain forming the outermost sublayer. For potentials near the PZC, the obtained data show only two sublayers, and it is not possible to clarify the ion arrangement. However, the authors assume a checkerboard-like arrangement of cations and anions, in contrast to XRR results on similar systems [116].

All these studies yielded important information about the vertical structure of ion layers in ILs, but they do not elucidate the lateral structure of the layers. In 2013, Atkin et al. for the first time reported data giving insight into the lateral structure of ion layers by means of AFM [144]. Using soft contact AFM and AM-AFM, they could image different ion layers at the mica | EAN and at the mica | [EMIm]TFSI interface, respectively. In both cases, a strong influence of the mica structure on the innermost ion layer could be observed. The templating effect becomes less and less important for ion layers further from the substrate surface. However, the study also revealed differences between the investigated ILs. The innermost EA⁺ layer showed

a worm-like structure resulting from the interaction of the cations with the negatively charged sites on the mica substrate, together with aggregation of the cations' alkyl chains. In the case of the mica | [EMIm]TFSI interface, the image of the innermost layer reveals discrete ions, since no aggregation of alkyl chains can take place.

Two years later, AM-AFM measurements were used to reveal the potential-dependent nanostructure between a graphite surface and [EMIm]TFSI [152]. It was shown that at the OCP, double rows of anions and cations are present in the innermost layer. The periodicity of the observed layer structure is much larger than that of the underlying graphite structure and, in contrast to hexagonal symmetry of graphite, exhibits a square symmetry. However, the observed rows are oriented via alignment with the underlying graphite structure. By increasing the potential to moderately positive values, an enrichment of anions could be observed, but cations were still detectable. For higher positive potentials, the images became featureless suggesting a poorly ordered layer of anions. At slightly negative potentials, the number of cations in the innermost ion layer increased, but anions were still detectable. However, the structure was much less ordered. Shifting the potential to more negative values led to a well-defined superstructure with a further increasing number of cations. Nevertheless, as long as the images showed features, anions were detectable as well.

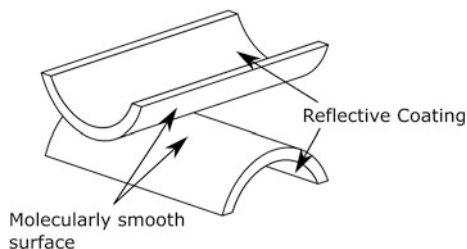
In conclusion, AFM techniques are very powerful tools for investigating interfaces between solids and ILs. The vertical structure of ion layers can be elucidated in a straightforward fashion by means of force–distance curves. Differences between different ILs and surfaces can easily be examined, and the electrode potential-dependent features are accessible using a suitable three-electrode setup. Modifying the tip by attaching molecules with neutral or charged end groups even allows for selectively increasing the sensitivity for specific ions or specific parts of a molecule. It is also possible to gain information about the lateral structure of interfacial layers. AM-AFM was proven to be a suitable technique for lateral imaging of the innermost ion layer. However, there are still considerable challenges in this field. In particular, the influence of the tip shape and tip chemistry on the obtained force–distance curves and lateral images is not yet completely understood.

7.5 Surface Force Apparatus

7.5.1 Introduction

The surface force apparatus (SFA) is an instrument that measures the forces between two atomically flat surfaces. It was first introduced by Tabor and Winter in 1969 [153]. This first version of the SFA was capable of measuring forces between two mica surfaces in air for separations from 5 to 30 nm (uncertainty of the

Fig. 7.11 Schematic illustration of a SFA setup, consisting of two orthogonally arranged glass cylinders. The concave part is coated with a thin silver film. The molecularly smooth substrates are glued onto the convex surface of the glass cylinders



separation: 3 Å). The mica substrates were glued to cylindrical glass formers, which were arranged orthogonally to each other, see Fig. 7.11. The concave surfaces of the glass cylinders were coated with a silver layer in order to measure the spacing between the mica substrates by means of multiple beam interferometry (MBI). The MBI measurement not only gave information about the surface separation, but also about the geometry of the contact area. One of the cylinders was held by a cantilever spring, while the other was moved towards it. At a certain point, the first cylinder *jumped* towards the other. The distance, at which this jump occurs, depends on the spring constant and on the attractive forces between the surfaces.

The apparatus was subsequently improved, and new features were added. By combining multiple types of movement control, the range of accessible distances was increased to a total range of seven orders of magnitude (from millimeters to ångströms) [154]. One of the most important improvements was achieved by Israelachvili and Adams in 1976 [155]. The new instrument allowed for measuring forces between surfaces immersed in liquids. This opened the possibility to investigate interfacial layers and electrochemical double layers in arbitrary solutions.

In general, the principle of measurement is rather simple [153–156]. In modern SFAs, the distance between the surfaces is controlled by a combination of micrometer screws, a spring mechanism, and a piezo tube. A precise measurement of the distance between the surfaces and of the geometry of the contact area is performed by MBI. The substrates are attached to the convex side of glass cylinders (see Fig. 7.11), one of which is mounted on a rigid support, while the other is mounted on a support attached to a cantilever spring. The concave back sides of the glass cylinders are coated with a highly reflective layer, such as silver. This layer is needed for performing the MBI measurement.

The cantilever spring is used to measure the force between the two surfaces down to the sub-pN regime. The resolution and available range of forces depends on the spring constant of the used spring. The force can be measured by applying a voltage to the piezo tube, leading to a known expansion or contraction. The difference between the expansion/contraction of the piezo tube and the resulting change of separation of the substrates corresponds to the deflection of the spring and therefore is a measure for the force.

The measurements performed by an SFA are quite similar to the measurement of force–distance curves by means of AFM. However, there are a few important

differences. In SFA measurements, the absolute distance between the surfaces is exactly measured by means of MBI, while in AFM measurements, the exact distance can only be determined, if strongly bound surface layers are absent. Furthermore, SFA experiments are usually carried out with two identical surfaces, while the solid surface and the AFM tip consist usually of different materials. The application of MBI leads to high demands on the quality of the substrates. Since light needs to be transmitted through the samples, the investigated system has to show a certain transparency for light. Because of this requirement, for a long time, only mica substrates have been practically used [157].

In 2008, Kawai et al. [158] introduced a new possibility for measuring the distance. Using two-beam interferometry it is possible to measure the displacement of the lower surface. To this end, a laser beam is split by means of a grating. The beams are then reflected at a fixed mirror and at the backside of the lower glass cylinder, respectively. By recombining the reflected beams, the phase shift can be obtained from the amplitude, and the displacement of the lower surface can be measured with a resolution of 2 \AA [157]. Using this method, the investigated samples do not need to be transparent. This allows for measuring many different materials including metals. However, one should be aware of the fact that this method does not measure the absolute distance between the surfaces, but only changes in distance. For obtaining force versus absolute distance curves, one needs a means to measure the absolute distance at the beginning of the measurement.

Britton et al. [159] introduced few-layer graphene as surfaces for SFA measurements. By means of a double-transfer procedure, it is possible to attach the graphene layer with an epoxy to the glass cylinders. The graphene layer is sufficiently transparent to use the standard MBI method for measuring the distance between the surfaces. This enables the investigation of interfaces between graphene and ILs. One major advantage of using graphene surfaces is the high conductivity of graphene. This allows for measuring force–distance curves under controlled potential of the surfaces.

Modern SFAs can also move one of the surfaces in horizontal direction and measure friction forces [154]. This can give additional information about the influence of interfacial layers on lubrication properties.

7.5.2 SFA Studies of Solid | IL Interfaces

The first study reporting on the interface between mica surfaces and an IL, namely EAN, was published in 1988 by Horn et al. [160]. They investigated the influence of water concentration on the interfacial structure. At water concentrations below 50 vol.%, they observed oscillatory force–distance curves. With decreasing water content, the number of oscillations increased. The periodicity of the oscillations was found to correspond to the size of an ion pair. The innermost layer was tightly bound to the surface and could not be squeezed out of the gap between the surfaces.

After this pioneering work, there were no further reports on SFA investigations of solid | IL interfaces for a long time. In 2010, multiple SFA studies on solid | IL interfaces were published. Perkin et al. [161] investigated the behavior of EMIm ethylsulfate ([EMIm]EtSO₄) between two mica surfaces with respect to normal force profiles and friction properties. This solid | IL interface exhibits oscillations in the force–distance curve at very low separations. The measured shear force shows a strong dependence on the separation of the surfaces. At a separation corresponding to the onset of the outermost oscillation, the shear stress is quite low, while at a separation that allows for only a single cation layer to be present, the shear stress is significantly higher.

Ueno et al. [162] reported results for the interface between silica and [BMIm]TFSI and [BMIm]BF₄, respectively, which are in good agreement with the work of Perkin et al. They also reported oscillatory forces at the interface due to bound ion layers and could show that [BMIm]TFSI shows more distinct oscillations than [BMIm]BF₄. The oscillations were observable up to separations from the surface of 10 nm for [BMIm]TFSI and 6.9 nm for [BMIm]BF₄, respectively. The authors suggested that this difference is related to the crystal-forming ability of the ILs. [BMIm]TFSI crystallizes easily, while [BMIm]BF₄ is a good glass former. Consequently, [BMIm]TFSI can more easily form ordered layers at the solid | IL interface.

Besides conventional force–distance curves, Ueno et al. also performed resonance shear measurements. This method was developed in the same lab by Dushkin and Kurihara [163] and allows for measuring viscoelastic properties of liquid films in confined geometries. Using this method, they were able to show that at high separations of the two surfaces, the viscosity of the confined IL is equal to the bulk viscosity. However, as soon as the separations are reduced to values, at which oscillations in force–distance curves are observable, the viscosity increases by up to three orders of magnitude. Furthermore, by comparing the data with data obtained for silica surfaces in direct contact (without a liquid film in between), they were able to show that the silica | [BMIm]BF₄ interface shows better lubricity than the silica | [BMIm]TFSI interface.

A short time later, Bou-Malham et al. illustrated the crucial influence of surface charges on the mica | IL interface by comparing negatively charged bare mica with mica covered by an uncharged CH₃-terminated self-assembled monolayer [164]. For bare mica substrates, the obtained results were in good agreement with the results reported earlier, showing a layered structure at the surface and enhanced viscosity [160–162]. However, the measurements with methyl-terminated mica surfaces revealed a quite distinct behavior. Neither a layered structure nor an enhancement of viscosity at the surface was observable.

Perkin et al. [165] demonstrated a significant influence of the amphiphilic nature of the cation. Instead of cation–anion bilayers as commonly found in most ILs (thickness of the layer corresponding to the size of an ion pair), the interface between 1-hexyl-3-methylimidazolium TFSI ([HMIm]TFSI) and mica is characterized by exceptionally thick layers. This observation can be explained by the

formation of cation bilayers due to the high amphiphilic nature caused by the long hydrocarbon chain.

In 2013 Gebbie et al. [166] published results that led to controversial discussions. They measured force–distance curves of [BMIm]TFSI between a mica surface and a polycrystalline gold surface under potential control of the gold surface. They detected long-range interactions up to separations of approximately 35 nm. From this they concluded that the surface potentials of the mica and the gold electrode are not completely screened by the adsorbed ion layers, leading to diffuse double layers which overlap. They postulated a very low effective dissociation of the IL of 0.003 % for [BMIm]TFSI at room temperature. However, if also for mica surfaces the surface charge is not completely screened by the adsorbed ion layers, long-range interactions should also be present for measurements utilizing two mica surfaces. This was not detected in independent measurements of four different groups [160–162, 164].

Shortly after this study, similar results were published by Espinosa-Marzal et al. for different ILs [167, 168]. They also observed long-range interactions extending to separations of 50 nm. However, the authors noted that there is no direct evidence for the origin of this interaction. Furthermore, the influence of relative humidity of the surrounding atmosphere was investigated. Absorption of water has a strong impact on the structure of layers nearby the surface, but on basis of this work, no general trends could be derived.

In 2015, Gebbie et al. [169] further investigated the long-range interactions between two mica substrates. They performed temperature-dependent experiments with two different ILs consisting of imidazolium cations and TFSI anions. With increasing temperature, they observed a decreasing length scale of long-range interaction and interpret this effect as an increasing effective dissociation of the ionic liquid.

In the same year, Jurado et al. [170] reported an ordered structure of dry [HMIm]EtSO₄ confined between two mica substrates, extending up to approximately 60 nm separation distance. In contrast to previous observations, these long-range interactions show an oscillatory behavior as well as growth during approach and retract cycles of the mica substrates. These results demonstrate that repeatedly applied nanoconfinement can induce an irreversible transition to a solid-like IL structure at the mica | IL interface.

In summary, the SFA is a powerful instrument for investigating the structure and properties of ILs in confined geometries. It allows for the easy measurement of the vertical structure of the solid | IL interface. Apart from forces due to near-surface layers, also long-range forces are measurable. In addition, friction forces can be studied.

Even though there are many similarities between SFA methods and certain AFM methods, SFA also exhibits some important advantages. One of the main advantages is the absolute measurement of distances between the samples. Furthermore, the possibility to use two identical surfaces ensures that the measurement is not disturbed by different surface chemistries. A major drawback is that absolute distance measurements by means of MBI can only be carried out on transparent samples. This is

the reason why mainly mica was used as substrate for SFA measurements. However, Britton, Cousens et al. introduced a method based on the usage of graphene sheets as substrates, allowing for electrochemically controlled measurements without losing the advantage of absolute distance measurement [159].

7.6 Surface-Enhanced Raman Spectroscopy (SERS) and Shell-Isolated Nanoparticle-Enhanced Raman Spectroscopy (SHINERS)

Surface-enhanced Raman spectroscopy makes use of rough metallic surfaces with plasmonic activity in the visible range, such as Au, Ag, and Cu. A laser beam excites localized surface plasmons, and plasmons oscillating perpendicular to the surface create large local electric fields, which lead to enhanced Raman scattering of molecules being chemisorbed or physisorbed to the surface.

The preparation of rough metallic surfaces is usually done by repeated oxidation/reduction cycles in an electrochemical cell (electrochemical activation) [171–175]. During the oxidation cycle, metal cations are dissolved in the electrolyte, and during the reduction cycle, the metal cations are preferentially reduced at protrusions existing on the surface. This leads automatically to a continuous roughening of the surface during cycling.

The first in situ SERS study on a metal | IL interface was reported by Santos et al. [171]. In this study, an Ag surface was activated by 10 oxidation/reduction cycles in the ionic liquid [BMIm]PF₆. Subsequently, Raman spectra were collected at different electrical potentials of the Ag surface in contact to [BMIm]PF₆. Potential-dependent SERS signals of the BMIm⁺ cations adsorbed on the surface were observed and analyzed. The results suggest that the orientation of the adsorbed BMIm⁺ cations depends strongly on the electrode potential. When the potential is larger than the PZC (Ag positively charged), the imidazolium ring is oriented nearly perpendicular to the surface. This implies the existence of empty space for PF₆⁻ anions, which are electrostatically bound to the surface. In contrast, at potentials smaller than the PZC (Ag negatively charged), the imidazolium ring is oriented almost parallel to the surface.

Similar observations were made by Brandão et al. on a Cu | [BMIm]BF₄ interface [172]. They found that the Raman band at 765 cm⁻¹, which is characteristic of the BF₄⁻ anions, does not show any change with the potential of the Cu electrode. This indicates a minimal chemical interaction of the BF₄⁻ anions with the Cu surface. At potentials > PZC, a CuO film exists on the surface. In this case, also the BMIm⁺ cations show no significant interaction with the surface. At potentials < PZC, CuO is reduced, and the interaction of the BMIm⁺ cations with the surface increases strongly. This manifests in a strong enhancement of the BMIm⁺ vibrational modes together with shifts in the wavenumber of the Raman bands.

Yuan et al. [173] compared the SERS spectra of the two interfaces Cu | [BMIm]BF₄ and Cu | [BMIm]Br and found that the reorientation behavior of the BMIm⁺ cations is similar at both interfaces. The imidazolium ring is nearly perpendicular to the surface at positive potentials, while there is a tilt and flat configuration of the ring at negative potentials. The onset potential for this change in orientation depends on the anion.

Liu et al. [176] studied the interfaces between Ag and different imidazolium-based ionic liquids R-methyl-imidazolium BF₄ with R = C_nH_{2n+1} and n = 2, 4, 6, 8, and 10. Their SERS results indicate that an increasing length of the alkyl chain R leads to a weaker interaction of the imidazolium cations with the silver surface, resulting in more negative values of the PZC.

An interesting approach for estimating the length scale of the electric potential drop at a metal | IL interface was published by Zhang et al. [175]. They prepared an Au | [BMIm]BF₄ interface and added dilute molecules with nitrile groups to the ionic liquid. These molecules were adsorbed at the Au surface with the nitrile group (CN group) pointing away from the surface. Then, potential-dependent SERS spectra were taken, and the vibrational Stark shift of the CN stretching frequency as a function of the potential were analyzed. The Stark shift is a measure for the local electric field at the CN group. For short nitrile molecules, significant Stark shifts were observed, while for the longest molecule 6-aminohexanenitrile (6-AHN) with a length of 6.6 Å, a Stark shift was absent. This suggests that the electric potential drops over 5–6 Å, i.e., mainly across the innermost ion layer.

In summary, SERS spectra of metal | IL interfaces point to a chemisorption of imidazolium-based cations on the metal surface, while the chemical interaction of typical anions, such as BF₄⁻, with the metal surface is weak. The binding of the anions seems to be mainly of electrostatic nature. The change in the orientation of the imidazolium cations with the electric potential exerts a significant influence on the SERS spectra, since the surface enhancement depends strongly on the orientation of the imidazolium vibrational modes relative to the excited surface plasmons. The length scale of the electric potential drop at the interface can be estimated from the vibrational Stark shift of suitable probe molecules.

A limitation of the SERS method is that it cannot be applied to flat metal surfaces, such as single-crystalline surfaces. In the case of flat surfaces, shell-isolated nanoparticle-enhanced Raman spectroscopy (SHINERS) can be used as an alternative method [174]. SHINERS is based on an electromagnetic field enhancement created by Au nanoparticles with a thin silica shell, which are placed on the flat metal surface. Up to now, only a single SHINERS study on metal | IL interfaces has been published [177]. In this study, an Au(111) surface in contact to the ionic liquid [BMIm]PF₆ was probed. At potentials > PZC, the obtained SHINERS spectra are very similar to the bulk spectra of the ionic liquids, suggesting weak interactions of the PF₆⁻ anions with the Au surface. In contrast, a potential dependence of the SHINERS spectra is observed at potentials < PZC. An analysis of potential-dependent band shifts and band intensities together with DFT calculations suggests that the BMIm⁺ cation interacts with the Au surface through

the HC4C5H side of the imidazolium ring. The ring orientation changes from flat-lying, to gradual up-leading and to finally vertical-standing with decreasing potential.

7.7 Sum-Frequency Generation (SFG) Vibrational Spectroscopy

Sum-frequency generation (SFG) vibrational spectroscopy is a second-order non-linear spectroscopy that is only sensitive to molecules in media that lack inversion symmetry. Thus, in the case of a metal | IL interface, molecules in the bulk phase of the IL do not contribute to the SFG signal. Experimentally, SFG vibrational spectroscopy uses the overlap of two laser beams, one laser with a visible light frequency and one laser with a tuneable IR frequency. A third beam with a frequency equal to the sum of the two incident beams (SFG signal) is generated, if the IR frequency matches the vibrational frequency of interfacial molecules. Using different polarization combinations of incident and generated laser beams, the orientation of molecules with respect to the surface normal can be deduced.

The first in situ SFG study on a metal | IL interface was carried out by Rivera et al. [178]. They considered polycrystalline Pt electrodes in contact to the ionic liquids [BMIm]PF₆ and [BMIm]BF₄, respectively, and obtained detailed information about the potential-dependent orientation of the imidazolium ring. The orientation changes from about 35° from the surface normal at positive surface charges (ring more perpendicular to the surface so that anions can adsorb) to about 60° at negative surface charges (ring more parallel to the surface) (see Fig. 7.12).

Shortly thereafter, Baldelli used the SFG method to measure the vibrational Stark shift of CO molecules adsorbed at a Pt | [BMIm]BF₄ interface [180]. The Stark shift together with interfacial capacitance values suggest that the length scale of the electric potential drop over the interfaces is in the range of 0.3–0.5 nm. Based on this result, the interfacial double layer was interpreted as a Helmholtz-type layer.

Subsequently, the SFG method was applied to various other metal | IL interfaces and to a three-layer graphene | IL interface [179, 181–183]. Detailed information was obtained on the potential-dependent orientation of the ions in the innermost

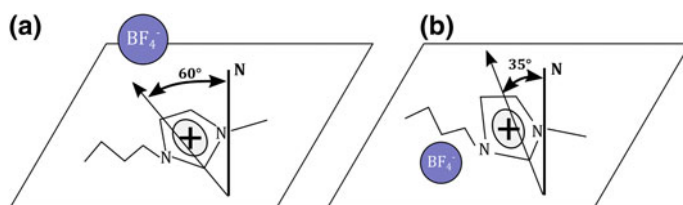


Fig. 7.12 Schematic illustration of the alignment of a BMIm⁺ cation on a metal electrode surface at negative (a) and positive (b) electrode potentials (adapted from [179])

layer. Overall, the SFG results provided no evidence for a multilayer arrangement of the ions, so that it was suggested that the electrode charge compensating ions are arranged in a single ion layer (Helmholtz-type layer).

Here, it is important to note that this interpretation of the SFG results is at variance with the results of various AFM studies [6, 136–146] and molecular dynamics computer simulation studies [93–95, 108, 184–186]. Based on the results of these studies, there seems to be a general consensus about the existence of a multilayer structure at the metal | IL interface. The multilayer structure leads to charge density oscillations over the length scale of 4–5 ion layers. Since the oscillation amplitude decreases with increasing distance from the electrode, a major part of the electric potential drop takes place between the electrode and the innermost ion layer [93, 94]. Consequently, a length scale of the potential drop in the range of 0.5 nm and the existence of a multilayer structure extending over several nm are by no means contradictory features of the metal | IL interface.

References

1. Buzzeo MC, Evans RG, Compton RG (2004) *ChemPhysChem* 5:1106
2. Endres F, Zein El Abedin S (2006) *Phys Chem Chem Phys* 8:2101
3. Galiński M, Lewandowski A, Stepniak I (2006) *Electrochim Acta* 51:5567
4. Hapiot P, Lagrost C (2008) *Chem Rev* 108:2238
5. Baker GA, Baker SN, Pandey S, Bright FV (2005) *Analyst* 130:800
6. Endres F, Höfft O, Borisenko N, Gasparotto LH, Prowald A, Al-Salman R, Carstens T, Atkin R, Bund A, Zein El Abedin S (2010) *Phys Chem Chem Phys* 12:1724
7. Endres F, Bukowski M, Hempelmann R, Natter H (2003) *Angewandte Chemie (International ed. in English)* 42:3428
8. Sillars FB, Fletcher SI, Mirzaeian M, Hall PJ (2012) *Phys Chem Chem Phys* 14:6094
9. Simon P, Gogotsi Y (2008) *Nat Mater* 7:845
10. Lewandowski A, Świdarska-Mocek A (2009) *J Power Sources* 194:601
11. Srouf HM, Giroud N, Rouault H, Santini CC (2012) 220th ECS meeting, pp 23–28
12. Grätzel M (2009) *Acc Chem Res* 42:1788
13. Yuan H, Shimotani H, Tsukazaki A, Ohtomo A, Kawasaki M, Iwasa Y (2006) *Adv Funct Mater* 2009:19
14. Blanke H, Bohlen O, Buller S, de Doncker RW, Fricke B, Hammouche A, Linzen D, Thele M, Sauer DU (2005) *J Power Sources* 144:418
15. Mirzaeian M, Hall PJ (2010) *J Power Sources* 195:6817
16. Li H, Huang X, Chen L (1999) *J Power Sources* 81–82:340
17. Gellert M, Gries KI, Zakel J, Kranz S, Bradler S, Hornberger E, Müller S, Yada C, Rosciano F, Volz K, Roling B (2015) *J Electrochem Soc* 162:A754–A759
18. Gellert M, Gries KI, Zakel J, Ott A, Spannenberger S, Yada C, Rosciano F, Volz K, Roling B (2014) *Electrochim Acta* 133:146
19. Landa-Medrano I, Ruiz de Larramendi I, Ortiz-Vitoriano N, Pinedo R (2014) Ignacio Ruiz de Larramendi, José, T. Rojo. *J Power Sources* 249:110
20. Buller S, Karden E, Kok D, de Doncker RW (2001) IEEE industry applications society 36th annual meeting—IAS'01, pp 2500–2504
21. Arbizzani C, Mastragostino M, Meneghello L (1995) *Electrochim Acta* 40:2223
22. Taberna PL, Simon P, Fauvarque JF (2003) *J Electrochem Soc* 150:A292
23. Taberna PL, Portet C, Simon P (2006) *Appl Phys A* 82:639

24. Selvakumar M, Pitchumani S (2010) *Korean J Chem Eng* 27:977
25. Lefebvre MC (1999) *Electrochim Solid State Lett* 2:259
26. Springer TE (1996) *J Electrochem Soc* 143:587
27. Wagner N (2002) *J Appl Electrochem* 32:859
28. Cisneros R, Beley M, Fauvarque J-F, Lapicque F (2015) *Electrochim Acta* 171:49
29. Fabregat-Santiago F, Bisquert J, Garcia-Belmonte G, Boschloo G, Hagfeldt A (2005) *Sol Energy Mat Sol C* 87:117
30. Garland JE, Crain DJ, Roy D (2014) *Electrochim Acta* 148:62
31. Wang Q, Moser J-E, Grätzel M (2005) *J Phys Chem B* 109:14945
32. Andrade C, Keddad M, Nóvoa XR, Pérez MC, Rangel CM, Takenouti H (2001) *Electrochim Acta* 46:3905
33. Dhouihi L, Triki E, Raharinaivo A (2002) *Cement Concrete Comp* 24:35
34. López DA, Simison SN, de Sánchez SR (2003) *Electrochim Acta* 48:845
35. Pech-Canul M, Castro P (2002) *Cement Concrete Res* 32:491
36. Xu L-N, Zhu J-Y, Lu M-X, Zhang L, Chang W (2015) *Int J Miner Metall Mater* 22:500
37. Bron P, Johansson S, Zick K, Schmedt auf der Günne J, Dehnen S, Roling B (2013) *J Am Chem Soc* 135:15694
38. Huber B, Rossrucker L, Sundermeyer J, Roling B (2013) *Solid State Ionics* 247–248:15
39. Takada K, Ohta N, Zhang L, Xu X, Hang BT, Ohnishi T, Osada M, Sasaki T (2012) *Solid State Ionics* 225:594
40. Takada K, Ohta N, Zhang L, Fukuda K, Sakaguchi I, Ma R, Osada M, Sasaki T (2008) *Solid State Ionics* 179:1333
41. Seino Y, Ota T, Takada K (2011) *J Power Sources* 196:6488
42. Menne S, Pires J, Anouti M, Balducci A (2013) *Electrochem Commun* 31:39
43. Zhang Q, Chen J-J, Wang X-Y, Yang C, Zheng M-S, Dong Q-F (2015) *Phys Chem Chem Phys* 17:10353
44. Zhang SS (2013) *J Power Sources* 231:153
45. Suo L, Hu Y-S, Li H, Armand M, Chen L (2013) *Nat Commun* 4:1481
46. Vijayakumar M, Li L, Graff G, Liu J, Zhang H, Yang Z, Hu JZ (2011) *J Power Sources* 196:3669
47. Arbizzani C, Gabrielli G, Mastragostino M (2011) *J Power Sources* 196:4801
48. Gellert M, Gries KI, Yada C, Rosciano F, Volz K, Roling B (2012) *J Phys Chem C* 116:22675
49. Gerstl M, Navickas E, Friedbacher G, Kubel F, Ahrens M, Fleig J (2011) *Solid State Ionics* 185:32
50. Gerstl M, Navickas E, Leitgeb M, Friedbacher G, Kubel F, Fleig J (2012) *Solid State Ionics* 225:732
51. Iguchi F, Chen C-T, Yugami H, Kim S (2011) *J Mater Chem* 21:16517
52. Mariappan CR, Gellert M, Yada C, Rosciano F, Roling B (2012) *Electrochem Commun* 14:25
53. Drüscler M, Borisenko N, Wallauer J, Winter C, Huber B, Endres F, Roling B (2012) *Phys Chem Chem Phys* 14:5090
54. Wallauer J, Drüscler M, Huber B, Roling B (2013) *Z Naturforsch B* 68
55. Lockett V, Sedev R, Ralston J, Home M, Rodopoulos T (2008) *J Phys Chem C* 112:7486
56. Fedorov MV, Komyshev AA (2014) *Chem Rev* 114:2978
57. Lasia A (2002) In: Conway BE, Bockris JO, White RE (eds) *Modern aspects of electrochemistry*, vol 32. Kluwer Academic Publishers, Boston, pp 143–248
58. Bard AJ, Faulkner LR (2001) *Electrochemical methods*. Wiley, New York
59. Armstrong RD, Burnham RA (1976) *J Electroanal Chem Interf Electrochem* 72:257
60. de Levie R (1965) *Electrochim Acta* 10:113
61. Jänsch T, Wallauer J, Roling B (2015) *J Phys Chem C* 119:4620
62. Alexander CL, Tribollet B, Orazem ME (2015) *Electrochim Acta* 173:416
63. Allison H (1982) Frequency response analyzer. Google Patents, <https://www.google.com/patents/US4322806>

64. Lai W (2010) *Electrochim Acta* 55:5511
65. Hsieh G, Ford SJ, Mason TO, Pederson LR (1996) *Solid State Ionics* 91:191
66. Hsieh G, Mason TO, Pederson LR (1996) *Solid State Ionics* 91:203
67. Klink S, Madej E, Ventosa E, Lindner A, Schuhmann W, La Mantia F (2012) *Electrochem Commun* 22:120
68. Klink S, Höche D, La Mantia F, Schuhmann W (2013) *J Power Sources* 240:273
69. Ender M, Weber A, Ivers-Tiffée E (2012) *J Electrochem Soc* 159:A128
70. Balabajew M, Roling B (2015) *Electrochim Acta* 176:907
71. Fletcher S (2001) *Electrochem Commun* 3:692
72. Sadkowski A, Diard J-P (1907) *Electrochim Acta* 2010:55
73. Kramers HA (1929) *Physikalische Zeitschrift* 30:522
74. Kronig RDL (1962) *J Opt Soc Am* 12:547
75. Boukamp B (1993) *Solid State Ionics* 62:131
76. Urquidi-Macdonald M, Real S, Macdonald DD (1990) *Electrochim Acta* 35:1559
77. Macdonald JR (1990) *Electrochim Acta* 35:1483
78. Macdonald JR (1883) *Electrochim Acta* 1993:38
79. Levenberg K (1944) *Q J Appl Math* II:164
80. Marquardt DW (1963) *J Soc Ind Appl Math* 11:431
81. Nelder JA, Mead R (1965) *Comput J* 7:308
82. Moré JJ (1978) *Numerical analysis*. Springer, Berlin, pp 105–116
83. Kornyshev AA (2007) *J Phys Chem B* 111:5545
84. Costa R, Pereira CM, Silva AF (2015) *Electrochim Acta* 167:421
85. Gomes C, Costa R, Pereira CM, Silva AF (2014) *RSC Adv* 4:28914
86. Su Y, Yan J, Li M, Zhang M, Mao B (2013) *J Phys Chem C* 117:205
87. Siinor L, Siimenson C, Ivaništšev V, Lust K, Lust E (2012) *J Electroanal Chem* 668:30
88. Bhuiyan LB, Lamperski S (2012) *Mol Phys* 111:807
89. Forsman J, Woodward CE, Trulsson M (2011) *J Phys Chem B* 115:4606
90. Henderson D, Wu J (2012) *J Phys Chem B* 116:2520
91. Jiang D-E, Meng D, Wu J (2011) *Chem Phys Lett* 504:153
92. Trulsson M, Algotsson J, Forsman J, Woodward CE (2010) *J Phys Chem Lett* 1:1191
93. Vatamanu J, Borodin O, Bedrov D, Smith GD (2012) *J Phys Chem C* 116:7940
94. Vatamanu J, Borodin O, Smith GD (2010) *J Am Chem Soc* 132:14825
95. Vatamanu J, Borodin O, Smith GD (2011) *J Phys Chem B* 115:3073
96. Vatamanu J, Cao L, Borodin O, Bedrov D, Smith GD (2011) *J Phys Chem Lett* 2:2267
97. Huber B, Roling B (2011) *Electrochim Acta* 56:6569
98. Drüschler M, Huber B, Roling B (2011) *J Phys Chem C* 115:6802
99. Binnig G, Rohrer H, Gerber C, Weibel E (1982) *Phys Rev Lett* 49:57
100. Binnig G (1982) *Appl Phys Lett* 40:178
101. Binnig G, Rohrer H (1987) *Rev Mod Phys* 59:615
102. Kelly KF, Sarkar D, Oldenburg SJ, Hale GD, Halas NJ (1997) *Synth Met* 86:2407
103. Kelly KF, Sarkar D, Hale GD, Oldenburg SJ, Halas NJ (1996) *Science* 273:1371
104. Hahn JR, Ho W (2001) *Phys Rev Lett* 87
105. Niimi Y, Matsui T, Kambara H, Tagami K, Tsukada M, Fukuyama H (2006) *Phys Rev B* 73
106. Reinert F, Nicolay G (2004) *Appl Phys A Mater Sci Process* 78:817
107. Poirier GE (1997) *Chem Rev* 97:1117
108. Kirchner K, Kirchner T, Ivaništšev V, Fedorov MV (2013) *Electrochim Acta* 110:762
109. Atkin R, Borisenko N, Drüschler M, El-Abedin SZ, Endres F, Hayes R, Huber B, Roling B (2011) *Phys Chem Chem Phys* 13:6849
110. Pan G-B, Freyland W (2006) *Chem Phys Lett* 427:96
111. Lin L (2003) *Electrochem Commun* 5:995
112. Endres F, Borisenko N, El Abedin SZ, Hayes R, Atkin R (2012) *Faraday Discuss* 154:221
113. Buchner F, Forster-Tonigold K, Uhl B, Alwast D, Wagner N, Farkhondeh H, Gross A, Behm RJ (2013) *ACS Nano* 7:7773

114. Wen R, Rahn B, Magnussen OM (2015) *Angewandte Chemie (International ed. in English)* 54:6062
115. Suto K, Magnussen OM (2010) *J Electroanal Chem* 649:136
116. Mezger M, Schröder H, Reichert H, Schramm S, Okasinski JS, Schöder S, Honkimäki V, Deutsch M, Ocko BM, Ralston J, Rohwerder M, Stratmann M, Dosch H (2008) *Science* 322:424
117. Mezger M, Ocko BM, Reichert H, Deutsch M (2013) *Proc Natl Acad Sci USA* 110:3733
118. Bazant MZ, Storey BD, Kornyshev AA (2011) *Phys Rev Lett* 106
119. Brkljača Z, Klimczak M, Miličević Z, Weissner M, Taccardi N, Wasserscheid P, Smith DM, Magerl A, Smith A-S (2015) *J Phys Chem Lett* 6:549
120. Binnig G, Quate CF, Gerber C (1986) *Phys Rev Lett* 56:930
121. Cappella B, Dietler G (1999) *Surf Sci Rep* 34:1
122. Mironov Viktor Leonidovitch (2004) *Fundamentals of the scanning probe microscopy. The Russian Academy of Sciences, Nizhniy Novgorod*
123. Martin Y, Williams CC, Wickramasinghe HK (1987) *J Appl Phys* 61:4723
124. García R, Pérez R (2002) *Surf Sci Rep* 47:197
125. Albrecht TR, Grütter P, Horne D, Rugar D (1991) *J Appl Phys* 69:668
126. Lübke J, Tröger L, Torbrügge S, Bechstein R, Richter C, Kühnle A, Reichling M (2010) *Meas Sci Technol* 21:125501
127. Perez-Cruz A, Dominguez-Gonzalez A, Stiharu I, Osornio-Rios RA (2012) *Ultramicroscopy* 115:61
128. Hölscher H, Schwarz UD (2007) *Int J Non-Linear Mech* 42:608
129. Giessibl FJ (1996) *Vorrichtung zum berührungslosen Abtasten von Oberflächen und Verfahren dafür*
130. Giessibl FJ (1998) *Appl Phys Lett* 73:3956
131. Edwards H, Taylor L, Duncan W, Melmed AJ (1997) *J Appl Phys* 82:980
132. Kubo K, Hirai N, Tanaka T, Hara S (2003) *Surf Sci* 546:L785–L788
133. Gao X, Hamelin A, Weaver MJ (1991) *Phys Rev Lett* 67:618
134. Gao X, Hamelin A, Weaver MJ (1992) *Phys Rev B* 46:7096
135. Schneider J, Kolb DM (1988) *Surf Sci* 193:579
136. Atkin R, Abedin SZE, Hayes R, Gasparotto LHS, Borisenko N, Endres F (2009) *J Phys Chem C* 113:13266
137. Carstens T, Hayes R, Abedin SZE, Corr B, Webber GB, Borisenko N, Atkin R, Endres F (2012) *Electrochim Acta* 82:48
138. Hayes R, Borisenko N, Corr B, Webber GB, Endres F, Atkin R (2012) *Chem Commun* 48:10246
139. Hayes R, Borisenko N, Tam MK, Howlett PC, Endres F, Atkin R (2011) *J Phys Chem C* 115:6855
140. Hayes R, El Abedin SZ, Atkin R (2009) *J Phys Chem B* 113:7049
141. Lahiri A, Carstens T, Atkin R, Borisenko N, Endres F (2015) *J Phys Chem C* 119:16734
142. Li H, Endres F, Atkin R (2013) *Phys Chem Chem Phys* 15:14624
143. McLean B, Li H, Stefanovic R, Wood RJ, Webber GB, Ueno K, Watanabe M, Warr GG, Page A, Atkin R (2015) *Phys Chem Chem Phys* 17:325
144. Segura JJ, Elbourne A, Wanless EJ, Warr GG, Voitchovsky K, Atkin R (2013) *Phys Chem Chem Phys* 15:3320
145. Wakeham D, Hayes R, Warr GG, Atkin R (2009) *J Phys Chem B* 113:5961
146. Atkin R, Warr GG (2007) *J Phys Chem C* 111:5162
147. Bovio S, Podestà A, Milani P, Ballone P, Del Pópolo MG (2009) *J Phys Condens Matt Inst Phys J* 21:424118
148. Bovio S, Podestà A, Lenardi C, Milani P (2009) *J Phys Chem B* 113:6600
149. Yokota Y, Harada T, Fukui K-I (2010) *Chem Commun* 46:8627
150. Ichii T, Fujimura M, Negami M, Murase K, Sugimura H (2012) *Jpn J Appl Phys* 51(08K):B08

151. Zhang X, Zhong Y-X, Yan J-W, Su Y-Z, Zhang M, Mao B-W (2012) *Chem Commun* 48:582
152. Elbourne A, McDonald S, Voichovsky K, Endres F, Warr GG, Atkin R (2015) *ACS Nano* 9:7608
153. Tabor D, Winterton RHS (1969) *Proc Roy Soc A Math Phys Eng Sci* 312:435
154. Israelachvili J, Min Y, Akbulut M, Alig A, Carver G, Greene W, Kristiansen K, Meyer E, Pesika N, Rosenberg K, Zeng H (2010) *Rep Prog Phys* 73:36601
155. Israelachvili JN, Adams GE (1976) *Nature* 262:774
156. Israelachvili JN, Tabor D (1972) *Proc Roy Soc A Math Phys Eng Sci* 331:19
157. Kasuya M, Kurihara K (2014) *Electrochemistry* 82:317
158. Kawai H, Sakuma H, Mizukami M, Abe T, Fukao Y, Tajima H, Kurihara K (2008) *Rev Sci Instrum* 79:43701
159. Britton J, Couzens NEA, Coles SW, van Engers CD, Babenko V, Murdock AT, Koós A, Perkin S, Grobert N (2014) *Langmuir ACS J Surf Colloids* 30:11485
160. Horn RG, Evans DF, Ninham BW (1988) *J Phys Chem* 92:3531
161. Perkin S, Albrecht T, Klein J (2010) *Phys Chem Chem Phys* 12:1243
162. Ueno K, Kasuya M, Watanabe M, Mizukami M, Kurihara K (2010) *Phys Chem Chem Phys* 12:4066
163. Dushkin CD, Kurihara K (1998) *Rev Sci Instrum* 69:2095
164. Bou-Malham I, Bureau L (2010) *Soft Matter* 6:4062
165. Perkin S, Crowhurst L, Niedermeyer H, Welton T, Smith AM, Gosvami NN (2011) *Chem Commun* 47:6572
166. Gebbie MA, Valtiner M, Banquy X, Fox ET, Henderson WA, Israelachvili JN (2013) *Proc Natl Acad Sci USA* 110:9674
167. Espinosa-Marzal RM, Arcifa A, Rossi A, Spencer ND (2014) *J Phys Chem C* 118:6491
168. Espinosa-Marzal RM, Arcifa A, Rossi A, Spencer ND (2014) *J Phys Chem Lett* 5:179
169. Gebbie MA, Dobbs HA, Valtiner M, Israelachvili JN (2015) *Proc Natl Acad Sci USA* 112:7432
170. Jurado LA, Kim H, Arcifa A, Rossi A, Leal C, Spencer ND, Espinosa-Marzal RM (2015) *Phys Chem Chem Phys* 17:13613
171. Santos VO, Alves MB, Carvalho MS, Suarez PAZ, Rubim JC (2006) *J Phys Chem B* 110:20379
172. Brandão CR, Costa LA, Breyer HS, Rubim JC (1846) *Electrochem Commun* 2009:11
173. Yuan Y-X, Niu T-C, Xu M-M, Yao J-L, Gu R-A (2010) *J Raman Spectrosc* 41:516
174. Li JF, Huang YF, Ding Y, Yang ZL, Li SB, Zhou XS, Fan FR, Zhang W, Zhou ZY, Wu DY, Ren B, Wang ZL, Tian ZQ (2010) *Nature* 464:392
175. Zhang N, Wang X-R, Yuan Y-X, Wang H-F, Xu M-M, Ren Z-G, Yao J-L, Gu R-A (2015) *J Electroanal Chem* 751:137
176. Liu Y, Yuan Y-X, Wang X-R, Zhang N, Xu M-M, Yao J-L, Gu R-A (2014) *J Electroanal Chem* 728:10
177. Zhang M, Yu L-J, Huang Y-F, Yan J-W, Liu GK, Wu D-Y, Tian Z-Q, Mao B-W (2014) *Chem Commun* 50:14740
178. Rivera-Rubero S, Baldelli S (2004) *J Phys Chem B* 108:15133
179. Baldelli S (2008) *Acc Chem Res* 41:421
180. Baldelli S (2005) *J Phys Chem B* 109:13049
181. Aliaga C, Santos CS, Baldelli S (2007) *Phys Chem Chem Phys* 9:3683
182. Baldelli S (2013) *J Phys Chem Lett* 4:244
183. Xu S, Xing S, Pei S-S, Ivaništšev V, Lynden-Bell R, Baldelli S (2015) *J Phys Chem C* 119:26009
184. Kislenco SA, Samoylov IS, Amirov RH (2009) *Phys Chem Chem Phys* 11:5584
185. Wang S, Li S, Cao Z, Yan T (2010) *J Phys Chem C* 114:990
186. Feng G, Qiao R, Huang J, Dai S, Sumpter BG, Meunier V (2011) *Phys Chem Chem Phys* 13:1152

Chapter 8

Dielectric Properties of Ionic Liquids at Metal Interfaces: Electrode Polarization, Characteristic Frequencies, Scaling Laws

A. Serghei, M. Samet, G. Boiteux and A. Kallel

Abstract The electrical and dielectric properties of ionic liquids measured by broadband dielectric spectroscopy are analyzed in detail, in order to determine the characteristic frequencies governing the spectral dependence of electrode polarization effects. A universal behavior is revealed: plotting the characteristic frequencies as a function of the DC-conductivity for a large variety of ionic liquids, single collapsing curves are obtained. This is due to the fact that the charge carriers present in ionic liquids have comparable molecular dimensions. Furthermore, an analytical approach is developed in order to determine, using the dielectric signature of electrode polarization effects, the dielectric properties of ionic liquids at metal interfaces. A new relaxation process taking place in the nanometric interphases formed at the contact with the measurement electrodes is reported. It is assigned to an exchange process between the interphase and the bulk.

8.1 Introduction

Due to their unique combination of properties, ionic liquids [1–16] represent an important class of materials with numerous applications in a large variety of technological domains. They have a high thermal stability, a negligible vapor pressure, a high electrical conductivity, good solvent properties, a high electrochemical window, a high heat capacity, nonflammability properties, etc. Ionic

A. Serghei (✉) · M. Samet · G. Boiteux
Université Lyon1, Ingénierie des Matériaux Polymères, CNRS UMR 5223,
69622 Villeurbanne, France
e-mail: anatoli.serghei@univ-lyon1.fr

M. Samet · A. Kallel
Faculté des Sciences de Sfax, Laboratoire des Matériaux Composites
Céramiques et Polymères, 3018 Sfax, Tunisia

liquids are thus used in applicative domains as various as electrolytes (for supercapacitors, fuel cells, sensors, and batteries), separation techniques (for extraction, extractive distillation, gas separation), lubricants and additives, solvents (in biocatalysis, organic reactions, polymerization, nanoparticles), heat storage (as thermal fluids), etc. One of the most important functionality of ionic liquids is related to their high value of ionic conductivity. However, due to the fact that the charge carriers are ions, a fundamental difference arises as compared to materials showing an electronic conductivity. Due to blocking effects of ions at the interfaces with the metal electrodes used for the measurements, the phenomenon of electrode polarization [17–36] appears in the low frequency range of the dielectric spectra and leads to a large decrease in the conductive properties of the ionic liquids. The conductivity of ionic liquids can be thus used only in a limited frequency range, in a spectral region not affected by the phenomenon of electrode polarization. The characteristic frequencies of this phenomenon are tightly related to the charge transport properties of ionic liquid in the interfacial layers formed at the contact with the metal electrodes used for the measurements [35]. Understanding the electric and dielectric properties of ionic liquids at metal interfaces represents thus a topic of fundamental importance. The current chapter aims to contribute to this subject, by analyzing in detail the characteristic frequencies and the scaling laws of the electrode polarization effects and, furthermore, by demonstrating how this phenomenon can be used to determine the complex dielectric function of ionic liquids at metal interfaces.

8.2 Materials and Methods

8.2.1 *Materials*

Several ionic liquids (purchased from Iolitec) were investigated in the current work: 1-hexyl-3-methylimidazolium chloride (HMIM Cl), 1-Hexyl-3-methylimidazolium-tetrafluoroborate (HMIM BF₄), 1-butyl-3-methylimidazolium-hexafluorophosphate (BMIM PF₆), methyl trioctylammonium bis(trifluoromethylsulfonyl)imide (N1888 Tf₂N), N Tributyl N Methyl ammonium bis(trifluoromethylsulfonyl)imide (N4441 NTf₂), 1-butyl-3-methylimidazolium-bis(trifluoromethane)sulfonamide (BMIM TFSI), 1-butyl-3-methylimidazolium-tetrafluoroborate (BMIM BF₄), 1-Ethyl-3-methylimidazolium thiocyanate (EMIM TCN), and 1-Butyl-1-methylpyrrolidinium bis(trifluoromethylsulfonyl)imide (BMPy TFSI). Polymer/ionic liquid blends prepared by solvent casting were examined as well. A polymeric material, polyvinylacetate (PVAc, Mw = 100.000 g/mol, from Sigma Aldrich), doped with 20 % of BMIM BF₄ (by volume), was used to prepare a polymeric material with a high value of ionic conductivity.

8.2.2 Methods

The dielectric measurements were carried out using a high resolution alpha analyzer (Novocontrol GmbH), assisted by a Quatro temperature controller. The samples were measured in a parallel plate geometry with a separation distance of 200 μm using Platinum electrodes and Teflon spacers. The applied voltage was 0.1 V. Before starting the measurements, the samples were annealed for several hours at 160 $^{\circ}\text{C}$ under flow of pure nitrogen, in the cryostat of the dielectric spectrometer. After that, the dielectric measurements were performed as a function of frequency (typically in the range between 10 MHz and 0.1 Hz) at constant temperatures. The temperature was controlled by heating the sample by a jet of pure nitrogen, which leads to stabilization conditions better than 0.1 $^{\circ}\text{C}$.

8.3 Dielectric Properties of Ionic Liquids: Characteristic Frequencies and Universal Scaling Laws

The typical electrical and dielectric properties of ionic liquids are presented in Fig. 8.1, showing the spectral dependence of the complex permittivity $\epsilon^*(\omega) = \epsilon'(\omega) - i\epsilon''(\omega)$ and of the complex conductivity $\sigma^*(\omega) = \sigma'(\omega) - i\sigma''(\omega)$ of HMIM Cl measured at different temperatures. The experimental features observed in spectra of $\epsilon^*(\omega)$ and $\sigma^*(\omega)$ are caused by the phenomenon of electrode polarization.

These spectral features reflect a balance of impedances between the contribution of the charge transport in the bulk and the dielectric properties of the interfacial layers formed at the contact with the metal electrodes used to carry out the dielectric measurements. With increasing temperature, the characteristic spectral dispersions related to the phenomenon of electrode polarization are shifted to higher

Fig. 8.1 Complex dielectric permittivity and complex conductivity of HMIM Cl versus frequency at different temperatures, as indicated

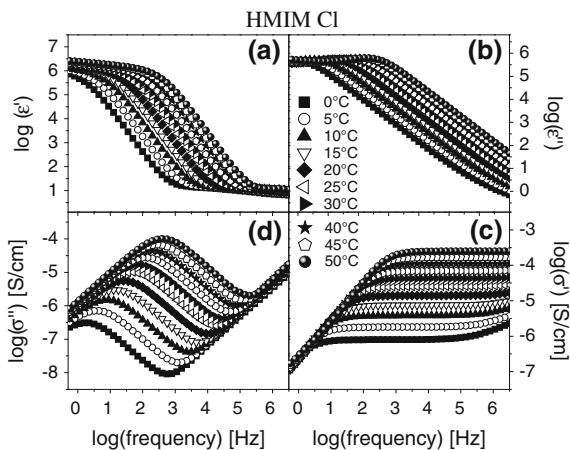
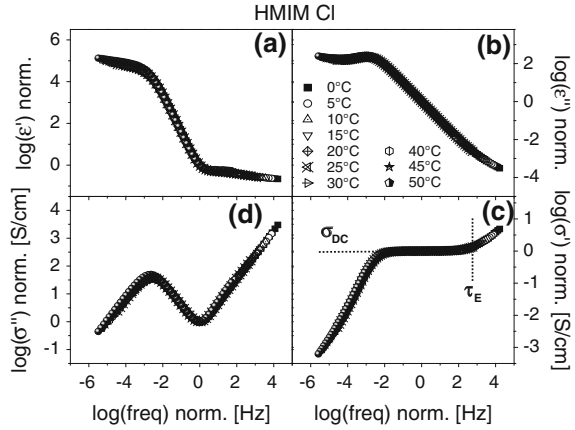


Fig. 8.2 The data shown in Fig. 8.1 are presented normalized. The normalization was carried out with respect to the minimum and the maximum observed in σ'' . In **c**, the values of the DC-conductivity σ_{DC} and of the hopping time of the charge carriers $\tau_E = 1/(2\pi f_E)$, where f_E represents the hopping rate, are marked by *dotted lines*



frequencies. Normalizing the experimental data presented in Fig. 8.1 leads—in a broad frequency and temperature range—to single collapsing curves in the spectral dependence of $\varepsilon^*(\omega)$ and $\sigma^*(\omega)$ (Fig. 8.2).

The collapsing curves obtained upon normalization indicate the existence of scaling laws governing the global dielectric response of ionic liquids. In order to derive these scaling laws, five characteristic frequencies can be defined (Fig. 8.3):

- $f_E = 1/(2\pi\tau_E)$, the hopping rate of the charge carriers [36] (where τ_E represents the hopping time), corresponding to the transition between the diffusive and the subdiffusion regime observed at high frequencies in the spectral dependence of $\sigma'(\omega)$ (Fig. 8.2).
- f_{on} , the “onset” of electrode polarization effects, is the frequency position where the net permittivity ε'_{net} starts to show an increase with decreasing frequency. This onset corresponds to a minimum in σ''_{net} and to a maximum in the second derivative of ε'_{net} .
- f_{max} , the “full development” of electrode polarization effects, is the frequency position where the enhanced values of ε'_{net} start to show a “saturation” plateau. This frequency corresponds to a maximum in σ''_{net} and to a minimum in the second derivative of ε'_{net} .
- f_{MWS} , the frequency position where a peak in the dielectric loss ε''_{net} is observed.
- f_i , the frequency position where the increase in ε'_{net} shows an inflection point and where, by definition, the second derivative $\frac{\partial^2(\log \varepsilon'_{net})}{\partial(\log f)^2} = 0$.

The scaling laws can be derived by analyzing the dependence of these characteristic frequencies on the DC-conductivity value σ_{DC} of the ionic liquid in the bulk. On a double-logarithmic plot, a linear dependence with a slope of 1.0 is observed between f_{on} , f_{max} , f_{MWS} , f_i and the values of σ_{DC} (Fig. 8.4). This obviously implies:

Fig. 8.3 The characteristic frequencies of electrode polarization effects: f_{on} , f_{max} , f_{MWS} and f_i , as measured in spectra of ϵ' , first derivative of ϵ' , second derivative of ϵ' , ϵ'' and σ''

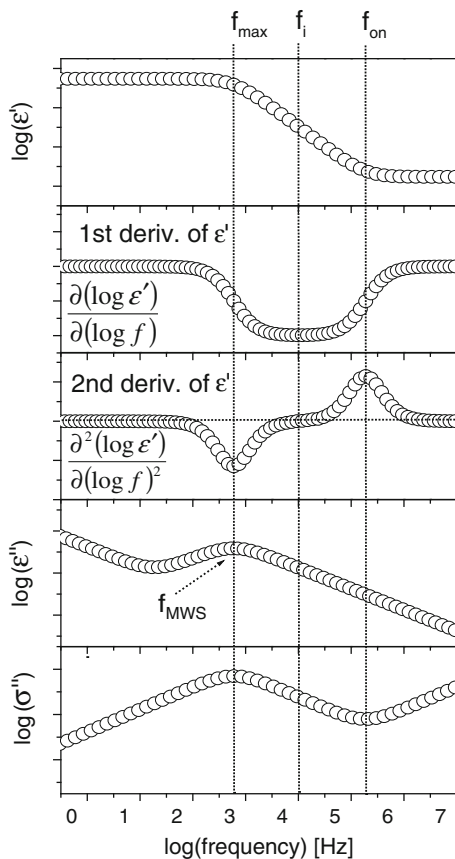
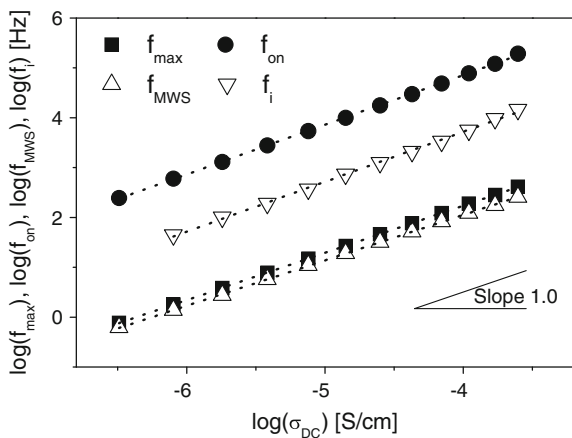


Fig. 8.4 The characteristic frequencies of electrode polarization effects for HMIM Cl, as a function of σ_{DC}



$$f_{\text{on}} \sim f_{\text{max}} \sim f_{\text{MWS}} \sim f_i \sim \sigma_{\text{DC}}, \quad (8.1)$$

which represents a first scaling law governing the global dielectric response of ionic liquids. A similar scaling law has been reported for other types of electrical polarization, as for instance the Maxwell–Wagner–Sillars interfacial polarization [36].

In addition to scaling laws relating the characteristic frequencies to different physical parameters, such as σ_{DC} , scaling laws expressing the interrelation between the characteristic frequencies can be derived as well. An example is given in Fig. 8.5, where the interrelation between f_i , f_{on} , f_{max} and f_{MWS} is examined.

A linear dependence is observed between f_i^2 and the product ($f_{\text{on}} f_{\text{max}}$) (Fig. 8.5a) and between f_{MWS} and f_i (Fig. 8.5c). A quantitative analysis of the experimental results (Fig. 8.5b, d) gives

$$f_i^2 \cong f_{\text{on}} f_{\text{max}} \quad (8.2)$$

and

$$f_{\text{MWS}} \cong f_{\text{max}} \quad (8.3)$$

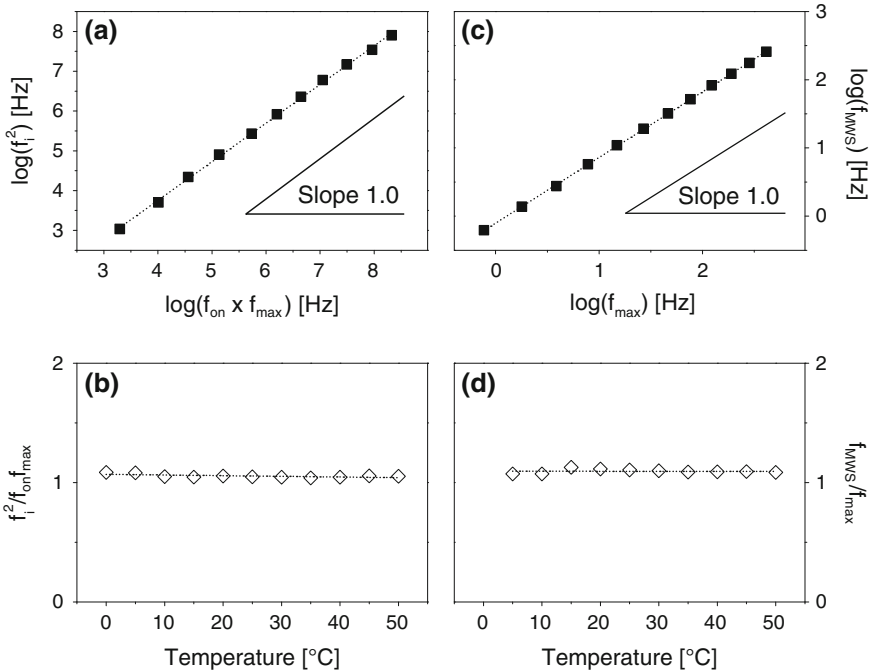


Fig. 8.5 **a** f_i^2 versus $f_{\text{on}} f_{\text{max}}$ for the measured data presented in Fig. 8.1; **b** $f_i^2 / f_{\text{on}} f_{\text{max}}$ versus temperature; **c** f_{MWS} versus f_{max} for the measured data presented in Fig. 8.1; **d** $f_{\text{MWS}} / f_{\text{max}}$ versus temperature

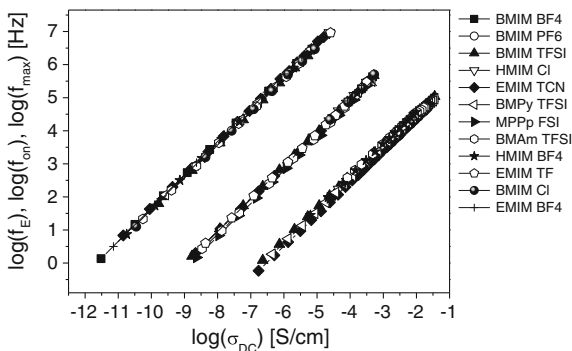
These two equations represent two other scaling laws expressing the interrelation between the characteristic frequencies of electrode polarization effects. One notes that f_{MWS} is nearly identical to f_{max} , meaning that the position of the peak measured in ϵ'' appears at the same frequency as the full development of the electrode polarization effects. As shown by a recent study [36], this interrelation appears to be fundamentally different for Maxwell–Wagner–Sillars interfacial polarization effects, where $f_{MWS} = f_i$ is reported [36]. Analyzing the interrelation between the characteristic frequencies opens thus the perspective of defining discrimination criteria between different types of electrical polarization, which can be of significant importance in disseminating the nature of different contributions appearing in the dielectric spectra of complex materials.

A universal behavior is revealed by plotting the characteristic frequencies f_{on} , f_{max} and f_E in dependence on σ_{DC} (Fig. 8.6). For a variety of ionic liquids of different chemical nature, identical values for the characteristic frequencies are found. The origin of this universal behavior has been explained in ref. [37]. It is essentially related to the fact that the charge carriers present in ionic liquids and, more generally, in electrolytes, have comparable molecular dimensions. This leads to negligible variations in the thickness of the interfacial layers, typically in the rage of 1 nm, as compared to the huge changes in the characteristic frequencies produced by temperature variations. The universal behavior revealed in Fig. 8.6 has far reaching consequences: knowing the value of the σ_{DC} of an ionic liquid leads immediately to a precise absolute determination of its characteristic frequencies, which means that the whole spectral dependence of its electrical and dielectric properties can be readily reconstructed using only the value of σ_{DC} . The scaling law presented in Eq. (8.1) can be thus reformulated as follows:

$$f_{on} \sim f_{max} \sim f_{MWS} \sim f_i \sim f_E \sim \sigma_{DC}, \tag{8.4}$$

This relation can be furthermore corroborated with the experimental observation that, at a given value of L , identical values for the characteristic frequencies are measured at a fixed value of σ_{DC} .

Fig. 8.6 The characteristic frequencies f_{on} , f_{max} , and f_E for a variety of ionic liquids, as indicated



Summarizing, the scaling laws governing the global electrical and dielectric responses of ionic liquids have been experimentally derived and it has been shown that they exhibit a universal behavior.

8.4 Electrode Polarization and Ionic Charge Transport at Metal Interfaces: Theoretical Model

The scaling laws of electrode polarization effects can be explained by a theoretical model [35] that takes into consideration the changes in the conductivity function of ionic liquids in the interfacial layers formed at the contact with the metal electrodes used to carry out the dielectric measurements. It has been shown [35] that the hopping rate of the charge carriers exhibit a pronounced decrease in the vicinity of the metal interfaces ($f_E(\text{interface}) \ll f_E(\text{bulk})$), which leads to a decrease by several orders of magnitude in the conductivity values ($\sigma_{\text{DC}}(\text{interface}) \ll \sigma_{\text{DC}}(\text{bulk})$). The global dielectric response can be thus expressed as a function of two parameters, the complex permittivity (or complex conductivity) of the bulk ϵ_{bulk}^* (respectively σ_{bulk}^*) and the complex permittivity (or complex conductivity) of the interfacial layers ϵ_{int}^* (respectively σ_{int}^*):

$$\epsilon_{\text{net}}^* = \frac{L\epsilon_{\text{bulk}}^*\epsilon_{\text{int}}^*}{d_{\text{int}}\epsilon_{\text{bulk}}^* + (L - d_{\text{int}})\epsilon_{\text{int}}^*} \quad (8.5)$$

with $\sigma_{\text{bulk}}^* = i\omega\epsilon_{\text{bulk}}^*$, $\sigma_{\text{int}}^* = i\omega\epsilon_{\text{int}}^*$ and $\sigma_{\text{net}}^* = i\omega\epsilon_{\text{net}}^*$, where L represents the sample thickness and d_{int} the total thickness of the interfacial layers (for simplicity, we consider $d_{\text{int}} = 2d_i$, d_i being the thickness of the interfacial layer formed at the contact with the metal electrodes). For materials exhibiting an ionic conductivity, Dyre-functions [38–40] can be used to simulate the global electrical properties:

$$\sigma_{\text{Dyre}}^*(\omega) = \sigma_{\text{DC}} \left[\frac{i\omega\tau_E}{\ln(1 + i\omega\tau_E)} \right] \quad (8.6)$$

where $\tau_E = 1/(2\pi f_E)$ represents the hoping time of the charge carriers and ω the radial frequency.

Thus

$$\epsilon^*(\omega) = \epsilon_{\infty} + \frac{\sigma_{\text{Dyre}}^*}{i\epsilon_0\omega} \quad (8.7)$$

with ϵ_{∞} being the permittivity value in the high frequency limit.

The results of this model are presented in Fig. 8.7, showing the measured dielectric spectra for the ionic liquid HMIM Cl and the global dielectric response calculated using the complex permittivity functions of the bulk ϵ_{bulk}^* and of the

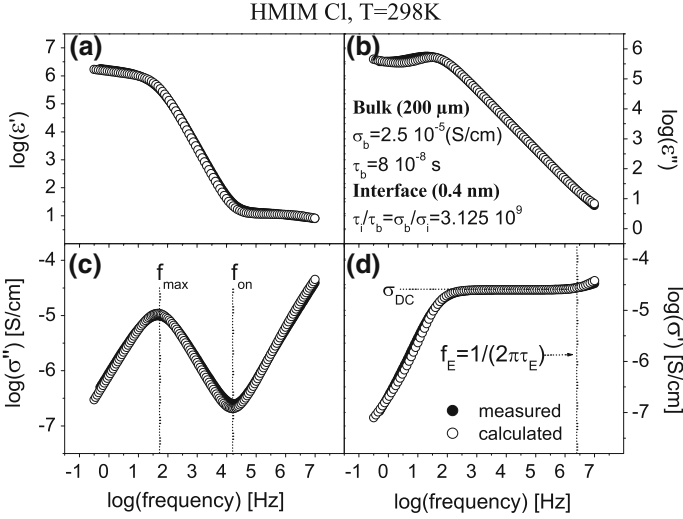


Fig. 8.7 Measured and calculated complex permittivity and complex conductivity for HMIM Cl at 298 K

interfacial layers ϵ_{int}^* . An excellent agreement between experimental results and calculations is found.

8.4.1 Analytical Calculations

8.4.1.1 The Onset and the Full Development of Electrical Polarization Effects

The global dielectric response of ionic liquids can be analyzed using formula (8.5). Separating the real and the imaginary part leads to

$$\epsilon'_{\text{int}} = \frac{[(\epsilon'_{\text{int}}\epsilon'_{\text{bulk}} - \epsilon''_{\text{int}}\epsilon''_{\text{bulk}})((1-x)\epsilon'_{\text{int}} + x\epsilon'_{\text{bulk}}) + (\epsilon''_{\text{int}}\epsilon'_{\text{bulk}} + \epsilon'_{\text{int}}\epsilon''_{\text{bulk}})((1-x)\epsilon''_{\text{int}} + x\epsilon''_{\text{bulk}})]}{[(1-x)\epsilon'_{\text{int}} + x\epsilon'_{\text{bulk}}]^2 + [(1-x)\epsilon''_{\text{int}} + x\epsilon''_{\text{bulk}}]^2} \quad (8.8)$$

$$\epsilon''_{\text{int}} = \frac{[(\epsilon''_{\text{int}}\epsilon'_{\text{bulk}} + \epsilon'_{\text{int}}\epsilon''_{\text{bulk}})((1-x)\epsilon'_{\text{int}} + x\epsilon'_{\text{bulk}}) - (\epsilon'_{\text{int}}\epsilon'_{\text{bulk}} - \epsilon''_{\text{int}}\epsilon''_{\text{bulk}})((1-x)\epsilon''_{\text{int}} + x\epsilon''_{\text{bulk}})]}{[(1-x)\epsilon'_{\text{int}} + x\epsilon'_{\text{bulk}}]^2 + [(1-x)\epsilon''_{\text{int}} + x\epsilon''_{\text{bulk}}]^2} \quad (8.9)$$

with $x = d_{\text{int}}/L$.

By definition, the onset and the full development of electrode polarization effects correspond to a minimum and a maximum in the spectral dependence of $\sigma'' = \varepsilon_0 \varepsilon'$, respectively. Analytical expressions for f_{on} and f_{max} can be thus derived by solving the equation:

$$\frac{\partial(\log(\sigma''))}{\partial(\log(f))} = 0 \quad (8.10)$$

The first derivative of σ'' gives

$$\frac{d\sigma''}{df} = \frac{Af^4 + Bf^2 + C}{D} \quad (8.11)$$

with

$$\begin{aligned} A &= (2\pi\varepsilon_0)^4 \varepsilon'_{\text{int}} \varepsilon'_{\text{bulk}} [(1-x)\varepsilon'_{\text{int}} + x\varepsilon'_{\text{bulk}}]^3 \\ B &= (2\pi\varepsilon_0)^2 [(1-x)\varepsilon'_{\text{int}} + x\varepsilon'_{\text{bulk}}] \left(3\varepsilon'_{\text{int}} \varepsilon'_{\text{bulk}} [(1-x)\sigma_{\text{int}} + x\sigma_{\text{bulk}}]^2 + \sigma_{\text{int}} \sigma_{\text{bulk}} [(1-x)\varepsilon'_{\text{int}} + x\varepsilon'_{\text{bulk}}]^2 - \right. \\ &\quad \left. (\sigma_{\text{int}} \varepsilon'_{\text{bulk}} + \sigma_{\text{bulk}} \varepsilon'_{\text{int}}) [(1-x)\sigma_{\text{int}} + x\sigma_{\text{bulk}}] [(1-x)\varepsilon'_{\text{int}} + x\varepsilon'_{\text{bulk}}] \right) \\ C &= [(1-x)\sigma_{\text{int}} + x\sigma_{\text{bulk}}]^2 ((\sigma_{\text{int}} \varepsilon'_{\text{bulk}} + \sigma_{\text{bulk}} \varepsilon'_{\text{int}}) [(1-x)\sigma_{\text{int}} + x\sigma_{\text{bulk}}] - \sigma_{\text{int}} \sigma_{\text{bulk}} [(1-x)\varepsilon'_{\text{int}} + x\varepsilon'_{\text{bulk}}]) \\ D &= [(1-x)\sigma_{\text{int}} + x\sigma_{\text{bulk}}]^2 + (2\pi\varepsilon_0)^2 [(1-x)\varepsilon'_{\text{int}} + x\varepsilon'_{\text{bulk}}]^2 f^2 / (2\pi\varepsilon_0) \end{aligned}$$

Hence

$$\frac{d\sigma''}{df} = 0 \Rightarrow f^2 = \pm \frac{\pm\sqrt{B^2 - 4AC} - B}{2A}$$

which leads to

$$f_{\text{on}}^2 = \frac{\sqrt{B^2 - 4AC} - B}{2A} \quad (8.12)$$

and

$$f_{\text{max}}^2 = \frac{\sqrt{B^2 - 4AC} + B}{2A} \quad (8.13)$$

In the situation when $\sigma_{\text{int}} \ll \sigma_{\text{bulk}}$, one can simplify the calculations by considering $\sigma_{\text{int}} \cong 0$ and $\sigma_{\text{bulk}} = \sigma_{\text{DC}}$ which leads to

$$f_{\text{on}}^2 = \frac{x\sigma_{\text{DC}}^2 \left(\sqrt{[2x\varepsilon'_{\text{bulk}} - (1-x)\varepsilon'_{\text{int}}]^2 - 4x\varepsilon'_{\text{bulk}} [(1-x)\varepsilon'_{\text{int}} + x\varepsilon'_{\text{bulk}}]} - [2x\varepsilon'_{\text{bulk}} - (1-x)\varepsilon'_{\text{int}}] \right)}{2(2\pi\varepsilon_0)^2 \varepsilon'_{\text{bulk}} [(1-x)\varepsilon'_{\text{int}} + x\varepsilon'_{\text{bulk}}]^2} \quad (8.14)$$

and

$$f_{\max}^2 = \frac{x\sigma_{DC}^2 \left(\sqrt{[2xe'_{\text{bulk}} - (1-x)e'_{\text{int}}]^2 - 4xe'_{\text{bulk}}[(1-x)e'_{\text{int}} + xe'_{\text{bulk}}]} + [2xe'_{\text{bulk}} - (1-x)e'_{\text{int}}] \right)}{2(2\pi\epsilon_0)^2 e'_{\text{bulk}} [(1-x)e'_{\text{int}} + xe'_{\text{bulk}}]^2} \quad (8.15)$$

In is immediately obvious that $f_{\text{on}} \sim f_{\max} \sim \sigma_{DC}$, which is in perfect agreement to the scaling laws revealed by the dielectric measurements.

8.4.1.2 The Inflection Point F_i

The frequency position f_i of the inflection point observed in the increase of ϵ' caused by electrical polarization phenomena can be determined by solving the equation:

$$\frac{\partial^2(\log \epsilon')}{\partial(\log f)^2} = 0 \quad (8.16)$$

with ϵ' being given by formula (8.8).

This leads to

$$\frac{4e'_{\text{int}}e'_{\text{bulk}}(2\pi\epsilon_0)^2 [(1-x)e'_{\text{int}} + xe'_{\text{bulk}}] [(1-x)\sigma_{\text{int}}^2 e'_{\text{bulk}} + x\sigma_{\text{int}}^2 \sigma_{\text{bulk}}^2] f_i^2}{\left((2\pi\epsilon_0)^2 f_i^2 e'_{\text{int}} e'_{\text{bulk}} [(1-x)e'_{\text{int}} + xe'_{\text{bulk}}] + [(1-x)\sigma_{\text{int}}^2 e'_{\text{bulk}} + x\sigma_{\text{bulk}}^2 e'_{\text{int}}] \right)^2} - \frac{4(2\pi\epsilon_0)^2 [(1-x)e'_{\text{int}} + xe'_{\text{bulk}}]^2 [(1-x)\sigma_{\text{int}} + x\sigma_{\text{bulk}}]^2 f_i^2}{\left((2\pi\epsilon_0)^2 f_i^2 [(1-x)e'_{\text{int}} + xe'_{\text{bulk}}]^2 + [(1-x)\sigma_{\text{int}} + x\sigma_{\text{bulk}}]^2 \right)^2} = 0$$

and results in

$$[(1-x)\sigma_{\text{int}}^2 e'_{\text{bulk}} + x\sigma_{\text{int}}^2 \sigma_{\text{bulk}}^2] [(1-x)\sigma_{\text{int}} + x\sigma_{\text{bulk}}]^2 - f_i^4 (2\pi\epsilon_0)^4 [(1-x)e'_{\text{int}} + xe'_{\text{bulk}}]^3 e'_{\text{int}} e'_{\text{bulk}} = 0$$

This gives the frequency position f_i of the inflection point observed in the increase of ϵ' :

$$f_i^4 = \frac{[(1-x)\sigma_{\text{int}}^2 e'_{\text{bulk}} + x\sigma_{\text{int}}^2 \sigma_{\text{bulk}}^2] [(1-x)\sigma_{\text{int}} + x\sigma_{\text{bulk}}]^2}{(2\pi\epsilon_0)^4 [(1-x)e'_{\text{int}} + xe'_{\text{bulk}}]^3 e'_{\text{int}} e'_{\text{bulk}}} \quad (8.17)$$

By considering $\sigma_{\text{int}} = 0$ and $\sigma_{\text{bulk}} = \sigma_{DC}$, one gets

$$f_i^4 = \frac{\sigma_{\text{DC}}^4 x^3}{(2\pi\epsilon_0)^4 [(1-x)\epsilon'_{\text{int}} + x\epsilon'_{\text{bulk}}]^3 \epsilon'_{\text{bulk}}} \quad (8.18)$$

which gives $f_i \sim \sigma_{\text{DC}}$, in full agreement with the scaling laws revealed in relation (8.1).

Combining Eq. (8.12) and (8.13) one gets

$$\begin{aligned} f_{\text{on}}^2 f_{\text{max}}^2 &= \left(\frac{\sqrt{B^2 - 4AC} - B}{2A} \right) \left(\frac{\sqrt{B^2 - 4AC} + B}{2A} \right) = \frac{(B^2 - 4AC) - B^2}{4A^2} = \frac{-C}{A} \Rightarrow \\ f_{\text{on}}^2 f_{\text{max}}^2 &= \frac{[(1-x)\sigma_{\text{int}} + x\sigma_{\text{bulk}}]^2 [\sigma_{\text{int}}\sigma_{\text{bulk}}[(1-x)\epsilon'_{\text{int}} + x\epsilon'_{\text{bulk}}] - (\sigma_{\text{int}}\epsilon'_{\text{bulk}} + \sigma_{\text{bulk}}\epsilon'_{\text{int}})] [(1-x)\sigma_{\text{int}} + x\sigma_{\text{bulk}}]}{(2\pi\epsilon_0)^4 \epsilon'_{\text{int}} \epsilon'_{\text{bulk}} [(1-x)\epsilon'_{\text{int}} + x\epsilon'_{\text{bulk}}]^3} \\ f_{\text{on}}^2 f_{\text{max}}^2 &= \frac{[(1-x)\sigma_{\text{int}}^2 \epsilon'_{\text{bulk}} + x\epsilon'_{\text{int}} \sigma_{\text{bulk}}^2] [(1-x)\sigma_{\text{int}} + x\sigma_{\text{bulk}}]^2}{(2\pi\epsilon_0)^4 [(1-x)\epsilon'_{\text{int}} + x\epsilon'_{\text{bulk}}]^3 \epsilon'_{\text{int}} \epsilon'_{\text{bulk}}} \end{aligned}$$

which gives $f_i^2 = f_{\text{on}} \times f_{\text{max}}$, in full agreement with the scaling law revealed by Eq. (8.2).

8.4.1.3 Electrode Polarization: The Asymptotic Behavior for $x \rightarrow 0$

The scaling laws derived for the general case of a sample consisting of two contributions of different conductivities can be simplified by setting $x \rightarrow 0$, in order to express the particular case of electrode polarization effects, where $d_{\text{int}} = 2d_1 \ll d_{\text{bulk}}$. It results:

$$f_{\text{on}} = \frac{\sigma_{\text{DC}} \sqrt{x}}{2\pi\epsilon_0 \sqrt{\epsilon'_{\text{int}} \epsilon'_{\text{bulk}}}} \quad (8.19)$$

$$f_{\text{max}} = \frac{x\sigma_{\text{DC}}}{2\pi\epsilon_0 \epsilon'_{\text{int}}} \quad (8.20)$$

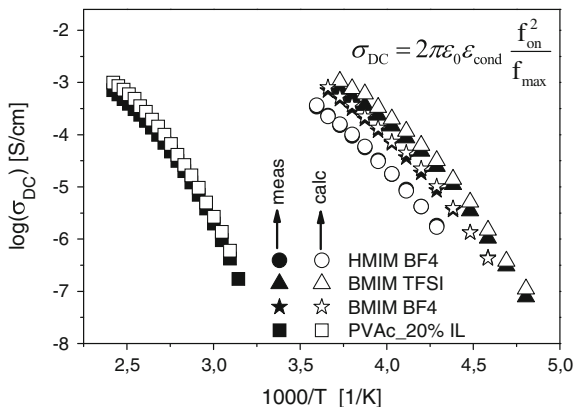
$$f_i = \frac{\sigma_{\text{DC}}}{2\pi\epsilon_0} \sqrt{\frac{x^3}{\epsilon_{\text{int}}^3 \epsilon_{\text{bulk}}}} \quad (8.21)$$

Quite evidently, Eqs. (8.19), (8.20), and (8.21) give directly $f_i^2 = f_{\text{on}} f_{\text{max}}$, in full agreement with the dielectric measurements.

Combining Eq. (8.19) and (8.20) gives

$$\sigma_{\text{DC}} = 2\pi\epsilon_0 \epsilon_{\text{bulk}} \frac{f_{\text{on}}^2}{f_{\text{max}}} \quad (8.22)$$

Fig. 8.8 Measured and calculated DC-conductivity values for HMIM BF₄, BMIM TFSI, BMIM BF₄ and a blend of PVAc with 20 % BMIM TFSI



This formula allows one to calculate the conductivity value σ_{DC} using only parameters determined from the capacitive response of the sample (ϵ_{bulk} , f_{on} , f_{max}). Its validity has been proven based on measurements on ionic liquids using metallic electrodes of different nature [35]. In Fig. 8.8, it is shown that formula (8.22) is valid not only for ionic liquids but also for blends of polymers/ionic liquids.

The characteristic frequency f_{MWS} , giving the spectral position of the peak observed in ϵ'' , can be calculated analytically by solving the equation:

$$\frac{\partial(\log \epsilon'')}{\partial(\log f)} = 0 \quad (8.23)$$

with $\epsilon'' = \epsilon''(f)$ being given by the formula (8.9).

This lead to

$$f_{\text{MWS}}^2 = \frac{\sqrt{(3\beta\gamma - \alpha\delta)^2 - 4\alpha\beta\gamma\delta} - (3\beta\gamma - \alpha\delta)}{2\alpha\gamma} \quad (8.24)$$

with

$$\alpha = [(\sigma_{\text{int}}\epsilon'_{\text{bulk}} + \sigma_{\text{bulk}}\epsilon'_{\text{int}})[(1-x)\epsilon'_{\text{int}} + x\epsilon'_{\text{bulk}}] - \epsilon'_{\text{int}}\epsilon'_{\text{bulk}}[(1-x)\sigma_{\text{int}} + x\sigma_{\text{bulk}}]] / (2\pi\epsilon_0)$$

$$\beta = [\sigma_{\text{int}}\sigma_{\text{bulk}}[(1-x)\sigma_{\text{int}} + x\sigma_{\text{bulk}}]] / (2\pi\epsilon_0)^3$$

$$\gamma = [(1-x)\epsilon'_{\text{int}} + x\epsilon'_{\text{bulk}}]^2$$

$$\delta = [(1-x)\sigma_{\text{int}} + x\sigma_{\text{bulk}}]^2 / (2\pi\epsilon_0)^2$$

By considering $\sigma_{\text{int}} = 0$ and $\sigma_{\text{bulk}} = \sigma_{\text{DC}}$ one gets

$$f_{\text{MWS}} = \frac{x\sigma_{\text{DC}}}{2\pi\epsilon_0[(1-x)\epsilon'_{\text{int}} + x\epsilon'_{\text{bulk}}]} \quad (8.25)$$

which gives $f_{\text{MWS}} \sim \sigma_{\text{DC}}$, identical to the scaling laws derived by dielectric measurements. In a recent study [36], it has been shown that this formula can be used to determine, from the frequency position of the Maxwell–Wagner–Sillars peak, either the volume fraction (when the conductivity is known) or the value of the conductivity σ_{DC} (when the volume fraction is known).

Imposing the limit $x \rightarrow 0$ on Eq. (8.25), leads to

$$f_{\text{MWS}} = \frac{x\sigma_{\text{DC}}}{2\pi\epsilon_0\epsilon'_{\text{int}}} \quad (8.26)$$

which is identical to formula (8.20) giving an analytical expression for f_{max} . Thus, $f_{\text{MWS}} = f_{\text{max}}$ in the limit of limit $x \rightarrow 0$, which is in full agreement with the experimental results obtained for electrode polarization effects.

8.4.1.4 Gradients of Local Dielectric Properties

Numerical simulations can be carried out to take into consideration transition regions where the local electrical properties of ionic liquids vary from the interface to the bulk (Fig. 8.9). In this situation, the global dielectric response of ionic liquids is treated as a three-phase problem, with three distinct contributions arising from the bulk, from the interface and from the transition region. Instead of Eq. 8.5, one has to use

$$\frac{L/2}{\epsilon_{\text{net}}^*} = \frac{d_i}{\epsilon_{\text{int}}^*} + \int_{d_i}^{L/2} \frac{dx}{\epsilon_{\text{gradient}}^*(x)} \quad (8.27)$$

with

$$\epsilon_{\text{gradient}}^*(\omega, x) = \epsilon'_{\text{gradient}}(\omega, x) - i\epsilon''_{\text{gradient}}(\omega, x).$$

Gradients of properties of different forms (linear, exponential) can be taken into account. The results are presented in Fig. 8.9, where the global response of ionic liquids is calculated and compared between the case of a two-phase model (bulk + interphase) and the case of a three-phase model (bulk + gradient + interphase). The results of the numerical calculations indicate a negligible impact of local gradients on the global response. In conclusion, the global response of electrode polarization effects and the corresponding scaling laws can be fully analyzed and understood in terms of a model considering the contributions of the bulk and of the interfaces.

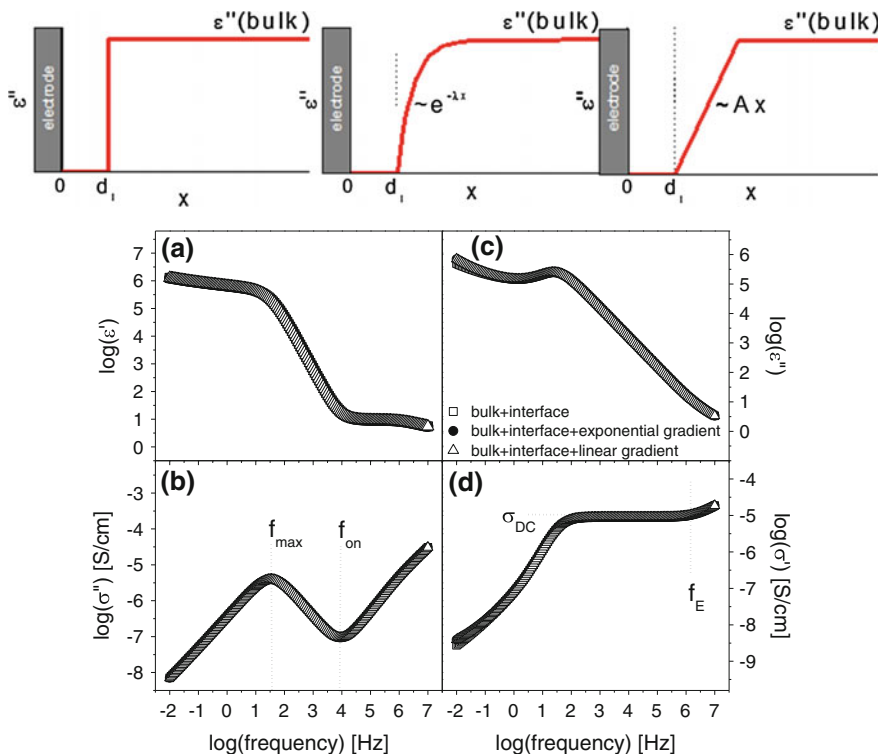


Fig. 8.9 Calculated complex permittivity and complex conductivity for electrode polarization effects of ionic liquids. Three situations are considered: (i) the global response is given by the bulk contribution and the contribution of the interfacial layers, without any gradients of properties; (ii) in addition to the contribution of the bulk and of the interfacial layers, exponential gradients in the local properties are considered; (iii) linear gradients in the local properties are considered

8.5 The Complex Dielectric Function of Ionic Liquids in the Interfacial Layers at Metal Electrodes

A first estimation for the range of the thickness of the interfacial layers can be done using simple considerations.

In the low frequency limit ($f \rightarrow 0$), $C'_{meas} \cong C'_{int}$ so that

$$d_{int} \cong \frac{\epsilon'_{int}}{\epsilon'_{meas}} L \tag{8.28}$$

But $\epsilon''_{int} < \epsilon''_{bulk} \rightarrow \epsilon'_{int} < \epsilon'_{bulk}$ (because of the Kramers–Kronig relation), and thus $1 < \epsilon'_{int} < \epsilon'_{bulk}$.

It results immediately

$$\frac{L}{\varepsilon'_{\text{meas}}} < d_i \cong \frac{\varepsilon'_{\text{int}}}{\varepsilon'_{\text{meas}}} L < \frac{\varepsilon'_{\text{bulk}}}{\varepsilon'_{\text{meas}}} L \quad (8.29)$$

which gives an interval for d_{int} , the thickness of interfacial layer. Applying this formula to the data presented in Fig. 8.1, leads to $0.34 \text{ nm} < d_{\text{int}} < 3.2 \text{ nm}$. Knowing the value of d_{int} , the dielectric properties of interfacial layers can be calculated by inverting Eq. (8.5). This leads to an expression relating $\varepsilon_{\text{int}}^*$ to the measurable parameters $\varepsilon_{\text{meas}}^*$ and $\varepsilon_{\text{bulk}}^*$:

$$\varepsilon_{\text{int}}^* = \frac{\varepsilon_{\text{meas}}^* \varepsilon_{\text{bulk}}^*}{\frac{L}{2d_i} \varepsilon_{\text{bulk}}^* + \left(1 - \frac{L}{2d_i}\right) \varepsilon_{\text{meas}}^*} \quad (8.30)$$

By separating the real and the imaginary part, one gets:

$$\varepsilon'_{\text{int}} = \frac{(1-y)\varepsilon'_{\text{bulk}}[\varepsilon_{\text{meas}}'^2 + \varepsilon_{\text{meas}}''^2] + y\varepsilon'_{\text{meas}}[\varepsilon_{\text{bulk}}'^2 + \varepsilon_{\text{bulk}}''^2]}{[(1-y)\varepsilon'_{\text{meas}} + y\varepsilon'_{\text{bulk}}]^2 + [(1-y)\varepsilon_{\text{meas}}'' + y\varepsilon_{\text{bulk}}'']^2} \quad (8.31)$$

and

$$\varepsilon''_{\text{int}} = \frac{(1-y)\varepsilon''_{\text{bulk}}[\varepsilon_{\text{meas}}'^2 + \varepsilon_{\text{meas}}''^2] + y\varepsilon''_{\text{meas}}[\varepsilon_{\text{bulk}}'^2 + \varepsilon_{\text{bulk}}''^2]}{[(1-y)\varepsilon'_{\text{meas}} + y\varepsilon'_{\text{bulk}}]^2 + [(1-y)\varepsilon_{\text{meas}}'' + y\varepsilon_{\text{bulk}}'']^2} \quad (8.32)$$

with: $y = \frac{L}{2d_i}$

A rigorous determination of the dielectric properties of the interfacial layers, however, implies a mathematical approach to calculate d_{int} . This can be done using the Kramers–Kronig relations applied to the dielectric function of the interfacial layers $\varepsilon_{\text{int}}^*$. In the most general situation, we consider the case when the dielectric properties in the interfacial layers $\varepsilon_{\text{int}}^*$ can be mathematically described by a function which vary with the distance x from the electrode, i.e., $\varepsilon_{\text{int}}^* = \varepsilon_{\text{int}}^*(\omega, x)$. This approach includes the both situations when the global dielectric response is analyzed in terms of two contributions (bulk + interfacial layers) as well as in terms of three contributions (bulk + interfacial layers + gradients of local properties at the interface).

One gets

$$\varepsilon_{\text{int}}^*(\omega, x) = \varepsilon_{\infty} + \frac{2}{\pi} \int_0^{\infty} \frac{\omega \varepsilon_{\text{int}}''(\omega, x)}{\omega^2 - \omega_0^2} d\omega \quad (8.33)$$

For the sake of simplicity, we consider the case when the variables ω and x are separable, meaning that the dielectric function $\varepsilon_{\text{int}}^*(\omega, x)$ can be written in the form of $\varepsilon_{\text{int}}^*(\omega, x) = X(x)Y(\omega)$. Imposing the condition of recovering the bulk behavior

in the limit of $x \rightarrow \infty$, the dielectric function at the interface can be written as $\epsilon_{\text{int}}^*(\omega, x) = X(x)\epsilon_{\text{bulk}}^*(\omega)$, with $X(x)$ approaching the value of 1 in the asymptotic limit of $x \rightarrow \infty$.

Using the Kramers–Kronig relation applied for bulk,

$$\epsilon'_{\text{bulk}}(\omega) = \epsilon_{\infty} + \frac{2}{\pi} \int_0^{\infty} \frac{\omega \epsilon''_{\text{bulk}}(\omega)}{\omega^2 - \omega_0^2} d\omega \quad (8.34)$$

and the Kramers–Kronig relation applied for the dielectric function of the interfacial layers (rel. 8.30), one can derive

$$\begin{aligned} \epsilon'_{\text{int}}(\omega, x) &= \epsilon_{\infty} + \frac{2}{\pi} \int_0^{\infty} \frac{\omega \epsilon''_{\text{int}}(\omega, x)}{\omega^2 - \omega_0^2} d\omega = \epsilon_{\infty} + \frac{2}{\pi} \int_0^{\infty} \frac{\omega \epsilon''_{\text{bulk}}(\omega) X(x)}{\omega^2 - \omega_0^2} d\omega \\ &= \epsilon_{\infty} + X(x) \left(\frac{2}{\pi} \int_0^{\infty} \frac{\omega \epsilon''_{\text{bulk}}(\omega)}{\omega^2 - \omega_0^2} d\omega \right) = \epsilon_{\infty} + X(x) (\epsilon'_{\text{bulk}}(\omega) - \epsilon_{\infty}) \end{aligned}$$

This leads to an equation relating the dielectric function of the bulk to the dielectric function of the interface:

$$\frac{\epsilon''_{\text{int}}}{\epsilon'_{\text{bulk}}} = \frac{\epsilon'_{\text{int}} - \epsilon_{\infty}}{\epsilon'_{\text{bulk}} - \epsilon_{\infty}} \quad (8.35)$$

With this relation, a system of 3 equations (Eqs. 8.31, 8.32, and 8.35) with three unknown parameters (d_{int} , ϵ'_{int} and ϵ''_{int}) can be defined in order to derive the complex dielectric function in the interfacial layers.

Analytical calculations lead to

$$2d_i = \frac{\epsilon_{\infty} \epsilon''_{\text{bulk}} (A + B - 2\alpha) L}{B\delta - \epsilon_{\infty} [\epsilon''_{\text{bulk}} (2\alpha - A) - B\epsilon''_{\text{meas}}]} \quad (8.36)$$

with

$$\begin{aligned} A &= \epsilon_{\text{meas}}'^2 + \epsilon_{\text{meas}}''^2 \\ B &= \epsilon_{\text{bulk}}'^2 + \epsilon_{\text{bulk}}''^2 \\ \delta &= \epsilon_{\text{meas}}' \epsilon_{\text{bulk}}'' - \epsilon_{\text{meas}}'' \epsilon_{\text{bulk}}' \\ \alpha &= \epsilon_{\text{meas}}' \epsilon_{\text{bulk}}' + \epsilon_{\text{bulk}}'' \epsilon_{\text{meas}}'' \end{aligned}$$

This equation can be used to directly calculate the thickness of the interfacial layer d_{int} using measurable parameters. The measurable parameters are the sample thickness L , ϵ_{meas}^* , ϵ_{meas}' , ϵ_{meas}'' , ϵ_{bulk}' and ϵ_{bulk}'' . The spectral dependence of ϵ'_{bulk} and ϵ''_{bulk} is well described by a model of charge transport in disordered systems developed by Dyre [38–40]. Results obtained for several ionic liquids are shown in Fig. 8.10.

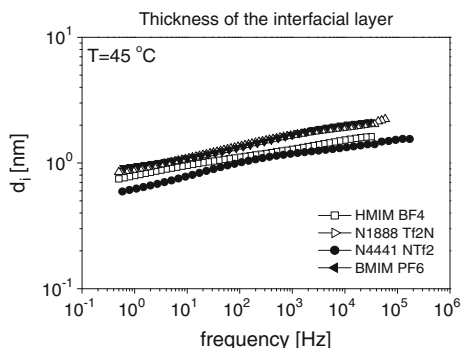


Fig. 8.10 The thickness of the interfacial layers calculated for different ionic liquids, as indicated

As expected, values in the order of 1 nm are obtained for the thickness of the interfacial layers. With this approach to calculate d_i , the complex dielectric permittivity of the interfacial layers can be directly determined using Eq. 8.30. Typical results are shown in Fig. 8.11, for the ionic liquid 1-butyl-3-methylimidazolium-hexafluorophosphate.

The dielectric losses in the interfacial layers are much smaller than the dielectric losses in the bulk, in accordance with a recent theoretical model of electrode polarization [35]. A detailed analysis is showing a relaxation peak in the dielectric loss of the interfaces (Fig. 8.12). The peak shifts to higher frequencies with increasing the temperature and it has been attributed to an ion exchange process between the interfacial layers and the bulk [41]. Plotting its frequency position as a function of inverse temperature, a Vogel–Fulcher–Tammann temperature dependence is observed. This indicates a strong correlation between the ion exchange process and the length-scale of cooperative fluctuations .

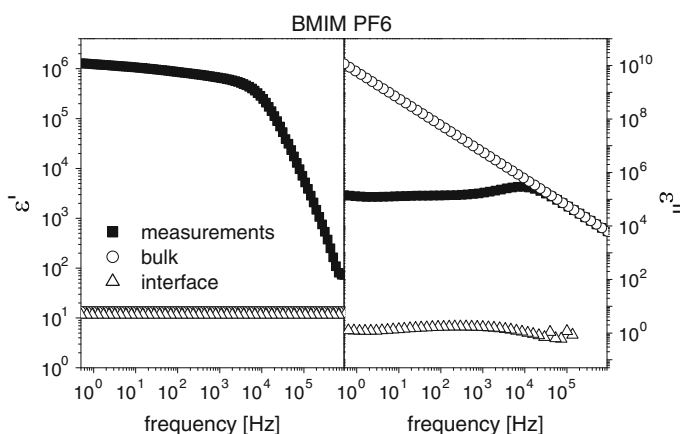
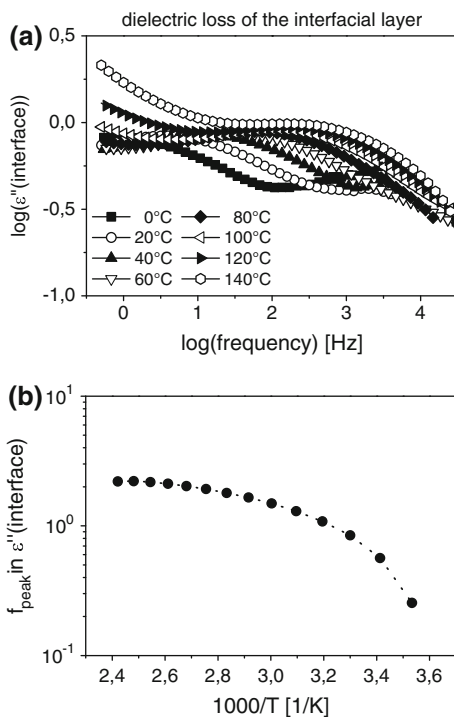


Fig. 8.11 The complex permittivity of the interfacial layers of BMIM PF6, formed at the contact with the electrodes used to carry out the dielectric measurements

Fig. 8.12 **a** The dielectric loss of the interfacial layers of BMIM PF6, at different temperatures, as indicated. The relaxation peak is attributed to an ion exchange process between the interfacial layers and the bulk; **b** the frequency position of the relation peaks observed in panel (a) as a function of inverse temperature. A VFT temperature dependence is observed



8.6 Conclusions

The dielectric properties of ionic liquids, as measured by broadband dielectric spectroscopy, have been systematically investigated as a function of frequency and temperature. The characteristic frequencies of electrode polarization effects and their corresponding scaling laws have been determined by analyzing the experimental results and have been analytically validated by calculations. We have shown that electrode polarization effects can be used to directly determine the complex dielectric function of ionic liquids at the interface with a metal electrode. A relaxation peak appearing in the dielectric loss of the interfacial layers have been observed. The relaxation peak shows a Vogel–Fulcher–Tammann temperature dependence and it is attributed to an ions exchange process between the interfacial layers and the ionic liquid in the bulk. Our approach allows thus a systematic investigation of the electric and dielectric properties of ionic liquids at metal interfaces and opens the perspectives of a better understanding of the physics of charge transport at solid interfaces.

References

1. Jordan A, Gathergood N (2015) *Chem Soc Rev* 44:8200–8237
2. Zhao Y, Bostrom T (2015) *Curr Org Chem* 19:556–566
3. Greaves TL, Drummond CJ (2015) *Chem Rev* 115:11379–11448
4. Somers AE, Howlett PC, MacFarlane DR (2013) *M Forsyth Lubricants* 1:3–21
5. Keskin S, Kayrak-Talay D, Akman U, Hortaçsu Ö (2007) *J Supercrit Fluids* 43:150–180
6. Buszewski B, Studzinska S (2008) *Chromatographia* 68:1–10
7. Marsh KN, Boxall JA, Lichtenthaler R (2004) *Fluid Phase Equilib* 219:93–98
8. Zhao H, Baker GA (2015) *Front Chem Sci Eng* 9:262–279
9. Hayes R, Warr GG, Atkin R (2015) *Chem Rev* 115:6357–6426
10. Marrucho IM, Branco LC, Rebelo LPN (2014) *Annu Rev Chem Biomol Eng* 5:527–546
11. Plechkova NV, Seddona KR (2008) *Chem Soc Rev* 37:123–150
12. Patel R, Kumari M, Khan AB (2014) *Appl Biochem Biotechnol* 172:3701–3720
13. MacFarlane DR, Tachikawa N, Forsyth M, Pringle JM, Howlett PC, Elliott GD, Davis JH, Watanabe M, Simon P, Angell CA (2014) *Energy Environ Sci* 7:232–250
14. Olivier-Bourbigou H, Magna L, Morvan D (2010) *Appl Catal A* 373:1–56
15. Armand M, Endres F, MacFarlane DR, Ohno H, Scrosati HB (2009) *Nat Mater* 8:621
16. Zakeeruddin SM, Grätzel M (2009) *Adv Funct Mater* 19:2187–2202
17. Sanabria H, Miller JH (2006) *Phys Rev E* 74:051505
18. Feldman Y, Nigmatullin R, Polygalov E, Texter J (1998) *Phys Rev E* 58:7561
19. Barbero G, Alexe-Ionescu AL (2005) *Liquid Crystals. J Phys Chem B* 32:943
20. Becchi M, Avendano C, Strigazzi A, Barbero G (2005) *J Phys Chem B* 105:23444
21. Klein RJ, Zhang S, Dou S, Jones BH, Colby RH, Runt J (2006) *J Chem Phys* 124:144903
22. Macdonald JR (1953) *Phys Rev* 92:4
23. Macdonald JR (2005) *J Phys: Condens Matter* 17:4369
24. Sawada A, Tarumi K, Naemura S (1999) *Jpn J Appl Phys Part 1* 38:1423
25. Coelho R, Non-Cryst J (1991) *Solids* 131:1136
26. Kohn P, Schröter K, Thurn-Albrecht T (2007) *Phys Rev Lett* 99:086104
27. MacDonald JR (1953) *Phys Rev* 92:4
28. Chang H, Jaffe G (1952) *J Chem Phys* 20:1071
29. Bates JB, Chu YT, Stribling WT (1988) *Phys Rev Lett* 60:627
30. Bordi F, Cametti C, Colby RH (2004) *J Phys: Condens Matter* 16:R1423
31. Yariv E, Frankel I (2002) *Phys Rev Lett* 89:266107
32. Alam MT, Islam MM, Okajima T, Ohsaka T (2008) *J Phys Chem C* 112:16600
33. Federov MV, Kornyshev AA (2007) *J Phys Chem* 112, 11868 (2008)
34. Kornyshev AA (2007) *J Phys Chem* 111:5545
35. Serghei A, Tress M, Sangoro JR (2009) *F. Kremer. Phys Rev B* 80:184301
36. Samet M, Levchenko V, Boiteux G, Seytre G, Kallel A, Serghei A (2015) *J Chem Phys* 142:194703
37. A. Serghei et al., in preparation
38. Dyre JC, Schroder TB (1996) *Phys Rev B* 54:14884
39. Dyre JC, Schroder TB (2000) *Rev Mod Phys* 72:873
40. Schroder TB (2000) Dyre JC (2000). *Phys Rev Lett* 84:310
41. A. Serghei et al., in preparation

Chapter 9

Decoupling Between Structural and Conductivity Relaxation in Aprotic Ionic Liquids

Evgeni Shoifet, Sergey P. Verevkin and Christoph Schick

Abstract For the $[C_nMIm][NTf_2]$ ionic liquids with $n = 4, 6,$ and 8 the dynamic calorimetric glass transition temperature $T_{g,dyn}$ was determined in a wide frequency range from 10^{-2} to 10^5 rad s^{-1} . The calorimetric glass transition temperature or vitrification temperature T_g from standard DSC with 10 K min^{-1} cooling rate was determined too. The obtained value for T_g in these ionic liquids is in very good agreement with the calorimetric $T_{g,dyn}$ at 100 s relaxation time. The obtained calorimetric data are compared to conductivity and other relaxation data available in the literature. In a relaxation map at short relaxation times ($\tau < 1$ μs), conductivity relaxation and calorimetric relaxation show a similar behavior. However, at low frequencies a significant decoupling between conductivity and calorimetric data is observed. Similar to other ionic conductors, the conductivity relaxation has a weaker temperature dependency than structural relaxation. Interestingly, there is no break in the conductivity data when crossing T_g . This is different from many other systems.

9.1 Introduction

A variety of experimental methods are capable of identifying dynamical processes occurring in glass forming melts on approaching its glass transition on cooling. The observed relaxation times and their temperature dependencies are not necessarily

E. Shoifet · C. Schick (✉)

Institute of Physics, University of Rostock, Albert-Einstein-Str. 23–24, 18051 Rostock, Germany

e-mail: christoph.schick@uni-rostock.de

E. Shoifet · S.P. Verevkin · C. Schick

Department Life Light and Matter, Competence Center CALOR, Albert-Einstein-Str. 25, 18059 Rostock, Germany

S.P. Verevkin

Institute of Physical Chemistry, University of Rostock, Dr.-Lorenz-Weg 1, 18059 Rostock, Germany

the same as known already for a long time [1–4]. Particularly for ion conducting materials, a significant difference between conductivity relaxation and shear relaxation (viscosity) was found. Similarly decoupling is also observed between translational diffusion and rotation [5, 6]. Since viscosity data are hardly available at or near the glass transition, other techniques are employed to study the decoupling between conductivity and main relaxation (dynamic glass transition) near T_g .

A very versatile tool for studying relaxation processes is broadband dielectric spectroscopy (BDS). Besides dipole relaxations of any kind, also conductivity relaxation is accessible by BDS. Nevertheless, in some cases it is not an easy task to assign definitely the dynamic glass transition to one of the observed relaxation processes. Particularly when more than one non-Arrhenius-like process occurs. Examples are the so-called Debye peak in alcohols [7, 8] or the end-to-end relaxation in type A polymers [9, 10] or liquid crystals [11].

In associated liquids, very similar relaxation times for different perturbations, e.g., dielectric, caloric, mechanical, NMR, etc., are often observed [12–14] and decoupling is not an issue. Particularly calorimetric techniques are very versatile tools to probe the dynamic glass transition (main relaxation). Calorimetric techniques practically detect only the main relaxation and not secondary or other relaxations like that of conductivity or flow. In several cases, mentioned above, specific heat spectroscopy [AC calorimetry, temperature-modulated differential scanning calorimetry (TMDSC)] was able to unambiguously identify the main relaxation [15–18]. Similarly, calorimetric techniques allow distinguishing conductivity relaxation from main relaxation. Paluch et al. demonstrated this recently for anhydrous ionic systems [19] and a polymerized ionic liquid [20].

For measurements where a periodic perturbation is used, the probed time scale of the relaxation process is well defined by the frequency of the perturbation. Commonly for isothermal frequency scans, the angular frequency ω_{\max} of the maximum of the imaginary part of the measured quantity provides the most probable relaxation time τ according

$$\tau = 1/\omega_{\max} \quad (9.1)$$

For temperature scans at constant frequency (isochronal experiments) Eq. (9.1) is applicable too. The situation becomes more complex when a quantity is measured during temperature scans, e.g., heat capacity at constant cooling or heating rate or viscosity. In calorimetric scan experiments at constant rate the step in the heat capacity is assigned to vitrification and the half step or the limiting fictive temperature are assigned as glass transition temperatures, T_g . For cooling rates of order of magnitude of 10 K min^{-1} for most materials, T_g corresponds to a time scale of 100–1000 s [21].

When the temperature of a liquid is approaching T_g , its viscosity increases by several orders of magnitude. Commonly, viscosity η at T_g is about 10^{10} to 10^{12} Pa s [22, 23]. On a sufficiently short time scale any liquid is elastic and behaves like a solid [24]. Considering a sudden shearing displacement starting from equilibrium or periodic shear in the high frequency limit the shear modulus will be termed

instantaneous or infinite-frequency shear modulus G_∞ . From viscosity, a characteristic time can be estimated from the Maxwell relation (Eq. (9.2)). The infinite-frequency shear modulus for molecular liquids below T_g equals to about $G_\infty = 10^8$ Pa. For many glass forming liquids, it is expected that G_∞ hardly changes with temperature [25].

$$\tau_\eta = \eta/G_\infty \quad (9.2)$$

A similar shear modulus of 10^8 Pa was found experimentally for several glassy room temperature ionic liquids (RTIL) [26, 27], so this value will be used as a scaling factor for viscosity data if not stated otherwise.

In case only temperature-dependent conductivity data, σ , are available, the Maxwell relation Eq. (9.3), as described in [28, 29], can make the link to a characteristic time.

$$\tau_\sigma = \frac{\epsilon_\infty \epsilon_0}{\sigma} \quad (9.3)$$

where ϵ_∞ is a high frequency dielectric permittivity and ϵ_0 that of vacuum.

An abundant number of works exist where authors used different relaxation techniques to compare the temperature dependences of their characteristic times. The correlation between different characteristic times in temperature is called coupling. There is no a priori reason that any of the characteristic times will exhibit even comparable temperature dependencies [13]. However, a class of liquids exists where the three usually independent isotropic scalar thermo-viscoelastic response functions (heat capacity, thermal expansivity, and thermal compressibility) collapse, with good approximation, on a single curve [30].

Jakobsen et al. [13] have shown on the example of a good glass-forming liquid 5-polyphenyl-4-ether (5PPE) that not only the thermo-viscoelastic data sets can be coupled but also dielectric and shear modulus relaxations. The coupling was analyzed in terms of time scale index that quantifies the parallel shift in a logarithmic scale as the distance from the dielectric relaxation data. The shift of the data was not larger than one order of magnitude and also the measured vitrification temperatures are close to the curves at 100 s relaxation time.

Shoifet et al. [14] measured the dynamic calorimetric glass transition of 5PPE in a wide frequency range. Again, a very good coincidence of the different data sets was observed (Fig. 9.1, orange stars).

The more common scenario for relaxation maps containing data from different relaxation processes is that of decoupling. The ratio between relaxation times may become temperature dependent. An example for such decoupling is the molten salt CKN (40 mol% $\text{Ca}(\text{NO}_3)_2$ -60 mol% KNO_3). In this ionic system with decreasing temperature, the dielectric conductivity relaxation times not only deviates from shear relaxation times but near vitrification temperature the behavior changes from non-Arrhenius to Arrhenius [28]. This decoupling of different relaxations is thought

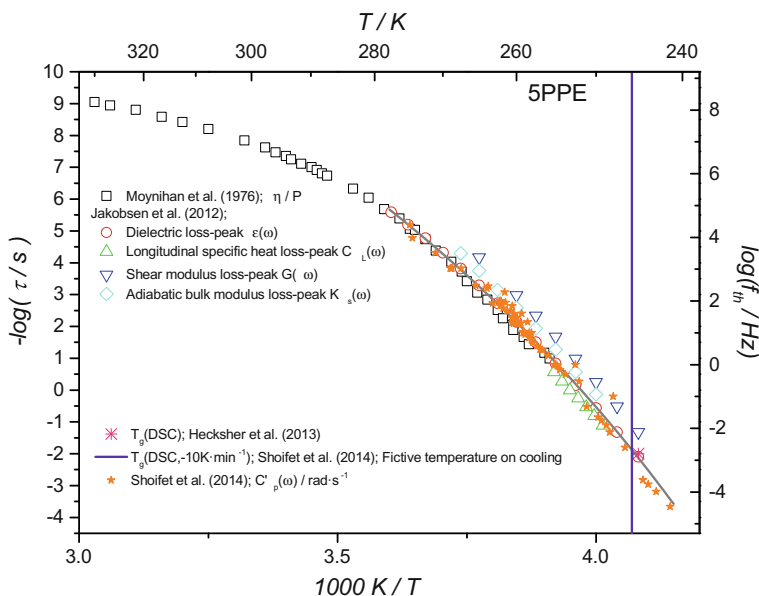


Fig. 9.1 Relaxation map for 5PPE. Viscosity data from Moynihan et al. [31] scaled as discussed above. The dielectric, longitudinal specific heat, shear modulus, and adiabatic bulk modulus data from Jakobsen et al. [13] were measured in the same cryostat. The dynamic calorimetric glass transition was taken from [14] and measured on several calorimetric devices. The vertical line indicating vitrification temperature measured with 10 K min^{-1} rate and T_g determined as limiting fictive temperature. For comparison the T_g from Hecksher et al. [32] is plotted and deviates by only 0.8 K. The *grey line* is a VFT fit to guide the eye

to come from unequal mobilities of the cations that become faster than the nitrate ions. Similar behavior was observed for several ion conducting materials [20].

However, recently, several authors reported about room temperature ionic liquids (RITLs) that exhibit perfect coupling between shear and dielectric relaxation spectroscopy [33, 34]. Russina et al. [33] demonstrated that for RTIL *1-hexyl-3-methylimidazolium bis[(trifluoromethyl)sulfonyl] imide*, shortly $[\text{C}_6\text{Mim}][\text{NTf}_2]$ a universal relaxation curve was obtained by finding the scaling factors between the different experimental techniques and no decoupling was observed in the vicinity of the vitrification temperature.

Figure 9.2 combines the relaxation times from different experimental techniques for the ionic liquid $[\text{C}_6\text{Mim}][\text{NTf}_2]$. The dielectric data were taken from Kwon et al. [35]. The data were digitalized from the plot and presented without further treatment. The data consist of an Arrhenius process and a non-Arrhenius process. The dielectric data from Leys et al. [36], Tokuda et al. [37], Russina et al. [33], and Wiedegren and Magee [38] were shifted to the Kwon et al. data by applying Eq. (9.3). The shifting factor was found to be $\epsilon_\infty \epsilon_0 = 10^{-9.8} \text{ F m}^{-1}$. Even though the ionic liquid is hydrophobic, the data exhibit a small shift to lower temperatures with increasing water content [38].

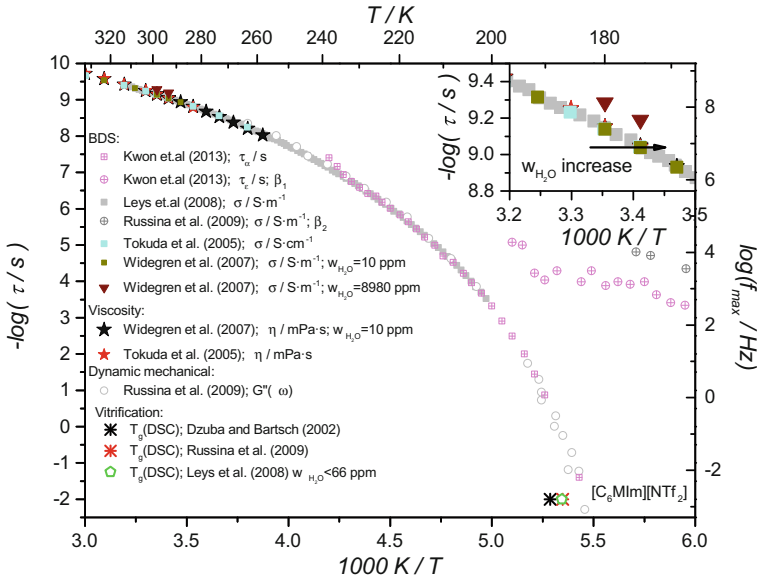


Fig. 9.2 The dielectric loss spectra of $[C_6MIm][NTf_2]$ by Kwon et al. [35] (magenta crossed squares and circles) were presented without further scaling. The viscosity data from Widegren et al. (dry: Table 1), Tokuda et al. (Fig. 3 in Ref. [37]). The conductivity relaxation data from Widegren et al. (dry and wet from Table 5 in Ref. [38]), Leys et al. (Fig. 4 in Ref. [36]), Tokuda et al. (Fig. 4 in Ref. [37]) and Russina et al. (Fig. 2 in Ref. [33]). The olive line is a VFT fit (Eq. (9.4)) to the data. The two extra Arrhenius-like dielectric relaxation processes by Russina et al. (gray crossed circles) and by Kwon et al. (magenta crossed circles) are included too. The vitrification temperature T_g from different references is plotted at 100 s relaxation time. The inset shows a zoom on the conductivity relaxation data for an easier observation of the shift due to increasing water content

The dynamic viscosity data were shifted according to Eq. (9.2) using infinite-frequency shear modulus $G_\infty = 10^8$ Pa. The dynamic mechanical data from Russina et al. [33] were shifted according to the above-mentioned procedure. The calorimetric T_g was placed at 100 s relaxation time.

As common, the data were analyzed and compared in terms of the Vogel–Fulcher–Tammann (VFT) Eq. (9.4) and its parameters.

$$\tau = \tau_0 \exp[B/(T - T_0)] \tag{9.4}$$

where τ_0 is high temperature limit of the α -relaxation time, B is the curvature, and T_0 is the Vogel temperature. A convenient classification for super cooled liquids is by the fragility index m [39]. It can be determination by focusing on the long relaxation time end of the activation diagram. At vitrification temperature the data show a characteristic slope as reviewed in Ref. [40]

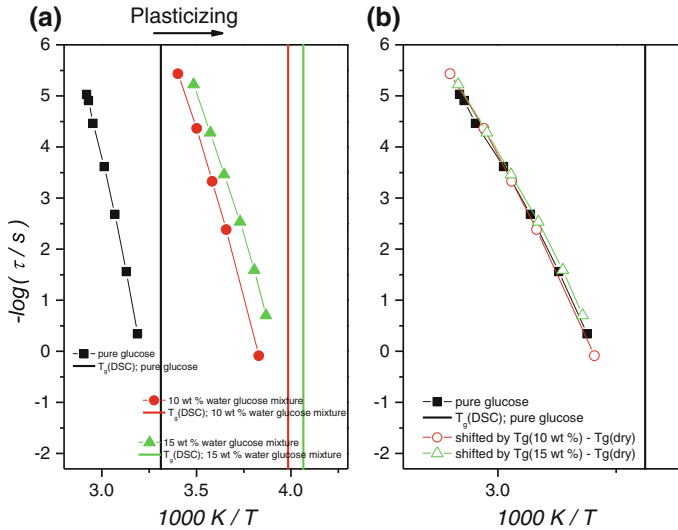


Fig. 9.3 **a** Plot of the frequency loss peaks of the primary relaxation in glucose (*square black*) and glucose–water mixtures (*red circle* 10 wt% water content; *green triangle* 15 wt% water content). **b** Shows all data after shifting by the shift in DSC T_g

$$m = \frac{d \log(\tau)}{d(T_g/T)}_{T=T_g} = \frac{B}{2.303} \frac{T_g}{(T_g - T_0)^2} \quad (9.5)$$

One can conclude from Eq. (9.5) that the low frequency range in the relaxation map, which is often hard to access, is of particular importance for the determination of m .

Interestingly, despite the perfect agreement between the different data sets in the Fig. 9.2 vitrification temperature T_g measured by DSC by several authors [33, 36, 41] are in good agreement with each other but they do not coincide with the other data and the VFT fit when plotted at 100 s relaxation time. Assuming a relaxation time of 1 s for the DSC T_g at 10 K min^{-1} , which is very unlikely, would collapse all data sets. It is therefore an interesting question if this deviation is true only for T_g or if it holds for $T_{g,dyn}$ from calorimetric data in a wider frequency range.

Properties of ionic liquids are known to be very sensitive to small amounts of water [42]. Since many ionic liquids are hydrophilic, drying and possible absorption of small amounts of water during sample preparation or during the measurements is a serious issue when comparing data from different experimental setups. Commonly water acts as a plasticizer and shifts T_g and the traces in the relaxation map toward lower temperatures. Chan et al. [43] investigated the relaxation behavior for a glucose–water system. The plasticizing effect of the water on the relaxation behavior of glucose is seen as a parallel shift of the whole data sets in the relaxation

map (Fig. 9.3a). The traces collapse by shifting the dielectric relaxation curves by the observed change in the vitrification temperature T_g (Fig. 9.3b).

A possible plasticizing effect of water or other contaminants on the relaxation behavior in the ionic liquids under investigation is finally compared with the general trend presented in Fig. 9.3.

In this contribution, we study the possible decoupling between conductivity and main relaxation for three ionic liquids. The chapter is structured as follows: after a short introduction into frequency-dependent heat capacity measurements (heat capacity spectroscopy) in a broad frequency range experimental results for room temperature ionic liquids from the series $[C_nMIm][NTf_2]$ with $n = 4, 6,$ and 8 are presented and compared to conductivity data available from the literature in relaxation maps. Finally, we summarize the observations.

9.2 Heat Capacity Spectroscopy

Measurements of complex heat capacity (entropy compliance) was successfully performed for the first time in 1971 by Gobrecht et al. [44]. A dramatic increase in the available frequency range was possible by employing the so-called 3ω -technique [45, 46], a thermal wave spectroscopy, using infinite extended samples in order to avoid reflections of the thermal wave [47–49]. This technique covers several orders of magnitude in frequency and it was named “heat capacity spectroscopy” (HCS). The necessity for using infinite large samples complicates the 3ω -measurements by an unavoidable interrelation of complex heat capacity with some of the mechanical relaxations. The Roskilde “Glass and Time” group repeatedly pointed to this issue [50–52]. Complex measurement geometries were suggested overcoming these limitations [53–56]. A direct measurement of isobaric complex heat capacity is possible if one succeeds to stay in the thermally thin limit [52]. We followed this approach by combining several devices employing samples of different sizes (thickness) depending on the frequency range under investigation. The advantage of this approach is the usage of commercially available calorimeters in the low frequency range. These devices allow beside frequency-dependent complex heat capacity measurements, conventional scanning experiments at cooling and heating rate of order of 10 K min^{-1} . With the same device, with similar temperature calibration [57–63], the two aspects of glass transition: vitrification at linear cooling and slowing down of the main relaxation are simultaneously accessible by TMDSC in the mHz range. Only in the high frequency regime, custom-made devices are needed. The fact that the accessible frequency range of measurements between different devices is overlapping gives us a solid basis to judge the quality of the data. Possible deviations from other measurements are therefore unambiguously detectable.

The fact that we have used different devices creates a restriction on the sample size. To probe relaxation times around and above vitrification temperature, we have used a PerkinElmer Pyris 1 DSC. The size of the sample is in the milligram range.

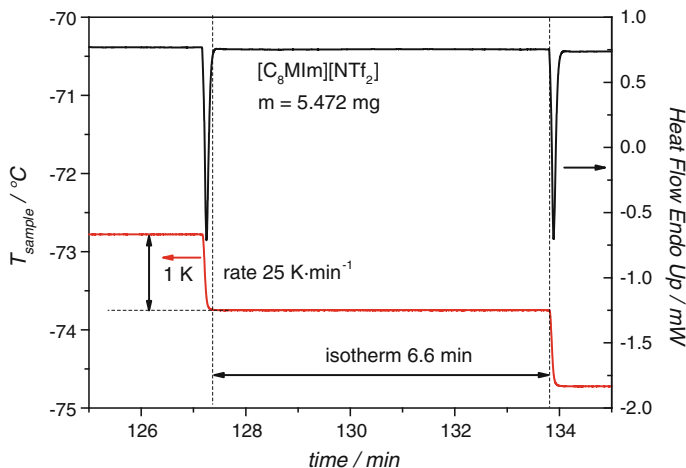


Fig. 9.4 The used TMDSC method with time–temperature profile (*red*) consisting of the cooling step of 1 K with 25 K min^{-1} followed by 6.6 min isotherm resulting in a base period of 398.4 s. The showed temperature–time profile is a sample temperature not programmed one. The baseline corrected sample response to this stepwise decrease is seen in the heat flow curve (*black*)

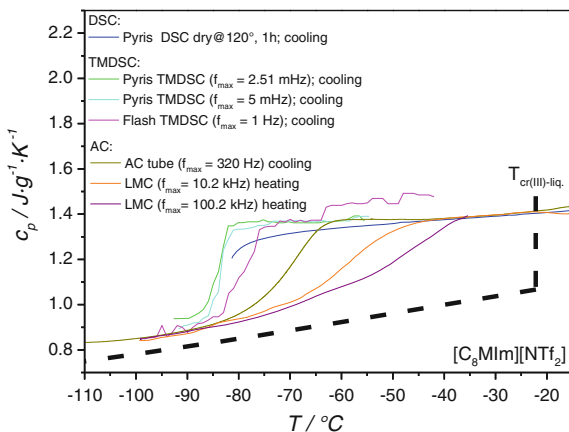
The sample was dried in situ for 60 min at $150 \text{ }^\circ\text{C}$ in dry nitrogen before the measurements. We have used the same sample and same drying procedure to determine the vitrification temperature, T_g , from scanning at constant rate and for studying the main relaxation, $T_{g,\text{dyn}}$ by frequency-dependent measurements of complex heat capacity. The frequency analysis was performed with the multifrequency TMDSC method [64] with a easy to program step like temperature–time profile (Fig. 9.4).

Complex specific heat capacity is available from a Fourier transform of the heating rate perturbation ($q = dT/dt$) and the heat flow rate response ($\text{HF} = dQ/dt$). Under conditions of linearity and stationarity [65, 66], temperature profiles as shown in Fig. 9.4 allow determination of an effective complex heat capacity at the base frequency and for higher harmonics [64, 67], Fig. 9.5. Further complex calibration algorithms must be applied to get specific complex heat capacity [65, 68–71]

$$c_{\text{eff}} = \frac{1}{m_s} \frac{\sum_{i=1}^n \text{HF}_i \cos(\omega t_i) - i \sum_{i=1}^n \text{HF}_i \sin(\omega t_i)}{\sum_{i=1}^n q_i \cos(\omega t_i) - i \sum_{i=1}^n q_i \sin(\omega t_i)} \quad (9.6)$$

The PerkinElmer Pyris 1 DSC with sample masses of order of 10 mg covers a frequency range from 10^{-3} to 10^{-2} Hz. For the next higher frequencies, the Mettler-Toledo Flash DSC 1, a chip-based calorimeter, was used. The typical sample size used in that device is in the microgram range. A similar step-scan program was utilized. The typical temperature step was 1 K with cooling rate of 1000 K s^{-1}

Fig. 9.5 Evolution of the heat capacity of *1*-octyl-3-methylimidazolium bis[(trifluoromethyl)sulfonyl] imide ($[C_8MIm][NTf_2]$) from a DSC cooling curve and from frequency-dependent complex heat capacity (dynamic glass transition). The black dashed line is the schematic representation of the specific heat of the crystal. The melting temperature as measured by adiabatic calorimetry [79] is indicated



followed by an isotherm of 0.999 s duration and resulting in base frequency of 1 Hz. The sample is much smaller compared to a Pyris 1 DSC, so 10 min at 110 $^{\circ}C$ in situ drying under dry nitrogen purge was enough to establish constant results. The Flash DSC 1 covers the frequency range from 0.1 to 100 Hz [14].

For frequencies above 100 Hz, we employed chip-based AC calorimeters. The chip calorimeter consists of a thin silicon nitride membrane with embedded polysilicon heaters and thermopiles. The sinusoidal modulated AC current passing through the heater is $I = I_0 \sin(\omega t/2)$. The block where the chip calorimeter is placed is temperature controlled and allows slow heating or cooling with rates of order 1 $K min^{-1}$ for isochronal experiments. The AC current at angular frequency $\omega/2$ yields an oscillating power at angular frequency ω with complex amplitude (P). The resulting temperature oscillation of the sample with complex amplitude (θ) is recorded by means of the thermopile and a lock-in amplifier [72–74]. The resulting effective heat capacity can be estimated with Eq. (9.7).

$$c_{eff} = \frac{P}{\omega\theta} \quad (9.7)$$

This AC calorimetry allows measurements of complex heat capacity, after careful calibration [72, 73], up to the kHz range. At higher frequencies, a contribution from the first harmonic dominates the signal and saturates the lock-in amplifier. In order to reach even higher frequencies, the AC current for heating was replaced by a modulated laser beam (light modulated calorimeter—LMC) [75]. This device can work up to frequencies of 1 MHz. Keeping the sample thin (<100 nm) the thin film limit can be still kept. The LMC device chamber is constantly purged with dry nitrogen and the humidity is monitored. The sample was not specifically dried, however due to the very thin sample the water under dry nitrogen

atmosphere was immediately removed. The relaxation data is in very good agreement with data from a purposely dried sample.

The sample for the high frequency AC calorimeters becomes so small that it has to be placed on the sample holder under a microscope. After sample placement and inserting the chip calorimeter into a vacuum tight thermostat, the sample was dried in situ at 60 °C under moderate vacuum (10^{-2} mbar). After drying, the chamber was filled with dry nitrogen. To verify that the drying procedure results in a dry enough sample, we have performed calorimetric measurements in a vacuum chamber at pressure of 10^{-8} mbar. This custom-made device [76] is utilizing the principle of AC calorimetry [77, 78]. No differences in the obtained temperatures were observed.

The combined calorimetric techniques in the current work cover the angular frequency range from 10^{-2} to 10^5 rad s $^{-1}$, corresponding to relaxation times between 100 s and 10 μ s.

9.3 Results

9.3.1 [C₆MIm][NTf₂]

Dynamic calorimetric measurements in the glass transition range for [C₆MIm][NTf₂] are now available over 7 orders of magnitude in frequency and are presented in a relaxation map (Fig. 9.6). For comparison, the VFT curve for the dynamic mechanical data reported by Russina et al. [33] and describing all data in Fig. 9.2 very well, is shown as olive curve. The dynamic glass transition temperatures determined from isochronic calorimetric experiments, utilizing different devices, are all following one trend and are mainly overlapping in the relaxation map. The coincidence of the vitrification temperature T_g acquired with DSC at cooling rate of 10 K min $^{-1}$ with the dynamic glass transition temperature $T_{g,dyn}$ at 100 s relaxation time confirms the common rule of thumbs, see a more detailed discussion in Ref. [21]. In general, the calorimetric data deviate increasingly from the data from Fig. 9.2 (olive line) with increasing relaxation time and approaching T_g . Only for relaxation times shorter 1 μ s the data seem to coincide. The VFT parameters for the calorimetric dynamic glass transition were obtained from a fit to all calorimetric data except the two highest frequencies, whose deviation from the total trend is apparent. They seem to follow the secondary relaxation process found by Kwon et al., which is indicated by the dashed line. Fragility from the calorimetric data equals to $m = 103$. Russina et al. report fragility $m = 71$. The fragility determined by Leys et al. equals $m = 57$ and deviates even more from the fragility obtained from the calorimetric data.

Some calorimetric data points for [C₆MIm][NTf₂] are positioned near the VFT curve from Fig. 9.2. Since water is always an issue for IIs, the sample was carefully

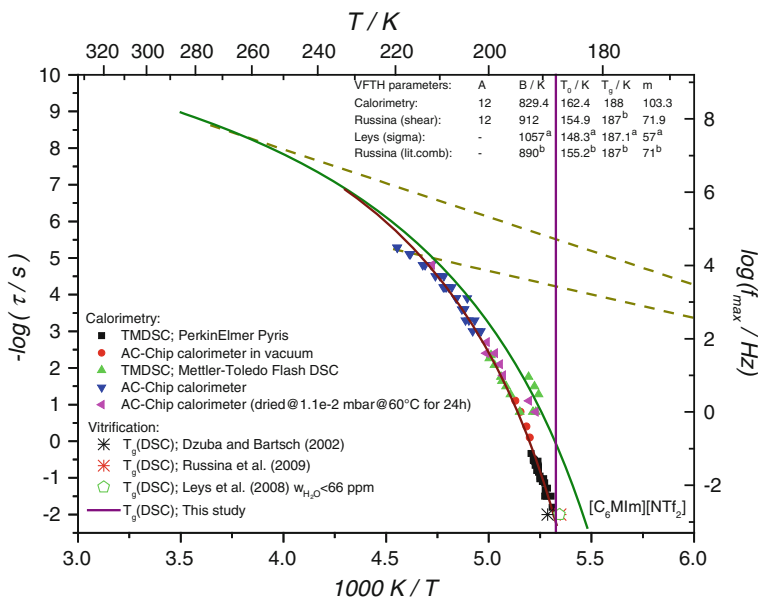


Fig. 9.6 The combined dynamic calorimetric data for $[C_6MIm][NTf_2]$ start from the vitrification temperature at cooling with 10 K min^{-1} (PerkinElmer DSC, purple vertical line). The lowest frequency data are collected with the same device from a multifrequency TMDSC analysis (black squares). Red circles present the data from the AC calorimeter in high vacuum. The points from the multifrequency TMDSC analysis employing the Mettler Toledo Flash DSC 1 (green triangle) overlap with the red circles (AC in vacuum). The points at higher frequencies are collected with an AC calorimeter (dried under vacuum at $60\text{ }^\circ\text{C}$ for a day; magenta triangles) and without additional drying at even higher frequencies (blue triangles). The VFT for the calorimetric data was fitted excluding the last two point (wine curve, first VFT parameter set). The mechanical data from Russina et al. [33] were fitted (olive line) and the second VFT set shows the parameters. For comparison, the fourth VFT set presents parameters as given by the authors for a combined study. The third set of VFT parameters is from Leys et al. [36]. The parameters in the inset are originating from Ref. [36] (superscript *a*) and Ref. [33] (superscript *b*)

dried and reexamined. This did not change the behavior and since the observed difference between the two curves is not constant as in Fig. 9.3, water as the reason for this difference is excluded. Actually, the reason for this behavior is not known and deserves further investigations. Generally speaking, the calorimetric data show decoupling from mechanical and conductivity data.

To see if decoupling between calorimetric and dielectric relaxation times is alkyl chain length dependent, as other thermo physical properties [80], we have investigated the neighboring IIs with *four* and *eight* carbon atoms in the alkyl chain. These ionic liquids were investigated by several other authors too.

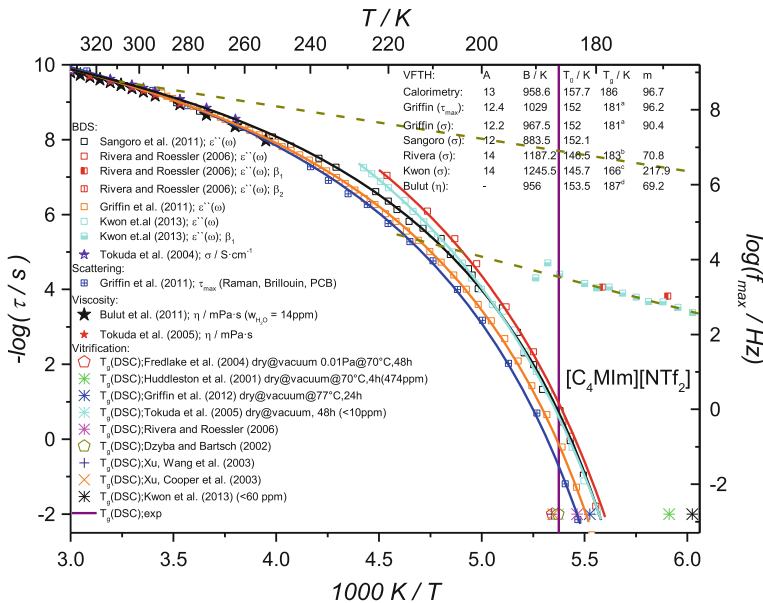


Fig. 9.7 Dielectric data for $[C_4MIm][NTf_2]$ from Sangoro et al. [34] (open black squares) was recalculated from diffusion ($\lambda_h^2 = 6D\tau$ with $\lambda_h = 0.26$ nm (parameters given by the authors). The viscosity data from Bulut et al. [84] (black stars) and Tokuda et al. [37] (red stars) and conductivity data [83] (half-filled violet star) was shifted as described above and applied for the previous RTIL ($[C_6MIm][NTf_2]$). The data from Rivera and Rössler [81] (red open squares, half-filled squares and squares with vertical line), Griffin et al. [82] (orange open squares and blue crossed squares) and Kwon et al. [35] (cyan open squares and half-filled squares) were digitalized from the figures and taken as presented by the authors. The dark yellow dashed lines are guides for the eye for the trend of the secondary relaxations. The slower secondary relaxation data is out of range in the plot. The color curves represent VFT fits to the data with parameters shown in the inset. The parameters in the inset originating from Ref. [82] (superscript a), Ref. [81] (superscript b), Ref. [35] (superscript c) and Ref. [84] (superscript d). The vitrification temperature plotted at 100 s relaxation time from the literature (variation of the large single points at $-\log(\tau) = -2$) and this study (purple vertical line)

9.3.2 $[C_4MIm][NTf_2]$

Surprisingly, already the reported vitrification temperature T_g in $[C_4MIm][NTf_2]$ is widely spread in a temperature region covering ~ 20 K. If remaining water is the reason for this spread is not clear since most of the reported data were collected on well-dried samples as indicated in the legend of Fig. 9.7. Nevertheless, the majority of the data is coinciding with the value from this work (purple vertical line) in Fig. 9.7.

Also the reported dielectric data are not superimposed. The dielectric data from Sangoro et al. [34] (black open squares) are shifted to lower temperatures compared to the data from Griffin et al. (orange open squares). The observed shift is similar to

that due to the plasticizing effect of water as demonstrated for another system in Fig. 9.3. However, data reported by Kwon et al. [35] (open cyan squares) and Rivera and Rössler [81] (open red squares) follow the data from Sangoro et al. near $\tau = 100$ s. However, they start to deviate from each other at shorter relaxation times. Additionally, decoupling between light scattering (crossed blue squares) and dielectric (orange squares) relaxation was observed by Griffin et al. [82]. The two characteristic times are following a similar temperature dependence at short relaxation times, however for relaxation times longer 10 ns they start to deviate. The conductivity data by Tokuda et al. [83] (half-filled violet star) add to this already complex relaxation picture another data set coinciding with Sangoro et al. (black open squares). However, they do not coincide with the dielectric data from Griffin et al. (orange open squares) which closely coincides with the dynamic viscosity data by Tokuda et al. [37] (red stars) and Bulut et al. [84] (black stars).

The aprotic ionic liquid $[C_4MIm][NTf_2]$ shows in the dielectric spectra two Arrhenius-like fast relaxation processes (Rivera and Rössler, red half-filled squares and red vertical-halved squares that are out of the range in the plot, however its trend is depicted by the dashed dark yellow line). The fast relaxation process that appears at longer relaxation times coincides with the fast relaxation process reported by Kwon et al. (cyan half-filled squares). Kwon et al. argued that the fast relaxation process seems to be similar to the alkyl chain relaxation as in the work of Hempel et al. [85]. The fast relaxation data are extrapolated with the dashed dark yellow lines as a guide for the eye.

The relaxation map (Fig. 9.8) for $[C_4MIm][NTf_2]$ includes the VFT curves from Fig. 9.7 and the calorimetric data in a wide frequency range from this study. The vitrification temperature from this study (purple vertical line) separates the glassy state from the supercooled liquid, right and left, respectively. The low frequency TMDSC data from the Pyris DSC are close to the vitrification temperatures at 10 K min^{-1} found in the majority of the references and in this study if placed at 100 s relaxation time. The data points (black spheres) measured on the AC vacuum calorimeter are keeping the trend set by the Pyris TMDSC data. The same holds for the TMDSC data from the Flash DSC. However, the AC relaxation data points are spread. Part of the data points is found to continue the previous trend. However, several of the data points are shifted to lower temperatures and are close to the data reported by Sangoro et al. By carefully drying the sample, we were not able to identify water as the reason for this spread. Other reasons must be considered too. Again, it requires more experiments under very well-controlled conditions to clarify this unusual behavior.

9.3.3 $[C_8MIm][NTf_2]$

Here, the studied ionic liquid with the longest alkyl chain $[C_8MIm][NTf_2]$, the broadest frequency range in calorimetric measurements was acquired. Relaxation data available in the literature are in good agreement and are included in the

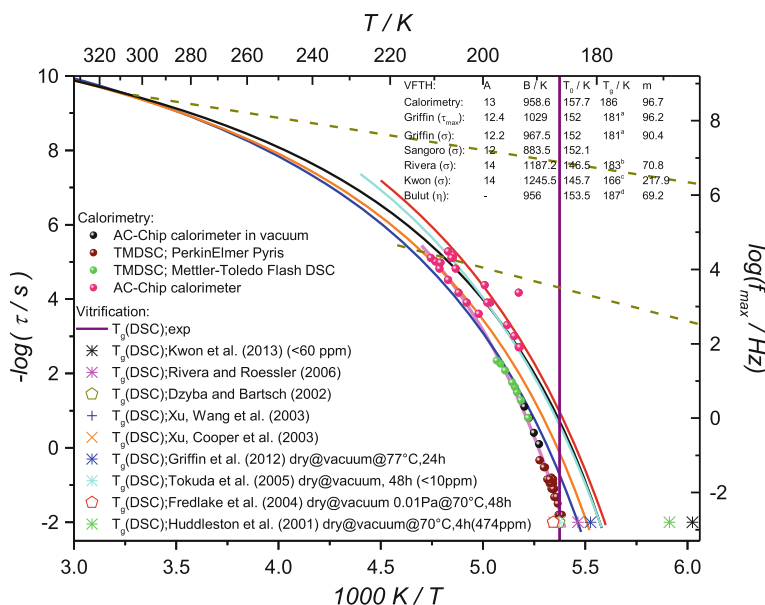


Fig. 9.8 Calorimetric data for the ionic liquid $[C_4MIm][NTf_2]$. For comparison the VFT curves from Fig. 9.7 are included without the data points. At $\tau = 100$ s the vitrification temperatures from the references and own data from a PerkinElmer DSC (purple vertical line) are shown. The lowest frequency-dependent data were collected with the same device applying the multifrequency TMDSC analysis (wine spheres). The data at higher frequencies are from the AC calorimeter in vacuum (black spheres). The multifrequency TMDSC analysis on the Mettler Toledo Flash DSC 1 (green spheres) overlaps with the AC calorimeter data in vacuum and extend the curve toward higher frequencies. High frequency data points are collected with the AC calorimeter (pink spheres). There are obvious deviations between the data, which are discussed in the text. The fitted VFT curve to the calorimetric data has light magenta color. Only the AC chip calorimeter data from the high temperature branch at highest frequencies were taken for the VFT fit

relaxation map Fig. 9.9. The calorimetric data are again located on two curves. A few data points in the 10 ms to 1 s range for the relaxation time are close to the dielectric data while all others, including data in the same relaxation time range, are significantly shifted to higher temperatures. This is similar to the behavior of $[C_4MIm][NTf_2]$ and $[C_6MIm][NTf_2]$. The underlying reason for the dynamic calorimetric data not to follow a single curve is puzzling and needs more investigations.

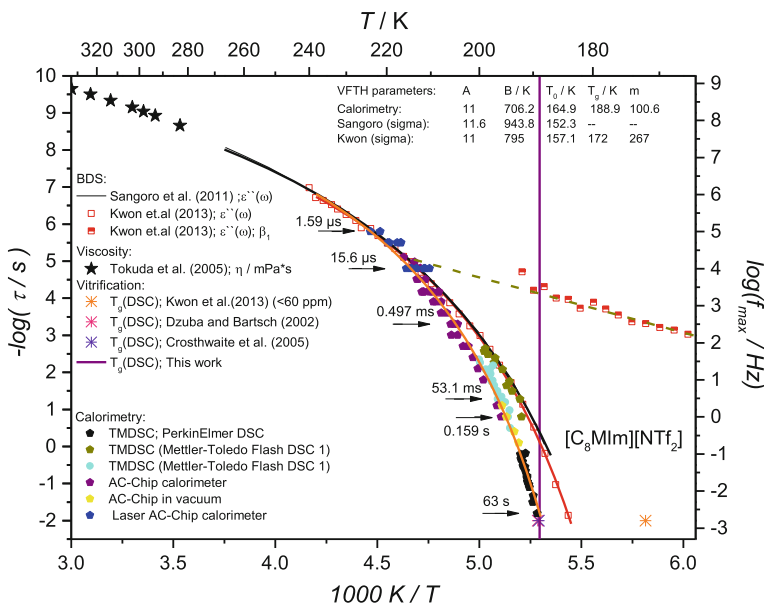


Fig. 9.9 Relaxation map for $[C_8MIm][NTf_2]$. Data from Sangoro et al. [34] (*open black circles*) were recalculated from diffusion $\langle \lambda_h^2 \rangle = 6D\tau$ with $\lambda_h = 0.31$ nm (parameters given by the authors). The *filled black stars* are viscosity data from Tokuda et al. [37]. The dielectric data from Kwon et al. [35] (*red open squares and half-filled squares*) were taken as presented by the authors. The *dark yellow dashed line* gives a guide for an eye for the trend of the secondary relaxation. The colors of the VFT fit correspond to data in the legend with parameters shown in the inset. The vitrification temperatures from the references are plotted at 100 s relaxation time (different large single points at $-\log(\tau/s) = -2$) and from this study (*purple vertical line*). The calorimetric data consist of additional branch (*dark yellow filled circles*). The laser modulated calorimeter was used (*blue filled circles*) to reach the highest frequencies. All calorimetric data except for right TMDSC branch were used for the VFT fit (*orange line*)

9.4 Summary

For the $[C_nMIm][NTf_2]$ ionic liquids with $n = 4, 6,$ and 8 available relaxation data from the literature were collected. The dynamic calorimetric glass transition temperature $T_{g,dyn}$ was determined in a wide frequency range from 10^{-2} to 10^5 rad s^{-1} . The calorimetric glass transition temperature or vitrification temperature T_g from standard DSC with 10 K min^{-1} cooling rate was determined too. The obtained value for T_g in these ionic liquids is in very good agreement with $T_{g,dyn}$ at 100 s relaxation time. In this respect, ionic liquids behave similar to molecular liquids. The relation between cooling rate and corresponding frequency as discussed by Donth [86] and verified for different systems in Ref. [21] holds for the studied ionic liquids too.

Figure 9.10 shows the VFT fits for all above-mentioned ionic liquids. The calorimetric data for $[C_6MIm][NTf_2]$ and $[C_8MIm][NTf_2]$ are almost the same near

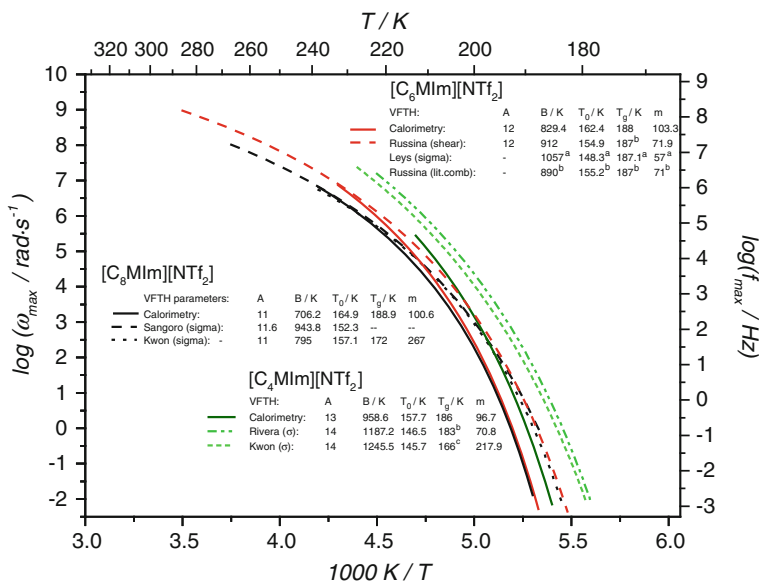


Fig. 9.10 Summarizing activation diagram for $[C_n\text{MIm}][\text{NTf}_2]$ ionic liquids with $n = 4, 6,$ and 8 . VFT fits from calorimetric data from this study (solid curves) are shown together with VFT fits to conductivity relaxations from the literature (dashed lines)

the vitrification temperatures. However, their temperature dependences are not similar. The ionic liquid with the shorter alkyl chain shows a stronger temperature dependence. For relaxation times shorter than about 10 ms the curves deviate from each other. The conductivity data show schematically the same behavior for those two liquids. However, at low frequencies a significant decoupling between conductivity and calorimetric data is observed. Interestingly, the relaxation time from which their behavior started to branch for dielectric and calorimetric data is very alike at about 10 ms. At higher frequencies the decoupling between calorimetric and conductivity data diminishes. This holds for relaxation times shorter than about 1 μs . Interestingly, there is no break etc. in the conductivity data when crossing T_g . This is different from many other systems. The calorimetric VFT curve for $[C_4\text{MIm}][\text{NTf}_2]$ ionic liquid, shows a similar behavior with significant decoupling between calorimetric and conductivity relaxation. The calorimetric behavior of this liquid does not merge the conductivity relaxation near 1 μs . Maybe at much shorter relaxation times both relaxations will coincide in the relaxation map. Similar to the other IIs shown here the conductivity relaxation has a weaker temperature dependency than structural relaxation.

When the alkyl chain length increases from $n = 4$ to $n = 6$ changes occur in the vitrification temperatures T_g and in the dynamic behavior, $T_{g,\text{dyn}}$. However, when changing from $n = 6$ to $n = 8$ only the dynamics starting from elevated temperatures around ~ 196 K are changing. From the DSC scans, we have also seen that

[C₄MIm][NTf₂] and [C₆MIm][NTf₂] are crystallizing on heating. The DSC scans for [C₈MIm][NTf₂] do not show any cold crystallization. This also highlights the importance of the alkyl chain length for the thermophysical properties of these ionic liquids.

It is possible to estimate the excess entropy of the liquid over the crystal at the glass transition, as described by Adam and Gibbs, $S_g = \Delta C_p \ln(T_g/T_0)$. Angell [87] suggested that this quantity may be calculated by using the T_0 values obtained from fitting the VFT equation to transport data. Another quantity in the equation, ΔC_p , is the change in the heat capacity at the temperature of the ideal glass transition T_0 . This is not experimentally accessible since it requires an infinitely slow cooling process. In case the substances under study show similar ΔC_p , with first approximation the change in heat capacity can be taken at T_g . Then the excess entropy equation shows that the departure from ideality for a given glass can be judged from the magnitude of the ratio T_g/T_0 . The following values were obtained: $n = 4$ $T_g/T_0 = 1.18$; $n = 6$ $T_g/T_0 = 1.16$; $n = 8$ $T_g/T_0 = 1.15$. Here the ionic liquid with the longest alkyl chain seems to form the most ideal glass. This may suggest that the alkyl chain is an important element that governs the structural relaxation and induce the system packing capabilities.

Acknowledgment We acknowledge M. Ahrenberg for the measurements with the vacuum AC calorimeter.

References

1. Angell CA (1964) Free volume model for transport in fused salts: electrical conductance in glass-forming nitrate melts. *J Phys Chem* 68(7):1917–1929. doi:10.1021/j100789a042
2. Moynihan CT, Balitactac N, Boone L, Litovitz TA (1971) Comparison of shear and conductivity relaxation times for concentrated lithium chloride solutions. *J Chem Phys* 55 (6):3013–3019. doi:10.1063/1.1676531
3. Rekhson SM, Mazurin OV (1974) Stress and structural relaxation in Na₂O–CaO–SiO₂ glass. *J Amer Ceramic Soc* 57(7):327–328
4. Stickel F, Fischer EW, Richert R (1996) Dynamics of glass-forming liquids. II. Detailed comparison of dielectric relaxation, dc-conductivity, and viscosity data. *J Chem Phys* 104 (5):2043–2055
5. Fujara F, Geil B, Sillescu H, Fleischer G (1992) Translational and rotational diffusion in supercooled orthoterphenyl close to the glass transition. *Z Physik B* 88:195–204
6. Cicerone MT, Ediger MD (1996) Enhanced translation of probe molecules in supercooled O-terphenyl—Signature of spatially heterogeneous dynamic. *J Chem Phys* 104(18):7210–7218
7. Hansen C, Stickel F, Berger T, Richert R, Fischer EW (1997) Dynamics of glass-forming liquids. III. Comparing the dielectric α - and β -relaxation of 1-propanol and o-terphenyl. *J Chem Phys* 107(4):1086–1093
8. Murthy SSN, Tyagi M (2002) Experimental study of the high frequency relaxation process in monohydroxy alcohols. *J Chem Phys* 117(8):3837–3847. doi:10.1063/1.1494428
9. Schonhals A, Schlosser E (1993) Relationship between segmental and chain dynamics in polymer melts as studied by dielectric-spectroscopy. *Phys Scr T49A*:233–236

10. Schonhals A (1993) Relation between main and normal mode relaxations for polyisoprene studied by dielectric spectroscopy. *Macromolecules* 26(6):1309–1312
11. Rozanski SA, Stannarius R, Groothues H, Kremer F (1996) Dielectric properties of the nematic liquid crystal 4-N-pentyl-4'-cyanobiphenyl in porous membranes. *Liq Cryst* 20(1):59–66
12. Litovitz TA, McDuffie GE (1963) Comparison of dielectric and mechanical relaxation in associated liquids. *J Chem Phys* 39(3):729–734. doi:[10.1063/1.1734316](https://doi.org/10.1063/1.1734316)
13. Jakobsen B, Hecksher T, Christensen T, Olsen NB, Dyre JC, Niss K (2012) Communication: Identical temperature dependence of the time scales of several linear-response functions of two glass-forming liquids. *J Chem Phys* 136(8):081102–081104
14. Shoifet E, Schulz G, Schick C (2015) Temperature modulated differential scanning calorimetry—extension to high and low frequencies. *Thermochim Acta* 603:227–236. doi:[10.1016/j.tca.2014.10.010](https://doi.org/10.1016/j.tca.2014.10.010)
15. Wang LM, Richert R (2005) Debye type dielectric relaxation and the glass transition of alcohols. *J Phys Chem B Lett* 109:11091–11094
16. Schick C, Sukhorukov D, Schönhals A (2001) Comparison of the molecular dynamics of a liquid crystalline side group polymer revealed from temperature modulated DSC and dielectric experiments in the glass transition region. *Macromol Chem Phys* 202(8):1398–1404
17. Brás AR, Dionísio M, Huth H, Schick C, Schönhals A (2007) Origin of glassy dynamics in a liquid crystal studied by broadband dielectric and specific heat spectroscopy. *Phys Rev E* 75:061708
18. Krause C, Yin H, Cerclier C, Morineau D, Wurm A, Schick C, Emmerling F, Schonhals A (2012) Molecular dynamics of a discotic liquid crystal investigated by a combination of dielectric relaxation and specific heat spectroscopy. *Soft Matter* 8:11115–11122. doi:[10.1039/c2sm25610j](https://doi.org/10.1039/c2sm25610j)
19. Wojnarowska Z, Paluch KJ, Shoifet E, Schick C, Tajber L, Knapik J, Włodarczyk P, Gzybowska K, Hensel-Bielowka S, Verevkin SP, Paluch M (2015) Molecular origin of enhanced proton conductivity in anhydrous ionic systems. *J Am Chem Soc* 137(3):1157–1164. doi:[10.1021/ja5103458](https://doi.org/10.1021/ja5103458)
20. Wojnarowska Z, Knapik J, Jacquemin J, Berdzinski S, Strehmel V, Sangoro JR, Paluch M (2015) Effect of pressure on decoupling of ionic conductivity from segmental dynamics in polymerized ionic liquids. *Macromolecules* 48(23):8660–8666. doi:[10.1021/acs.macromol.5b02130](https://doi.org/10.1021/acs.macromol.5b02130)
21. Hensel A, Schick C (1998) Relation between freezing-in due to linear cooling and the dynamic glass transition temperature by temperature-modulated DSC. *J Non-Crystal Solids* 235–237:510–516
22. Angell CA (1995) Formation of glasses from liquids and biopolymers (Review). *Science* 267(5206):1924–1935
23. Scopigno T, Ruocco G, Sette F, Monaco G (2003) Is the fragility of a liquid embedded in the properties of its glass? *Science* 302(5646):849–852. doi:[10.1126/science.1089446](https://doi.org/10.1126/science.1089446)
24. Lamb J (1978) Viscoelasticity and lubrication: a review of liquid properties. *J Rheol* 22(4):317–347. doi:[10.1122/1.549482](https://doi.org/10.1122/1.549482)
25. Dyre JC (2006) The glass transition and elastic models of glass-forming liquids. *Rev Mod Phys* 78:953–972. doi:[10.1103/RevModPhys.78.953](https://doi.org/10.1103/RevModPhys.78.953)
26. Griffin PJ, Holt AP, Wang Y, Novikov VN, Sangoro JR, Kremer F, Sokolov AP (2014) Interplay between hydrophobic aggregation and charge transport in the ionic liquid methyltrioctylammonium bis(trifluoromethylsulfonyl)imide. *J Phys Chem B* 118(3):783–790. doi:[10.1021/jp412365n](https://doi.org/10.1021/jp412365n)
27. Iacob C, Sangoro JR, Serghei A, Naumov S, Korh Y, Kärger J, Friedrich C, Kremer F (2008) Charge transport and glassy dynamics in imidazole-based liquids. *J Chem Phys* 129(23):234511. doi:[10.1063/1.3040278](https://doi.org/10.1063/1.3040278)
28. Howell FS, Bose RA, Macedo PB, Moynihan CT (1974) Electrical relaxation in a glass-forming molten salt. *J Phys Chem* 78(6):639–648. doi:[10.1021/j100599a016](https://doi.org/10.1021/j100599a016)

29. Angell CA, Ngai KL, McKenna GB, McMillan PF, Martin SW (2000) Relaxation in glassforming liquids and amorphous solids. *J Appl Phys* 88(6):3113–3157. doi:[10.1063/1.1286035](https://doi.org/10.1063/1.1286035)
30. Bailey NP, Christensen T, Jakobsen B, Niss K, Olsen NB, Pedersen UR, Schröder TB, Dyre JC (2008) Glass-forming liquids: one or more ‘order’ parameters? *J Phys: Condens Matter* 20(24):244113. doi:[10.1088/0953-8984/20/24/244113](https://doi.org/10.1088/0953-8984/20/24/244113)
31. Moynihan CT et al (1976) Structural relaxation in vitreous materials. *Ann NY Acad Sci* 279:15–35
32. Hecksher T, Olsen NB, Nelson KA, Dyre JC, Christensen T (2013) Mechanical spectra of glass-forming liquids. I. Low-frequency bulk and shear moduli of DC704 and 5-PPE measured by piezoceramic transducers. *J Chem Phys* 138(12):12A543-512
33. Russina O, Beiner M, Pappas C, Russina M, Arrighi V, Unruh T, Mullan CL, Hardacre C, Triolo A (2009) Temperature dependence of the primary relaxation in 1-hexyl-3-methylimidazolium bis(trifluoromethyl)sulfonylimide. *J Phys Chem B* 113(25):8469–8474. doi:[10.1021/jp900142m](https://doi.org/10.1021/jp900142m)
34. Sangoro JR, Iacob C, Naumov S, Valiullin R, Rexhausen H, Hunger J, Buchner R, Strehmel V, Karger J, Kremer F (2011) Diffusion in ionic liquids: the interplay between molecular structure and dynamics. *Soft Matter* 7(5):1678–1681
35. Kwon H-J, Seo J-A, Iwahashi T, Ouchi Y, Kim D, Kim HK, Hwang Y-H (2013) Study of alkyl chain length dependent characteristics of imidazolium based ionic liquids [C_nMIM]⁺[TFSA]⁻ by Brillouin and dielectric loss spectroscopy. *Curr Appl Phys* 13(1):271–279. doi:[10.1016/j.cap.2012.07.023](https://doi.org/10.1016/j.cap.2012.07.023)
36. Leys J, Wubbenhorst M, Menon CP, Rajesh R, Thoen J, Glorieux C, Nockemann P, Thijs B, Binnemans K, Longuemart S (2008) Temperature dependence of the electrical conductivity of imidazolium ionic liquids. *J Chem Phys* 128(6):064509
37. Tokuda H, Hayamizu K, Ishii K, Susan MABH, Watanabe M (2005) Physicochemical properties and structures of room temperature ionic liquids. 2. Variation of alkyl chain length in imidazolium cation. *J Phys Chem B* 109(13):6103–6110. doi:[10.1021/jp044626d](https://doi.org/10.1021/jp044626d)
38. Widegren JA, Magee JW (2007) Density, viscosity, speed of sound, and electrolytic conductivity for the ionic liquid 1-hexyl-3-methylimidazolium bis(trifluoromethylsulfonyl)imide and its mixtures with water. *J Chem Eng Data* 52(6):2331–2338. doi:[10.1021/je700329a](https://doi.org/10.1021/je700329a)
39. Angell CA (1991) Relaxation in liquids, polymers and plastic crystals—Strong/fragile patterns and problems. *J Non-Crystal Solids* 131(1):13–31
40. Bohmer R, Ngai KL, Angell CA, Plazek DJ (1993) Nonexponential relaxations in strong and fragile glass formers. *J Chem Phys* 99(5):4201–4209
41. Sergei V, Dzyuba RAB (2002) Influence of structural variations in 1-alkyl(aralkyl)-3-methylimidazolium hexafluorophosphates and bis(trifluoromethylsulfonyl)imides on physical properties of the ionic liquids. *ChemPhysChem* 3(2):161–166. doi:[10.1002/1439-7641\(20020215\)3:2<161:AID-CPHC161>3.0.CO;2-3](https://doi.org/10.1002/1439-7641(20020215)3:2<161:AID-CPHC161>3.0.CO;2-3)
42. Andanson JM, Meng X, Traikia M, Husson P (2016) Quantification of the impact of water as an impurity on standard physico-chemical properties of ionic liquids. *J Chem Thermodyn* 94:169–176. doi:[10.1016/j.jct.2015.11.008](https://doi.org/10.1016/j.jct.2015.11.008)
43. Chan RK, Pathmanathan K, Johari GP (1986) Dielectric relaxations in the liquid and glassy states of glucose and its water mixtures. *J Phys Chem* 90:6358–6362
44. Gobrecht H, Hamann K, Willers G (1971) Complex plane analysis of heat capacity of polymers in the glass transition region. *J Phys E: Sci Instruments* 4:21–23
45. Corbino OM (1911) Periodische Widerstandsänderungen feiner Metallfäden, die durch Wechselströme zum Glühen gebracht werden, sowie Ableitung ihrer thermischen Eigenschaften bei hoher Temperatur. *Physik Zeitschr XII*:292–295
46. Corbino OM (1910) Thermische Oszillationen wechselstromdurchflossener Lampen mit dünnem Faden und daraus sich ergebende Anwesenheit geradzahligter Oberschwingungen. *Physik Zeitschr XI*:413–417
47. Birge NO, Nagel SR (1987) Wide-frequency specific heat spectrometer. *Rev Sci Instrum* 58(8):1464–1470

48. Birge NO, Nagel SR (1985) Specific-heat spectroscopy of the glass transition. *Phys Rev Lett* 54(25):2674–2677
49. Christensen T (1985) The frequency dependence of the specific heat at the glass transition. *J Phys (Paris)* 46(12):C8-635–C638-637
50. Christensen T, Olsen NB (1997) How to compare the frequency-dependent adiabatic compressibility with other thermoviscoelastic response functions at the glass-transition. *Prog Theor Phys Suppl* 126:273–276
51. Christensen T, Olsen NB, Dyre JC (2007) Conventional methods fail to measure $c_{\text{sub}}^{\text{p}}$ (omega) of glass-forming liquids. *Phys Rev E (Stat Nonlinear Soft Matter Phys)* 75(4):041502–041511
52. Christensen T, Olsen NB, Dyre JC (2008) Can the frequency dependent isobaric specific heat be measured by thermal effusion methods? In: AIP conference proceedings, pp 139–141
53. Igarashi B, Christensen T, Larsen EH, Olsen NB, Pedersen IH, Rasmussen T, Dyre JC (2008) A cryostat and temperature control system optimized for measuring relaxations of glass-forming liquids. *Rev Sci Instr* 79(4):045105–045113
54. Roed LA, Niss K, Jakobsen B (2015) Communication: high pressure specific heat spectroscopy reveals simple relaxation behavior of glass forming molecular liquid. *J Chem Phys* 143(22):221101. doi:[10.1063/1.4936867](https://doi.org/10.1063/1.4936867)
55. Christensen T, Jakobsen B, Papini J, Hecksher T, Dyre JC, Olsen NB (2011) A combined measurement of thermal and mechanical relaxation. *J Non-Crystal Solids* 357(2):346–350. doi:[10.1016/j.jnoncrysol.2010.07.051](https://doi.org/10.1016/j.jnoncrysol.2010.07.051)
56. Jakobsen B, Olsen NB, Christensen T (2010) Frequency-dependent specific heat from thermal effusion in spherical geometry. *Phys Rev E* 81(6):061505
57. Cammenga HK, Eysel W, Gmelin E, Hemminger W, Hohne GWH, Sarge SM (1993) The temperature calibration of scanning calorimeters: Part 2. Calibration substances. *Thermochim Acta* 219:333–342
58. Hohne GWH, Cammenga HK, Eysel W, Gmelin E, Hemminger W (1990) The temperature calibration of scanning calorimeters. *Thermochim Acta* 160(1):1–12
59. Sarge SM, Gmelin E, Hohne GWH, Cammenga HK, Hemminger W, Eysel W (1994) The calorimetric calibration of scanning calorimeters. *Thermochim Acta* 247(2):129–168
60. Sarge SM, Hemminger W, Gmelin E, Hohne GWH, Cammenga HK, Eysel W (1997) Metrologically based procedures for the temperature, heat and heat flow rate calibration of DSC. *J Therm Anal* 49:1125–1134
61. Hensel A, Schick C (1997) Temperature calibration of temperature-modulated differential scanning calorimeters. *Thermochim Acta* 305:229–237
62. Schick C, Jonsson U, Vassilev T, Minakov A, Schawe J, Scherrenberg R, Lörcinzy D (2000) Applicability of 8OCB for temperature calibration of temperature modulated calorimeters. *Thermochim Acta* 347:53–61
63. Neuenfeld S, Schick C (2006) Verifying the symmetry of differential scanning calorimeters concerning heating and cooling using liquid crystal secondary temperature standards. *Thermochim Acta* 446(1–2):55–65
64. Merzlyakov M, Schick C (2001) Simultaneous multi-frequency TMDSC measurements. *Thermochim Acta* 377(1–2):193–204
65. Merzlyakov M, Schick C (1999) Complex heat capacity measurements by TMDSC Part 1. Influence of non-linear thermal response. *Thermochim Acta* 330:55–64
66. Hensel A, Merzlyakov M, Schick C (1998) Nonlinear response in TMDSC. DPG Frühjahrstagung
67. Merzlyakov M, Schick C (2001) Step response analysis in DSC—A fast way to generate heat capacity spectra. *Thermochim Acta* 380(1):5–12
68. Merzlyakov M, Hohne GWH, Schick C (2002) Calibration of magnitude and phase angle of a TMDSC signal Part 2: calibration practice. *Thermochim Acta* 391(1–2):69–80. doi:[10.1016/S0040-6031\(02\)00164-8](https://doi.org/10.1016/S0040-6031(02)00164-8)
69. Hohne GWH, Merzlyakov M, Schick C (2002) Calibration of magnitude and phase angle of a TMDSC signal Part 1: basic considerations. *Thermochim Acta* 391(1–2):51–67

70. Merzlyakov M, Schick C (1999) Complex heat capacity measurements by TMDSC Part 2: algorithm for amplitude and phase angle correction. *Thermochim Acta* 330:65–73
71. Weyer S, Hensel A, Schick C (1997) Phase angle correction for TMDSC in the glass-transition region. *Thermochim Acta* 305:267–275. doi:[10.1016/S0040-6031\(97\)00180-9](https://doi.org/10.1016/S0040-6031(97)00180-9)
72. Huth H, Minakov AA, Serghei A, Kremer F, Schick C (2007) Differential AC-chip calorimeter for glass transition measurements in ultra thin polymeric films. *Eur Phys J Spec Top* 141 (1):153–160
73. Huth H, Minakov AA, Schick C (2006) Differential AC-chip calorimeter for glass transition measurements in ultrathin films. *J Polym Sci B Polym Phys* 44:2996–3005
74. Huth H, Minakov A, Schick C (2005) High sensitive differential AC-chip calorimeter for nanogram samples. *Netsu Sokutei* 32(2):70–76
75. Shoifet E, Chua YZ, Huth H, Schick C (2013) High frequency alternating current chip nano calorimeter with laser heating. *Rev Sci Instr* 84(7):073903–073912. doi:[10.1063/1.4812349](https://doi.org/10.1063/1.4812349)
76. Ahrenberg M, Shoifet E, Whitaker KR, Huth H, Ediger MD, Schick C (2012) Differential alternating current chip calorimeter for in situ investigation of vapor-deposited thin films. *Rev Sci Instr* 83(3):033902–033912
77. Kraftmakher Y (2004) Modulation calorimetry, vol XII. In: Theory and applications. Springer, Berlin
78. Sullivan P, Seidel G (1967) AC temperature measurement of changes in heat capacity of beryllium in a magnetic field. *Phys Lett* 25A(3):229–230
79. Paulechka YU, Blokhin AV, Kabo GJ, Strechan AA (2007) Thermodynamic properties and polymorphism of 1-alkyl-3-methylimidazolium bis(triflamides). *J Chem Thermodyn* 39 (6):866–877. doi:[10.1016/j.jct.2006.11.006](https://doi.org/10.1016/j.jct.2006.11.006)
80. Verevkin SP, Zaitsau DH, Emel'yanenko VN, Ralys RV, Yermalayeu AV, Schick C (2013) Does alkyl chain length really matter? Structure-property relationships in thermochemistry of ionic liquids. *Thermochim Acta* 562:84–95. doi:<http://dx.doi.org/10.1016/j.tca.2013.04.003>
81. Rivera A, Rössler EA (2006) Evidence of secondary relaxations in the dielectric spectra of ionic liquids. *Phys Rev B* 73(21):212201
82. Griffin P, Agapov AL, Kisliuk A, Sun X-G, Dai S, Novikov VN, Sokolov AP (2011) Decoupling charge transport from the structural dynamics in room temperature ionic liquids. *J Chem Phys* 135(11):114509. doi:[10.1063/1.3638269](https://doi.org/10.1063/1.3638269)
83. Tokuda H, Hayamizu K, Ishii K, Susan MABH, Watanabe M (2004) Physicochemical properties and structures of room temperature ionic liquids. 1. Variation of anionic species. *J Phys Chem B* 108(42):16593–16600. doi:[10.1021/jp047480r](https://doi.org/10.1021/jp047480r)
84. Bulut S, Eiden P, Beichel W, Slattery JM, Beyersdorff TF, Schubert TJS, Krossing I (2011) Temperature dependence of the viscosity and conductivity of mildly functionalized and non-functionalized [Tf₂N]⁻ ionic liquids. *ChemPhysChem* 12(12):2296–2310. doi:[10.1002/cphc.201100214](https://doi.org/10.1002/cphc.201100214)
85. Hempel E, Huth H, Beiner M (2003) Interrelation between side chain crystallization and dynamic glass transitions in higher poly(n-alkyl methacrylates). *Thermochim Acta* 403 (1):105–114
86. Donth E (1992) Relaxation and thermodynamics in polymers, glass transition. Akademie, Berlin
87. Angell CA (1968) Oxide glasses in light of the “Ideal Glass” concept: I, ideal and nonideal transitions, and departures from ideality. *J Am Ceram Soc* 51(3):117–124. doi:[10.1111/j.1151-2916.1968.tb11854.x](https://doi.org/10.1111/j.1151-2916.1968.tb11854.x)

Index

A

AC-calorimetry, 214, 221
Activation energy, 79, 90, 108
Activation volume, 77, 79–81, 86
Adam and Gibbs, 229
Ammonium, 2, 17
Anisotropy, 62, 64
Aprotic, 10, 80, 98
Aprotic ionic liquids, 1, 3, 6, 9, 14, 30, 96, 100, 225
Arrhenius law, 77, 87
Atomic force microscopy, 158, 174
Avramov model, 91, 92, 102

B

Bis(trifluoromethylsulfonyl)imide, 4, 6, 9, 11, 16, 32, 115
Broadband dielectric spectroscopy (BDS), 29, 31, 33, 115, 117
Broadband impedance spectroscopy, 158

C

Capacitor, 74, 135
Carvedilol, 80, 87, 96
Charge transport, 30, 32, 36–39, 42, 45, 47, 48, 92, 115, 122, 125, 194, 209
Charge transport rate, 42
CKN, 86, 98, 215
C₈MIM NTf₂, 78, 88, 225, 227
Cole-Cole equation, 37, 134
Complex heat capacity, 219–221
Compression, 89, 110, 140
Conductivity relaxation times, 83, 88, 99–101, 108
Cooling rate, 6, 9, 82, 213, 220, 227
Counterions, 100, 109, 131
Coupling, 16, 63, 153

D

Dc- conductivity, 29, 36, 39, 41, 43, 56, 77, 132, 133, 135, 138
Debye length, 135, 136
Debye–Stokes–Einstein, 42, 101, 103, 153
Decoupling, 94, 100, 104, 108, 122, 125, 140, 149, 151, 153, 214, 215, 219, 228
Decoupling index, 103, 105, 108, 110
Density, 13, 14, 44, 87, 93, 109, 135, 137, 138, 154, 168
Density fluctuations, 87, 91, 173
Density scaling, 89, 94, 102
Dicyanamide, 6, 9, 56, 58
Dielectric loss, 55, 57, 59, 62, 132, 133, 196, 210, 217
Dielectric relaxation, 37, 54, 131, 133, 134, 138, 146, 154, 216, 219, 223
Differential scanning calorimetry (DSC), 9, 29, 40, 116
Diffusion, 10, 17, 29, 38, 41, 43, 46–48, 62, 86, 99, 104, 107, 125, 146, 160
Dilatometric, 82, 102
Dimethylphosphate, 9
Dimethylsulfoxide (DMSO), 11, 15
Dipolarity, 14
Dissociation energy, 137
Double layer capacitance, 158, 163, 164, 167
DTg/dP coefficient, 84
Dynamic Bond Percolation model, 141, 142, 148, 149, 153

E

Effective medium approximation (EMA), 123, 124
Effective number density, 41, 43, 48
Einstein relation, 43, 145
Einstein–Smoluchowski relations, 41, 44, 46–48

- Electrode polarization, 29, 34, 38, 117, 124, 137, 138, 145, 194, 195, 199, 202, 206, 210, 211
- Ethylammonium nitrate (EAN), 62–64, 66, 176
- Ev/Ep ratio, 94
- F**
- FAP, 11, 164, 166, 178
- Force-distance curves, 175, 177, 178, 182, 184
- Formate, 3
- Fragile, 84
- Fragility, 84, 86, 153, 222
- Free-volume, 146, 148
- Functionalized ionic liquid, 3, 5, 6
- G**
- Glass, 77, 99, 107, 147
- Glass transition pressure, 82, 99, 106
- Glass transition temperature, 1–3, 6, 8, 9, 17, 19, 38–40, 75, 77, 81, 82, 84, 86, 90, 99, 102, 116, 121, 122, 125, 142, 214, 222, 227
- Glassy dynamics, 32, 48, 115, 122, 124–126
- Green-Kubo relations, 43, 44
- Grotthuss mechanism, 86, 97, 101, 108
- H**
- Havriliak-Negami, 37, 38, 118, 120, 133
- Heat capacity, 82, 116, 193, 214, 215, 219–221, 229
- Heat capacity spectroscopy, 219
- Herringbone reconstruction, 166, 167
- Hexafluorophosphate, 6, 11, 12, 16, 32, 179
- High-pressure, 74–76, 80, 81, 83, 84, 87, 89, 95, 99, 100, 102, 109, 140
- High-pressure chamber, 76
- Hydrochloride, 80, 91, 96, 100, 107
- Hydrogen bond accepting ability, 15, 16
- Hydrogen bond donating ability, 15, 16
- Hyperfine coupling constant, 16
- I**
- Imidazolium, 4, 6, 9, 10, 12, 16, 17, 32, 35, 45, 54, 56, 61, 80, 96, 97, 171, 179, 184–186
- Intermolecular potential, 89, 93
- Ionicity, 17
- Ionic transport, 43, 44, 77, 131, 132, 142, 145–149, 151–154
- Ion number density, 135–137
- Isobaric expansivity, 90
- Isochronal, 82, 86, 90, 99, 100, 214, 221
- Isochronal expansivity, 90
- K**
- Kamlet–Taft equation, 14
- Kramers-kronig relations, 37, 56, 134, 162, 207–209
- L**
- Lidocaine, 81, 83, 98, 100, 105, 107–109
- Light modulated calorimeter (LMC), 221
- Liquid range, 3, 5, 6, 9, 10, 44
- LiTFSI, 132, 134, 152
- Litium perchlorate, 132, 138
- M**
- Macdonald–Trukhan model, 135
- Maxwell relation, 42, 105, 108, 215
- Melting point, 2, 6, 9, 30, 44, 132, 173
- Microphase separation, 132, 141, 143
- Modulus, 37, 38, 76, 77, 89, 118, 119, 214, 215, 217
- Molecular dynamics, 31, 37, 53, 54, 59, 61, 64–66, 84, 96, 116, 125, 126, 169, 173, 188
- Molecular dynamics simulations, 173
- Multilayer Structure, 169, 188
- N**
- Nafion, 81
- O**
- Optical Kerr effect, 61, 62
- P**
- Phase separation, 132, 141
- pK_a , 106, 107
- Poisson equation, 135
- Polarity, 3, 14, 16, 17
- Polarizability, 15, 16, 36, 55, 59, 61, 62
- Poly-BuVIm NTf₂, 99, 101
- Polymer, 2, 3, 5, 17, 120, 125, 132–134, 138, 142, 145, 146, 148–151, 153, 154, 214
- Polymer electrolytes, 131, 132, 134, 138, 140, 143, 145–149, 151, 153, 154
- Polymerized ionic liquid (PIL), 1, 3, 17–19, 98, 99, 101, 108, 110, 116, 117, 126, 131, 132, 152, 154, 214
- Propylene glycols, 132, 138
- Protic ionic liquid, 1–4, 10, 12, 17, 30, 78, 80, 96, 103, 107, 108
- Proton transfer, 97, 98, 101, 102, 107–109
- PVT, 89, 102
- Pyrrrolidinium, 6, 10, 12, 165, 167
- R**
- Random barrier model, 36, 38
- Reichardt's dye, 14, 16
- Relative permittivity, 14, 55

S

Salts, 1, 2, 10, 57, 73, 80, 96, 100, 107, 115, 132, 137, 143, 149

Scaling exponent, 94–96, 102

Scanning tunneling microscopy, 167

Segmental relaxation, 101, 103, 138, 140–143, 145, 147, 149, 150, 153

Shear modulus, 42, 214–217

Shell-isolated nanoparticle-enhanced Raman spectroscopy, 185, 186

Solvation dynamics, 60, 61

Solvatochromic dye, 14–16

Solvent, 2, 5, 10, 14, 18, 32, 45, 54, 56, 58, 60, 61, 98, 116, 145, 146, 149, 151, 194

Spin probes, 14, 16

Stokes shift, 60

Structural relaxation time, 90, 103–105, 108, 145

Sum-frequency generation vibrational spectroscopy, 158

Supercooled, 30, 48, 78, 82, 93, 225

Surface-enhanced Raman spectroscopy, 158, 185, 186

Surface force apparatus (SFA), 158, 180–182, 184

T

Tait formula, 102

Temperature-modulated differential scanning calorimetry (TMDSC), 103, 105, 214, 223

Terahertz spectroscopy, 54

Tetrafluoroborate, 11, 12

Thermal compressibility, 215

Thermal energy fluctuations, 88

Thermal expansion coefficient, 14, 82, 147

Thermogravimetric analysis (TGA), 9

Time-resolved infrared spectroscopy, 55

Triflate, 6

Tris(pentafluoroethyl)trifluorophosphate, 6, 11, 164

Turnbull and Cohen, 146

V

Van der Waals, 45, 80, 84, 90

Vehicle conduction, 99, 102

Vehicle-type mechanism, 98

Viscosity, 10, 13, 39, 42, 66, 84, 93, 100, 116, 151, 214, 217

Vogel–Fulcher–Tammann–Hesse equation, 13

W

Walden rule, 84, 96, 100, 102

X

X-ray reflectivity, 158, 171, 172